THESIS DISSERTATION

Pouch cell fabrication process optimisation through physico-chemical modelling and characterisation

LAURA OCA PEREZ

Electronics and Computer Science Department
Mondragon Unibertsitatea

Directed by
DR. UNAI IRAOLA
Electronics and Computer Science Department
Mondragon Unibertsitatea

Codirected by
DR. EMILIE BEKAERT
Battery Post-Mortem Analysis and Ageing
CIC energiGUNE

In ARRASATE, 10th December 2020

PHD PROGRAM IN

APPLIED ENGINEERING

Mondragon Unibertsitatea
Goi Eskola Politeknikoa
Faculty of Engineering

CIC energiGUNE
MEMBER OF BASQUE RESEARCH & TECHNOLOGY ALLIANCE

Pouch cell fabrication process optimisation through physico-chemical modelling and characterisation

LAURA OCA PEREZ
Electronics and Computer Science Department
Mondragon Unibertsitatea

Directed by
DR. UNAI IRAOLA
Electronics and Computer Science Department
Mondragon Unibertsitatea

Codirected by
DR. EMILIE BEKAERT
Battery Post-Mortem Analysis and Ageing
CIC energiGUNE

Submitted in partial fulfillment of the requirements
for the Degree of Philosophy under the program:
APPLIED ENGINEERING

Thesis Committee:

President: Dr. Mikaël Cugnet (French Atomic and Alternative Energy Commission)
Vocal: Dr. Nicolas Guillet (French Atomic and Alternative Energy Commission)
Vocal: Dr. Fridolin Röder (University Bayreuth)
Vocal: Dr. Laida Otaegui (CIC energiGUNE)
Secretary: Dr. Eduardo Miguel (Mondragon Unibertsitatea)

In ARRASATE, 10th December 2020

Dedicated to Xabi

"Science and everyday life cannot and should not be separated"

— Rosalind Franklin

STATEMENT OF ORIGINALITY

I hereby declare that the research recorded in this thesis and the thesis itself were developed entirely by myself at the Energy Storage group, Electronics and Computer Science Department, at Mondragon Unibertsitatea.

The simulations and experiments of this thesis were developed entirely by myself, with the following exceptions:

- Experimental measurements identified with footnotes in Chapters 3, 4 and 5.
- The interface between COMSOL Multiphysics® and MATLAB® that was generated by Eduardo Miguel.

ACKNOWLEDGMENTS

First, I would like to thank my supervisor Dr. Unai Iraola for the guidance and support during the thesis. Ha sido y será siempre un placer trabajar contigo y poder complementar el trabajo con tu punto de vista y perspectiva.

I would also like to thank Mondragon Unibertsitatea for giving me the opportunity of performing this thesis, specially to Dr. Jon Andoni Barrena and José Maria Canales. Burura etortzen zait 2017ko ekaina bukaerako Jonanen telefono deiak tesirako dokumentuak prest zeudela esanez. Tesia egitea nahi nuela banekien, baino tesiko laburpena irakurri nuenean gaiaz maitemindu nintzen. Special thanks to "P2D team" (Edu, Eneko Agirrezabala and Iker). Aipamen berezia egin nahi dut Eneko Agirrezabalaren ekarpenentzako. Zure lana izugarri erraztu du test experimentalen post-prozesua. Moreover, to the energy storage systems research group (Ander, Iosu, Argiñe, Erik, Oier, Xabier...) your work and perseverance inspired me and the support during the thesis was of great importance to finish this work. Moreover I would like to thank to "Bazkaria team" for all the coffee and meal breaks which help me to disconnect (Eneko, Julen, Carlos, Dani, Edu, Santiso, Imanol, Iosu Marzo, Xabier Badiola, Irati, Txef). Porque está "estadísticamente demostrado" que una parada es suficiente para desconectar, si la haces adecuadamente. I would also like to acknowledge all the Electronics and Computing department members.

I would also like to express my gratitude to CIC energiGUNE, my co-supervisor Dr. Emilie Bekaert and Aitor Villaverde for welcoming me in the center. Mila esker Laida aholku eta nireking egondako denbora guztiagatik, zure esperientzia eta aholkuak asko lagundu dute tesian zehar. Special thanks for all the prototyping and post-mortem team for the experimental support (Alvaro, Emanuele, Ander, Haizea, Leire, Guillermo, Silvia, Amaia Quintela, Amaia Saenz de Buruaga, Marta, Jon Ajuria, Nick, Maica, Maria Arnaiz, June, Julen, Laida, Aitor, Emilie). Alvaro, tu afán de superación y tu perseverancia en investigación me han inspirado, no cambies. Por esos días de esperado café, Joseba y Gorka.

This research was financially supported by the Basque Government with the predoctoral program (PRE-2017-1-0272, PRE-2018-2-0117 and PRE-2019-2-0154).

A todos los amigos que han estado conmigo, a la cuadrilla de Vitoria (Ane, Álvaro, Laura, David, Marlon), a la de Lazkao (Naiara, Barandi, Lago, Salinas, Eren, Kepa y Myriam) y a los amigos que me han ayudado a desconectar de la tesis y a ser feliz (Alba, Leire, Maite, Garazi, Joseba, Alazne, Borjita, Ugaitz, Igarki, Ander).

A mi familia, a ama y aita por la paciencia que habéis tenido a lo largo de estos años, sobre todo en los momentos finales de este período. A mis abuelos, porque su valor y sacrificio han facilitado que hayamos tenido una educación de calidad y unos valores familiares fuertes. Nos han inculcado los valores del esfuerzo y sacrificio tan necesarios para prosperar en la vida. Gracias también a todos mis tíos y primos por arroparme y comprenderme durante la tesis. A Anun, Luis, Iñaki y toda la familia por preocuparse tanto por mi bienestar y acogerme en la familia. Para terminar, me gustaría agradecerle y dedicarle la tesis a Xabi, por la paciencia que ha tenido durante toda mi etapa académica y por el nuevo camino que nos espera.

ABSTRACT

The world is facing an energy revolution, seeking more sustainable based energy solutions while the global energy demand is increasing. New trends in energy consumption and new applications have arisen in which energy storage systems are essential. Nevertheless, available energy storage systems do not meet the requirements for these new applications. Current options do not achieve energy density goals and the fast charging rate necessary for electro-mobility, which is slowing the entrance of such vehicles into the market.

In order to enhance energy storage systems, new concepts and materials are being developed with the objective of achieving better performance, efficiency and sustainability. To that end, accelerated redesigns based on physics-based models are of great importance, linking the desired material properties to process parameters. Models reduce the time and cost of development of new technologies and the redesign of existing ones, as they decrease the number of experiments that are necessary for proof of concept.

In this context, the main objective of this thesis is to optimise the fabrication process of a pouch cell based on physico-chemical modelling and characterisation. To achieve this objective, a characterisation procedure based on physico-chemical measurements was developed. Then, the cross-linked influences of the battery fabrication process parameters and final cell performance were evaluated based on the previously developed procedure. Finally, a model-based optimisation methodology for inverse cell design was proposed and validated.

Among the contributions of this thesis, two points can be highlighted. On the one hand, a new characterisation protocol for a pseudo-two-dimensional model of commercial and prototyping pouch cells was validated. The characterisation methodology is of great importance for optimisation and comparison analysis as the experimental data must be significant and reliable. On the other hand, an inverse cell design methodology was proposed based on design of experiments and electrochemical modelling. A general model was developed to describe different process parameter changes. The material-process-model relationships implemented in this thesis were then validated against experimental results.

LABURPENA

Gizartea trantsizio energetiko batean murgilduta dago; erregai fosilengan dagoen dependentziatik energia iturri jasangarrirantz, mundu mailako energia kontsumoa handitzen ari den bitartean. Gainera, energia kontsumo joera eta aplikazio berriak sortzen ari dira; non energia metatzeko sistemak ezinbestekoak diren. Hala ere, merkatuan dauden energia metatzeko sistemek ez dituzte aplikazio berri hauetarako eskakizunak betetzen. Egungo aukerek ez dituzte elektromugikortasunerako beharrezkoak diren helburuak lortzen: energia dentsitate altua eta karga azkarra. Muga horiek, merkatuan ibilgailu elektrikoen sarrera moteltzea ekarri du.

Energia metatzeko sistemak hobetzeko asmoz, kontzeptu eta material berriak garatzen ari dira portaera, eraginkortasun eta iraunkortasun hobea bilatuz. Horretarako, alderantzizko diseinu metodologia eraginkorren erabilera funtsezkoa da. Metodologia horietan, fisikan oinarritutako ereduak erabiltzeak prozesu parametroen influentzia baterien portaeran aurreikustea laguntzen du. Gainera, alderantzizko metodologiek diseinu berriak edo birmoldaketak garatzeko denbora eta prezioa murriztu dezakete. Izan ere, kontzeptua frogatzeko beharrezkoak diren esperimentu kopurua gutxitu dezakete.

Testuinguru honetan, tesi honen helburu nagusia "pouch cell" motako fabrikazio prozesua optimizatzea da, eredu eta ezaugarritze fisiko-kimikoetan oinarrituta. Helburu hori lortzeko lehenik eta behin, neurketa fisiko-kimikoetan oinarritutako ezaugarritze prozedura garatu zen. Ondoren, prozesu-parametroen eta zeldaren portaeraren arteko influentziak ebaluatu ziren aurretik garatutako prozedurarekin. Azkenik, zelden diseinurako alderantzizko metodologia proposatu eta balioztatu zen.

Tesi honen ekarpenen artean, bi puntu nabarmendu daitezke. Alde batetik, "P2D" motako eredu elektrokimikorako beharrezkoak diren parametroak metodologia berri batekin lortu dira. Ezaugarritze fisiko-kimikoan oinarrituko metodologia balioztatua izan da. Ezaugarritze metodologiak garrantzi handia du optimizazio eta alderatze analisientzako. Izan ere, datu esperimentalak esanguratsuak eta fidagarriak izan behar dira optimizatzeko joerak ikusi ahal izateko. Bestalde, zelden diseinurako alderantzizko metodologia proposatu da esperimentu diseinu metodologian eta eredu elektrokimikoetan oinarrituta. Eredu orokor bat proposatu da prozesuaren parametro aldaketa desberdinak deskribatzeko. Material-prozesu-eredu erlazioak emaitza esperimentalen bidez balioztatu dira.

RESUMEN

El mundo se encuentra inmerso en una revolución energética buscando soluciones energéticas más sostenibles, mientras que la demanda mundial de energía está aumentando. Además, están surgiendo nuevas tendencias en el consumo de energía y nuevas aplicaciones en las que los sistemas de almacenamiento de energía son fundamentales. Sin embargo, los sistemas de almacenamiento de energía disponibles no cubren los requisitos para estas nuevas aplicaciones. Las tecnologías actuales no logran el objetivo de densidad energética y la velocidad de carga rápida necesarias para la electromovilidad, lo que está frenando la entrada de los vehículos eléctricos al mercado.

Con el fin de mejorar los sistemas de almacenamiento de energía, se están desarrollando nuevos conceptos y materiales que buscan mejorar su comportamiento, eficiencia y sostenibilidad. Para eso, los rediseños acelerados basados en modelos basados en la física son de gran importancia, analizando las influencias entre las propiedades deseadas de la celda con los parámetros del proceso de fabricación. Los modelos electroquímicos pueden reducir el tiempo y el dinero empleado en el desarrollo de nuevas tecnologías y el rediseño de las existentes, ya que pueden disminuir el número de experimentos que son necesarios para la prueba de concepto.

En este contexto, el objetivo principal de esta tesis es optimizar el proceso de fabricación de una celda ”pouch” a partir de modelos y caracterización físico-química. Para lograr este objetivo, en primer lugar, se ha desarrollado un procedimiento de caracterización basado en mediciones físico-químicas. A continuación, se evaluaron las influencias cruzadas entre los parámetros de proceso de fabricación de la batería y el comportamiento final de la celda basándose en el procedimiento desarrollado previamente. Finalmente, se ha propuesto y validado una metodología de optimización basada en modelos electroquímicos y diseño de experimentos para el diseño rápido de celdas.

Entre las aportaciones de esta tesis, cabe destacar dos puntos. Por un lado, se ha validado un nuevo protocolo de caracterización para el modelo electroquímico ”P2D” para celdas tipo ”pouch” comerciales y prototipadas. La metodología de caracterización es de gran importancia para la optimización y comparación entre distintas celdas, ya que los datos experimentales deben ser significativos y fiables. Por otro lado, se ha propuesto una metodología de rediseño de celda basada en el diseño de experimentos y modelos electroquímicos. Se ha propuesto un modelo general para describir diferentes cambios en los parámetros del proceso. Las relaciones material-proceso-modelo implementadas a lo largo de la tesis han sido validadas con resultados experimentales.

CONTENTS

ABBREVIATIONS

AI	**A**rtificial **I**ntelligence
ANN	**A**rtificial **N**eural **N**etwork
AM	**A**ctive **M**aterial
BMS	**B**attery **M**anagement **S**ystem
CAES	**C**ompressed **A**ir **E**nergy **S**torage
CC	**C**onstant **C**urrent
CE	**C**ounter **E**lectrode
CMC	**C**arboxyl**M**ethyl **C**ellulose
C-rate	**C**urrent**R**ate
DLS	**D**ynamic **L**ight **S**cattering
DOE	**D**esign **O**f **E**xperiments
DMC	**D**i**M**ethyl **C**arbonate
DOD	**D**epth **O**f **D**ischarge
DST	**D**ynamic **S**tress **T**est
EA	**E**volutionary **A**lgorithms
EC	**E**thylene **C**arbonate
ECM	**E**quivalent **C**ircuit **M**ethods
EDLC	**E**lectric **D**ouble **L**ayer **C**apacitor
EDS	**E**nergy **D**ispersive X-Ray **S**pectroscopy
EIS	**E**lectrochemical **I**mpedance **S**pectroscopy
EMC	**E**thy **M**ethyl **C**arbonate
ESS	**E**nergy **S**torage **S**ystem
FESS	**F**lywheel **E**nergy **S**torage **S**ystem
FFD	**F**ull **F**actorial **D**esign
FTIR	**F**ourier **T**ransform **I**nfrared spectroscopy
GA	**G**enetic **A**lgorithms
GCMS	**G**as **C**hromatography **M**ass **S**pectrometry
GITT	**G**alvanostatic **I**ntermittent **T**itriation **T**echnique
GT	**G**ame **T**heory-based optimisation
ICP	**I**nductively **C**oupled **P**lasma
ID	**ID**entification profile
HPPC	**H**ybrid **P**ulse **P**ower Characterization
KIB	Potassium **I**on **B**attery
KMC	**K**inetic **M**onte **C**arlo
LCO	**L**ithium **C**obalt **O**xide
LFP	**L**ithium Iron **P**hospate

LIB	**L**ithium **I**on **B**attery
LIC	**L**ithium **I**on **C**apacitor
LMO	**L**ithium **M**anganese **O**xide
LNCO	**L**ithium **N**ickel **C**obalt **O**xide
LSM	**L**east **S**quares **M**ethod
LTO	**L**ithium **T**itanate **O**xide
NCA	Lithium **N**ickel **C**obalt **A**luminium oxide
NIB	Sodium **I**on **B**attery
NIC	Sodium **I**on **C**apacitor
NiCd	**Ni**ckel **C**admium Battery
NiMH	**Ni**ckel **M**etal **H**ydride
NC	**N**on-**c**alendered electrode
NMC	Lithium **N**ickel **M**anganese **C**obalt oxide
NMR	**N**uclear **M**agnetic **R**esonance spectroscopy
NMP	**N**-**M**ethyl-2-**P**yrrolidone
MCMB	**M**eso**C**arbon **M**icro **B**eads
OCP	**O**pen**C**ircuit**P**otential
OCV	**O**pen**C**ircuit**V**oltage
P2D	**P**seudo **2** **D**imensional model
P3D	**P**seudo **3** **D**imensional model
PbA	Lead-acid battery
PDE	**P**artial **D**ifferential **E**quation
PE	**P**oly**E**thylene
PEIS	**P**otentiostatic **E**lectrochemical **I**mpedance **S**pectroscopy
PHES	**P**umped **H**ydroelectric **E**nergy **S**torage
PITT	**P**otentiostatic **I**ntermittent **T**itriation **T**echnique
PSO	**P**article **S**warm **O**ptimisation
PVDF	**P**oly**V**inyli**D**ene **F**luoride
qOCV	**q**uasi **O**pen**C**ircuit**V**oltage
RE	**R**eference **E**lectrode
RSM	**R**esponse **S**urface **M**ethodology
SAXS	**S**mall **A**ngle **X**-ray **S**cattering
SBR	**S**tyrene **B**utadiene **R**ubber
SEI	**S**olid **E**lectrolyte **I**nterphase
SEM	**S**canning **E**lectron **M**icroscopy
SIMS	**S**econdary **I**on **M**ass **S**pectroscopy
SMES	**S**uperconducting **M**agnetic **E**nergy **S**torage
SOC	**S**tate **O**f **C**harge
SOL	**S**tate **O**f **L**ithiation
SPM	**S**ingle **P**article **M**odel
SSB	**S**olid **S**tate **B**attery
SSPP	**S**teady **S**tate **P**otentiostatic **P**olarization

TEM	**T**ransmission **E**lectron **M**icroscopy
TGA	**T**hermo **G**ravimetric **A**nalysis
TES	**T**hermal **E**nergy **S**torage
TRL	**T**echnology **R**eadiness **L**evel
UDDS	**U**rban **D**ynamometer **D**riving **S**chedule
WE	**W**orking **E**lectrode
XPS	**X**-ray **P**hotoelectron **S**pectroscopy
XRD	**X**-**R**ay **D**iffraction
80D35M	T_{roll} =80 °C and G_{roll} = 35 µm.
80D55M	T_{roll} =80 °C and G_{roll} = 55 µm.
80D85M	T_{roll} =80 °C and G_{roll} = 85 µm.
100D55M	T_{roll} =100 °C and G_{roll} = 55 µm.
100D85M	T_{roll} =100 °C and G_{roll} = 85 µm.

GLOSSARY

Parameters

A_{cell} (m^2)	Total cell area
AM_{per} (%)	AM percentage
a_s (m^2 m^{-3})	Specific surface area
α (-)	Charge transfer coefficient
brug (-)	Bruggeman exponent
$c_{e,0}$ (mol m^{-3})	Initial electrolyte salt concentration
$c_{s,max}$, $c_{s,min}$ (mol m^{-3})	Maximum and minimum solid phase concentrations
C_{dl} (F m^{-2})	Electric double layer capacitance
D_e (m^2 s^{-1})	Salt diffusivity in the electrolyte
D_s (m^2 s^{-1})	AM diffusion coefficient
δ (m)	Prototyped cell thickness
E_m (Wh kg^{-1})	Specific energy
η (V)	Overpotential
ε_e (-)	Liquid phase volume fraction
ε_s (-)	Solid phase volume fraction
$\varepsilon_{non-act}$ (-)	Non-electrochemically active solid volumes
E_{act} (kJ mol^{-1})	Activation energies
f (s^{-1})	frequency
f_{excess} (-)	Negative excess capacity (electrode balancing parameter)
f_{loss} (-)	Positive lithium loss due to SEI formation (electrode balancing parameter)
G_{roll} (m)	Calendering step roller gap
H (m)	Height of the electrode
I_{ct} (A)	Electrode current
i_0 (A m^{-2})	Exchange current density
i_{loc} (A m^{-2})	Electrode current density
κ (S m^{-1})	Electrolyte conductivity
k (mol m^{-2} s^{-1})	Reaction rate coefficient
L (m)	P2D model domain thickness
L_{tot} (m)	Total cell thickness
m_{tot} (kg)	Total mass of all cell components
$m_{pen,Hg}$ (kg)	Weight of penetrometer and mercury
$m_{pen,Hg,sam}$ (kg)	Assembly weight (penetrometer, mercury and sample)
M_w (kg mol^{-1})	Molecular weight
M_L (kg m^{-2})	Mass loading of the electrode

N_{elec} (-)	Number of the electrode within the stack of a pouch cell
$offset_{EOD}$ (-)	Negative electrode SoL offset due to irreversible processes
n (-)	levels of the DOE matrix
P_m (W kg^{-1})	Specific power
Q (Ah)	Nominal cell capacity
q_L (N mm^{-1})	Calendering step line load
R_{film} (Ω m^2)	Particle film resistance
R_s (m)	AM particle radius
R_{SL} (-)	Slurry solid to liquid ratio
ρ_e (kg m^{-3})	electrolyte density
ρ_{slurry} (kg m^{-3})	Slurry density
ρ_{AM} (kg m^{-3})	Active material density
$\rho_{bulk,coating,Hg}$ (kg m^{-3})	Mercury porosimeter bulk coating density
ρ_{cc} (kg m^{-3})	Current collector density
ρ_{ph} (kg m^{-3})	Pycnometry coating density
$\rho_{skeletal,coating,Hg}$ (kg m^{-3})	Mercury porosimeter skeletal coating density
ρ_{Hg} (kg m^{-3})	Mercury density
r (m)	Radial coordinate
$scale_{coinTOpouch}$ (-)	Correction factor to correlate coin to pouch cell capacity
$scale_{corr}$ (-)	Capacity correction factor of each electrode
t (s)	time
σ (S m^{-1})	Solid phase conductivity
S (m^2)	Effective surface area between electrode and electrolyte
t_0^+ (-)	Transport number
T (K)	Temperature
T_{ref} (K)	Reference temperature for Ahrrenius equation
T_{roll} (K)	Calendering step roller temperature
τ (-)	Electrode tortuosity
θ_0 (-)	SoL of the electrode at 0% SoC
θ_{100} (-)	SoL of the electrode at 100% SoC
U_{ocp} (V)	AM open circuit potential
$V_{p,HL}$ (mL)	Maximum intruded mercury volume at the lowest considered pore diameter
$V_{p,LL}$ (mL)	Minimum intruded mercury volume at the highest considered pore diameter
W (m)	Width of the electrode
x (m)	Spatial coordinate across cell thickness
Z (mΩ)	Cell impedance
z_+	Cation charge number

Superscripts

c	Cell
e	Electrolyte
k	Factors of the DOE matrix
Li	Lithium metal foil
n	Negative electrode
p	Positive electrode
s	Separator

Subscripts

AM	Active material
add	Additive
avg	Average
binder	Binder content of the electrode
blade	Coating blade
bulk	Bulk measurement
cal	Calendered electrode
cc	Current collector
coin	Coin cell
CT	Coating thickness
dry	Coating after drying step
eff	Effective
irrev	Irreversible
exp	Experimental
max	Maximum
min	Minimum
ML	Mass loading
pouch	Pouch cell
rev	Reversible
rough	Electrode roughness
SA	Sample area
ske	Skeletal measurement
solid	Solid content in a slurry
solvent	Liquid content in a slurry
wet	Wet electrode

P2D Variables

c_e $(x,\ t)$ (mol m^{-3})	Concentration of Lithium in the electrolyte
$c_s(x,\ r,\ t)$	Lithium concentration in the solid particles
$c_{s,e}(x,\ t)$ (mol m^{-3})	Lithium concentration in the solid particles on the surface
j_{BV} $(x,\ t)$ (A m^{-2})	Butler-Volmer contribution to j_{tot}
j_{DL} $(x,\ t)$ (A m^{-2})	Double layer contribution to j_{tot}
j_{tot} $(x,\ t)$ (A m^{-2})	Flux of lithium out of a particle
$\phi_e(x,\ t)$ (V)	Potential of lithium in the electrolyte
$\phi_{dl}(x,\ t)$ (V)	Double layer potential
$\phi_s(x,\ t)$ (V)	Lithium in the solid particles

Constants

e	Elementary charge (1.60217662 10^{-19} C)
F	Faraday's constant (96485 sA mol^{-1})
N_A	Avogadro's constant (6.022 10^{23} mol^{-1})
R	Gas constant (8.314472 (J mol^{-1} K^{-1}))

Chapter 1

INTRODUCTION

Due to new trends in energy consumption, we are currently in a moment of energy transition in which energy storage systems are a key factor. For that reason an overview of the main challenges of energy storage systems are discussed in this chapter and our main objectives are presented. Furthermore, the outline of the document and the scientific contributions made throughout the thesis are summarised.

1.1 FRAMEWORK OF THE THESIS

The world is dealing with an energy revolution moving from the unsustainable fossil-fuel based energy approach to renewable energies. At the same time, there is an increase in global energy demand over the next three decades due to the industrialization of non-developed countries and new applications [1]. In Figure 1.1 a) the expected battery demand classified by application and region is presented for 2030. In the next 10 years the global battery demand is expected to increase by a factor of 14 [2]. In addition, energy storage systems will enable more than 850 million people to access electricity, combining batteries with microgrids, solar home systems and solar lanterns [2]. Figure 1.1 b) identifies the countries which have more difficulties accessing electricity. For this reason, we need to update the energy generation, transmission, distribution and storage to cope with future demand [3].

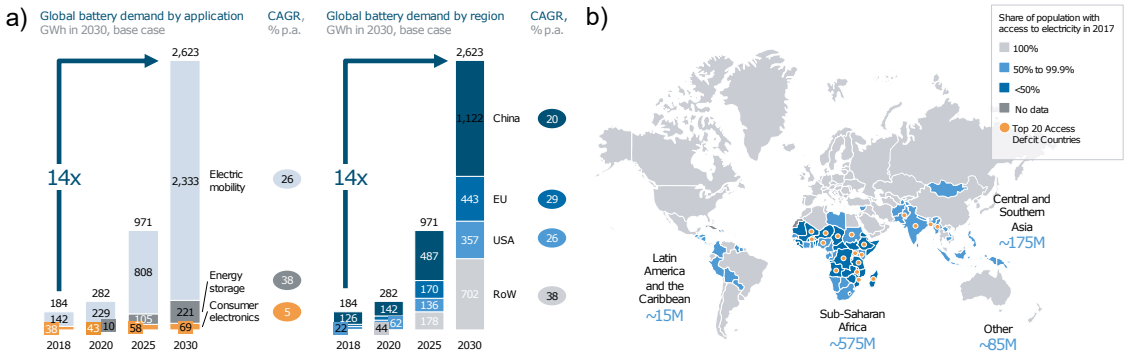

Figure 1.1: a) Global battery demand by application and region for 2030. Source: World Economic Forum, Global Battery Alliance (McKinsey analysis) [2]; b) Population share with access to electricity in 2017. Source: World Bank, 2017 (McKinsey analysis) [2].

While the worldwide energy demand rises, concerns about climate change on a global scale are also increasing. To counteract irreversible impacts, in the Paris Climate Conference 2015 (COP21) 195 countries reached the first universal climate agreement to promote a global action against climate change. In that global framework, participating countries agreed to keep the increase in global temperatures to below 2°C above pre-industrial levels, and to pursue efforts to limit the increase to 1.5°C [4].

Europe is committed to achieving a climate-neutral society by 2050. To that end, the European climate targets (Horizon 2030) for the next 10 years are [5]:

- Reduce EU domestic greenhouse gas emissions to at least 40% below the 1990 level.
- Achieve energy savings of 30%. The transition to a low-emission economy concerns sectors such as power generation, industry, transport, buildings, construction etc.
- Become gradually less dependent on externally generated energy, and to rely more on local renewable green resources.

At the Basque Country level, EnergyBasque has defined an energy strategy for 2030 [6]. The most relevant objectives are: a reduction of 17% in energy savings, promote renewable energies to increase their share in the energy mix up to 21%, reach a 25% share of alternative energies in on-road transport, and reduce annually 3Mt of greenhouse gases.

Therefore, energy storage systems are essential for energy transition as a wide range of applications require them. Stand-alone photovoltaic systems are one example of this,

as their energy generation is random and heavily dependent on climatic conditions [7]. Renewable energies could be integrated in a distributed generation environment in which smart grids are of great importance [8]. In addition, electro-mobility (trains, trams, electric vehicles etc.) is a critical area of research, as it is highly dependent on the advances of new storage systems [9]. Characteristics such as reduction of weight or volume are key for electro-mobility and portable devices, whereas for stationary applications the main point could be price or temperature range. There is no single solution for all applications, and many alternatives (technologies and formats) are available on the market.

The energy storage market underwent a major upheaval after Sony Corporation introduced the lithium-ion battery (LIB) in 1991 [10]. However, their potential cannot be fully exploited as manufacturers establish conservative voltage, temperature and current rate limits to prevent safety issues and premature battery failure in real applications. For this reason, there is clearly a need to upgrade cells to improve safety, durability and performance while decreasing the cost.

Nowadays, the battery manufacturing process is well-established for LIBs [11]. Although advances in the manufacturing process have upgraded the quality and reproducibility of the products [12, 13], and therefore the performance, there is still great scope for improvement. New concepts and materials are being developed so as to minimise scrap and energy consumption without an increase of manufacturing costs [14–16]. Performance, efficiency and sustainability of new cell designs will define future generations of batteries.

Modelling could be used [17, 18] to deal with the constant change in materials and manufacturing processes. Accelerated redesigns based on physics-based models are of great importance, cross-linking the desired material properties to process parameters. Physics-based models can help to understand the phenomena occurring inside batteries, and simulate cell behaviour under different operational conditions [19]. Moreover, models can reduce the time and cost of development of new technologies and the redesign of existing ones, as they can decrease the number of experiments that are necessary for proof of concept [20]. To this end, as shown in Figure 1.2, the European research initiative Battery 2030^{+} has defined a framework for inverse cell design, comprising modelling, experimental data and artificial intelligence [11].

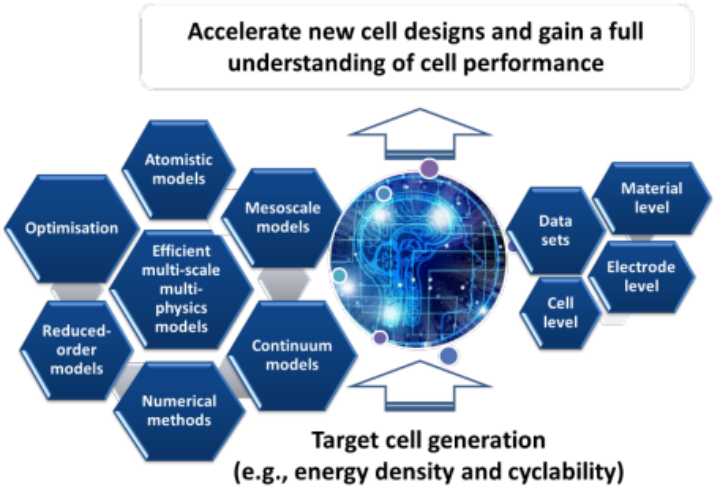

Figure 1.2: Battery 2030^{+} Roadmap vision for inverse cell design. Created by Elixabete Ayerbe [11].

Experimental data comprises material, electrode and cell-level characterisations. Such tests must be performed so as to introduce the battery component characteristics into an electrochemical model. The accuracy and predictions of the model will depend on the appropriateness of those characterisations and the consistency between model parameters [21]. Thus, parameter measurement or identification is of great importance in this research field. Equally important is the model validation. Currently, electrochemical models are being validated against device-level and non-invasive tests, allowing the quantification of the maximum differences between numerical predictions and cell experimental responses [22]. In order to use physics-based models for inverse cell design, internal variables need also to be checked. In the Battery 2030+ Roadmap [11] new types of embedded sensors have been identified (i.e. optical fibers, plasmonics, acoustics, electrochemical sensors), with the aim of integrating them in sophisticated Battery Management Systems (BMS).

Physic-based models are generally used for direct engineering problems. Nevertheless, for cell redesign purposes, an inverse engineering problem should be defined. In order to perform realistic optimisations, process limitations should be included in the proposal. Additionally, the synergism between numerical simulations, characterisation methodologies and fabrication processes will enable the enhancement of energy storage systems while reducing manufacturing costs.

1.2 OBJECTIVES

The main objective of this thesis is to optimise the fabrication process of a pouch cell based on physico-chemical modelling and characterisation. To this end three specific objectives have been defined which are set out in Figure 1.3:

[O1] Develop and validate a new physico-chemical parameter measurement methodology for a pseudo-two-dimensional model of commercial or prototyped cells.

[O2] Analyse the influence of the material processing stage on the final properties of the cell and include those influences in the model.

[O3] Design and validate a model-based optimisation tool capable of obtaining optimised cells with better performance than the reference.

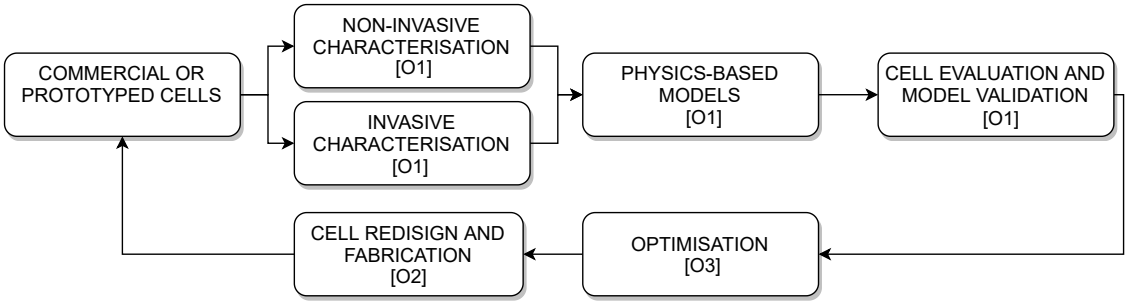

Figure 1.3: Link between the specific objectives of the thesis.

1.3 OUTLINE OF THE DOCUMENT

The structure of this document is shown in Figure 1.4, where the relationship between specific objectives, main contributions (see Section 1.4) and research gap identification with the thesis chapters and their description is presented.

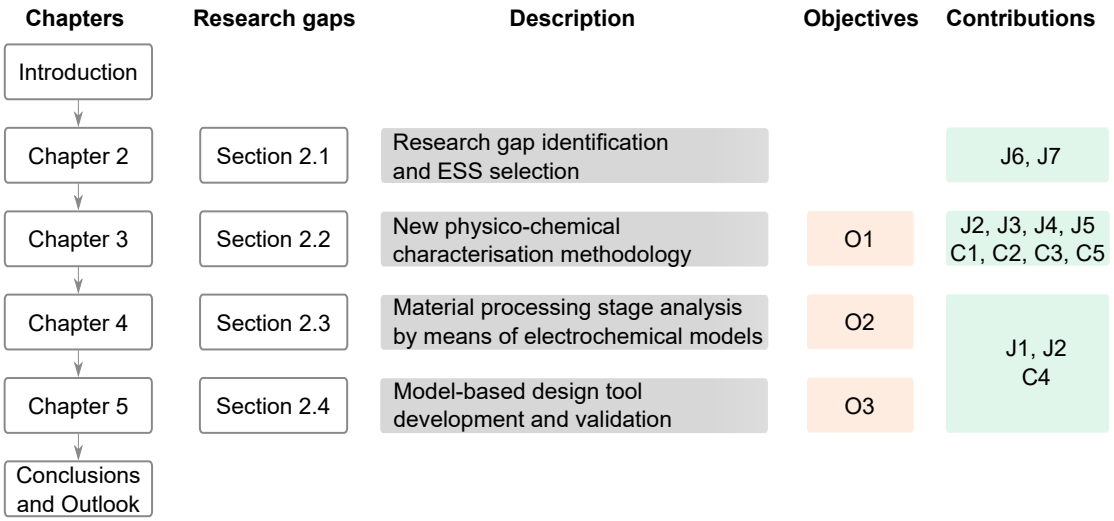

Figure 1.4: Thesis document outline and its relationship to the specific objectives and contributions.

In Chapter 2 a review of the main topics of the thesis: Energy Storage Systems (Section 2.1); Electrochemical modelling (Section 2.2); Battery manufacturing process (Section 2.3), and Battery design optimisation (Section 2.4) is outlined. The aim of this chapter is to identify the research gaps of the literature so as to tackle the highlighted problems and propose solutions to go beyond the state-of-the art. Moreover, a comparison and selection of the technology that is analysed during this thesis (i. e. lithium-ion battery, sodium-ion battery, solid-state battery, metal-air battery, supercapacitor and hybrid supercapacitors) is done.

Next, in Chapter 3 a new methodology for physico-chemical parameter measurement and validation is presented. In order to use an electrochemical model, first of all, the model parameters need to be determined and a complete validation of a wide operation range should be performed. Moreover, an insight into internal variable validation is addressed.

Chapter 4 is focused on the manufacturing process of batteries. Material processing stage is experimentally analysed to assess the influence of process parameters on the final performance of the prototyped cells. In addition, correlations between process and cell parameters are analysed so as to include those in the simulations.

In Chapter 5 the DOE methodology is used in conjunction with the electrochemical models to evaluate energy and power density responses of the cell as a function of design cell parameters variation. This evaluation procedure maximises cell performance and provides parameter trends so as to optimise the fabrication process of the studied cell.

Finally, in Chapter 6, the main conclusions are presented together with the future lines.

1.4 LIST OF CONTRIBUTIONS AND ORIGINAL WORK

In this section, the main scientific contributions and original work are presented.

1.4.1 Publications

Journal papers

[J1] L. Oca, L. Otaegui, A. Villaverde, E. Bekaert, E. Miguel, U. Iraola, Calendering process analysis by means of electrochemical modelling of NCA-graphite cells. **In preparation**.

[J2] L. Caizán, E. Gucciardi, L. Oca, E. Bekaert, I. Gandiaga, M. Arnaiz, J. Ajuria, Unraveling the technology behind the frontrunner LIC ULTIMO® to serve as a guideline for optimum lithium ion capacitor design, assembly and characterization. **Sent to Advanced Energy Materials.**

[J3] E. Miguel , Gregory L. Plett, M. Scott Trimboli, I. Lopetegi, L. Oca, U. Iraola, E. Bekaert, Electrochemical Model and Sigma Point Kalman Filter based Online Oriented Battery Model. **Sent to IEEE Access, under review, 2021.**

[J4] L.Oca, E. Miguel, E. Agirrezabala, A. Herran, E. Gucciardi, L. Otaegui, E. Bekaert, A. Villaverde, U. Iraola, Physico-chemical parameter measurement and model response evaluation for a pseudo-two-dimensional model of a commercial lithium-ion battery. **Sent to Electrochimica Acta, accepted.**

[J5] E. Miguel, Gregory L. Plett, M. Scott Trimboli, L. Oca, U. Iraola, E. Bekaert, Review of computational parameter identification methods for electrochemical models.**Sent to Journal of Energy Storage, under review, 2021.**

[J6] L. Oca, N. Guillet, R. Tessard, U. Iraola, Lithium-ion Capacitor Safety Assessment under Electrical Abuse Tests based on Ultrasound Characterization and Cell Opening, Journal of Energy Storage, **23**, 29-36 (2018).

[J7] L. Oca, J.M. Campillo-Robles, M. Mounir Bou-Ali, Review and Analysis of Thermophysical Properties of Sulfuric Acid–Water Electrolyte, Journal of Chemical and Engineering Data, **63**, 9, 3572–3583 (2018).

Conference papers

[C1] L. Oca, E. Gucciardi, E. Miguel, I. Lopetegi, L. Caizán-Juanarena, A. Herrán, A. Celaya, E. Bekaert, U. Iraola, Electrode ageing evaluation for non-accelerated degradation conditions at 25°C, Advanced Automotive Battery Conference, January 19-21 2021, online.

[C2] L. Caizán-Juanarena, E. Gucciardi, L. Oca, I. Gandiaga, U. Iraola, E. Bekaert, Ageing characterization of Lithium-ion capacitors on post-mortem analysis, Advanced Automotive Battery Conference, January 12-16 2020, Wiesbaden, Germany.

[C3] M. Echeverría, L. Oca, M. Arrese-Igor, I. Lozano, F. Bonilla, Synergy between ion milling and scanning electron microscopy. The study of electrode materials for energy

storage systems, Power our Future, July 2019, Vitoria-Gasteiz.

[C4] L. Oca, E. Miguel, L. Otaegui, A. Villaverde, U. Iraola, Methodology to assess the impact of electrochemical model parameters based on design of experiments, COMSOL Conference 2018, 22 - 24 October Lausanne, Switzerland.

[C5] E. Miguel, E. Gucciardi, L. Oca, E. Bekaert and U. Iraola, Model identification through parameter estimation of a commercial $LiFePO_4$/graphite cylindrical battery, 69th annual meeting - International Society of Electrochemistry, 2 - 7 September 2018 Bologna, Italy.

1.4.2 Original work

Chapter 3: A new methodology for physico-chemical parameter measurement of a commercial lithium-ion battery for a pseudo-two-dimensional model is proposed. A full model response evaluation is performed based on galvanostatic cycles, pulses and impedance measurements in a wide range of temperatures (5 - 45 °C). The internal variables are partially validated with *ex-situ* XRD and a 3 electrode T-cell. Moreover, original literature reviews in model parameter measurement methodologies, parameter identification procedures and electrochemical model validation techniques are presented.

Chapter 4: Half-cell P2D model accounting for material processing stage relationships is proposed and validated experimentally for different positive and negative electrode calendering conditions (different gap and temperature between rollers).

Chapter 5: This chapter incorporates the numerical and experimental knowledge of the previous chapters into a model-based design tool capable of obtaining enhanced cell performances. The effects and interactions of design and process parameters related to the material processing stage are analysed by means of the design of experiments methodology and electrochemical models.

Chapter 2

RESEARCH GAP IDENTIFICATION

The current climate crisis is driving the need for more sustainable energy production and storage, resulting in increased governmental support for the development of energy storage systems (ESS) [11]. Moreover, stationary, traction and portable applications are demanding better storage solutions to cope with the energy demands of society.

This chapter presents an overview of four pillars of energy storage research: current and emerging energy storage technologies, battery modelling, the device fabrication process, and optimisation methodologies. At the end of each section, the identified research gaps are presented.

2.1 ENERGY STORAGE SYSTEMS

The classification of energy storage systems is shown in Figure 2.1. According to their storage mechanisms, six groups can be distinguished: mechanical, thermal, chemical, electromagnetic, electrostatic, and electrochemical storage mechanisms.

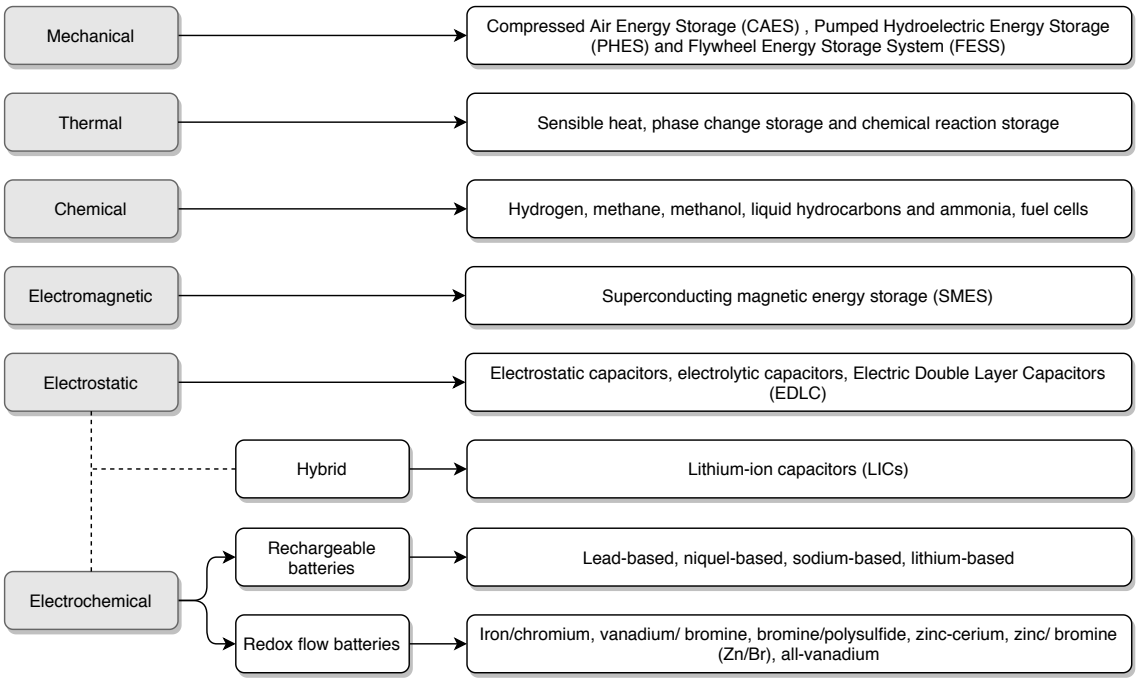

Figure 2.1: Energy Storage Systems classification. Based on [23–29].

Pumped Hydroelectric Energy Storage (PHES) is a well-established mechanical storage system which has been used since the early 1890s for utility-scale electricity storage [30]. Hydro power storage is not only a renewable energy source, but also improves grid stability and compensates for intermittent energy sources (i.e. wind and solar) [30]. PHES is the best solution for autonomous and small island grids, as it is a mature, low cost and efficient (70% - 80%) large-scale ESS [30]. Another manner to store energy mechanically is the Compressed Air Energy Storage System (CAES). In this group, energy is converted from electric into potential energy by compressors, and an air turbine is used to recover that energy [31]. Some economic and technical aspects have slowed down the increase of CAES compared to PHES, such as lower cycle efficiencies and geological restrictions [31]. In spite of these drawbacks, CAES could be a comparably cheap storage technology for periods of hours or days on discharge [31]. Moreover, Flywheel Energy Storage System (FESS) can be used in certain applications with a maximum speed of 100,000 rpm [32].

The second group is related to thermal energy storage (TES). It is used in areas such as buildings, textiles, automotive and health care [27]. The main disadvantage of this group remains in the initial capital cost, although there are some cheaper TES systems like seasonal TES which have very large capacity and the working temperature range is wide (-40°C - 600°C) [27].

Thirdly, chemical storage systems are used for power generation as well as transport, as they are ready to use products [26]. The main chemical fuels are: hydrogen (H_2), methane (CH_4), methanol, liquid hydrocarbons, and ammonia (NH_3) [26]. Due to their instantaneous heat release (high heat capacity) chemical fuels are the current leaders of the auto-

motive sector. Nevertheless, fossil fuel resources are decreasing and their pollution must be reduced. In addition, hydrogen based fuel cells are being developed as an alternative to fossil fuel resources [33].

Next, electromagnetic storage devices are presented. Among this group, superconducting magnetic energy storage systems (SMES) are highlighted. Their main advantage is that they can provide power almost instantaneously (which it not possible with CAES and PHES) [26].

Electrostatic devices have been the subject of much study and are generally used in electronics (small electrostatic or electrolytic capacitors) [34]. Among them, the double-layer capacitors (EDLC) have higher capacitance and are used in trams, buses etc. In addition, they can be combined with electrochemical storage systems to increase energy and power density for the final application. External or internal hybridisations can be found in the literature [23, 35][1].

The last group is related to electrochemical storage systems. Two groups can be distinguished: rechargeable and redox flow batteries. These storage systems are key in applications such as electro-mobility, portable devices and renewable energies. But, much work is required to enhance those technologies in terms of energy density, lifetime and cost [2].

In this thesis, electrochemical storage systems were selected due to their versatility to adapt to different applications. In the following sections current and emerging electrochemical storage systems are described highlighting the differences between them. Moreover, these technologies are compared based on different criteria so as to define the technology for this thesis.

2.1.1 Current electrochemical storage systems

In Figure 2.2 a comparison between electrochemical technologies is shown based on energy and power density. While supercapacitors (EDLC or LICs) are able to supply high power density, they are limited in energy density. In contrast, batteries can provide higher energy densities than supercapacitors, but lower power densities.

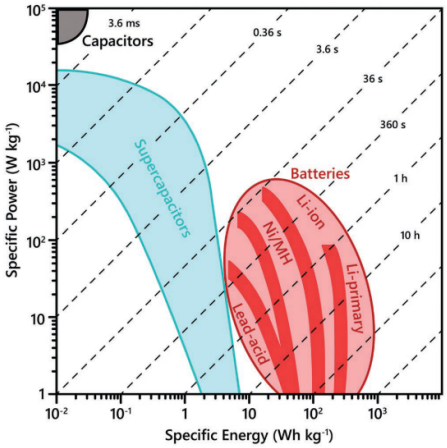

Figure 2.2: Ragone plot: comparison between main energy storage technologies. Original source: T. S. Mathis et al. [36] with the permission of John Wiley and Sons.

[1] J6 publication is related to lithium-ion capacitor safety
[2] J7 journal publications is about lead-acid electrolyte properties

A quantitative comparison of the key characteristics for different technologies are summarised in Table 2.1.

Table 2.1: Comparison of main characteristics of current technologies. Adapted from [37].

Technology	**Specific energy (Wh kg^{-1})**	**Specific power (W kg^{-1})**	**Cycle life (self - discharge % per month)**	**Operating T range (°C)**
PbA	30 - 40	60 - 180	300 - 800 (3 - 5%)	-20 - 60
NiCd	40 - 60	150	1000 - 2000 (20%)	-40 - 60
NiMH	30 - 80	250 - 1000	500 - 1500 (30%)	-20 - 60
NiZn	**70 - 110**	280 - 2500	300 - 900 (20%)	-20 - 50
NaNiCl	**100 - 120**	150	1000 **(0%)**	300 - 400
NaS	**90 - 110**	150 - 160	1000 - 2500 **(0%)**	300 - 400
Na-$AlCl_4$	**90 - 120**	150 - 180	1000 - 1500	270 - 350
LFP	**80 - 130**	1400 - 2400	1000 - 2000 **(< 1%)**	-20 - 60
LMO	**105 - 120**	1000	> 500 (5%)	-20 - 60
LTO	70	750	> 4000 (2 - 10%)	-40 - 55
LCO	**120 - 150**	600	> 700 (1 - 5 %)	-20 - 60
NCA	**80 - 220**	1500 - 1900	> 1000 (2 - 10%)	-20 - 60
NMC	**140 - 180**	500 - 3000	1000 - 4000 **(1%)**	-20 - 55
EDLC	0.1 - 10	**10 - 10^6**	**> 500000**	**-40 - 85**
LIC	1 - 37	**10^2 - 10^5**	**> 100000**	**-30 - 70**

Among all the electrochemical storage systems, lithium-ion batteries are leaders in the market due to their versatility. It is worth mentioning that there are hundreds of manufacturers in the marketplace [37–39] and the competitiveness among suppliers is increasing. Lithium-ion batteries are designed as high power or high energy cells depending on the application. Moreover, their long life, recent reduction in cost, together with increased global energy consumption, has led to investment in the development of enhanced batteries.

2.1.2 Emerging electrochemical storage systems

At present, there are several options to overcome current technology problems (low energy and power density, short lifetime, slow charges etc.). These devices are focused mostly on the improvement of lithium-ion batteries (LIBs) and EDLCs. Four groups of emerging technologies are identified: solid-state batteries (SSB), advanced post-lithium-ion technologies (Li-S / Na-S and Li-O_2 / Na-O_2), emerging non-lithium-ion batteries (sodium-ion batteries (NIB), potassium-ion batteries (KIB) etc.) and hybrid capacitors (LICs and sodium-ion capacitors (NICs)). A comparison in terms of energy density is plotted in Figure 2.3, in which theoretical and practical gravimetric energy densities are presented.

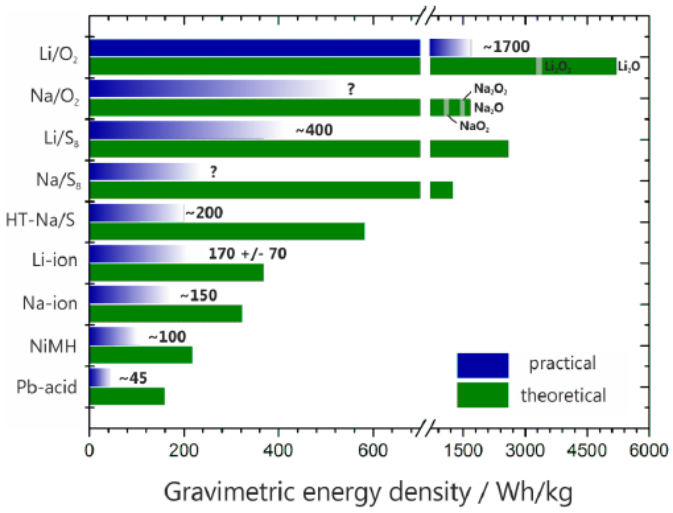

Figure 2.3: Comparison of theoretical and practical gravimetric energy densities for different technologies. Original source: Adelhelm et al. [40]. The license is subject to the Beilstein Journal of Nanotechnology (CC BY 2.0)

2.1.2.1 *Solid-state batteries*

In Table 2.2 a comparison between conventional Li-ion batteries and solid-state batteries is shown. The main advantage is that SSBs are safer than conventional batteries. However, several problems have arisen that had hampered the commercialization of these devices, such as poor ionic conductivity of electrolytes and poor electrode - electrolyte interfacial compatibility [41]. Moreover, due to the high cost of lithium, these devices are used for small-scale applications [42]. The most analysed solid electrolytes include perovskite-type, NASICON-type, garnet-type and nitride/sulfide glass-ceramics [41].

Table 2.2: LIB versus SSB [43].

	Conventional Li-ion	**Solid-state technology**
Fire Hazard	Low flashpoint of solvents, lithium plating and Hydrogen Fluoride formation	No liquid components
Performance	Not compatible with high-voltage cathodes, separator cannot be thinner	High-voltage cathode compatible, wide temperature range, high power possible
Form factor	Planar geometry	Possible through additive manufacturing
Cost	Steadily decreasing	Depends on the manufacturing process

2.1.2.2 *Advanced post-lithium-ion technologies*

Metal-oxygen and metal-sulphur batteries are being studied due to their high energy density compared to lithium-ion batteries [40]. Some of the materials used in these products are abundant in the earths crust (sulphur and oxygen) [40]. A comparison of the three batteries with their respective reactions is represented in Figure 2.4. In metal-oxygen batteries, the positive electrode consists of a porous support which enables the reduction of oxygen, creating products of Li_2O_2, Na_2O_2, NaO_2. The positive electrode of metal-

sulphur batteries hosts sulphur before discharge and Li_2S/Na_2S after discharge [40]. The negative electrode in metal-oxygen and metal-sulphur batteries are lithium or sodium metal.

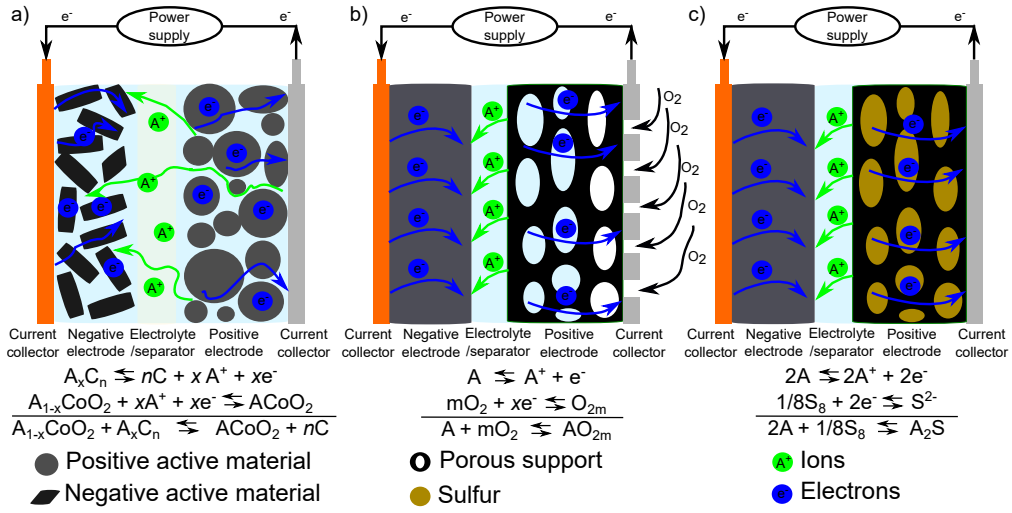

Figure 2.4: Operating principles of different technologies (A = Li, Na): a) Lithium-ion or sodium-ion battery; b) Metal-oxygen battery (non-aqueous electrolyte); c) Metal-sulphur battery. Based on Adelhelm et al. [40]. The license is subject to the Beilstein Journal of Nanotechnology (CC BY 2.0).

2.1.2.3 *Emerging non-lithium-ion batteries*

In solid-state, metal-oxygen and metal-sulphur batteries, the mechanism that drives the reaction is different to LIBs, as is presented in Figure 2.4. Non-lithium-ion batteries maintain the insertion mechanism of ions into the porous electrodes, but the insertion element is changed from lithium to another element of the periodic table. The most promising element properties are set out in Table 2.3. The element with the greatest volumetric capacity is aluminium, whereas lithium has the greatest specific capacity.

Table 2.3: Theoretical capacities, reduction potential and effective ionic radius [44].

Species	**Volumetric capacity (mAh mL^{-1})**	**Specific capacity (mAh g^{-1})**	**Reduction potential (V vs. SHE)**	**Effective ionic radius (Å)**
Li	2026	3861	-3.04	0.76
Na	1128	1165	-2.71	1.02
K	591	685	-2.93	1.38
Mg	3833	2205	-2.37	0.72
Ca	2073	1337	-2.87	1.00
Zn	5851	820	-2.20	0.74
Al	8040	2980	-1.67	0.54

Depending on the number of ions exchanged in the reaction, batteries can be classified as monovalent or multivalent. The advantages and disadvantages of both groups are shown in Table 2.4.

Table 2.4: Non-lithium-ion batteries: advantages and drawbacks to overcome [44].

Emerging battery	**Advantages**	**Drawbacks**
Monovalent alkali metal ions (Na^+ and K^+)	High abundance Low price	Insufficient cycle life Anode and cathode materials with lower specific energy capacity than LIBs
Multivalent metal ions (Mg^{2+}, Ca^{2+}, Zn^{2+} and Al^{3+})	Safety and transference of more electrons in a single redox couple	Lack of high-voltage electrolytes and electrode materials

From all those options, research efforts are currently focused on sodium-ion batteries, due to their high energy density (slightly inferior than LIBs), low cost of sodium, and high cyclability.

2.1.2.4 *Hybrid supercapacitors*

Lithium-ion or sodium-ion capacitors are hybrid energy storage devices which combine faradaic and non-faradaic electrodes. These devices are therefore in between LIBs and EDLCs in terms of energy and power density. A rapid lithium or sodium ion adsorption/desorption process occurs at the surface area of the positive electrode. In contrast, Li^+ or Na^+ insertion/deinsertion mechanism predominates in the negative electrode. In Figure 2.5 the comparison between LIB, EDLC and LIC are presented. In the case of LICs / NICs only the potential of the positive electrode varies linearly, while the potential of the negative is almost constant. Therefore, the voltage range of the LICs is higher than EDLCs, and thus the energy density increases [45].

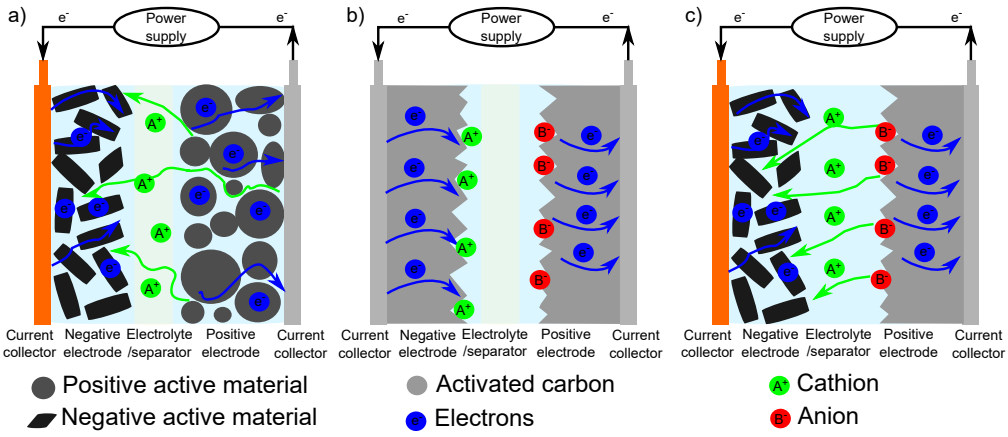

Figure 2.5: Operating principles of different technologies (A = Li, Na): a) Lithium-ion battery; b) EDLC; c) Lithium-ion capacitor. Based on [45].

A commercial solution of LIC is composed of graphite and activated carbon electrode, in which the required pre-lithiation level is adquired by means of a sacrificial electrode to provide cyclable lithium ions to the system. Different pre-lithiation mechanisms and approaches are being developed to provide lithium ions to the system: sacrificial electrode, increasing the electrolyte concentration, and using a positive electrode with lithium or sodium content with a high irreversible process [45, 46].

2.1.3 ESS selection for this thesis

In order to select the technology for this thesis, a comparison between technologies was carried out focusing on the following five criteria:

1. Technology readiness level (TRL). TRLs between 4 -5 are favoured. Low TRL levels are out of the scope of this thesis as they are far from scale-up process. Moreover, a high TRL indicates a high level of maturity, i.e. there is no scope for innovation.
2. Cell performance. In general, energy density, power density and life cycle of the devices are compared.
3. Application. Depending on the application, different characteristics are required. The main applications of each technology are presented. Note that there could be more than one technological solution for any given application.
4. Raw material and cell production cost. This criteria focuses on raw material cost as well as production process complexity.
5. Sustainability of the technology. Toxicity, recyclability and abundance of elements are evaluated.

A comparison between TRL, energy density and cycle number of the six different options for this thesis are presented in Table 2.5 (explained in subsections 2.1.1 and 2.1.2). These criteria were selected because they are quantitative and therefore directly comparable. Other criteria are more difficult to evaluate (applications, raw materials and manufacturing costs, element abundance, and recyclability). Those are analysed qualitatively.

Table 2.5: Quantitative comparison of different energy storage technologies [25] ([a]Solidenergy, [b]OXIS energy, [c] RS2E).

	TRL	E_m **(Wh kg^{-1})**	**Cycle number**
Lithium-ion Batteries (LIB)	9	170 ± 70	1000
Solid-State Batteries (SSB)[a]	4 - 5	600	>150
Lithium-Sulphur Batteries (Li-S)[b]	5 - 6	400	180
Lithium-Oxygen Batteries (Li-O_2)	2 - 3	1700	poor cycle life
Sodium-ion Batteries (NIB)[c]	4 - 5	90	4000
Lithium-ion Capacitors (LIC)	7 - 8	1 - 37	>100000

Among the options, Lithium-Oxygen batteries were discarded due to their low TRL level. Although Li-S and Li-O_2 could replace LIBs in certain applications in which high energy density is needed, they are still in development and have low cycle life. Moreover, the manufacturing processes of Li-S and Li-O_2 differ from those of LIBs, which makes them less attractive from a manufacturing standpoint.

The manufacturing cost of lithium-ion batteries is approximately 190 € kWh^{-1}, of which almost 75% of the total budget corresponds to material costs [47]. In sodium-ion batteries the cost variability is believed to be lower [25], as the raw materials are less located on Earth. In LICs, as a pre-lithiation step is requiered, this could increment the manufacturing cost, although cheaper materials and facilities could be used. In the case of Li-S and Li-O_2 lithium metal foil is necessary which also increases the raw material cost.

The sustainability of cells is evaluated by the abundance of raw material and recycling process. For batteries which contain lithium, the recycling rate is less than 40% [25], which is the case for almost all batteries. For sodium-ion batteries there is no recycling data available as nowadays there are no commercial cells. Nevertheless, sodium is the second most abundant element, whereas abundance of lithium is the lowest.

For the abovementioned reasons, dual-insertion batteries have been selected to be studied in this thesis. In order to reduce the uncertainty of new materials and the fabrication process, a commercial lithium-ion battery is used in order to develop and validate the methodologies explained in this thesis. LIBs are a well-established technology in the battery market, and are the benchmark for emerging technologies. In addition, lithium-ion battery prototyped cells are studied so as to gain knowledge and characterise cell-process relationships for different process conditions, thus presenting a novel methodology directly transferable to sodium-ion batteries. In fact, both technologies are governed by the same mechanisms, so the developed characterisation protocols, physic-based models and inverse cell design optimisations are valid for both chemistries.

2.2 ELECTROCHEMICAL MODELLING FRAMEWORK

In recent years, fabrication and material advances have only been obtained with experimental work. However, as these processes consume a large amount of resources (time and money) and the number of experiments are limited [20], trial-error experiments cannot be the only development area for a long-term solution. For this reason, there is a need for modelling as an advanced technique to improve the design and fabrication process of electrochemical energy storage systems. There is a favourable prospective for numerical modelling due to the recent technological advances, which have improved hardware capabilities (solid-state-disc, higher RAM memory etc.) and enhanced the performance of in-house and commercial software. As a result, considerable progress has been made in applying computational techniques to energy storage systems [48].

Cell behaviour and mechanisms occurring inside batteries can be analysed through electrochemical models. In fact, it is possible to optimise the cell performance without the need for fabrication and experimental testing of all the studied options. Using electrochemical models can optimise the fabrication process and reduce the development time, money and resources of current and emerging chemistries. However, there are few studies available in which cells are physico-chemically characterised and analysed with electrochemical models and validated with experimental methods [22, 49–52]. Therefore, there is still a considerable research gap to fill.

2.2.1 Model scale and scope

Depending on the final purpose of the simulation, different scales and approaches can be used (see Figure 2.6). At small time and length scale, model predictability increases, but computational cost is also higher [20]. One of the current challenges of modelling is to understand and represent the mechanisms that take place inside a battery. Interactions between time and length scales make the model more complex [20]. Four main groups have been identified taking into account the model scales. The analysed systems, models and scope of the models are summarised in Table 2.6.

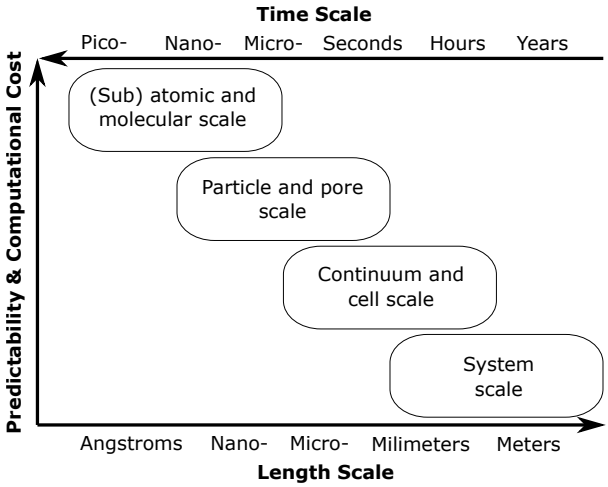

Figure 2.6: Model length and time scales. Based on [53, 54].

Table 2.6: Model approaches for batteries and electrochemical systems. Based on [53, 55].

(Sub) atomic and molecular scale	
System	Ion, electron, atom, clusters and interfaces
Model	Electronic structure simulation, molecular dynamics, KMC
Scope	Atomic structures and properties (structural integrity), molecular mechanics and dynamics, crack formation and propagation, or electrochemical and interfacial chemical reactions
Particle- and pore-scale	
System	Electrode particles, pores, porous electrodes
Model	Phase field model, porous electrode model
Scope	Mesoscopic transport of ionic species, resistance at secondary particle level, material phases
Continuum- and cell-scale	
System	"Sandwich" system and full electrochemical cells
Model	P2D model, P2D + Population balance, P2D + Stress strain, Thermal model (P3D stack), SPM (single particle model), Equivalent circuit model (ECM)
Scope	Spatio-temporal varying fields (ions and species) for safety and performance optimisation, life prediction, ageing phenomena, abuse scenarios
System Scale	
System	Battery packs, machines, processes, process chains
Model	Battery pack cooling (thermal model), Equivalent circuit model (ECM), machine simulation, process simulation, production system simulation
Scope	Performance and life prediction of battery packs, manufacturing processes optimisation

In this thesis, the main reason for using modelling is to help in the design of cells. Therefore, the model should be able to provide data about the physico-chemical processes occurring inside the cells in order to optimise the fabrication process. Not only should the electrical characteristics be recorded, but also the internal variables (electrolyte salt concentration, solid concentration of the particles, and electrolyte and electrode potentials). Atomic, molecular, particle and pore scales are not suitable for this purpose, as those models are highly complex and only small volumes inside electrodes (small clusters of particles) can be analysed [54]. Therefore, in this work, continuum electrochemical models were selected for further analysis.

2.2.2 Modelling challenges of this thesis

In this section three research gaps were identified (see Figure 2.7): (1) P2D model parameter measurement or identification methodology selection, (2) adaptation of the electrochemical model for cell design purposes, and (3) selection of the most suitable validation approach.

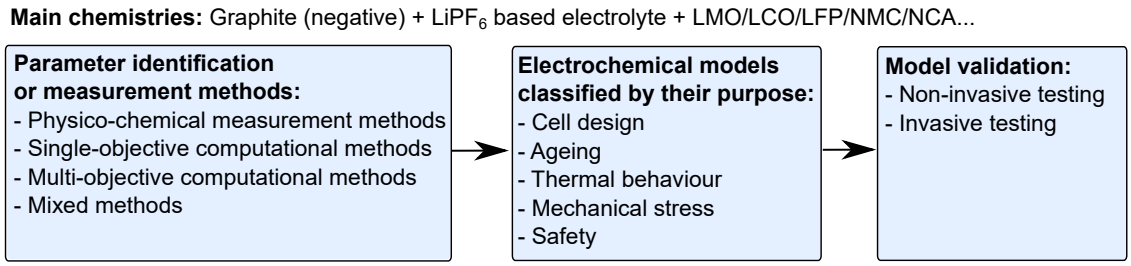

Figure 2.7: Electrochemical model research gaps.

There has been an exponential number of publications related to electrochemical modelling of LIBs since 2013 [22, 49–52, 56–84]. Based on literature analysis, it is possible to conclude that there are no doubts about the importance of electrochemical models as a tool to aid in the design and study of lithium-ion batteries. Regarding the materials, different negative electrodes (graphite (Li_xC6) or MesoCarbon MicroBeads (MCMB)), electrolytes (lithium hexafluorophosphate ($LiPF_6$) with different solvents) and multiple cathode materials (i.e. lithium manganese oxide (LMO), lithium cobalt oxide (LCO), lithium iron phospate (LFP), lithium nickel manganese cobalt oxide (NMC) and lithium nickel cobalt aluminium oxide (NCA) have been studied. Moreover, manufacturers combine different active materials in the same electrode, which are called blend materials, to increase power and energy density without compromising safety or durability [85]. In order to reproduce the studied cell, model parameters need to be measured, estimated, identified, assumed or calculated. In recent years, model parameter measurement, identification or estimation has been the subject of much research. There is a big gap in model parameter measurement or identification methods. Schmalstieg et al. [22, 52] propose and validate a methodology for a commercial cell. In such methodology, the voltage error was inferior to 1% for different profiles. Those methodologies can provide accurate model predictions, but are costly in terms of time and resources. The aim of this thesis is to propose a methodology which obtains reliable results, while minimising the number of experimental tests. In subsection 3.2.2 an intensive review of these methods is presented and a new methodology is assessed in Chapter 3.

As regards the purpose of the analysed works, different paths can be found since the early beginnings of the P2D model. In Figure 2.7 electrochemical models have been classi-

fied into different groups: cell design, ageing models, thermal behaviour, mechanical stress and safety are among the most predominant. Furthermore, modelling to improve battery production lines is one of the newest topics under research [86]. In this thesis the electrochemical model is used for battery design optimisation. The model equations, boundary conditions and assumptions are presented in subsection 3.2.3. Moreover, in order to align computational effort to support cell design and fabrication, some model enhancements are needed to include cell-process relationships. The model predictions will be as good as the model, which means that model assumptions and parameter measurement simplifications will affect the model responses.

Finally, model validation techniques should be used to validate the cell behaviour. Most of the articles present experimental voltage curves on charge and discharge compared to the simulations [87–89]. Internal variables should be also measured in order to gain knowledge about the internal processes and enhance the proposed model parameter measurement methodology and the model. The validation methods are discussed in subsection 3.2.4.

2.3 BATTERY MANUFACTURING PROCESS

Battery production is a complex and multi-step process that takes place in part in a controlled environment (dry room). Since the lithium-ion battery was introduced into the market, the battery manufacturing process has been improving so as to obtain better performance of the cells from the same raw materials. However, it is still the subject of research in order to reduce fabrication inhomogeneities. In addition, the fabrication process needs to be adapted to emerging technologies, for instance sodium-ion batteries, and for this reason the process parameters need to be modified. Thus, the battery manufacturing process faces a number of challenges to be able to achieve the goals set out in Figure 2.8.

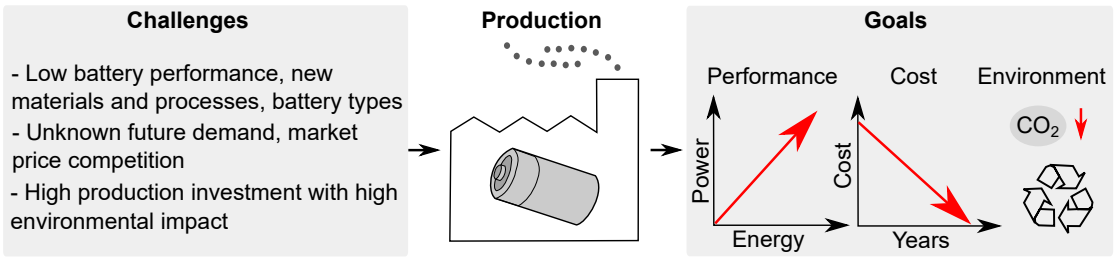

Figure 2.8: Challenges and goals of battery production. Based on [90].

Four topologies can be found in the market if cells are classified according to different package solutions: cylindrical, button or coin, prismatic, and pouch cells. Cylindrical cells present good mechanical stability and lend themselves to automated manufacturing. Common sizes for this topology are the 18650 and 20500 formats. Cells with this packaging present the highest specific energy, although pouch packaging is in continuous improvement. Button cells or coin cells are generally used in the research and development of new devices, as well as for small portable devices. Prismatic cells are encased in aluminum or steel to improve mechanical stability. The manufacturing cost of prismatic cells is normally higher than cylindrical and pouch cells due to the casing cost. Generally, prismatic cells are used in powertrain applications or similar. Pouch cells are constructed with a laminated architecture in a metal foil-type package. This package is light and cost-effective but long-term exposure to humidity and high temperatures can shorten cell life. That problem is minimised by adding a light stack pressure, which prevents electrode delamination. The safety of this type of cell is less than for hard casings (prismatic and cylindrical). In addition, the swelling rate is higher. Despite these disadvantages, the pouch cell configura-

tion is growing in popularity and serves similar applications to prismatic cells as they can provide higher energy density [37].

2.3.1 Pouch cell fabrication stages and steps

In this thesis, a Z-fold pouch cell topology was selected for analysis. In Table 2.7 manufacturing steps for this type of cell are described.

Table 2.7: Fabrication process of Z-fold pouch-type batteries. Based on [90].

Stage	Step	Process description
Material processing	Mixing	Active materials, binder, conductive additives and solvents are mixed according to an specific formulation. The desired slurry characteristics are obtained adjusting raw material quantities and mixing conditions, affecting the processability and final characteristics of the cell.
	Coating and drying	This is a high precision process in which the slurry is coated on top of the current collector foil with a defined thickness and mass loading. After, the solvent is evaporated in a dryer with an specific temperature profile.
	Calendering	With the combined action of pressure and temperature, the thickness and porosity of the electrodes is optimised. This step improves the contact between particles (cohesion) and the adhesion between the current collector and the coated layer, while minimising thickness inhomogeneities.
Cell assembly	Electrode notching	For a Z-fold pouch cell, electrodes must be cut into electrode sheets. Cutting lines must be straight and precise to eliminate the risk of internal short-circuits in the following steps.
	Electrode stacking	For Z-fold stacking, positive and negative electrode sheets are alternated and placed between the continuously fed separator.
	Tab welding	All the negative and positive current collectors need to be welded to the battery tabs.
	Three side cell housing	A metal-foil package is used for the housing. The housing must be sealed on three sides.
	Electrolyte filling and full sealing	A specific volume of electrolyte is added to the cell under vacuum conditions. Electrolyte components react with water to form HF; therefore, this step is performed under extremely dry conditions. It must be ensured that the liquid penetrates the whole electrode layers and separator.
	Formation cycles	Cycles at current rates are performed to form the solid electrolyte interphase (SEI) which is created in the first charge-discharge cycles. Lithium from the cathode is consumed in the anode in an irreversible way, and gases are formed through this reaction.
	Degassing and final sealing	The extra housing left for gas storage is punched under vacuum to remove the gases produced during the formation cycles. Final sealing of the cell (fourth side) is performed.
Cycling	Performance and ageing cycles	Performance and ageing cycles are done to test the characteristics of the cells obtained in the process.

The sequence of the process can vary depending on the materials, product technology and manufacturer. In the first stage of the manufacturing process electrodes are created and the electrode shape and properties are decided. In the second stage, the cell is assembled using the selected configuration and it is filled with the electrolyte. Next, after the cell is completely sealed, performance and ageing testing of the device is carried out.

An important aspect of any manufacturing process is the cost of raw materials and processing. Almost three quarters of the total budget corresponds to materials costs, although this could vary depending on the market (cost is not controlled by the manufacturer) [47]. From the remaining 25%, 17.4% is required for energy during the fabrication process [91,92]. In Figure 2.9, the Li-ion battery manufacturing cost is presented.

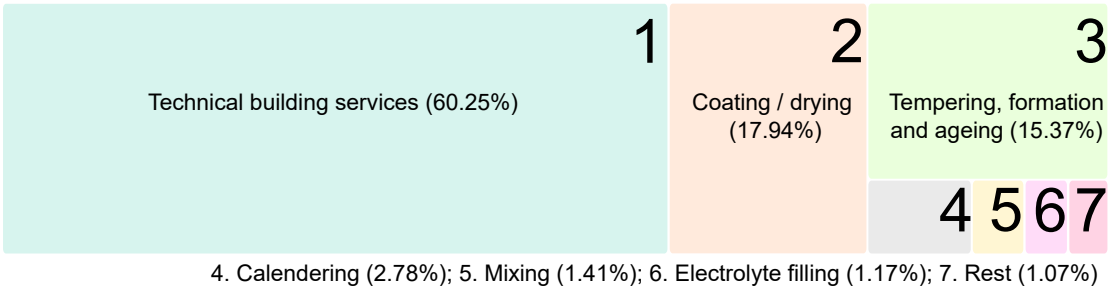

Figure 2.9: Normalized production cost of a battery cell. Total energy demand of 24.80 [kWh] for one cell. Adapted from [91].

Among the three stages, the material processing stage (mixing, coating, drying and calendering steps) is highly energy demanding. In addition, in this stage, electrode properties (coating density, porosity, thickness etc.) are defined. Therefore, this thesis is focused on the first stage of the fabrication process.

2.3.2 Battery manufacturing challenges

Li-ion battery manufacturing poses a number of challenges and these are outlined in this section. The Battery 2030+ Roadmap initiative [11], encourages the use of numerical studies to overcome problems associated with trial-error methodologies for optimisation, and shorten the development time. The overall aim is to accelerate new cell concepts and design so as to enhance cell performance, efficiency and sustainability, while reducing manufacturing costs and scrap.

In line with these objectives, three research gaps are identified in this thesis which are shown in Figure 2.10: (1) build a quantitative methodology to assess the differences between process parameter variations, (2) cell-process relationship enhancements to include the influence of the material processing stage, and (3) Model calibration and validation with experimental data.

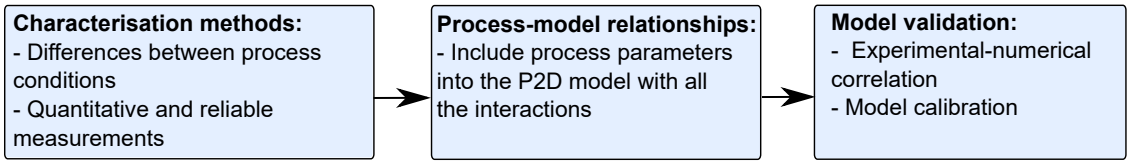

Figure 2.10: Battery manufacturing research gaps.

There are several works in which process parameter variations are conducted [47,93–95]. However, they are based on experimental measurements of specific materials and different quality control techniques are used. Thus, a direct comparison between them of the obtained results is not straightforward. In this thesis, first of all, an experimental design of experiments to study the process parameter cross-linked influences is proposed. To evaluate the different process conditions, a fast model parameter measurement procedure is also required. A reduced physico-chemical parameter measurement methodology is proposed based on Chapter 3.

The obtained model parameters are valid for the studied experimental conditions. So as to minimise the experiments to be carried out during the optimisation process, cell-process relationships are needed. Meyer et al. [86, 95–97] proposed a relationship and a measurement methodology for calendering step, which relies on mercury porosimetry and helium pycnometry tests, and the measured line load of the calendering machine. However, most calender machines does not measure the applied force while electrode calendering [98], and thus a simpler relationship should be found. Moreover, material processing stage before calendering step affects the final cell performance and those process relationships need to be accounted [99]. The aim of this thesis therefore, is to find a cell to process relationship for the material processing stage with the minimum set of experiments possible. One further objective is to take into account promising future technologies (i.e. sodium-ion batteries or solid state batteries) while designing the methodology to expand its validity.

Finally, cell-process relationships need to be included into the electrochemical model. Lenze et al. [89] added the influence of calendering into the cell response with a calendering dependent factor in the specific surface area parameter, and then fitted calender dependent parameters for galvanostatic discharges. Moreover, Schmidt et al. [99] included relationships for mixing, coating, drying and calendering steps with the objective of studying the impact of manufacturing uncertainties. The aim of this thesis is to construct a general half-cell positive and half-cell negative model capable of describing all experimentally characterised process conditions. Moreover, the final objective is to build a general full cell model taking into account the electrode balancing of the cells. This general model is the baseline for cell optimisation which is the topic of next section.

2.4 BATTERY DESIGN OPTIMISATION

This section presents an overview of the generic optimisation procedure for experimental and numerical approaches. Then, the main challenges for battery optimisation are defined.

2.4.1 Optimisation methodology

In Figure 2.11 the generic optimisation steps for any system are presented. This methodology can be used in both experimental and numerical analyses, and follows 6 basic steps. (1) To define the problem, the case study should be properly defined (input factors, output responses, studied space, optimization constraints etc.). (2) A design of experiment methodology is selected, providing a sequence in which experiments or simulations are executed. (3) The experimental characterisation or simulation is performed. (4) The results are fitted and evaluated to obtain a meta-model which relates the input factors to the output responses. (5) Different optimisation algorithms can then be used to obtain the global optimum point. (6) Experimental or numerical output response validation.

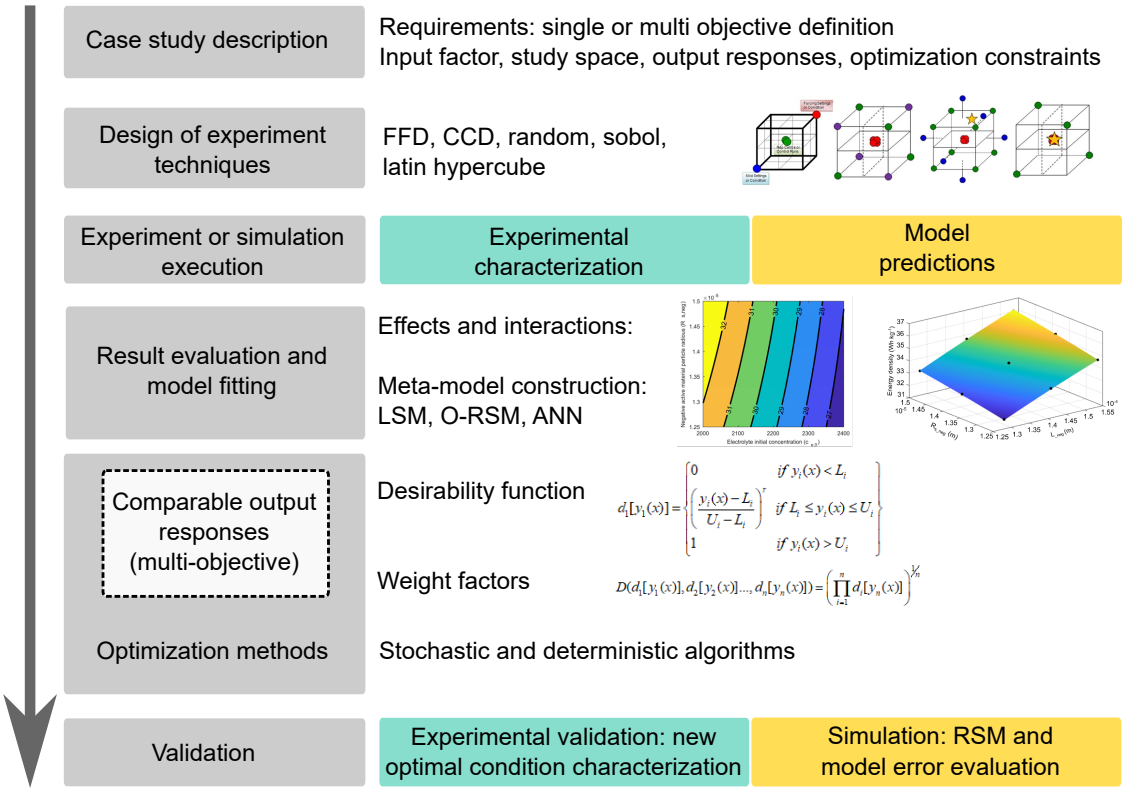

Figure 2.11: Optimisation methodology.

2.4.1.1 *Case study description*

In the first instance, the specific requirements for any given case study must be defined. For example, the target could be to increase energy density of a cell for electrical vehicle application. Or it could be a multi-objective problem, with two or more objectives (i.e. increase energy density while maintaining cell volume and price).

Once the optimisation purpose is known, the number of design parameters (factors), their study space, the output responses and the optimisation constraints are defined. This step is important because the optimisation methodology will only give accurate results if the problem is well stated. Input factors must fulfill three conditions: independence, physically possible, and significant to a certain response.

The independence of factors has been studied in computational and mixed parameter identification methodologies for battery models. Before applying mixed parameter identification methodologies, parameters are grouped, thus ensuring that condition. The interaction between parameters should be checked to ensure the independence in any system.

A factor is considered physically possible when it is feasible to obtain that design parameter experimentally. Material and process constraints should be defined (optimisation constraints) according to that feasibility, and therefore expertise and reliable information of the system is required. If process or material limitations are not considered or unknown, it could happen that the optimised solution cannot be implemented. The study space must also be carefully selected to avoid optimisation results which in reality cannot be obtained (i.e. electrode thickness should be in the range of microns, not millimetres).

The output responses must be selected on the basis of the design parameters and the study space. In order to analyse a design parameter, the response must be sensitive to

the applied parameter variation. Otherwise, the design parameter cannot be evaluated and optimised. One way to ensure the parameter is significant to a response is to conduct a sensitivity analysis. Sensitivity analyses evaluate each parameter separately, assuming that model parameters are independent from each other. Moreover, output responses in multi-objective optimisations must also be independent. Multi-objectives are commonly desired which requires a compromise between responses.

2.4.1.2 *Design of experiment techniques*

The aim of design of experiment (DOE) techniques is to obtain the desired information of the study space with the least number of experiments. In experimental and numerical characterisations, the number of experiments are limited and must be reduced to the minimum to decrease cost. There are several DOE techniques to choose the samples from the study space, and careful selection of representative samples to avoid biased data is essential for an optimal analysis. When optimising a system, a discrete number of points must be selected. Depending the number of experiments, factors (k), levels (n) and objective of the design of experiment, some techniques will be more suitable than others for a certain problem.

In most DOE techniques the number of experiments increase exponentially with the parameter number, thus a proper selection of design parameters is critical (see Figure 2.12). The purpose of the DOE is highly significant. Some techniques are suitable for screening a large number of factors and provide valuable data of the main effects (Plackett-Burman design). However, to understand the interaction between design factors, techniques such as full factorial design (FFD) and fractional factorial design are required. If the final purpose is to construct a meta-model based on response surface methodology (RSM), central composite design, FFD, box-behkin design, and space filling designs (random, sobol, latin hypercube) can be used [100, 101].

The number of levels also exponentially increases the number of experiments. In Figure 2.12 the correlation between the number of experiments to be performed and the number of factors for different techniques shows a difference between 2^k (two level) and 3^k (three level) full factorial designs. If a small number of levels is selected, the design space will not be well defined (lack of good interpolation). Thus if an irregular behaviour is expected from the output responses, the studied levels should be as high as possible.

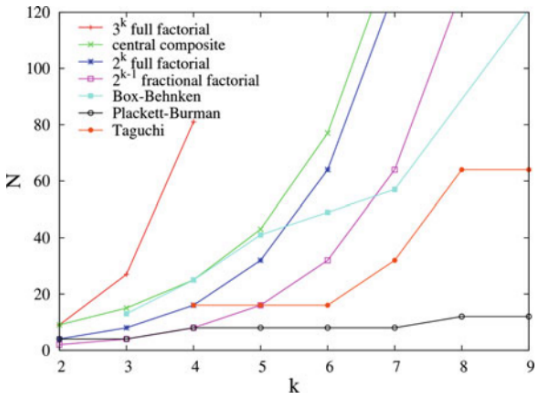

Figure 2.12: Design of experiment technique comparison [100] (k: factors, n: levels). Reprinted by permission from Springer Nature [100].

2.4.1.3 *Experiment or simulation execution*

Once the plan for representative data collection is developed (design of experiments) the experiment or simulation is executed. In this step, several considerations must be taken into account to obtain reliable results.

In experimental characterisations, procedures should be well defined to avoid dispersions and uncontrolled variables which affect the measured response. To obtain the minimum variability, experiments should be performed (if possible) by the same researcher, in a controlled environment (i.e. same environmental conditions: humidity, temperature etc.) and eliminating noise factors which could affect the studied response. The experimental sequence should also be conducted randomly to prevent possible tendencies derived from non-controlled variables.

In simulations, model assumptions, equations and boundary conditions should be precise enough to be capable of accurately predicting system responses. Initialisation of the model (full set of input parameters) is of great importance to find a reliable and optimum response. If these input parameters are not consistent the optimisation results will never be accurate.

2.4.1.4 *Result evaluation and model fitting*

For some case studies, the effects and interactions between parameters are required (purpose of the DOE analysis) for a predefined output responses [102]. This analysis is useful, for example, when defining the input parameters to be optimised. Such studies can identify the interrelationships between parameters and the significant factors. In these cases, full or fractional factorial designs are required.

If the purpose is to find the global optimum in the study space, the response surface methodology (RSM) can be used. A meta-model is constructed for each output response based on the input design parameters. This is an approximation function which is constructed to describe the response in the design space, and can help to achieve the optimal solution by means of optimisation algorithms. As the meta-model is an analytical function, the optimisations are very fast and do not require more experiments or simulations to be performed. Special care must be taken when choosing the approximation function, since an unsuitable approximation could result in a far from realistic optimisation solution. In addition, if the design space exploration is poor (i.e. low number of levels, experiments) and the output response is highly irregular, it could also be difficult to obtain results close to the true value.

Among RSMs, the least squares method (LSM) and artificial neural networks (ANN) stand out. Neural networks need large amounts of data sets for training and sometimes can not be used [100]. Several LSM data fitting functions can be found in the literature: linear, quadratic, cubic, nth-degree polynomial, bilinear and biquadratic are among the most common.

2.4.1.5 *Comparable output responses for multi-objective optimisations*

Once the meta-model is obtained, the output responses should be combined and analysed together to achieve an optimal design. If multiple responses need to be optimised simultaneously, a desirability function can be used to obtain comparable output responses. Moreover, different weights can be applied to establish the priority of the optimisation.

2.4.1.6 *Optimisation methods*

There are two main optimisation groups: stochastic and deterministic methods. Stochastic methods include randomness throughout the optimisation procedure whereas deterministic methods are those algorithms which do not include a random component. Stochastic methods are population-based algorithms derived from observation of natural phenomena (i.e. geology, biology). They are simpler (from the mathematical point of view) but have slower convergence towards the optimum solution. If a deterministic optimisation algorithm converges to a local optimum they are not capable of changing to another design space point. However as stochastic algorithms proceed with pseudo-random mutations of individuals, they can change that point to explore the whole design space, thereby achieving the global optimum. A downside of stochastic methods however, is that they require more time than deterministic optimisations. Deterministic algorithms know where to move from the precedent iteration, whereas the stochastic methods randomly select the next point from the population. Therefore, in optimisation problems, it can be desirable to combine both methods to first find the area in which global optimum is located (stochastic methods), and then refine the solution (deterministic methods).

There are several different families of stochastic optimisation methods, such as particle swarm optimisation (PSO), Game theory-based optimisation (GT), evolutionary algorithms (EA), and genetic algorithms (GA). The speed of GT methods makes them suitable for the initialization of an optimisation problem, but then a more robust algorithm should be used, such as GA. PSO is most suitable for irregular objective function when many local minima are present. EA is a robust and reliable method to explore the design space, although it is less suitable for multi-objective optimisations. Genetic algorithms are best suited for multi-objective optimisation, but less appropriate for exploring the design space than EA. This drawback can be minimised, however, if the influence of the mutation operator is enhanced. Furthermore, GA have proved to be valid for a wide variety of optimisation problems.

On the other hand, in Figure 2.13 a comparison between different unconstrained deterministic optimisation methods is presented. In the figure the "simplicity" of the method indicates that the required mathematical development is easy to implement, "reliability" refers to a method with is unlikely to fail to find a solution, and "efficiency" means that convergence is achieved.

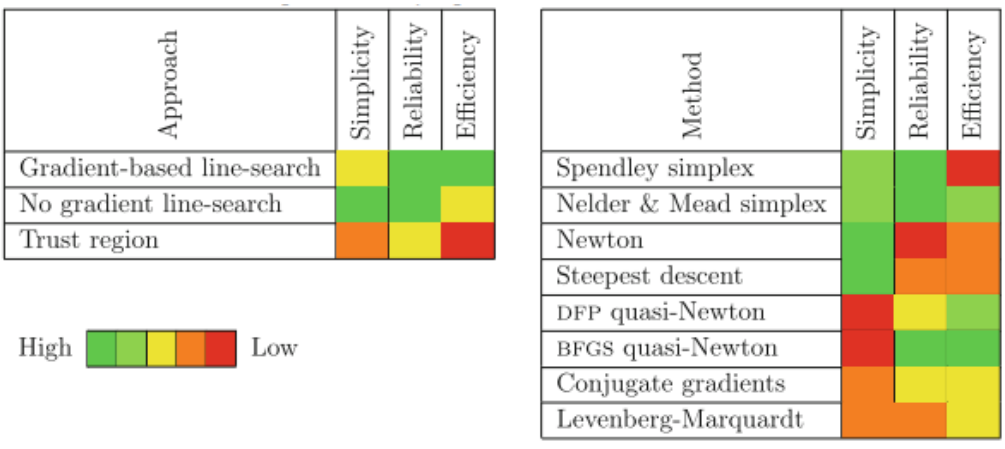

Figure 2.13: Unconstrained deterministic optimisation method comparison [100]. Reprinted by permission from Springer Nature [100].

2.4.1.7 *Experimental or numerical output response validation*

The optimisation result depends on the approximation function built. Validation of the results obtained by the optimisation methodology can be carried out either numerically or experimentally. In the numerical approach, the results obtained with RSM are compared to the results obtained from the model, thus comparing and calculating the error between the RSM and the model. To confirm that the equations, boundary conditions, and assumptions of the model accurately describe the problem an experimental validation should be performed. This assesses the validity of the methodology and provides an optimal solution for the analysed system.

2.4.2 Battery design optimisation challenges

In Figure 2.14 the identified research gaps are presented.

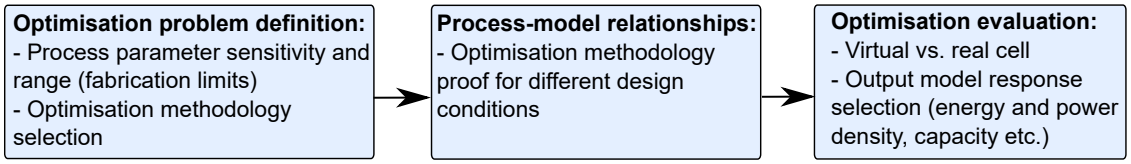

Figure 2.14: Battery design optimisation research gaps.

Historically, experimental approaches have been used for battery performance optimisation, with or without the help of systematic design of experiments. In the last few years combination of experimental and numerical approaches have arisen, so as to reduce the number of time-consuming and costly experiments. Different design of experiment strategies and optimisation algorithms are available in the literature. However, usually, in the numerical studies, do not consider experimental constraints (material and process limitations), nor do they validate the virtual optimisation experimentally. It is challenging to identify a suitable methodology to optimise cell design accounting for fabrication limits.

Moreover, only one recent study accounts for material-process-model relationships [99]. Therefore, it is a challenge to develop a tool and validate it at different process conditions for cell design optimization. The final aim is to predict the impact of processing parameters on final cell performance (optimum processing parameters to obtain the best performance of the reference materials). For example, a reduction in energy use during the prototyping process (minimise scrap, faster manufacturing, less time in the formation step, etc.) is desired. Moreover, rapid prototyping tools and reliable characterisation methods are needed nowadays to help into the decision taking process in the prototyping line.

Last but not least, this design tool should be validated against experimental work to assess its predictability and quantify the time that is saved with this technique. A good definition of the output responses (energy and power density, cyclability) is required according to the sensitivities of the desired design parameters under study. Further work need to be done towards the evaluation methods (responses). Other cycling regimes could be analysed (pulses) to evaluate the cell dynamics or impedance spectroscopy model could also be used for transport and kinetic response evaluation. The objective of the design tool is to keep the optimisation problem as simple as possible (in terms of computational cost) while obtaining the maximum information of the internal electrochemical process limits.

2.5 MAIN WORKFLOW OF THE RESEARCH

In Figure 2.15 the workflow of this thesis is presented.

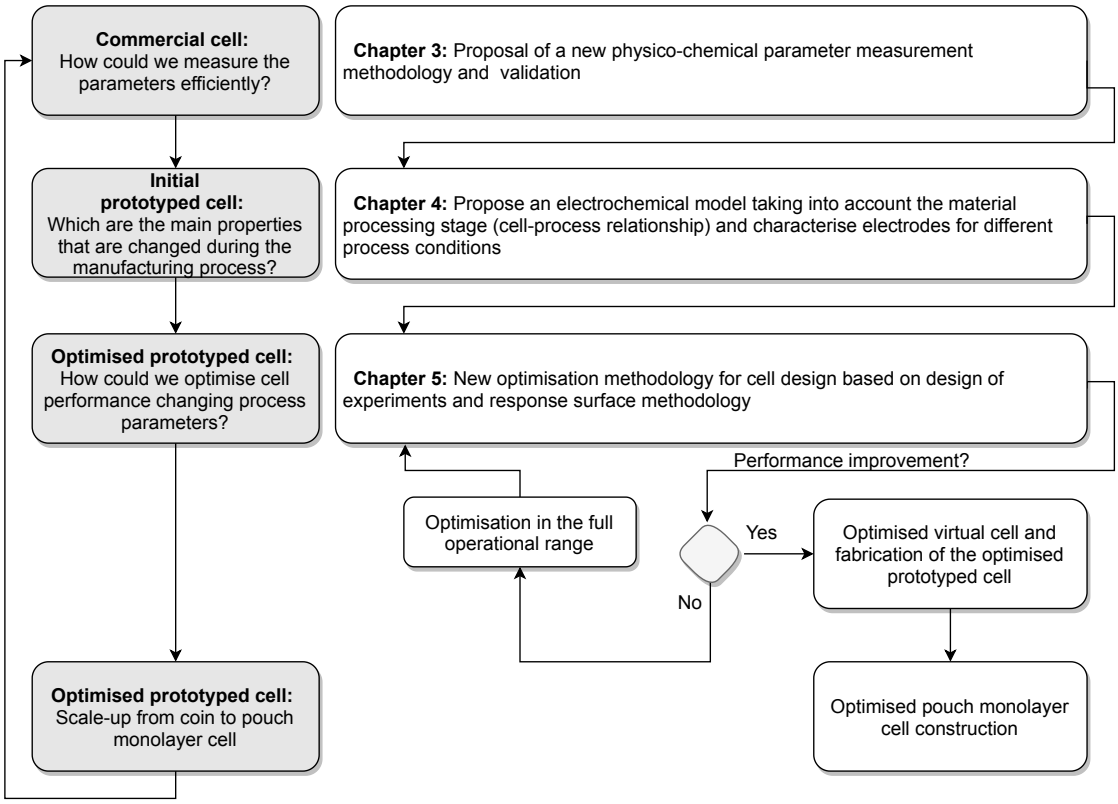

Figure 2.15: Workflow of this research.

In Chapter 3, a full parameter measurement methodology for a P2D model with a commercial cell is proposed. A commercial cell was selected for two reasons: (1) to set a reference cell for the prototyped cells, and (2) commercial cells have low dispersion between cells (quality controls are ensured) thereby providing reliable validation results.

In Chapter 4 prototyped cells are fabricated to study the material processing stage and propose a new cell-process relationship. It is not possible to study process relationships in commercial cells, as the manufacturers do not give any information about the fabrication process. Electrode characterisation for different calendering conditions are performed, and a P2D half-cell model for those conditions was validated.

Finally a model based design tool is developed in Chapter 5 to provide assistance to the prototyping line. The adjustable parameters of the cells are evaluated and optimised taking into account the calendering and material fabrication limits and its electrode balancing. This is done with three case studies, starting with the analysis within the experimental range (characterised calendering conditions in Chapter 4). Then, the optimisation is expanded to the full optimisation range and the methodology is validated with the pouch monolayer cell. Finally, proposals for further optimisations are discussed.

Chapter 3

PHYSICO-CHEMICAL MODELLING AND CHARACTERISATION OF A COMMERCIAL LITHIUM-ION BATTERY

This chapter presents a new methodology for parameter measurement and validation of a commercial lithium-ion cell for a pseudo-two-dimensional model. A comprehensive discussion and comparison of different experimental measurement techniques is presented with the aim of enhancing model predictions or simplification of measurement methods. Particular emphasis has been placed on model validation procedures, providing non-invasive and invasive tests to evaluate the differences between experimental and numerical results.

In Figure 3.1 the main workflow of the thesis is presented in which the topics discussed in this chapter are highlighted in grey.

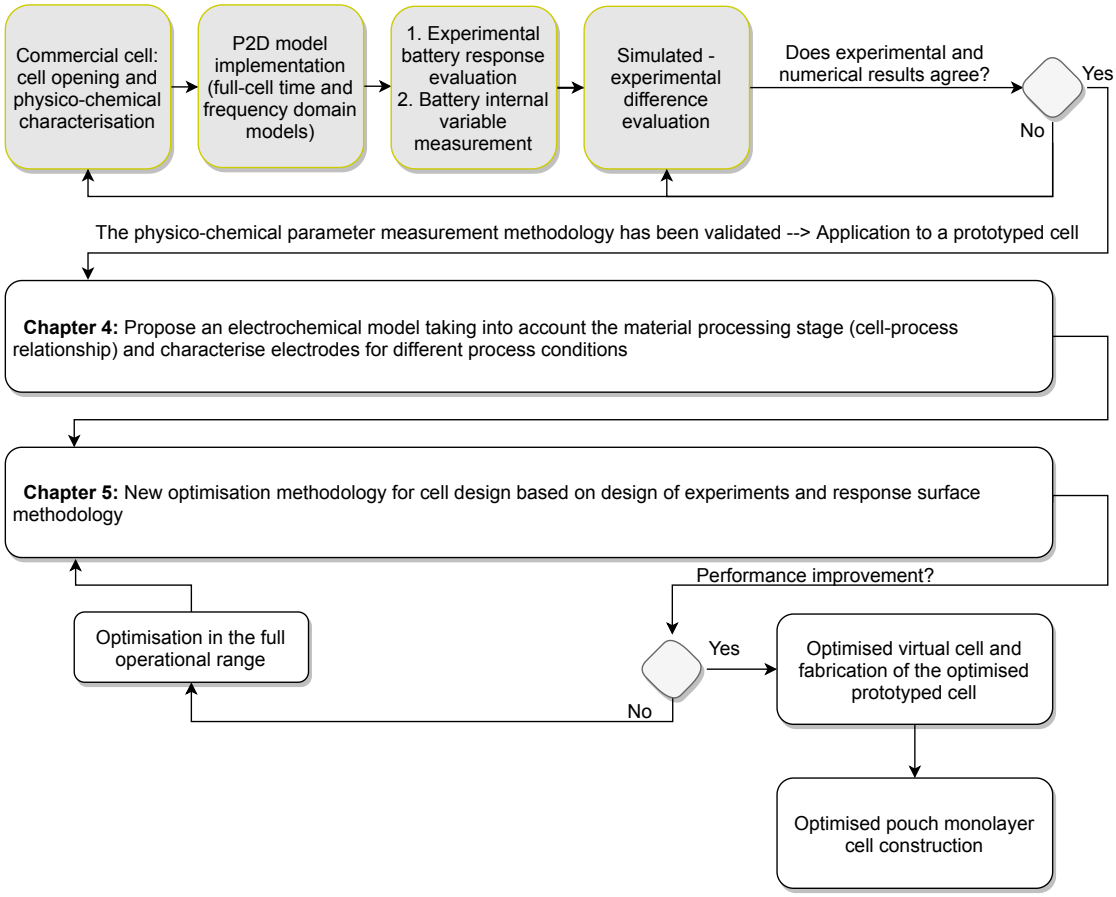

Figure 3.1: Main workflow of this research highlighting Chapter 3.

3.1 LI-ION BATTERY COMPONENTS AND WORKING PRINCIPLES

In Figure 3.2 Li-ion battery components and mechanisms are presented. The cell is composed of three porous materials: positive and negative electrode, and separator.

Each electrode is composed of a solid matrix of a mixture of active material, binder and additives. That solid matrix is coated onto a current collector (copper foil for negative electrodes and aluminium foil for positive electrodes). All the current collectors are welded to a tab, which are the terminals of the battery. The purpose of the separator is to prevent the contact between electrodes while allowing the ions to flow through the porous matrix. An electrolyte fills the void spaces of all the porous structures, which is usually composed of a lithium salt, a mixture of solvents (Ethylene Carbonate (EC), Dimethyl Carbonate (DMC), Ethyl Methyl Carbonate (EMC) etc.), and some additives.

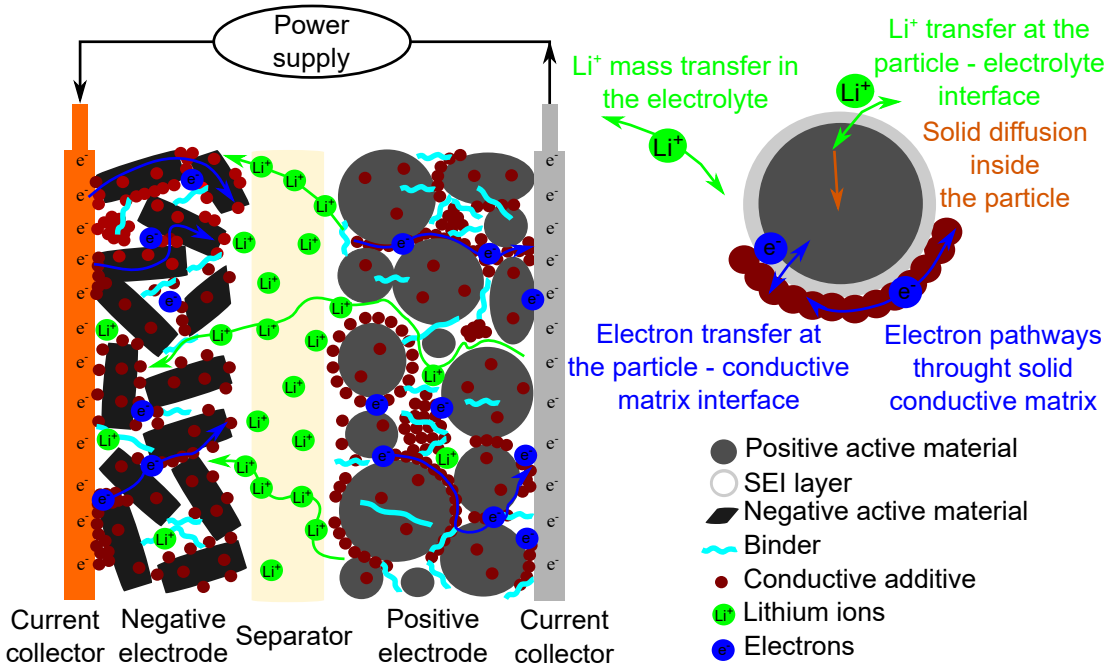

Figure 3.2: Lithium-ion battery charge process: Components and mechanisms.

In the charge process, Li^+ ions are deinserted from the positive electrode and transported through the electrolyte. Then, the ions are intercalated into the negative porous structure. In the discharge, lithium ions are deintercalated from the negative and inserted again in the positive electrode (rocking chair phenomena [29]).

In Figure 3.2 the main mechanisms that occur inside a battery are shown: charge and mass transport in solid and liquid phases, and the solid-liquid interface reaction. In subsection 3.2.3 the PDE equations of the electrochemical model related to those mechanisms is presented.

The battery cell voltage is given by the potential difference of the electrodes. In Figure 3.3) different positive and negative materials used for lithium-ion batteries are presented.

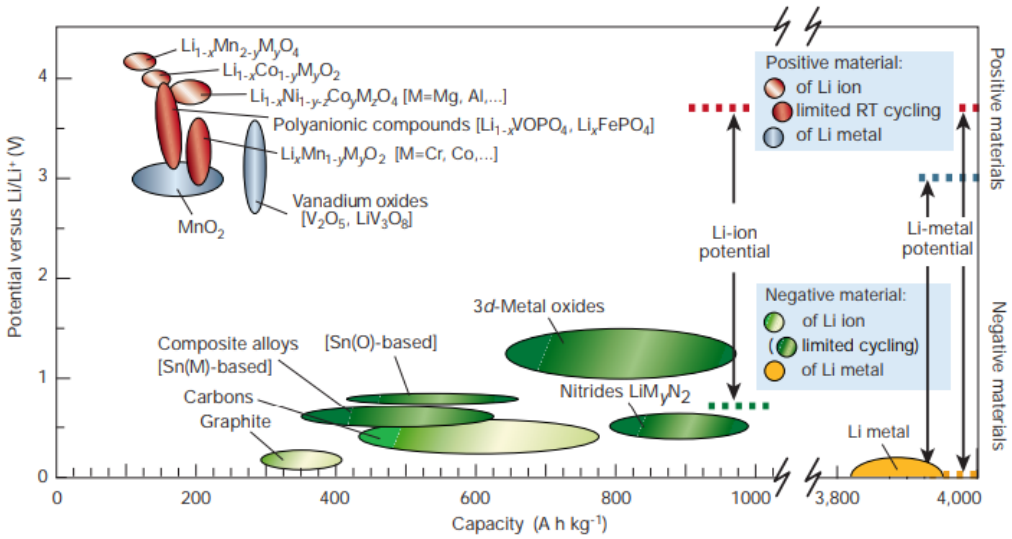

Figure 3.3: LIBs electrode materials, voltage versus capacity. Original source: Tarascon et al. [103]. The license is subject to Nature (CC BY 2.0).

3.2 STATE OF THE ART OF P2D MODEL

In the early 1960s, Newman and Tobias introduced for the first time the effects of concentration variations on electrode kinetics and the mass and momentum conservation equations in porous electrodes [104]. Later, in 1975, Newman and Tiedemann developed the porous electrode theory for batteries [105]. In these works, the governing equations associated with the complex geometry of porous media were derived based on average quantities and continuous functions. Later, in 1985, Bernardi et al. [106] set the general energy balance for batteries.

It was in 1993 when Doyle, Fuller and Newman established the mathematical model of galvanostatic charge/discharge behaviour of a half-cell system [57] which was based on the porous electrode theory. This is a general model, which can analyse all the materials available for constructing a lithium/polymer/insertion system with binary electrolyte and single-phase polymer solvent. The model uses a combination of the porous electrode theory and the concentrated solution theory. Concentrated solution theory was used as it takes into account ion pairing and ion association as well as solute-solvent interactions [57]. The diffusion of lithium into the active material was treated by superposition. Moreover, variable physical properties were also taken into account (for example, ionic conductivity variation as a function of the electrolyte concentration). Nowadays, the work of Doyle et al. [57] is considered the reference for modelling lithium-ion cells.

One year later (1994), based on the previous work of Doyle et al. [57], Fuller, Doyle and Newman developed a general model of a dual insertion cell (full-cell model), which could simulate any particular choice of insertion-type materials [107]. A Li_xC_6/PC + 1M $LiClO_4/Li_yMn_2O_4$ cell was simulated. One of their main conclusion was that the increase in concentration overpotential, due to the depletion of the electrolyte, does not allow batteries to work at high current rates. Moreover, in the same year, Fuller, Doyle and Newman [107] also analysed the relaxation phenomena in lithium-ion-insertion cells.

In 1995, a general overview of the use of mathematical models in battery design was presented by Doyle and Newman [21]. In that paper, a summary of the general equa-

tions of the P2D model, the characterisation techniques to physico-chemically measure the necessary parameters, and evaluation methods to analyse the system limitations were discussed. Afterwards, in 1996, Doyle and Newman [49] compared model predictions with experimental data of three different $Li_xC_6/LiPF_6$ EC:DMC pVdF-HFP/$Li_yMn_2O_4$ cells. The model was in good agreement with the experimental results presented in the paper.

Further improvements to the model were added in 1997, in which Darling and Newman [108] studied porous intercalation electrode modelling with two characteristic particle sizes. Moreover, in 1999, Ong and Newman [109] incorporated into the Fuller et al. model [107] the double layer capacitance effect, as it has considerable effect on the impedance of the battery. The double layer capacitance theory was developed by Helmholtz [110], Gouy-Chapman [111, 112] and finally Stern, who combined the previous studies [113].

All those works have established the mathematical framework of current models. From those models to the present, researchers have been improving the model extending the analysis to thermal effects, ageing mechanisms, mechanical and structural variations etc.

3.2.1 Full and half cell P2D model description

This model is based on the mathematical framework developed by Newman et al. [49, 57, 107, 109]. The model can simulate any insertion cell if physical properties and system parameters are given, and is based on the porous electrode and concentrated solution theory. It is not possible to describe perfectly the complex multiphysic behavior of batteries, and for this reason a clarification of the continuum model approach and model assumptions must be well defined to establish the model framework. More detailed information on the P2D model description can be found in [54]. This continuum model consists of a 1-D macroscopic model coupled with a pseudo dimension that is represented in Figure 3.4.

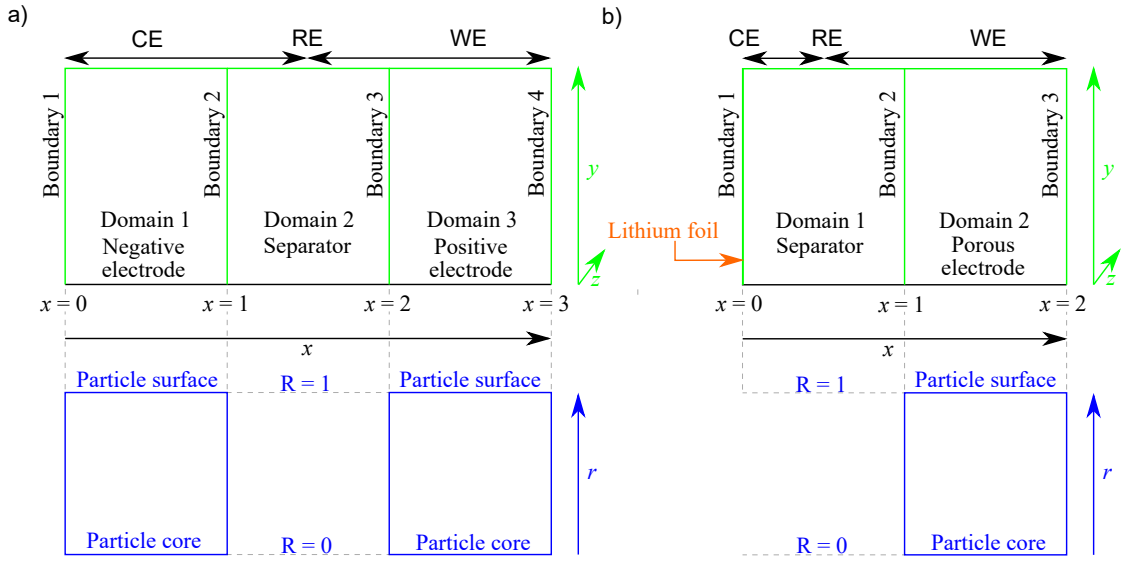

Figure 3.4: Schematic representation of the electrochemical model. a) Full-cell configuration; b) Half-cell configuration. Blue represents the pseudo-dimension (r) in which a particle is presented. Black represents the 1D dimension (x) of the model, thicknesses of the components of the cell (3 domains and 4 boundaries for full-cells / 2 domains and 3 boundaries for half-cells). Green represents y and z dimensions that are used to calculate the cross-sectional area. CE: counter electrode; RE: reference electrode; WE: working electrode.

In the full-cell model, the macroscopic level consists of three domains (see Figure 3.4 a)): a negative electrode, a separator and a positive electrode. There are four boundaries: the first and fourth boundaries correspond to the interface between the electrode and the current collectors, while the second and third boundaries are the interface between the electrodes and separator. The half-cell model (see Figure 3.4 b)) consists of three boundaries and two domains. One electrode (domain) of the full-cell model is replaced by a boundary condition representing a non-porous lithium metal foil.

The macroscopic description of this model is defined by volume averaging over small finite volume units of microscopic quantities. As a result, the electrodes are considered as the superposition of two continua, representing the solid and the liquid phases. Moreover, the electrodes are considered as porous matrices of electrochemically reactive and electrically conductive solids. The model assumes that the electrolytic solution completely fills the voids of the porous solid matrix. This means that solid and liquid matrices are considered separately. The microscopic level describes the active material particles and is represented in the pseudo-dimension (see Figure 3.4), and each electrode has one domain and two boundaries in which R = 0 corresponds to the particle core and R = 1 to the particle surface. Microscale geometries are described assuming volume-averaging theorems.

3.2.2 P2D model parameter identification and measurement methods

The purpose of this analysis is to obtain an overview of coherent sets of parameters that can be implemented into electrochemical models. Different approaches can be followed to obtain the parameters which can be grouped into:

(1) Physico-chemical measurement methods
(2) Single-objective computational parameter identification methods
(3) Multi-objective computational parameter identification methods
(4) Mixed methods (physico-chemical combined with computational)[1]

The parameter measurement or identification complexity can increase if temperature, state of charge, local concentration etc. are taken into account.

3.2.2.1 *Physico-chemical parameter measurement methods*

To our knowledge, only Falconi [56] has performed a review of parameter values for P2D models. The author provides a comparison between parameters of 31 works specifying if those parameters are measured, fitted, taken from another author or if the source is not mentioned. Only a few authors have performed a complete physico-chemical characterisation [21, 22, 49–52, 61, 62].

A similar concept introduced by Falconi [56] was used for the construction of Table 3.1. Authors that provide a full or almost full physico-chemical parameter measurement were reviewed. Special attention was paid to whether the authors have measured each parameter or not, and which technique was used. The characters corresponding to the used techniques follows the characters of Table 3.6.

[1] Computational and mixed method review is based on J5 journal publication.

Table 3.1: Overview of the measured physico-chemical parameters for electrochemical models.

Symbol	Doyle 1996 [49]	Doyle 2003 [88]	Fang 2010 [58]	Safari 2011 [114]	Prada 2012 [60]	Ecker 2015 [50, 51, 61]	Schmalstieg 2017 [22, 52, 62]	Falconi 2018 [56]
OCP (V)	h	h	h	h	h	h	h	h
AM (%)	pt	-	-	-	-	-	-	ns
ρ_{AM} (g cm^{-3})	ni	-	-	-	-	-	-	-
$c_{s,max}$ (mol m^{-3})	calc	-	ns	h	-	calc	calc	calc
θ_0 (-)	h	h	h	h	h	e, h	e, h	i
θ_{100} (-)	h	h	h	h	h	e, h	e, h	h
R_s (m)	ni	ns	ns	m	ns	o	o	m
a_s (m^{-1})	calc	calc	calc	calc	calc	o	o	calc
D_s (m^2 s^{-1})	-	-	ns	i	-	k	k	-
$E_{act,Ds}$ (kJ mol^{-1})	-	-	ea	-	-	k	k	-
A_{cell} (m^2)	l	l	ns	-	ns	l	l	l
L (m)	l	l	ns	m	ns	l	l	m
σ (S m^{-1})	h	ns	-	-	-	h	-	-
$E_{act,\sigma}$ (kJ mol^{-1})	-	-	-	-	-	h	-	-
brug (-)	-	calc	-	-	ea	o	o	-
ε_s (-)	calc	ns	-	i	calc	calc	calc	calc
ε_e (-)	calc	ns	ns	-	ea	o	o	calc
$\kappa_{ref,0}$ (S m^{-1})	k	-	-	-	-	k	k	-
$E_{act,\kappa}$ (kJ mol^{-1})	-	-	ea	-	-	k	k	-
D_e (m^2 s^{-1})	-	ns	-	-	-	calc	calc	-
$E_{act,De}$ (kJ mol^{-1})	-	-	ea	-	-	calc	calc	-
t_0^+ (-)	-	-	-	-	-	-	-	-
$c_{e,0}$ (mol m^{-3})	pt	-	pt	-	ea	-	-	-
k (mol m^{-2} s^{-1})	ni	ns	-	k	ea	k	k	-
$E_{act,k}$ (kJ mol^{-1})	-	-	ea	-	ea	k	k	-
R_{film} (Ω m^2)	h	calc	-	ea	ea	h	h	-
C_{dl} (F m^{-2})	-	-	-	-	-	-	h	-
α (-)	-	ns	-	ea	ea	k	-	-

(-): Not measured parameters (dash).
calc: calculated, fitted from other experimental results.
ns: no measurement source is specified and the value is not referenced to another work (own measurement).
pt: value taken directly from prototype cell fabrication.
ni: no information (measured or not).
ea: estimated or assumed parameter.
Experimental techniques: e: ICP-OES; h: cycling; i: PEIS; k: PITT; l: Micrometer-balance; m: SEM-EDS; o: Hg-porosimetry.

In the literature, two groups can be distinguished: partial and full parameter measurement methodologies.

On the one hand, partial characterisations are commonly found in the literature [49, 56–60]. In general, these methods consist of a cell opening and performing a basic physico-chemical characterisation (geometrical parameter measurement, Open Circuit Potential (OCP) measurement, full-cell balancing estimation and microstructural/composition analysis by scanning electron microscopy with Energy Dispersive X-Ray Spectroscopy (SEM-EDS)). However, transport and kinetic parameters are usually estimated or taken from other sources. Thus the model variable predictions are not accurate, although the voltage response behaves similarly to the experimentally measured data. If those parameters are identified by optimisation procedures, those are considered mixed methods. Furthermore, there is a lack of information about the specific experimental procedure that is used for obtaining some of the parameters (i.e. in Doyle et al. [88]).

On the other hand, very few articles show an almost complete physico-chemical characterisation [22, 50–52, 61, 62] and explain the procedure followed to obtain the parameters. Ecker et al. [50,51,61] performed an exhaustive work for the parameterisation of a commercial cell. However, they did not measure the active material content of the electrodes and the true density. Furthermore, the transport number, the electrolyte concentration and the capacitance were not measured. Schmalstieg et al. [22, 52, 62] improved the parameterisation of Ecker et al. [50,51,61], by identifying the electrolyte solvents with gas chromatography coupled to mass spectrometry (GC-MS), providing a new fitting for the solid diffusion coefficient based on galvanostatic intermittent titriation technique (GITT) results, and measuring thermal parameters (heat capacity and thermal conductivity). Schmalstieg et al. [22,52,62] did not measure two parameters in their work. Those are the transference number and the electronic conductivity of the electrodes. In addition, the active material content and initial salt concentration were not analysed. Those two parameters are known in prototyped cells but are difficult to measure in commercial cells [38].

3.2.2.2 *Single-objective computational parameter identification methods*

Since 2002, different attempts to obtain parameters computationally have been made [63–75]. All these authors aimed to find the combination of parameters that best fit the experimental data with the voltage response of the model, and only a few considered temperature predictions [69–71]. Different optimisation methods were employed by the authors (i.e. linear, non-linear or genetic algorithms) and were solved differently (series or parallel computing).

Starting from the simpler approach, some authors try to fit model parameters based on constant current cycles at different current rates. However, this method can lack precision as there are some parameters that are not sensitive to the voltage curve [75, 115]. The single-objective computational parameter identification methodology is not valid for obtaining the full set of parameters. As a result, only partial parameter identification can be performed with this method. Thus, voltage validation is not enough to ensure good model parameter identification. Authors who did not provide information about the obtained final parameters are not further studied in this thesis, as it is not possible to validate parameters that are far from their physical meaning. Therefore, only [72–75] were selected because they provided validation against voltage curve and information about the identified parameters.

Forman et al. [72] obtained computationally OCP curves of the electrodes based on OCV full-cell measurements, however this makes the optimisation process even more complex and some parameters remain unidentifiable. Genetic algorithms were used for parameter identification, and were validated against several drive cycles. The best fit was found in the Naturalistic2 cycle, in which a maximum voltage error of less than 118.9 mV in all the cases.

Rajabloo et al. [73] used a single particle model and carried out a sensitivity analysis based on voltage curves at different discharge rates. Two or three domains of the voltage curve depending on the chemistry (LCO, LMO or LFP) were identified for better parameter sensitivity (high SOCs, middle SOCs and low SOCs). The optimisation was performed using the genetic algorithm approach with constrained parameters. A maximum and minimum parameter value was set for the optimisation guaranteeing that the result was physically possible. The maximum deviations were found at high rates (4C) with LMO chemistry with a 0.01 RMS voltage error.

Masoudi et al. [74] used single particle modelling and the homotopy optimisation procedure for parameter identification. This optimisation method proved to be an effective technique to identify parameters in dynamic systems [74]. The authors noted that model parameters should be identified based on experimental data or a more accurate model, in order to enhance model predictions. In addition, partial parameter identification (four parameters) were presented in that analysis.

In the work of Deng et al. [75] a reduced-order model (ROM) based on the P2D model was employed to identify the parameters. The authors grouped the parameters into single identifiable, group identifiable or unidentifiable. A perturbation of 0.1% of parameters was used to calculate their sensitivities. It is worth mentioning that geometric parameters and electrolyte properties were not included in the optimisation as they were obtained directly or from the literature (experimental process). Among the 14 parameters analysed, 5 of them could not be identified and those remaining could only be identified as a grouping parameter (cross-influence between parameters occurs). Two validation cycles were performed (pulses and UDDS cycle) in which the best results were obtained with the pulsed cycle. The maximum deviation was found in the negative electrode solid diffusion parameter (18.6% with respect to the true P2D value).

3.2.2.3 *Multi-objective computational parameter identification methods*

The main difference between single- and multi-objective computational parameter identification methods is that in the latter a combination of electrical and electrochemical tests and sequenced optimisation procedures are proposed [76–78].

In Table 3.2 the methodologies considered key in this field are summarised. There, the methodology, the model used, grouping of parameters, and the experimental profiles used for the identification (ID) and validation are presented.

Table 3.2: Multi-objective computational parameter identification methods.

Namor 2017 [76]	
Methodology	Three identification problems formulated as a non-linear least-square fitting problem.
Model and grouped parameters	SPM grouped parameters (∗1): (A) Related to low-rate testing: Q_n, Q_p; (B) Related to pulse testing: $k_0^{*,\mathrm{n}}$, $k_0^{*,\mathrm{p}}$, R_{cell}; (C) Related to GITT testing: $D_{\mathrm{s}}^{*,\mathrm{n}}$, $D_{\mathrm{s}}^{*,\mathrm{p}}$
Experimental profile and validation	ID profile: (i) Low rate tests; (ii) Pulse tests; (iii) Galvanostatic Intermittent Titration Technique (GITT) tests. Validation: (i) Realistic profile for grid-level application, and (ii) Dynamic Stress Test (DST) profile.
Li 2018 [77]	
Methodology	Three identification problems formulated as a non-linear least-square fitting problem.
Model and grouped parameters	SP model simplification with grouped parameters: (A) Related to OCV testing:θ_0^{n}, θ_0^{p}, $\theta_{100}^{\mathrm{n}}$, $\theta_{100}^{\mathrm{p}}$, Q^n, Q^p; (B) Related to ohmic resistance and reaction polarization: P_{act}; (C) Related to diffusion processes: P_{con}, τ_s
Experimental profile and validation	ID profile: (i) OCV testing, (ii) Designed dynamic cycle; Validation: Charge /discharge behaviours.
Park 2018 [78]	
Methodology	(i) Sensitivity analysis; (ii) Normalization; (iii) Linear dependence ranking calculation; (iV) Parameter fitting by means of nonlinear least-squares with the Levenberg-Marquardt algorithm.
Model and grouped parameters	P2D model. Grouped parameters: (A) $R_{\mathrm{s}}^{\mathrm{n}}$, $R_{\mathrm{s}}^{\mathrm{p}}$; (B) $D_{\mathrm{s}}^{\mathrm{n}}$, $D_{\mathrm{s}}^{\mathrm{p}}$, $\varepsilon_{\mathrm{e}}^{\mathrm{n}}$, κ, D_e, $\partial \ln f_{\pm}/\partial \ln c_{\mathrm{e}}$; (C) $R_{\mathrm{film}}^{\mathrm{n}}$, $R_{\mathrm{film}}^{\mathrm{p}}$, k_0^{n}, $\varepsilon_{\mathrm{e}}^{\mathrm{p}}$, $c_{\mathrm{e},0}$; (D) k_0^{p}, σ^{n}, σ^{p}, $\varepsilon_{\mathrm{e}}^{\mathrm{s}}$, t_+^0; Fixed parameters: L^{n}, L^{s}, L^{p}, A_{cell}
Experimental profile and validation	ID procedure: 738 different profiles: pulses, sinusoids and driving cycles. Validation: 9 profiles ranging from constant current pulses to driving cycles.

(∗1) Parameter should be lumped as specified: $Q = FR_s a_s c_{s,max}$; $k_0^* = (k_0 c_e^{0.5})/R_s$; $D_s^* = D_s/R_s$;
P_{act}: coefficient of anode reaction polarization.
P_{con}: proportional coefficient of liquid-phase diffusion.
τ_s: solid-phase diffusion time constant.

In the literature it has been demonstrated that only a galvanostatic discharge curve is not enough to identify all the P2D model parameters [79–81]. Thus, procedures with cycles at different current rates, pulses and impedance measurements are proposed. Those procedures require more experimental tests (more time consuming tests and not only a cycler, but also a potentiostat is sometimes required). The works that are considered in this group did not need to open the cell, therefore, the methodology is based on non-invasive tests.

3.2.2.4 *Mixed methods*

Mixed methods are those which measure some model parameters experimentally (tear-down of the cells) and apply computational optimisations to finish the identification procedure. The summary of methods proposed in the literature is presented in Table 3.3.

Table 3.3: Mixed methods.

Zhang 2013 [79, 80] and Zhang 2014 [81]	
Methodology	Parameter sensitivity analysis is performed (fuzzy clustering method) [79], genetic algorithms are proposed to speed up the identification [80] and temperature sensitivity is added [81].
Model and grouped parameters (*1)	P2D model. 4 clusters [80]: (A) σ^{p}, c_{e}, κ, k_0^{p}, $E_{act}^{\mathrm{n}}k_0$, $E_{act}^{\mathrm{p}}k_0$, $E_{act}^{\mathrm{n}}D_e$, $E_{act}^{\mathrm{n}}\kappa_e$; (B) $\varepsilon_{\mathrm{e}}^{\mathrm{n}}$, $\varepsilon_{\mathrm{s}}^{\mathrm{n}}$; (C) $R_{\mathrm{s}}^{\mathrm{n}}$, $R_{\mathrm{s}}^{\mathrm{p}}$, $D_{\mathrm{s}}^{\mathrm{n}}$, $D_{\mathrm{s}}^{\mathrm{p}}$, $\varepsilon_{\mathrm{s}}^{\mathrm{p}}$, D_e, $\varepsilon_{\mathrm{e}}^{\mathrm{p}}$, $E_{act}^{\mathrm{n}}D_s$; (D) $R_{\mathrm{film}}^{\mathrm{n}}$, R_{ext}; (NC) θ_0^{n}, θ_0^{p}, k_0^{n}; (IS) σ^{n}, $R_{\mathrm{film}}^{\mathrm{p}}$, ρ_e, $\varepsilon_{\mathrm{e}}^{\mathrm{s}}$, $E_{act}^{\mathrm{p}}D_s$ 3 clusters [81]: (A) $R_{\mathrm{s}}^{\mathrm{p}}$, $D_{\mathrm{s}}^{\mathrm{p}}$, c_{e}, R_{ext}, $\varepsilon_{\mathrm{e}}^{\mathrm{p}}$, k_0^{n}, k_0^{p}, $E_{act}^{\mathrm{n}}k_0$, $E_{act}^{\mathrm{p}}k_0$, $E_{act}^{\mathrm{n}}D_s$, $E_{act}^{\mathrm{p}}D_s$, λ; (B) $R_{\mathrm{s}}^{\mathrm{n}}$, $D_{\mathrm{s}}^{\mathrm{n}}$, σ^{p}, θ_0^{n}, $\varepsilon_{\mathrm{s}}^{\mathrm{n}}$, κ, $E_{act}^{\mathrm{n}}D_e$, h; (C) $\varepsilon_{\mathrm{s}}^{\mathrm{p}}$, $R_{\mathrm{f}}^{\mathrm{n}}$, D_e, $\varepsilon_{\mathrm{e}}^{\mathrm{n}}$, $\varepsilon_{\mathrm{e}}^{\mathrm{s}}$; (NC) θ_0^{p}, $E_{act}^{\mathrm{n}}\kappa_e$; (IS) σ^{n}, $R_{\mathrm{film}}^{\mathrm{p}}$, ρ_e
Experimental profile and validation	ID best profiles: very low temperature/very high rate, room temperature/medium rate and very high temperature/very high rate. Validation: Five different temperatures (-5, 10, 25, 40, 55) °C and five different discharge rates (0.2, 0.5, 1, 2, 4) C.
Jobman 2016 [82, 83] and Chu 2019 [84]	
Methodology	Three identification problems formulated as non-linear least-square fitting problems.
Model and grouped parameters (*2)	Reformulated P2D model. Non-lumped parameters grouped according to the optimisation groups: (A) Related to OCV testing: $\theta_{0,coin}^{\mathrm{n}}$, $\theta_{100,coin}^{\mathrm{n}}$, $\theta_{0,coin}^{\mathrm{p}}$, $\theta_{100,coin}^{\mathrm{p}}$; (B) Related to pulse testing: $\kappa_{\mathrm{eff}}^{\mathrm{n}}$, $\kappa_{\mathrm{eff}}^{\mathrm{s}}$, $\kappa_{\mathrm{eff}}^{\mathrm{p}}$, $\sigma_{\mathrm{eff}}^{\mathrm{n}}$, $\sigma_{\mathrm{eff}}^{\mathrm{p}}$, k_0^{n}, k_0^{p}, $R_{\mathrm{f}}^{\mathrm{n}}$, $R_{\mathrm{film}}^{\mathrm{p}}$, θ_0^{n}, θ_0^{p}, $\theta_{100}^{\mathrm{n}}$, $\theta_{100}^{\mathrm{p}}$; (C) Related to frequency testing: $c_{\mathrm{e},0}^{n}$, $c_{\mathrm{e},0}^{s}$, $c_{\mathrm{e},0}^{p}$, $D_{\mathrm{e,eff}}^{\mathrm{n}}$, $D_{\mathrm{e,eff}}^{\mathrm{s}}$, $D_{\mathrm{e,eff}}^{\mathrm{p}}$, $D_{\mathrm{s}}^{\mathrm{n}}$, $D_{\mathrm{s}}^{\mathrm{p}}$, t_+^0
Experimental profile and validation	ID procedure: (i) Half-cell OCP data (coin cells) C/30 CC process; (ii) OCV/R_{ss} data (full-cell) C/30 CC process; (iii) Full cell frequency data; (iv) Full cell R_0 data (0.1 s pulses at different C rates) (v) (i to iV) for different temperatures. Validation: At different temperatures (0, 10, 25, 30, 40) °C.

(*1) R_{ext}: extra resistance; ρ_e: electrolyte density; λ: thermal conductivity; h: heat transfer coefficient; (NC): Not clustered; (IS): insensitive.
(*2) For better understanding of the studied works, the original non-lumped parameters are presented in the table.

The tear-down of the cell is performed to extract open circuit voltage curves and geometrical parameters (generally). It is worth mentioning that the OCV curves are obtained cycling half cells built with samples of the electrodes extracted from the full cell. In addition, as the cell is disassembled to obtain the OCV curves geometrical parameters can be directly obtained with very little effort and high accuracy, keeping the optimisation problem simple enough to be solved.

Many different combinations of parameters can lead to the same model output, which means that even if the optimised set of parameters fits the experimental data, internal variables are not necessarily correct. In order to overcome this, different approaches can be

followed: group parameters according to their sensitivities [79–81, 116] or reformulate the model [83]. Reduced order models solves the dependent variables without losing accuracy but minimising the computational cost [54, 83]. It is worth noting that the optimisation method (non-linear solvers, genetic algorithms etc.) is only significant when the problem is well stated or not excessively complicated to solve.

Zhang et al. [79–81, 116] presented only computational results for identification of a P2D model. As all the model parameters were taken from experimental sources [60, 114] it is considered as a mixed procedure. They grouped the model parameters based on its sensitivity for different profiles. They achieved a maximum error of 20.86% for the less accurate parameter and the remaining parameter error was lower than 10%.

Jobman et al. and Chu et al. [82–84] present a reformulation of the P2D model using lumped parameters. The number of parameters to be identified was reduced to a minimum and cross-linked interactions were prevented by including design adjustable parameters in the lumped parameters (L, A, a_s, ε_e, ε_s and R_s). The error for all parameters was below 10.1% except ne_0 terms (related to electrolyte concentration). The authors reported that this error could be reduced by improving the optimisation methodology.

3.2.3 Governing equations, assumptions and cell characteristics

In this subsection model variables (highlighted in blue), parameters (highlighted in orange), assumptions, governing equations, boundary conditions and cell characteristics are described.

The P2D model solves spatial and time evolution of five variables:

- Potential ($\phi_s(x,\, t)$) of lithium in the solid particles
- Concentration ($c_s(x,\, r,\, t)$) of lithium in the solid particles, specifically on the surface of the solid ($c_{s,e}(x,\, t)$)
- Potential ($\phi_e(x,\, t)$) of lithium in the electrolyte
- Concentration ($c_e\ (x,\, t)$) of lithium in the electrolyte
- Flux of lithium out of a particle ($j_{tot}\ (x,\, t)$)

3.2.3.1 *Governing equations and boundary conditions*

The model is composed of a set of four partial-differential equations (PDEs) and one algebraic equation. These equations describe the dynamics of a cell. The PDEs solve the charge and material balance in the liquid and solid-phases. Those equations are coupled with the pore wall flux algebraic equation.

Charge conservation in the solid-phase: The first PDE is related to the charge conservation in the solid-phase. The solid-state potential (ϕ_s) in the electrodes is derived from Ohm's law (equation 3.1). The applied boundary conditions for the current conservation of the solid-phase are presented in 3.2, where $x = 0$ starts from the negative current collector (boundary 1 in Figure 3.4), and $x = L_{tot}$ represents the positive current collector.

$$\frac{\partial}{\partial x}\left(\sigma_{eff}\frac{\partial}{\partial x}\phi_s(x,t)\right) - a_s F j_{tot}(x,t) = 0 \tag{3.1}$$

where σ_{eff} is the effective electronic conductivity, a_s is the specific surface area, and F is the Faraday's constant.

$$-\sigma^n_{eff}\frac{\partial}{\partial x}\phi_s(0,t) = \sigma^p_{eff}\frac{\partial}{\partial x}\phi_s(L_{tot},t) = \frac{I_{ct}}{A} \tag{3.2}$$

where L_{tot} is the total thickness of all the cell components and i_{app} is the current density.

Mass conservation in the solid-phase: The second PDE models the pseudo-dimension (r) of the continuum model. The solid-state lithium concentration (c_s) in the electrodes is derived from Fick's law of diffusion for spherical particles (equation 3.3). The boundary conditions are presented in equation 3.4.

$$\frac{\partial c_s(x,r,t)}{\partial t} = \frac{D_s}{r^2}\frac{\partial}{\partial r}\left(r^2\frac{\partial c_s(x,r,t)}{\partial r}\right) \tag{3.3}$$

$$D_s\frac{\partial c_s(x,0,t)}{\partial r} = 0; t \geq 0; D_s\frac{\partial c_s(x,R_s,t)}{\partial r} = -j_{tot}(x,t) \tag{3.4}$$

where D_s is the solid diffusion coefficient and R_s is the AM particle radius.

Charge conservation in the liquid-phase: The liquid-phase potential (ϕ_e) in the electrolyte and in the separator is calculated using Kirchhoff's and Ohm's laws (equation 3.5). The boundary conditions are shown in equations 3.6 and 3.7.

$$\frac{\partial}{\partial x}\left(\kappa_{eff}\frac{\partial}{\partial x}\phi_e(x,t)\right) + a_s F j_{tot}(x,t) + \frac{\partial}{\partial x}\left(\kappa_{D,eff}\frac{\partial}{\partial x}\ln(c_e(x,t))\right) = 0 \tag{3.5}$$

where κ_{eff} is the effective electrolyte conductivity.

$$\kappa_{eff}\frac{\partial}{\partial x}\phi_e(0,t) + \kappa_{D,eff}\frac{\partial}{\partial x}\ln(c_e(0,t)) = 0 \tag{3.6}$$

$$\kappa_{eff}\frac{\partial}{\partial x}\phi_e(L_{tot},t) + \kappa_{D,eff}\frac{\partial}{\partial x}\ln(c_e(L_{tot},t)) = 0 \tag{3.7}$$

Mass conservation in the liquid-phase: The liquid-phase Li^+ ion concentration (c_e) in the electrolyte and in the separator is based on the conservation of Li^+ ions (equation 3.8), which is again modelled using Ohm's law. The boundary conditions are shown in equation 3.9.

$$\frac{\partial(\varepsilon_e c_e(x,t))}{\partial t} = \frac{\partial}{\partial x}(D_{e,eff}\frac{\partial}{\partial x}c_e(x,t)) + a_s(1-t_0^+)j_{tot}(x,t) \tag{3.8}$$

where ε_e is the electrode porosity, $D_{e,eff}$ is the effective electrolyte diffusion coefficient, and t_0^+ is the transport number.

$$\frac{\partial(c_e(0,t))}{\partial x} = \frac{\partial(c_e(L_{tot},t))}{\partial x} = 0 \tag{3.9}$$

Solid-liquid interface via Butler-Volmer equation: Finally, the pore wall flux of Li^+ ions (j) in the electrodes is described by the Butler-Volmer kinetics equation (equation 3.10). From a macroscopic point of view, the overall reaction rate in the battery is depicted by the current. On a microscopic scale, the local reaction rate is governed by the physical microstructure and chemical environment.

$$j_{tot} = \frac{i_0}{F}\left\{\exp\left(\frac{(1-\alpha)F}{RT}\eta\right) - \exp\left(-\frac{\alpha F}{RT}\eta\right)\right\} \tag{3.10}$$

Where i_0 is the exchange current density defined as (equation 3.11):

$$i_0 = F k_{0,norm} \left(\frac{c_e}{c_{e,0}} \right)^{1-\alpha} \left(\frac{c_{s,\max} - c_{s,e}}{c_{s,\max}} \right)^{1-\alpha} \left(\frac{c_{s,e}}{c_{s,\max}} \right)^{\alpha} \tag{3.11}$$

where $c_{s,max}$ is the maximum solid lithium concentration, α is the transfer coefficient, $k_{0,norm}$ is the reaction rate, and $c_{e,0}$ initial electrolyte concentration.

The reaction overpotential (η) is:

$$\eta = \phi_s - \phi_e - U_{ocp}(c_s) - F R_{film} j_{tot} \tag{3.12}$$

where U_{ocp} is the open circuit potential of the active materials, and R_{film} is the film resistance of the electrodes.

Lithium counter-electrode for the half cell model: To this point, P2D model equations for a full-cell model have been described, in which two porous electrodes are modelled. In the case of half-cell modelling, one of the electrodes is represented as a non-porous lithium metal foil. In the metallic lithium foil a charge transfer reaction occurs on the surface. The following redox reaction at 0V vs Li^+/Li occurs (equation 3.13):

$$Li \leftrightarrow Li^+ + e^- \tag{3.13}$$

Butler-Volmer equation is applied as a boundary condition replacing one of the electrode domain in Figure 3.4 a) (equation 3.14). Thus, the half-cell model representation is as presented in Figure 3.4 b).

$$j^{Li} = \frac{i_0^{Li}}{F} \left\{ \exp\left(\frac{(1-\alpha^{Li}))F}{RT} \eta \right) - \exp\left(-\frac{\alpha^{Li} F}{RT} \eta \right) \right\} \tag{3.14}$$

Where the reaction overpotential (η) is (equation 3.15):

$$\eta = \phi_s - \phi_e - U_{ocp}^{Li} \tag{3.15}$$

where U_{ocp}^{Li} is the open circuit potential of the lithium metal foil, α^{Li} is the transfer coefficient, and i_0^{Li} lithium exchange current density.

Frequency domain model: The impedance response of the model allows us to study and distinguish the different processes occurring inside batteries at certain time-scales. At high frequencies the ion transport in the electrolyte can be identified. Then, a semi-circle related to the SEI layer is defined. After, at medium frequencies charge-transfer through solid-liquid interfase occurs. Finally, at low frequencies particle diffusion occurs.

In order to describe the impedance behaviour of the battery, first of all, the double layer effect needs to be added to the impedance model as it affects the simulation results [83,117]. Therefore, the work of Ong and Newman has been taken as a reference [109] to modify the model equations. Equation 3.1 is modified including the double layer capacitance (equation 3.16).

$$\frac{\partial}{\partial x} \left(\sigma_{eff} \frac{\partial}{\partial x} \phi_s(x,t) \right) - a_s F j_{tot}(x,t) - a_s C_{dl} \left(\frac{\partial}{\partial t} \phi_{dl}(x,t) \right) = 0 \tag{3.16}$$

where C_{dl} is the electric double layer capacitor, and ϕ_{dl} is the double layer potential.

Then, the total flux previously defined as the faradaic contribution of the electrodes (j_{BV}) with the Butler-Volmer equation (equation 3.10) is now redefined to take into account the non-faradaic contribution (j_{DL}) (equation 3.17).

$$j_{tot}(x,t) = j_{BV}(x,t) + j_{DL}(x,t) \tag{3.17}$$

After the contribution of the double layer is added into the model, time-dependent equations and their corresponding boundary conditions need to be converted into the frequency domain with the Fourier transform. Different examples can be found in the literature with the P2D model equations in the frequency domain [109, 117–119]. As the perturbation of the EIS measurement is maintained sufficiently small, model responses can be treated as linear and the concentration change of the parameters disregarded. Then, the dependent variables of the model are described as a perturbation around an equilibrium value (equation 3.18):

$$m = \bar{m} + Re\{\widetilde{m}e^{jwt}\} \tag{3.18}$$

where m is a frequency dependent variable, $\bar{m}$ is the variable equilibrium value, $\widetilde{m}$ is the complex perturbation from the equilibrium value, Re is the real value, j is the imaginary unit, w perturbation frequency, and t time.

To simulate a Potentiostatic Electrochemical Impedance Spectroscopy (PEIS) measurement a sinusoidal excitation signal is applied as a boundary condition at the boundary 4 in Figure 3.4 a) (full-cell configuration) and boundary 3 in Figure 3.4 b) (half-cell configuration) (equation 3.19). On the boundary 1, the condition is fixed to 0 V (grounded).

$$\phi_s(L_{tot},t) = U_{ocp} + V_{pert}sin(2\pi ft) \tag{3.19}$$

The cell impedance (Z) is then calculated as follows (equation 3.20):

$$\widetilde{Z}_{cell} = \frac{\widetilde{\phi_s}}{\widetilde{i_{cell}}} \tag{3.20}$$

In order to calculate the contribution of the cell impedance from each electrode or subtract the contribution of lithium metal foil from the total impedance a reference electrode is defined in the model. In this case, the reference electrode is assumed to be in the middle of the electrolyte/separator domain in both half- and full-cells, as represented in Figure 3.4 a) and b). Therefore, in the full-cell, the positive impedance (equation 3.21) is calculated. The contribution to the total impedance of the lithium metal foil or the negative electrode is calculated by the difference between the full-cell impedance and the positive electrode impedance.

$$\widetilde{Z}^p = \frac{(\widetilde{\phi_s} - \widetilde{\phi_{RE}})}{\widetilde{i_{cell}}} \tag{3.21}$$

3.2.3.2 *Model assumptions*

In the aforementioned governing equations, several assumptions and corrections are needed to describe the porous media of the electrodes and separator [120], the particle shape, and the temperature dependence of the parameters.

Effective parameter calculation: Different cases can be found in a real porous electrode. Figure 3.5 shows the different ion paths from the ideal (case A), through case B (assuming spherical, homogeneously distributed particles), to the real tortuosity (case

C). In reality, particles are not spherical, not-uniform sized and not-uniformly distributed through the electrode.

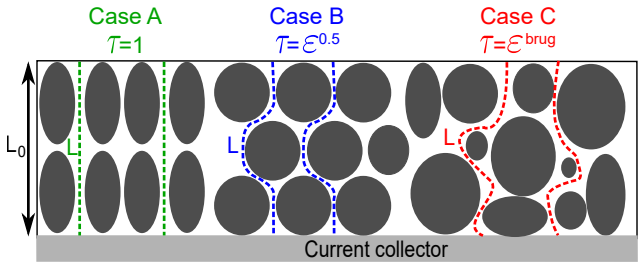

Figure 3.5: Different tortuosity scenarios. Green, blue and red dashed lines show the ion diffusion paths in the three different cases. Based on [56].

The tortuosity can be defined as a ratio between the shortest and real path of the ion diffusing in a porous media (equation 3.22). So as to relate the tortuosity with the volume fraction, equation 3.23 is applied to the model. This equation represents the Bruggeman exponent [120].

$$\tau = \frac{L_{diff}}{L} \tag{3.22}$$

$$\tau = \varepsilon_s{}^{brug} \tag{3.23}$$

where τ is the tortuosity of the electrode, ε_s is the solid volume fraction of the electrode, and L_{diff} is the real path of ions to diffuse in a porous media.

Bearing in mind the porous media, the bulk properties need to be corrected so as to obtain the effective properties. Therefore, the Bruggeman exponent has been applied to electrolyte conductivity, electrolyte diffusivity and electronic conductivity as follows:

$$D_{e,eff} = \frac{\varepsilon_e D_e}{\tau} = \varepsilon_e^{brug} D_e \tag{3.24}$$

$$\kappa_{eff} = \frac{\varepsilon_e \kappa}{\tau} = \varepsilon_e^{brug} \kappa \tag{3.25}$$

$$\sigma_{e,eff} = \frac{\varepsilon_s \sigma_0}{\tau} = \varepsilon_s^{brug} \sigma_0 \tag{3.26}$$

Particle shape and active area: The specific surface area is calculated assuming that the model has spherical particles of uniform size and distribution (equation 3.27) [49].

$$a_s = \varepsilon_s \frac{4\pi R_s^2}{(4/3)\pi R_s^3} = \frac{3\varepsilon_s}{R_s} \tag{3.27}$$

This parameter is particularly important for the solid diffusion coefficient, exchange current density, double layer capacitance and electrode film resistance. A significant difference can be found between the real and geometrical specific surface area, which affects the reaction occurring at the solid-liquid interface [121] and thus affecting the pore wall flux of the model, which is coupled to all the PDEs of the model.

Parameter temperature dependence: Moreover, the temperature dependence of the parameters (σ, κ, k and D_s) are accounted for by the Arrhenius equation [122] which is defined as $e^{\left(\frac{E_{act}}{R}\left(\frac{1}{T}-\frac{1}{T_{ref}}\right)\right)}$, where E_{act} is the activation energy and T_{ref} is the reference temperature.

3.2.3.3 *Cell characteristics*

The total voltage of the cell is set at the boundary of the positive electrode and aluminium current collector, as the negative-copper current collector boundary is grounded (equation 3.28).

$$V(t)[V] = \phi_s(L_{tot}, t) - \phi_s(0, t) = \phi_s(L_{tot}, t) \tag{3.28}$$

Positive and negative capacities are dependent on the respective solid volume fraction,the electrode thickness, as well as the solid concentration. Equation 3.29 and 3.30 shows the calculation for the nominal capacity of the cell.

$$Q^n[Ah] = (AFL^n\varepsilon_s^{neg}c_{s,\max}^n\,|\theta_{100}^n - \theta_0^n|)/3600 \tag{3.29}$$

$$Q^p[Ah] = (AFL^p\varepsilon_s^{pos}c_{s,\max}^p\,|\theta_{100}^p - \theta_0^p|)/3600 \tag{3.30}$$

Therefore, the total capacity of the cell is the minimum of positive and negative capacities (equation 3.31):

$$Q^c[Ah] = \min(Q^n, Q^p) \tag{3.31}$$

The state of charge (SoC) of the battery is calculated as (equation 3.32):

$$SOC = \frac{c_{s,avg}^n/c_{s,\max}^n - \theta_0^n}{\theta_{100}^n - \theta_0^n} = \frac{c_{s,avg}^p/c_{s,\max}^p - \theta_0^p}{\theta_{100}^p - \theta_0^p} \tag{3.32}$$

Energy and power densities are calculated with equation 3.33 and 3.34 respectively:

$$E_m[Wh\ kg^{-1}] = \frac{I_{ct}}{m_{tot}}\int_0^{t_{end}} V dt \tag{3.33}$$

$$P_m[Wkg^{-1}] = \frac{E}{t} \tag{3.34}$$

3.2.4 P2D model validation

In this subsection, an overview of the validation procedures used in the literature for P2D model validation are presented. Once parameter measurement or identification and model implementation is carried out, the model performance is evaluated to assess its validity. This overview is divided in non-invasive and invasive methods. Non-invasive methods are commonly used to evaluate the performance at different operating conditions, whereas invasive methods are focused on the validation of internal variable predictions of the model (electrode potentials, lithium content inside particles, electrolyte concentration etc.).

3.2.4.1 *Non-invasive testing*

Non-invasive tests are based on electrical, electrochemical or thermal tests. Voltage, current and temperature data are commonly acquired. The equipment necessary for these validations generally requires a cycler, a climatic chamber, a thermocouple and sometimes a potentiostat. All the works presented in Table 3.1 have been taken as a reference to study the tests that are usually used for a P2D model validation. The summary of the analysis is presented in Table 3.4. These test could be divided into three categories: capacity tests (galvanostatic or potentiostatic charge discharge cycles at different DoD, current rates and temperatures), dynamic tests (pulse tests at different current rates, SoCs, temperatures, standard HPPC tests, EIS tests, realistic profiles) and temperature validation tests.

Table 3.4: P2D model non-invasive validation methods.

Non-invasive test	Doyle 1996 [49]	Doyle 2003 [88]	Fang 2010 [58]	Safari 2011 [114]	Prada 2012 [60]	Ecker 2015 [50, 51, 61]	Schmalstieg 2017 [22, 52, 62]	Falconi 2018 [56]
CC_{dch} (C_{rate}, T)	T_{25}	T_{25}	T_{r1}	T_{25}	T_{r2}	T_{r3}	T_{r3}	T_{25}
CC_{cha} (C_{rate}, T)	-	T_{25}	T_{r1}	T_{25}	T_{r2}	T_{r3}	T_{r3}	T_{25}
Pulse (C_{rate}, SoC, T)	-	-	T_{r1}	-	-	T_{r3}	T_{r3}	-
EIS (SoC, T)	-	-	-	-	-	-	T_{r1}	-
R_{drive}	-	-	-	-	-	-	T_{r3}	-
T_{surf}	-	-	T_{25}	-	T_{r2}	-	T_{r3}	-

CC_{dch}: Validation with galvanostatic discharge process at different current rates.
CC_{cha}: Validation with galvanostatic charge process at different current rates.
Pulse: Validation with pulse power charges/discharges at different C-rates and SoCs.
EIS: Validation with Electrochemical impedance spectroscopy tests at different SoCs.
R_{drive}: Realistic driving profile.
T_{surf}: Validation with cell surface temperature; T_{25}: Temperature control at 25 °C; T_{r1}: Temperature control between 0 and 25 °C; T_{r2}: Temperature control between 0 to 33 °C; T_{r3}: Temperature control between -10 to 40 °C.

As mentioned in subsection 3.2.2, model parameters have different sensitivities to different responses. For example, Zhang et al. [79–81] studied the voltage and temperature sensitivity of the parameters, concluding that not all the parameters are sensitive to those responses. Moreover Jobman, Chu et al. [82–84] proposed a sequenced methodology (low galvanostatic cycles, pulse tests and EIS) where parameters were identified with different responses in which higher sensitivity was expected. Therefore, in order to validate the accuracy of all model parameters, a response in which high sensitivity of the parameter is presented must be selected.

In Table 3.4 all authors validate their results against capacity tests. However, only some of them validate the dynamic responses of the model [58, 61, 62]. Some of the works also present battery surface temperature validation, which corresponds to the addition of a fifth PDE (energy balance equation) into the P2D model and its validation. Schmalstieg et al. provided the most complete work between the analysed researches. In Figure 3.6 some of the results obtained by Schmalstieg et al. [22] with the parameter measurement methodology and model validation are plotted.

A good experimental-numerical match in those results describes the behaviour of cells and model validity at different operating conditions. However, to use those models for internal variable control (overvoltage evolution, ageing evolution etc.) it is necessary to ensure that the model predictions are in good concordance with the experimental evolution. Therefore, in the next section a review of experimental techniques that can be applied to validate these internal variables is presented.

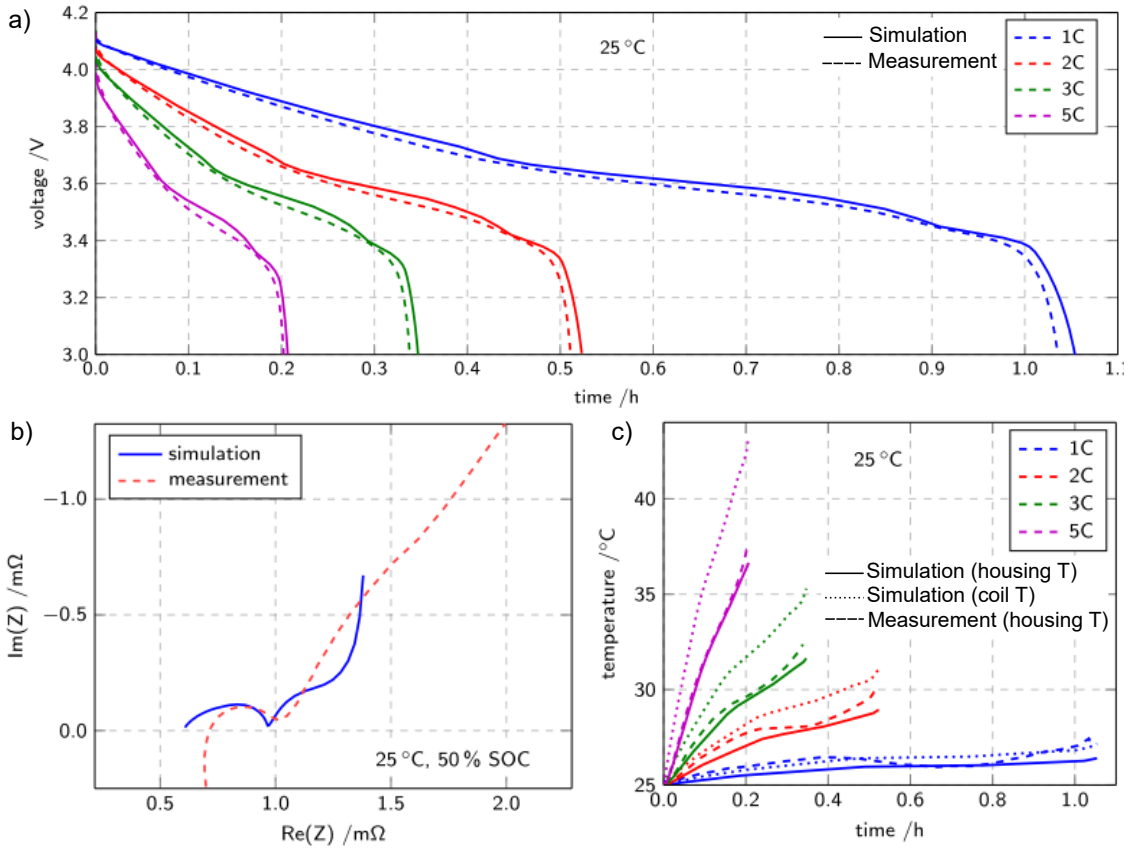

Figure 3.6: Model validation: a) Galvanostatic discharges at 298 K; b) Nyquist representation of cell impedance at 298 K; c) Cell temperature response at different current rates for 298 K. Creative Commons Attribution 4.0 License [22]

3.2.4.2 *Invasive testing*

Invasive characterisation tests are focused on the experimental measurements of model variables (ϕ_s, ϕ_e, c_e, c_s and j_{tot}). Several attempts have been performed to directly measure the internal variables of the model. On the one hand, variables related to electrode potentials can be measured. In Figure 3.7 the simulation results obtained using the parameters of Doyle et al. [49] are presented as an example.

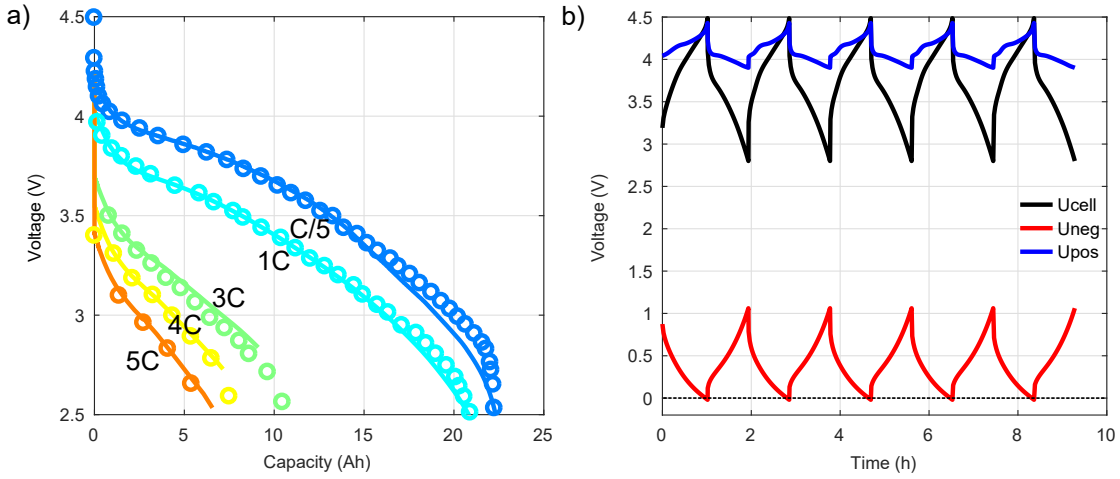

Figure 3.7: Validation example. Galvanostatic discharges at different current rates using Doyle et al. [49] parameters. a) Full cell experimental-numerical correlation (non-invasive testing); b) Positive and negative electrode potentials (invasive testing).

In Figure 3.7 a) the simulated cell is compared to experimentally obtained results (experimental curves are taken from [49]). Those graphs are the results expected for non-invasive validation. In the full cell, the electrode potentials are coupled and it is not possible to differentiate the positive and negative contribution to the overall potential. The model gives that information which could help, for example, for lithium plating (negative electrode potentials below 0V) or electrolyte gassing (above 4.5V) analyses. In Figure 3.7 b) the positive and negative electrode potentials are presented for a galvanostatic 1C cycling with extended voltage limits.

Experimentally, a three electrode cell can be constructed to study the electrode potentials separately within a full cell. Different approaches can be used depending on the cell configuration and reference electrode position [123] (see Figure 3.8). It is worth mentioning that the reference electrode material is also under study with the aim of reducing the experimental artefacts created by the insertion of the electrode. Lithium metal, LTO or LFP materials are some of the options [123–128].

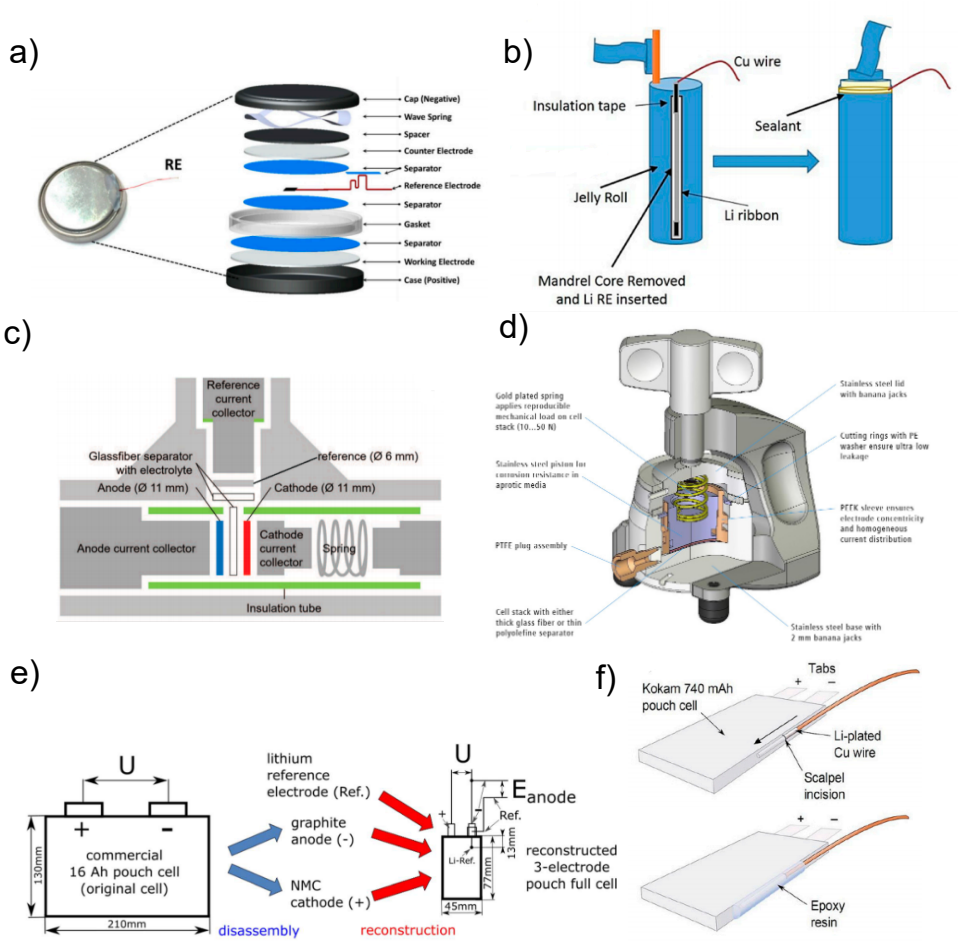

Figure 3.8: Three-electrode cell configurations: a) Coin cell. Original source: Juarez-Robles et al. [129]. The license is subject to Journal of The Electrochemical Society (CC BY-NC-ND BY 4.0); b) Final cylindrical cell including a reference electrode. Original source: Somerville et al. [126]. Licensee MDPI is subject to Batteries (CC BY 4.0); c) T-cell format. Original source: Solchenbach et al. [128]. The license is subject to Journal of The Electrochemical Society (CC BY 4.0); d) ECC-Ref from EL-Cell GmbH; e) Monolayer pouch cell. Original source: Waldmann et al. [127]. The license is subject to Journal of The Electrochemical Society (CC BY 4.0); f) Final pouch cell including a reference electrode. Original source: McTurk et al. [125]. The license is subject to ECS Electrochemistry Letters (CC BY 4.0).

On the other hand, solid and electrolyte concentration related variables can be measured after cell disassembling or with *in-operando* techniques (see Figure 3.9).

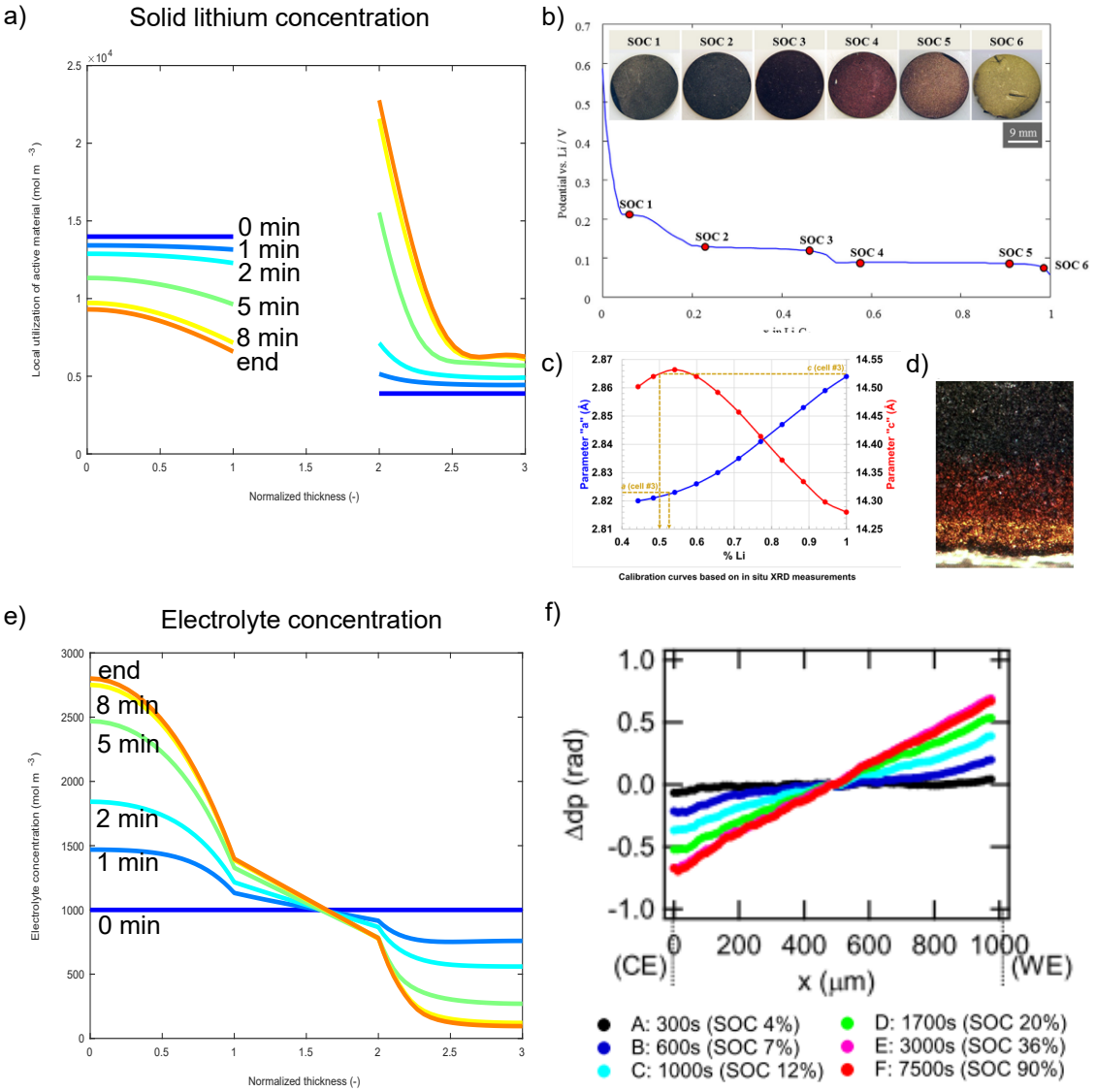

Figure 3.9: a) Simulation of solid particle concentration of a 3C galvanostatic discharge; b) Lithium concentration in the solid particles in a graphite electrode for different SOCs. Original source: Uhlmann et al. [130], with permission from Elsevier; c) Correlation with *in-operando* XRD measurements of NMC based positive electrode and solid lithium content. Original source: Matadi et al. [124]. The license is subject to Journal of The Electrochemical Society (CC BY 4.0); d) Direct *in situ* measurements of Li transport in a graphite electrode with optical micrography. Original source: Harris et al. [131], with permission from Elsevier; e) Electrolyte concentration of a 3C galvanostatic discharge; f) Electrolyte concentration variation during a charge process. Reprinted with permission [132] from American Chemical Society (Copyright 2018)

In Figure 3.9 a) an example of the solid lithium concentration variation of the electrodes for a certain discharge is presented in simulation. In Figure 3.9 b), c) and d) the experimental studies for this variable is presented. Uhlmann et al. [130] studied the lithiation photograps of a graphite electrode at different SOCs in disassembled electrodes (Figure 3.9 b)). Moreover, in 2010, Harris et al. [131] measured the lithium transport of a graphite electrode during cell operation with an optical half cell (Figure 3.9 d)). There, it is possible to see the different lithiation steps in a graphite electrode (for time and spatial domains). Other works used optical cells to study the ageing mechanisms [133,134]. However,

these optical techniques are not valid for material which does not change colour during the lithiation (positive electrodes). An alternative option is to use XRD measurements to correlate the diffraction patterns with different states of lithiation. This has also been used as a technique to quantify the degradation of the electrodes [124] (Figure 3.9 c)). The electrolyte concentration during a charge-discharge process could also be studied (Figure 3.9 e)). The Toyota Motor Corporation claims to have developed the world's first method to observe lithium-ions in the electrolyte while the cell is charging and discharging. The measurement is performed with high-intensity X-ray (synchrotron radiation) to see the electrolyte concentration variation during cycling [135]. In addition, in Figure 3.9 f) the lithium concentration variation during the charge process is measured with X-ray Phase Imaging by Takamantsu et al. [132].

3.3 CHARACTERISTICS OF THE ANALYSED COMMERCIAL CELL

Kokam cells, reference SLPB554374H, were used for the parameter measurement methodology[2]. Cells manufactured by Kokam have been extensively been studied in the literature [50, 51, 61, 118, 136–139], and for this reason these cells have been taken as a reference for this thesis. The electrical specifications of the cell are shown in Table 3.5.

Table 3.5: Main characteristics of SLPB554374H battery [140].

Characteristics	**Units**	**Value**	**Comments**
Voltage Range	V	4.2 - 2.7	
Charge Current	A	2.50	2C, 23 ± 3°C
Discharge Current	A	18.75	15C, 23 ± 3°C
Discharge Current Peak	A	37.50	30C, 23 ± 3°C
Rated Capacity	Ah	1.25	0.2C, 23 ± 3°C
Internal Resistance	mΩ	Max. 10	AC, 1 kHz
Gravimetric Energy Density	Wh kg^{-1}	140	
Volumetric Energy Density	Wh L^{-1}	310	Excluded tab and seal
Mass	g	Max. 33	
Charging Temperature	°C	0 - 45	
Discharging Temperature	°C	-20 - 55	
External dimensions	mm	40 x 65 x 5.3	

According to the manufacturer, the negative electrode is composed of a proprietary graphite, the positive electrode is a mixture of Lithium Cobalt Dioxide ($LiCoO_2$) and Lithium Nickel Cobalt Oxide ($LiNiCoO_2$), the separator is composed of Poly(Vinylene Fluoride) (PVDF), and the electrolyte is a mixture of $LiPF_6$ with EMC and EC.

[2] J4 journal publication is based on this parameter measurement methodology

3.4 METHODOLOGY AND SAMPLE PREPARATION

Figure 3.10 shows an overview of the procedure implemented to obtain all the model parameters. There, a summary of the obtained parameters together with the type of sample under study and the characterisation techniques are presented. All the parameters used in Figure 3.10 that are needed to fully define the P2D model are described in the list of symbols.

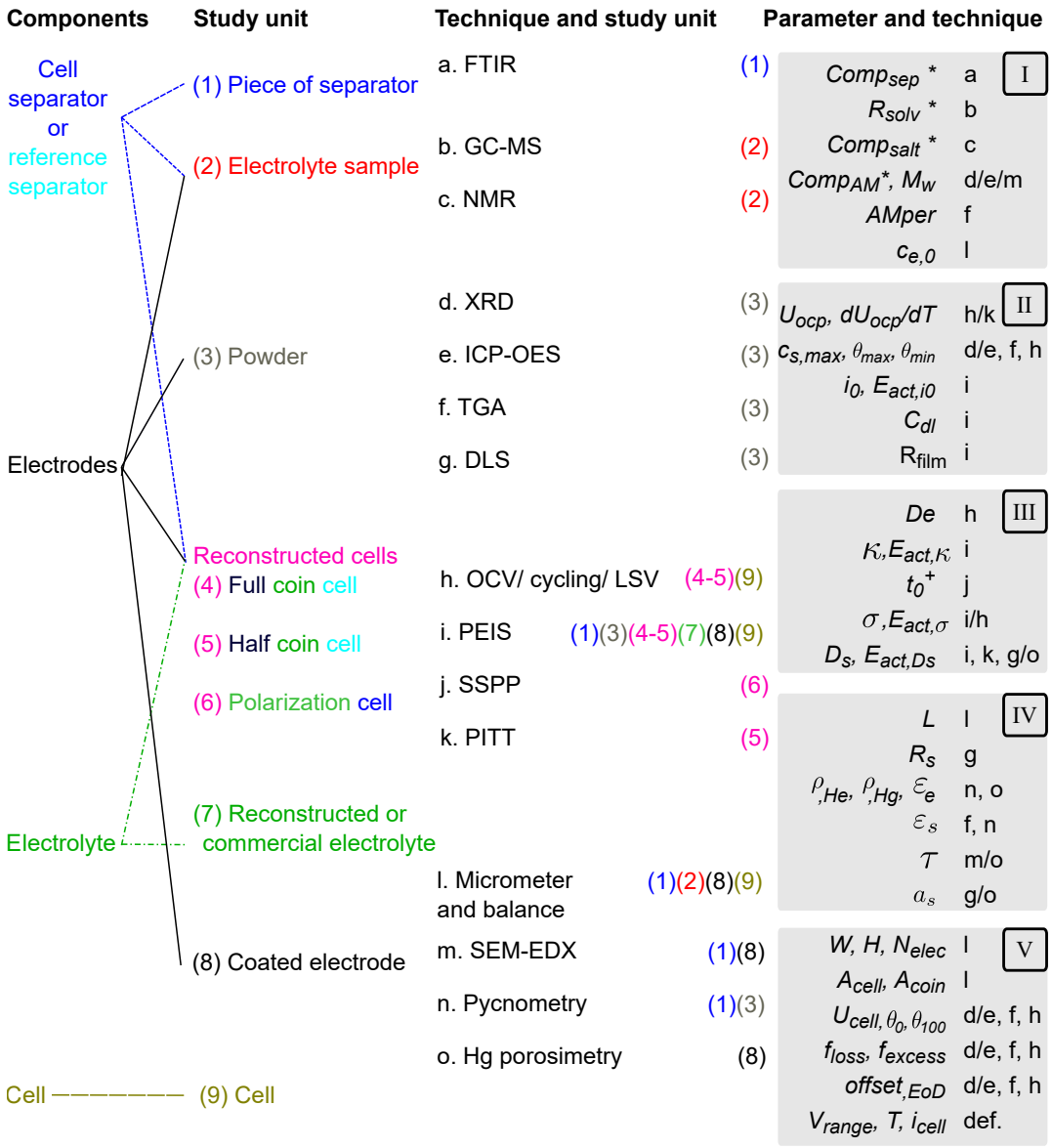

Figure 3.10: Schematic representation of the full physico-chemical parameter measurement methodology. Parameter groups are presented in grey boxes: I. Component composition (*not used directly as a parameter for the model, but necessary for verification of the datasheet), II. Thermodynamic and kinetic parameters, III. Transport properties, IV. Parameters related to the porous structures and adjustable design parameters, and V. Cell internal configuration and electrode balancing determination.

It is worth noting that, for some parameters, more than one technique was used for verification or adding information. The parameters were divided into five groups, as highlighted in grey in Figure 3.10. First, the component composition identification was determined (I). Second, thermodynamic and kinetic parameters were extracted (II). Third, the transport properties were obtained (III). Then, parameters related to the porous structures and ad-

justable design parameters were characterised (IV). Finally, full-cell electrode balancing and internal configuration of the battery is described (V).

The techniques used for the physico-chemical characterisation are presented in Table 3.6, in which the associated character (used in Figure 3.10), the acronym, the full name of each technique and the equipment used in this work is gathered. Additional information of each technique is presented in Appendix A.

Table 3.6: Characterization techniques: character, acronym, full name and used equipment.

Character. Acronym	Full name of the technique	Equipment used in this thesis
a. FTIR	Fourier Transform Infrared spectroscopy	Vertex70. Bruker
b. GC-MS	Gas Chromatography–Mass Spectrometry	Perkin Elmer Mass Spectrometer. Clarus SQ8T
c. NMR	Nuclear Magnetic Resonance spectroscopy	H-NMR Bruker Avance III 300 MHz
d. XRD	X-Ray powder Diffraction	Bruker D8 Discover
e. ICP-OES	Inductively Coupled Plasma Optical Emission Spectrometry	Ultima 2, ICP optical emission spectrometer. Horiba Scientific
f. TGA	Thermogravimetric Analysis	TG 209 Libra. Netzsch
g. DLS	Dynamic Light Scattering	Mastersizer 3000. Malvern
h. OCV/cycling/LSV	Open Circuit Voltage, cycling, Linear Sweep Voltammetry	BioLogic VMP3 and Gamry Interface 1000
i. PEIS	Potentiostatic Electrochemical Impedance Spectroscopy	BioLogic VMP3
j. SSPP	Steady-State Potentiostatic Polarization	BioLogic VMP3
k. PITT	Potentiostatic/Galvanostatic Intermittent Titration Technique	BioLogic VMP3
l. Micrometer/balance	Micrometer and precision balance	Mitutoyo IP65 and Practum: Sartorius
m. SEM-EDS	Scanning Electron Microscopy and Energy Dispersive X-Ray spectroscopy	FEI Quanta 200 FEG-SEM
n. Pycnometry	Helium pycnometer	Accupyc II 1340. Micromeritics
o. Hg-porosimetry	Mercury intrusion porosimetry	Autopore V, Micromeritics

Two commercial cells were taken for the physico-chemical characterisation. The first cell was fully discharged at C/10 until the lower cut-off voltage (2.7 V). The other cell was fully charged at C/10 until the upper cut-off voltage (4.2 V). In Figure 3.11 a) the cycling procedure for cell opening is presented. The disassembly of the cells was done within 3 hours of the cycling procedure. The same methodology explained by Waldmann et al. [141] was used for dismantling the cells. The cells were opened inside an Ar filled Jacomex brand glove box ($O_2 < 0.1$ ppm and $H_2O < 0.1$ ppm) as the samples are reactive to O_2 and H_2O. In Figure 3.11 b-e) the cell components during the opening procedure are presented, and the lithiation differences between complete discharge (dark), and charge (gold), of the negative electrode can be seen.

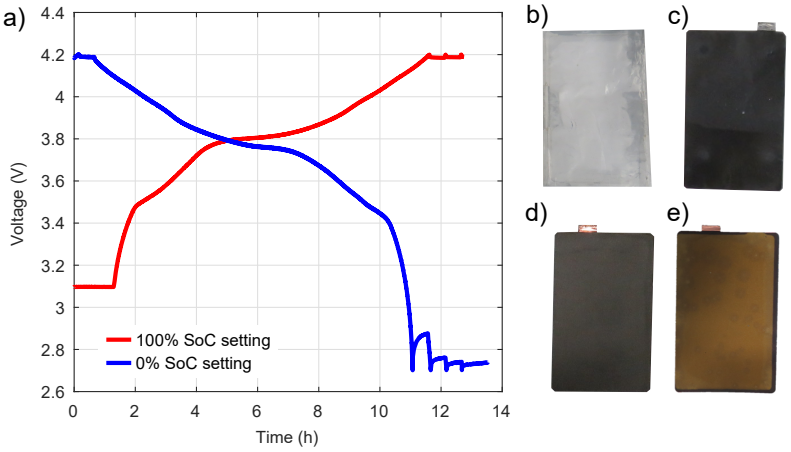

Figure 3.11: a) Pre-opening cycling procedure for charged (100% SoC) and discharged (0% SoC) states; Cell components during the teardown of the cells: b) Separator; c) Positive electrode; d) Negative electrode (0% SoC); e) Negative electrode (100% SoC).

The electrolyte extraction was performed during cell opening. Due to the high cost of electrolyte (9.9 to 16% of the battery cost) among other reasons, manufacturers tend to optimise, reducing the amount of electrolyte to the minimum [52]. In commercial pouch cells there is usually no excess of electrolyte. Therefore, in this work, after the cell was opened, a sample including both electrodes and separator (all impregnated in electrolyte) were rapidly immersed in dichloromethane and then analysed with the Gas Chromatography–Mass Spectrometry (GC-MS) technique. A similar procedure was used by Pilipili [124].

After the electrolyte extraction, the battery components were separated. Unit samples of the separator, positive and negative electrodes to be studied were carefully selected to collect a representative sample with no visual defects, and washed with DMC to perform the remaining physico-chemical tests. The punched electrodes were reassembled into reconstructed coin cells in an argon filled glove box to perform the electrochemical measurements. The procedure for cell building and experimental set-up are presented in Figure 3.12.

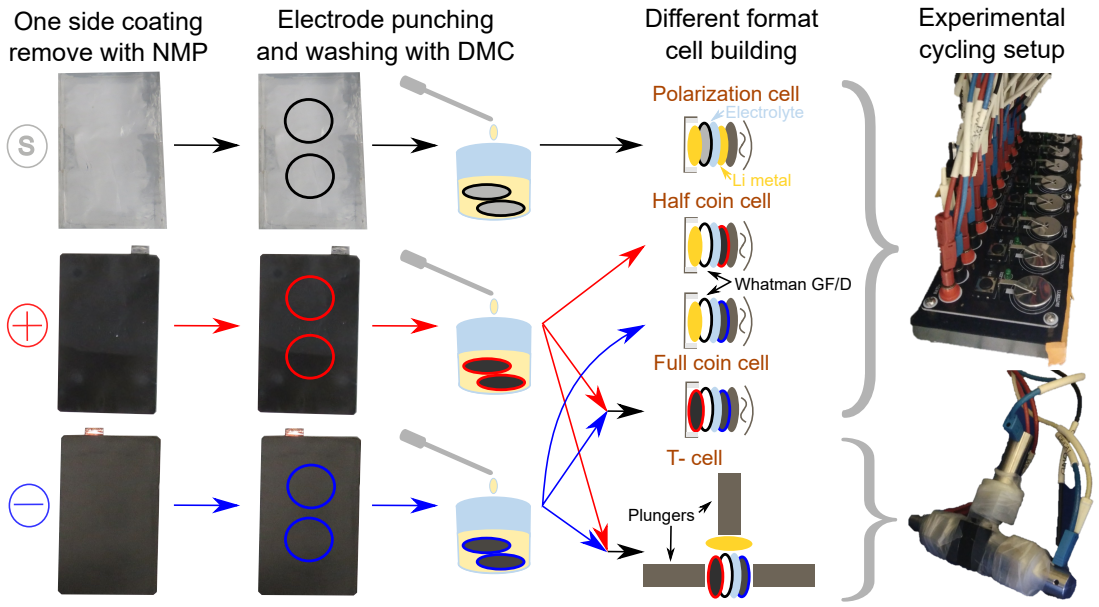

Figure 3.12: Teardown and procedure for reconstructed cells for the electrochemical characterisation.

First of all, one side coating of the electrodes was removed with N-Methyl-2-pyrrolidone (NMP). The electrodes were punched into 12 mm diameter samples and washed with DMC. Then, different types of cells were constructed (half coin cells, full coin cells, polarization cells and three-electrode cells) as illustrated in Figure 3.12. Finally, the cells were studied with the set-up presented in Figure 3.12 in a Biologic VMP3 potentiostat.

The configuration and materials of the studied cells are listed below:

- Polarization cell (CR2032): symmetrical lithium metal discs of 12 mm of diameter separated by a 16 mm diameter separator of the cell under study impregnated with 1M $LiPF_6$ in EC:EMC (50:50 v%) LP50 (battery grade, Sigma Aldrich) electrolyte.
- Half coin cells (CR2032): a 12 mm diameter one side coated positive or negative electrode and a 12 mm diameter lithium metal disc separated by a Whatman glass fibre (Grade GF/D) separator of 16 mm impregnated with 1M $LiPF_6$ in EC:EMC (50:50 v%) electrolyte.
- Full coin cells (CR2032): 12 mm diameter one side coated positive and negative electrodes separated by a Whatman glass fibre (Grade GF/D) separator of 16 mm impregnated with 1M $LiPF_6$ in EC:EMC (50:50 v%) electrolyte.
- T-cell type three electrode cells: 12 mm diameter one side coated positive and negative electrodes separated by a Whatman glass fibre (Grade GF/D) separator of 13 mm impregnated with 1M $LiPF_6$ in EC:EMC (50:50 v%) electrolyte.

The polarization cell was constructed in order to study the electrolyte and separator properties (i.e. effective conductivity in the separator, bruggeman coefficient, tortuosity and porosity), taking as a reference specific works dealing with separator characterisation [142]. In the remaining cells, the separator was not from the cell under study. In full and half coin cells Whatman glass fibre (Grade GF/D) separators were used because these are commonly used in the literature thereby reducing the uncertainty of the analysed system [22, 50–52, 61, 62, 124].

Finally, the electrodes were analysed so as to define the parameters related to the porous structures (i.e. porosity, specific surface area and tortuosity). Additional sample preparation was required for techniques such as XRD, ICP-IOS, TGA, DLS, and electronic conductivity in which electrodes were scratched and the recovered powder was analysed.

3.5 PHYSICO-CHEMICAL CHARACTERISATION

In this section the proposed methodology was applied to the 1.25 Ah kokam cell so as to test its efficacy.

3.5.1 Component composition

Firstly, the component composition provided by the manufacturer was checked and completed. This was performed for all the materials (electrodes, separator and electrolyte) using the techniques presented in Figure 3.10.

In order to determine the active material composition of both electrodes, the XRD technique was used, which was complemented with ICP-IOS and SEM-EDS in the posit-

ive electrode. The XRD pattern[3] was refined using the Rietveld Method. The analysis was performed with the cell opened at the discharged state (0% SoC), which corresponds to an almost delithiated negative electrode and almost lithiated positive electrode.

The negative powder XRD pattern analysis shows that the electrode is composed of graphite (for the discharged cell) (see Figure 3.13 a)). The positive powder XRD pattern (see Figure 3.13 b)) clearly shows that the sample contains two phases. The refined parameters for the Phase 1 ($a = b = 2.851(6)$ Å, $c = 14.214(2)$ Å, $\alpha = \beta = 90°$, $\gamma = 120°$) can be compared with cell parameters of $Li_yNi_{0.8}Co_{0.15}Al_{0.05}O_2$ (NCA) [143], whereas the refined parameters for Phase 2 ($a = b = 2.816(7)$ Å, $c = 14.017(2)$ Å, $\alpha = \beta = 90°$, $\gamma = 120°$) can be related to Li_yCoO_2 (LCO) [144]. A small amount of graphite [145], which could be used as a conductive additive, was also identified in the positive electrode diffraction pattern (see Figure 3.13 a)). The fact that the c parameter of Phase 1 is larger than those reported in the literature suggests that Phase 1 is partially delithitated. Indeed, the delithiation of the layered $LiMO_2$ phases (M = Ni, Co, Mn or combination of them) is known to produce an increase in the c cell parameter (due to an increase of electrostatic repulsion between the anions [146]). A deeper analysis of the electrode state of lithiation (SoL) and its correlation with the OCV of the electrodes is discussed in subsection 3.5.2. Moreover, the correlation between the electrode SoL and the cell state of charge (SoC) is discussed in subsection 3.5.5.

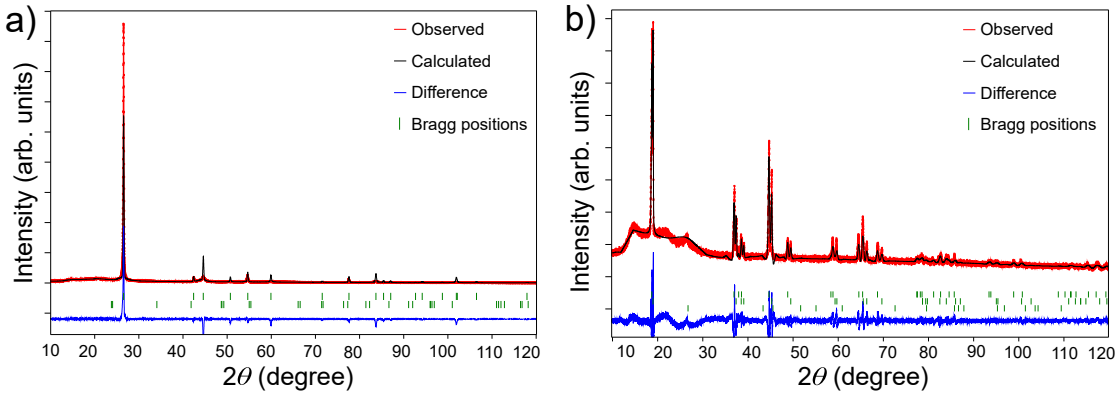

Figure 3.13: XRD patterns and Rietveld refinement of the a) Negative electrode at 0% SoC of the cell (opened at 2.7 V); b) Positive electrode at 0% SoC of the cell.

The obtained results are in good concordance with Mayur et al. [138] who analysed the positive electrode composition by means of the SEM-EDS technique for a similar battery (kokam 0.35 Ah, reference SLPB283452H) and reported a compound based on a blend between NCA and LCO particles. Moreover, Fuchs et al. [139] studied the composition of a 3.3 Ah kokam battery (reference SLPB526495) with the ICP-OES and SEM-EDS techniques, obtaining an average composition of $LiNi_{0.64}Co_{0.35}Al_{0.01}O_2$ (ICP-OES results). The elements reported by these authors are in good agreement with the ICP-OES[4] results of the analysed cell of this thesis, although the identified ratios differ (0.40 ± 0.05 of nickel, 0.56 ± 0.04 of cobalt and 0.03 ± 0.03 of aluminium). The identified aluminium content was slightly higher than the expected values due to the preparation of the experimental test (scratching process). As stated in Fuchs et al. [139], the aluminium content could also be due to current collector contamination during the ICP-OES sample preparation. Neverthe-

[3] The XRD measurements were carried out by Maria Jauregui, sample preparation and post-process were done by the author.

[4] The ICP-IOS measurements were carried out by Guillermo Liendo and Ander Celaya, sample preparation and post-process were done by the author.

less, SEM-EDS mapping[5] was performed in which the two phase blend was clearly visible, and it was thus possible to confirm the aluminium content of Phase 1 (see Figure 3.14). A ratio between the two phases can be estimated with the ICP-OES results. Therefore, an approximate composition of 50 ± 2% of $LiCoO_2$ and 50 ± 2% of $LiNi_{0.8}Co_{0.15}Al_{0.05}O_2$ was identified for the blended active material (confirmed by the XRD results).

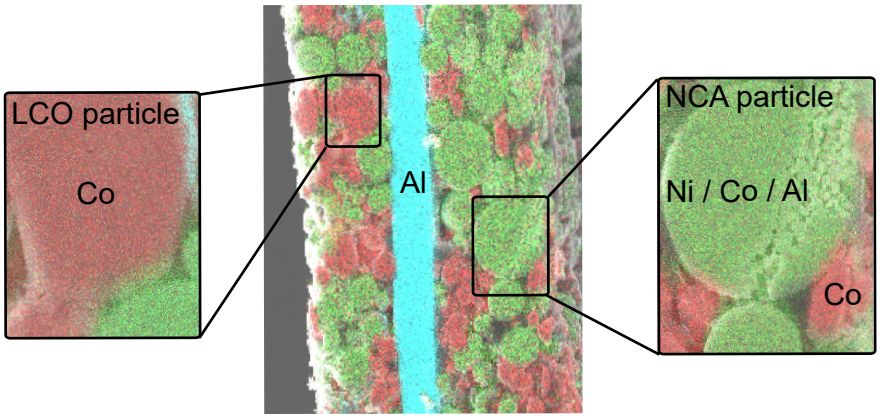

Figure 3.14: EDS mapping of the blended positive electrode, showing Ni, Co and Al in a general cross-sectional view of the electrode and zoomed into LCO and NCA particles.

In addition, thermogravimetric analysis[6] was conducted to determine the AM percentage of the electrode coatings, which directly affects the cell theoretical capacity calculation. The samples have been heated at 10 K min^{-1} until 973.15 K, and maintained for 15 minutes at that maximum temperature. The active material percentage calculations are based on the mass loss during the heating process corresponding to:

- Water evaporation (until 373.15 K)
- Binder decomposition (minimum dmdT in a range between 673.15 K and 773.15 K for binders composed of PolyVinyliDene Fluoride (PVDF), with a minimum peak around 723.15 K [147]; pyrolysis of the Styrene Butadine Rubber (SBR) elastomer between 573.15 and 823.15 K, with a minimum peak around 753.15 K [148]; and Carboxylmethyl Cellulose (CMC) with a minimum around 573.15 K [149])
- Conductive additive decomposition (up to 9% and 24% of mass loss at 815 K of a similar graphite and carbon black (C65), respectively)

In the negative electrode (see Figure 3.15 a)), we identified mass to time derivative minimums at 584.15 K and 753.15 K which could correspond to CMC and SBR binders, respectively. A small quantity of carbon black can be expected (around 1%), which was degraded before 584.15 K. Therefore, the negative electrode is composed of 95 ± 3% graphite, 3 ± 2% CMC/carbon black, and 2 ± 2% SBR. In the positive electrode (see Figure 3.15 b)), we identified mass to time derivative minimums at 700.15 K and 815.15 K, which could be related to a binder composed of PVDF and graphite additive, respectively (a small quantity of graphite was expected based on the results obtained from the XRD pattern refinement). The formulation of the positive electrode was found to be 93 ± 2% LCO/NCA, 3 ± 2% PVDF, and 4 ± 2% graphite additive/carbon black (from that 4% a small amount of carbon black was expected (around 1 - 2%)). For both electrodes, similar

[5] The SEM-EDS measurements were carried out by Alvaro Herrán and the author, sample preparation and post-process were done by the author.

[6] The TGA measurements were carried out by Ander Celaya, sample preparation and post-process were done by the author.

formulations are found in the literature [150]. Even if it is possible to correlate the mass to time derivative as a function of the temperature for the expected materials in each electrode, it is worth mentioning that the decomposition processes are a characteristic of the tested specific materials. As no previous information of the formulation is available, the uncertainty of this technique is high.

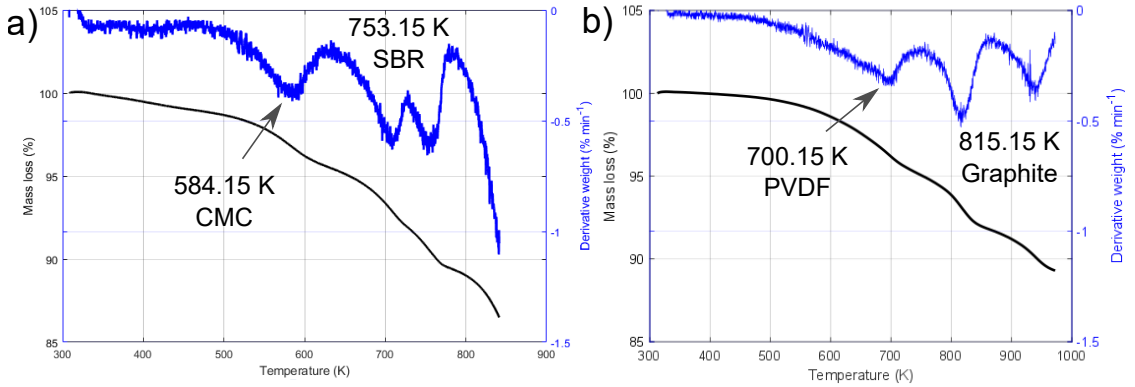

Figure 3.15: TGA decomposition curves in air atmosphere of the a) Negative electrode; b) Positive electrode.

In order to characterise the separator film, FTIR[7] (see Figure 3.16 a)) was performed. The obtained FTIR spectrum was compared with the literature which indicates that the characteristic absorbance bands of polyethylene (PE) are located at 2914 cm^{-1}, 2847 cm^{-1}, 1470 cm^{-1} and 718 cm^{-1} [151]. The characteristic bands of the analysed sample were obtained at 2916 cm^{-1}, 2848 cm^{-1}, 1471 cm^{-1} and 714 cm^{-1}. A non-identified peak is located at 1031 cm^{-1}, which could be due to electrolyte traces. The FTIR result confirms that the separator composition is PE, which differs from the datasheet. The manufacturer reports that the separator is composed of PVDF, which could be a thin coating layer that could be added as a safety agent to prevent short-circuits [152].

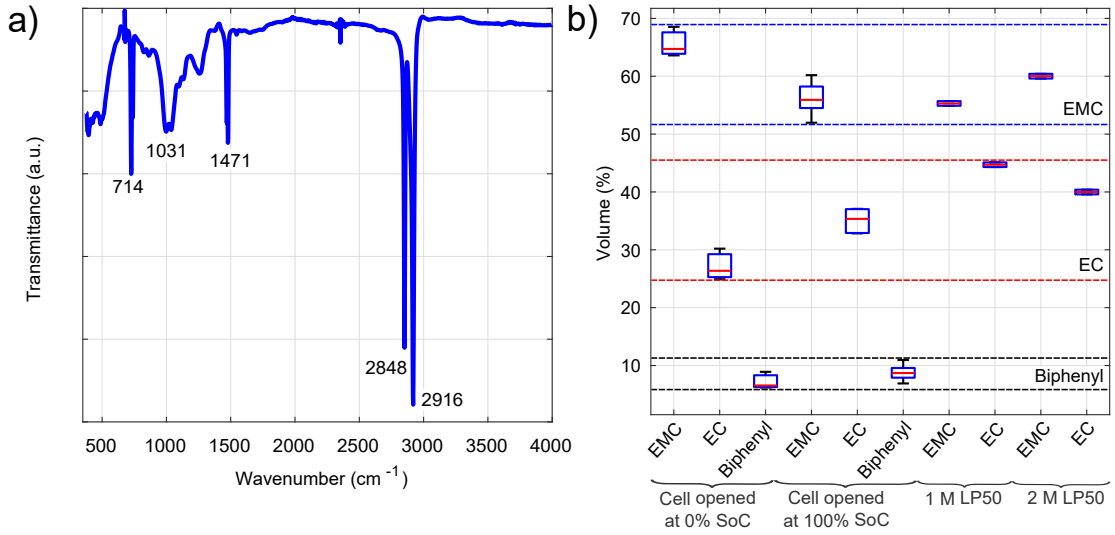

Figure 3.16: a) FTIR analysis of the separator; b) GC-MS analysis of the sampled electrolyte.

For the electrolyte characterisation, GC-MS and NMR techniques were used, for electrolyte solvent ratio and salt composition identification, respectively. Both opened cells,

[7] The FTIR measurements were carried out by Alvaro Herrán, sample preparation and post-process were done by the author.

at charged and discharged states were analysed by means of GC-MS[8]. In this technique, it should be taken into account that the list of the identified components and ratios are not precise, as the evaporation process of the solvents under Argon atmosphere is not negligible [124]. The volume percentages of the detected elements are shown in Figure 3.16 b)), in which the dispersion between measurements are also plotted. The solvents that were identified are EMC and EC which are in good agreement with the datasheet. We also found biphenyl traces in the analysed samples. Biphenyl is commonly used as a fire-retardant additive in LIBs [124]. The dotted lines correspond to the maximum and minimum values obtained for each of the components. A range between 50 - 70% for EMC (blue), 25 – 45% for EC (red) and 5 -10% Biphenyl (black) were found. Additionally, a 1 M and 2 M $LiPF_6$ EC/EMC (50/50 v%) commercial electrolytes (LP50) were characterised for comparison purposes.

^{19}F and ^{31}P NMR spectra[9] were recorded to confirm that the electrolyte salt is $LiPF_6$, as expected from the datasheet. Comparing our results with those obtained from the commercial electrolytes, it is possible to approximate the sample electrolyte to $LiPF_6$ EC/EMC (50/50%v) or $LiPF_6$ EC/EMC (30/70%v) with a small percentage of biphenyl additive. The electrolyte identification allowed us to use a similar electrolyte in the remaining characterisation procedures.

An accurate determination of the salt concentration is not possible if a sample of the bare electrolyte (not impregnated in the separator) cannot be extracted from the cell. If there is an excess of electrolyte, a known volume can be analysed by NMR for a quantitative analysis (which requires internal references), although interpretation of the results should be carefully analysed due to the decomposition products of the $LiPF_6$ (i.e. LiF) [153] or the solvents [154]. Unfortunately, no electrolyte could be recovered from this specific cell; therefore, electrolyte salt concentration was calculated by means of weight differences between cleaned and not cleaned electrodes, applying equation 3.35.

$$c_{e,0} = \frac{m_{no-clean} - m_{clean}}{V_{external} - V_{inactive} + V_{extra}} \tag{3.35}$$

where the $V_{external}$ is the total external volume of the cell (43 x 75 x 5.3 mm), $V_{inactive}$ represents the inactive parts of the components (current collector, separator and electrode solid-phase volumes (ε_s)), and V_{extra} represents the added extra volume in the pouch cell filling step process.

A value of 2 ± 0.5 M was calculated without including any extra electrolyte volume. However, in the electrolyte filling process, extra electrolyte are added into the process (if 3 mL extra are added, a value of 1.5 ± 0.5 M was obtained) and during the formation cycles some lithium ions get trapped into the electrodes irreversibly and decomposition products are produced and removed during the degassing process. This leads to the conclusion that the uncertainty of this procedure is high as the calculation are based on indirect measurements and results are based on the weighted salt of the cell after the formation cycles of the cell.

[8] The GC-MS measurements were carried out by Haizea Etxebarria, sample preparation and post-process were done by the author.

[9] The NMR preparation, measurement and post-process were carried out by Ander Celaya and the author.

3.5.2 Thermodynamic and kinetic parameters

The thermodynamic and kinetic parameters accounts for the OCV curve, the film resistance, the charge transfer resistance, and the double layer capacitance for each half reaction as a function of the state of lithiation (SoL) and temperature.

Quasi-steady-state curves (qOCV) were obtained by means of galvanostatic charge-discharge processes at C/30. Additionally, PITT was used to check the suitability of qOCV curves [137]. It is well known that OCVs present a dependency on temperature and hysteresis [83, 137]. Therefore, both tests were performed at three temperatures (278.15, 298.15, and 318.15 K). Moreover, in order to reduce the error in the model due to the hysteresis effect, charge and discharge curves were averaged following the procedure proposed by Schmalstieg et al. [52]. First, the charge and discharge curves were split at half experimental capacity into two pieces each (low and high lithiation ranges, which corresponds to high and low voltage ranges, respectively). In that point (half experimental capacity), the difference between charge and discharge curves was calculated. Then, low lithiation range of the charge process and high lithiation range of the discharge process were shifted by half the voltage difference to obtain the averaged OCV curve. The results for the negative and positive electrodes are shown in Figure 3.17 a) and b), in which experimental points from PITT and charge-discharge averaged OCV curves are presented[10]. The temperature dependency is taken into account with the voltage to temperature derivative (shown in Figure 3.17 a) and b)).

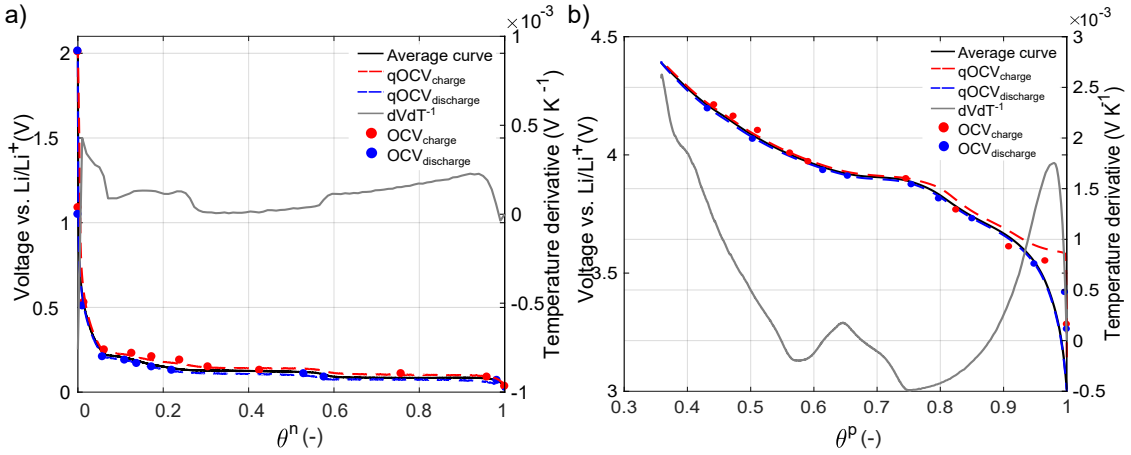

Figure 3.17: OCV curve and temperature derivative (dVdT) as a function of SoL a) Negative electrode; b) Positive electrode.

The maximum and minimum lithiation levels of the electrodes depends on the formation process and electrode voltage limits. The reconstructed electrodes were tested in a half-cell configuration, and thus the influence of the other electrode was removed. When the cell is constructed for the first time, the negative electrode starts completely delithiated (x = 0) and the positive electrode completely lithiated (y = 1).

In the negative electrode, due to the irreversible lithium insertion into the structure at low SoL levels, the electrode does not reach a fully delithiated level after formation cycles. This small shift in the negative electrode is discussed in subsection 3.5.5 during the electrode balancing process as an offset. Therefore, in this section we assume that all

[10]The post-process of the OCV points based on PITT tests was carried out by Eneko Agirrezabala, cell preparation and measurement were done by the author.

cyclable lithium is lost due to formation of the initial SEI layer so as to establish $\theta^n_{min} = 0$. When the SEI layer is created during the first formation cycles or re-created in the reconstructed cell [51], some lithium ions are irreversibly consumed. In a full-cell configuration, this lithium ion consumption affects the positive electrode. However, as a lithium foil is placed against the negative electrode, the lithium source is assumed infinite in this study. Therefore, the maximum lithiation level of the electrode ($\theta^n_{max} = 1$) is obtained as the half-cell is cycled in the full lithiation window (between 0.01 and 2 V). This is confirmed by the asymptotic behaviour of the graphite at high lithiation level.

In the positive electrode a complete reversible extraction/insertion of lithium ions is not possible due to the high voltages needed to completely delithiate the layered oxide (common electrolytes are not stable at these voltages), and low stability of those structures [56, 61]. As an approximation, the amount of Li ions per formula unit that remain in the cathode structure was calculated with equation 3.36. This corresponds to the non-usable part of the cathode and is calculated with the relationship between the real capacity with respect to the theoretical capacity of the active material of the positive coin cell (θ^p_{min}). The theoretical electrode capacity is calculated with Faraday's law, taking into account the active material content, composition of the electrode (described in subsection 3.5.1), and the measured electrode mass of the coin cell (13.0 ± 0.1 mg of the electrode positive mass ($m_{electrode}$)).

$$\theta^p_{min} = 1 - \frac{\max(C^p_{coin,\text{exp}})}{(zFAM_{per}(m_{AM} - m_{cc}))/(3600M_w)} \tag{3.36}$$

where $Q_{coin,\text{exp}}$ is the maximum experimental coin cell discharge capacity obtained at C/30, AM_{per} is the AM percentage, m_{AM} is the one side coated electrode mass including current collector, m_{cc} is the mass of the current collector, and M_w the molecular weight of the active material.

As a first approach, the maximum lithiation level (θ^p_{max}) is assumed to be 1, although re-lithiation does not fully occur in the electrode due to structural changes [150]. All in all, as half-cell configuration is used (lithium foil is placed against the electrode) the lithium source allows an almost full lithium ion insertion within the positive structure.

The interaction between the negative and positive electrode during the formation and usage of the full-cell is explained in subsection 3.5.5.

In addition to the thermodynamic parameters, PEIS technique was used to determine the film resistance, charge transfer resistance, and the double layer capacitance for both electrodes. The experiments were performed in half-coin cells at different SoLs and temperatures. The analysed voltages are presented as dots in Figure 3.17 a) and b). Half-coin cells with maximum voltage amplitude of 10 mV and a frequency range between 11 mHz and 1 MHz were chosen. In this work, the equivalent circuit model proposed in Aurbach et al. [155] was used to correlate measured impedance spectra to different processes occurring inside the battery (shown in Figure 3.18 a)). The Butler-Volmer equation (equation 3.37) was used to calculate the exchange current density (i_0):

$$I_{ct}(A) = i_{loc}S = i_0 S\left[\exp\left(\frac{\alpha_a zF\eta}{RT}\right) - \exp\left(\frac{-\alpha_c zF\eta}{RT}\right)\right] \tag{3.37}$$

where I_{ct} is the electrode current (A), i_{loc} is the electrode current density (A m^{-2}), S is the effective surface area between the electrode and electrolyte (m^2), α_a and α_c are the anodic and cathodic charge transfer coefficients respectively, R is the universal gas

constant, T is the temperature, and η is the overvoltage.

In order to include the active material concentration (c_s) and electrolyte concentration (c_e) dependencies in the model, equation 3.38 is generally used [52]:

$$i_0 = F(k_c)^{\alpha_a}(k_a)^{\alpha_c}(1 - {}^{c_s}/_{c_{s,\max}})^{\alpha_a}({}^{c_s}/_{c_{s,\max}})^{\alpha_c}(c_e/c_{e,0})^{\alpha_a} \tag{3.38}$$

where k_a and k_c are the anodic and cathodic reaction constants, respectively.

Considering a charge transfer coefficient of 0.5, those equations could be simplified in equations 3.39 and 3.40:

$$I_{ct}(A) = i_0 S\left(\frac{zF\eta}{RT}\right) \tag{3.39}$$

$$i_0 = Fk\sqrt{(1 - {}^{c_s}/_{c_{s,\max}})({}^{c_s}/_{c_{s,\max}})\,(c_e/c_{e,0})} \tag{3.40}$$

Finally, to obtain the experimental exchange current density, the charge transfer resistance is used. Assuming small overvoltage potentials the following relationship is applied (equation 3.41):

$$i_0 = \frac{I_{ct}}{\eta}\left(\frac{RT}{zFS}\right) = \frac{1}{R_{ct}}\left(\frac{RT}{zFS}\right) \tag{3.41}$$

The exchange current density needs to include the effective surface area taking part in the electrochemical reaction. The effective surface area (S) is calculated with the procedure explained in subsection 3.5.4. The same effective surface area value was used for exchange current density and the solid diffusion coefficient calculations, as it corresponds to the effective electrolyte-electrode surface area of the reconstructed coin cells. The values for negative and positive electrodes are 33.99 ± 0.1 and 10.01 ± 0.1 cm^2, respectively. The exchange current density results obtained with this procedure are shown in Figure 3.18 b) and c).

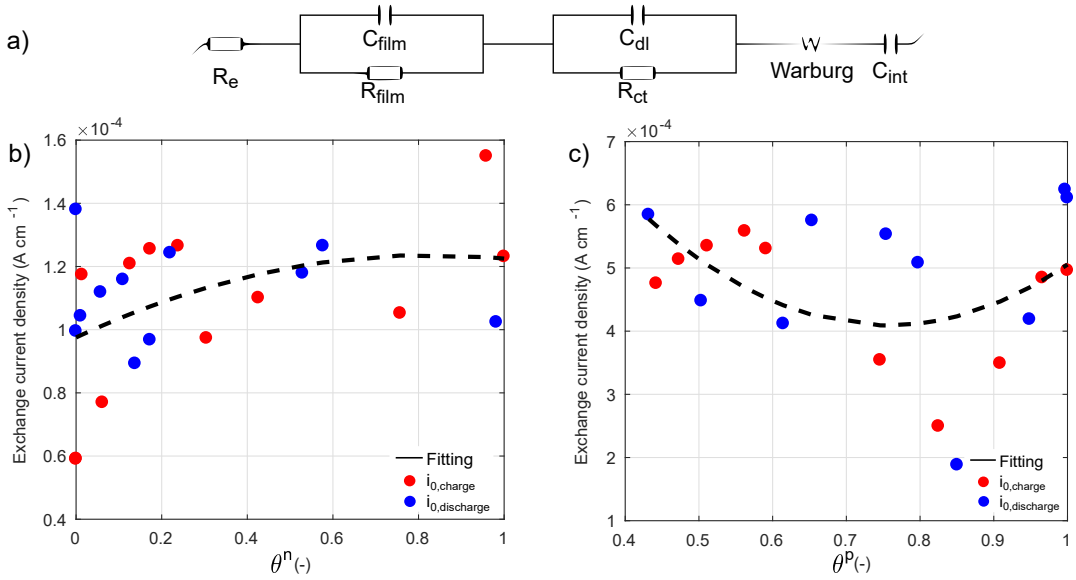

Figure 3.18: a) Equivalent circuit model used to correlate PEIS measurements with battery internal phenomena; Exchange current density for b) Negative electrode; c) Positive electrode.

The obtained exchange current density results show good agreement with the literature. Schmalstieg et at. [52] at 50% of lithiation obtained a value of 7.43 10^{-4} (A cm^{-2}) for

graphite, and 5.03 10^{-4} (A cm^{-2}) for NMC. Similarly, at the same lithiation level, Ecker et al. [50] reported values of 7.05 10^{-5} (A cm^{-2}) and 2.23 10^{-4} (A cm^{-2}) for graphite and $Li(Ni_{0.4}Co_{0.6})O_2$ electrodes, respectively.

In order to account for the temperature dependence, the exchange current density at three temperatures (278.15, 298.15, and 318.15 K) for 50% of the SoL range of the electrodes ($\theta^n = 0.5$ and $\theta^p = 0.68$) was analysed. The activation energies calculated with Arrhenius law were 11.8 ± 2 kJ mol^{-1} and 9.2 ± 2 kJ mol^{-1} for negative and positive electrodes, respectively. The average values of the double layer capacitance were 6.746 ± 0.2 (F m^{-2}) and 0.27 ± 0.2 (F m^{-2}), and the average film resistances were 0.014 ± 0.005 (Ω m^2) and 0.178 ± 0.005 (Ω m^2) for the negative and positive electrodes, respectively. Schmalstieg et al. [52] obtained values of 1.47 F m^{-2} and 0.198 F m^{-2} for double layer capacitance for graphite and NMC electrodes, which are in good concordance with our results.

3.5.3 Transport properties

In this subsection, the transport properties of the solution-phase and solid-phase are discussed. The parameters that describe the solution-phase are ionic conductivity, diffusivity, activity coefficient, and the transport number. Together, these four transport properties describe a binary and concentrated electrolyte [21]. They are concentration dependent and cannot be directly determined in commercial cells since the recovered electrolyte is at a specific concentration. For that reason, 1 M and 2 M $LiPF_6$ EC:EMC (50:50 v%) commercial electrolytes were used in this analysis. The ionic conductivity, measured by EIS, is shown in Figure 3.19 a), which is in good agreement with the literature [156].

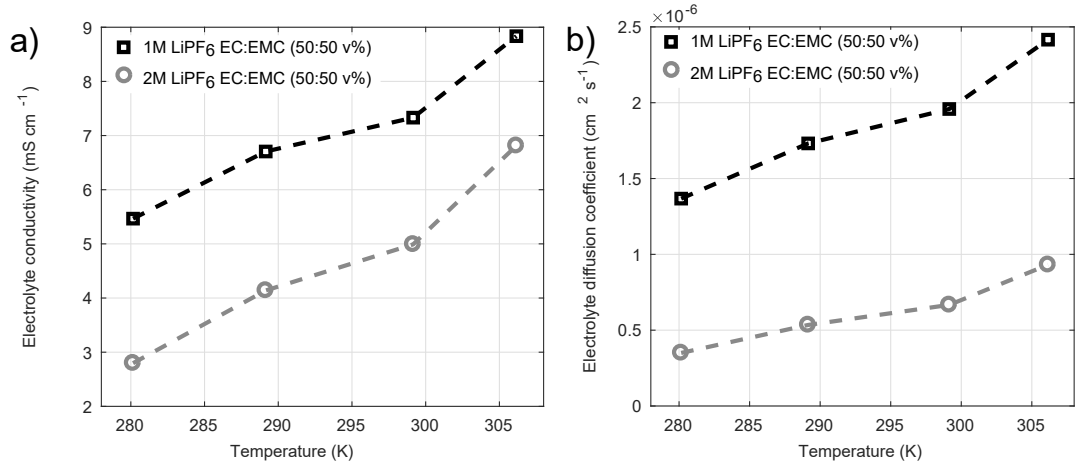

Figure 3.19: a) Ionic conductivity of the reference 1 and 2 M LP50 commercial electrolytes; b) Electrolyte diffusion coefficient.

The transport number was measured with Steady-State Potentiostatic Polarization test (SSPP) using a polarization cell with the reference 1 M electrolyte. The calculations are based on Bruce and Vincent's procedure [156]. A value of 0.28 ± 0.05 was experimentally obtained, which is in good concordance with literature values 0.34 ± 0.07 [52, 56]. No concentration dependencies were measured in this case.

The diffusion coefficient was calculated with the Einstein relationship assuming a constant transport number and measuring the ionic conductivity [52, 61, 83] (see equation 3.42). The activation energies of the conductivity and diffusivity were 14.67 ± 2 kJ mol^{-1}

and 17.13 ± 2 kJ mol^{-1}, respectively. In Figure 3.19 b), the values for diffusivity calculated with Einstein relationship are presented.

$$D_e = \frac{\kappa k_B T}{e^2 N_A c_e} \tag{3.42}$$

where κ is the ionic conductivity, k_B is the Boltzmann constant, e is the elementary charge, N_A is the Avogadro constant, and c_e is the lithium concentration of the electrolyte.

In the solid-phase of the electrodes, electronic conductivity and solid diffusion coefficient were determined. The dc-four point probe technique was used when the cell was in the discharged state (0% SoC). The experimental set-up is presented in Figure 3.20 a). A commercial EL-CELL® brand product was used so as to ensure the reproducibility of the measurements, and to apply a constant mechanical load to the cell (dependent on the thickness of the studied sample). In Figure 3.20 b) the two measurements performed in this work, together with the detail of the resistances taking place in the measurement are presented for powder and one side coating. The bulk electronic conductivity was determined in the scrapped powder of the active materials. Differences were found depending on whether the measurements were taken directly, or after a heat treatment to remove binder and conductive additives. This property was also measured in the coated electrode (one side or two side coatings), although we included the resistance between AM and coating in the measurement.

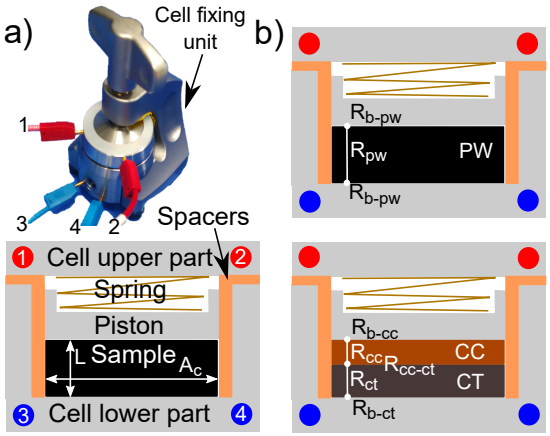

Figure 3.20: a) Experimental cell for electronic conductivity measurement (top) and schematic representation of the inner part of the cell with component names (bottom); b) Measured resistances for powder (PW) (top) and one side coating (CC- current collector and CT - coating) (bottom).

In this work both bulk and coating measurement types were performed and compared to assess the new procedure. First, the electronic conductivity was determined from the powder collected from the electrodes. The pycnometry powder density of the electrodes (2.1472 ± 0.001 g cm^{-3} and 3.8001 ± 0.001 g cm^{-3} for negative and positive electrodes, respectively) was measured to calculate the average thickness of the powder in the electronic conductivity measurements. Equation 3.43 was used to calculate the electronic conductivity based on resistance measurements from EIS and LSV measurements.

$$\sigma = \frac{L}{\mathrm{R}_0 A_{cell}} = \frac{m_{sample}}{\mathrm{R}_0 {A_{cell}}^2 \rho_{ph}} \tag{3.43}$$

where R_0 is the measured electrical resistance (Ω), A_{cell} is the cross sectional area of contact (m^2), m_{sample} is the powder sample mass (kg) (needed to estimate the powder

thickness of the measurement), and ρ_{ph} is the helium powder density (kg m^{-3}).

An average value of 6.6 ± 0.1 (S m^{-1}) and 2.0 ± 0.1 (S m^{-1}) for the negative and positive electrode were recorded, respectively. The effective electronic conductivities (taking the Bruggeman exponent and solid volume fraction of subsection 3.5.4 and equation 3.26) were 3.9 ± 0.1 and 0.9 ± 0.1 (S m^{-1}) for the negative and positive electrodes, respectively.

In order to obtain measurements that were comparable with the literature, electronic conductivities were also measured in a one sided coated electrode (same as Ecker et al. [61]. The graphite electrode was in the same order of magnitude as values given by Ecker et al. following a similar procedure. The effective conductivity value (the property is measured in the porous electrode) includes the contact resistance between the coating and the current collector. The values obtained in this work were lower than expected; therefore, the measurement methodology should be enhanced. However, several orders of magnitude of variation is found in the literature of electronic conductivity values [52, 56, 61].

The solid diffusion coefficient (D_s) can be measured using potential-step techniques as a function of SoC and temperature. A mixed method combining PITT and PEIS techniques was used taking the methodology from [157]. The equation accounts for morphological $(V_m/zFS)^2$, thermodynamic $(dE_0/dx)^2$ and dynamic $\left(1/\sqrt{2}A_w\right)^2$ factors (equation 3.44):

$$D_s = \left(\frac{V_m}{zFS}\right)^2 \left(\frac{dE_0}{dx}\right)^2 \left(\frac{1}{\sqrt{2}A_w}\right)^2 \tag{3.44}$$

where V_m is the molar volume of the insertion material, dE_0/dx is the equilibrium potential-concentration profile of the material (from PITT), and A_w is the Warburg coefficient (from PEIS).

The solid diffusion coefficient results for positive and negative electrodes are presented in Figure 3.21 a) and b).

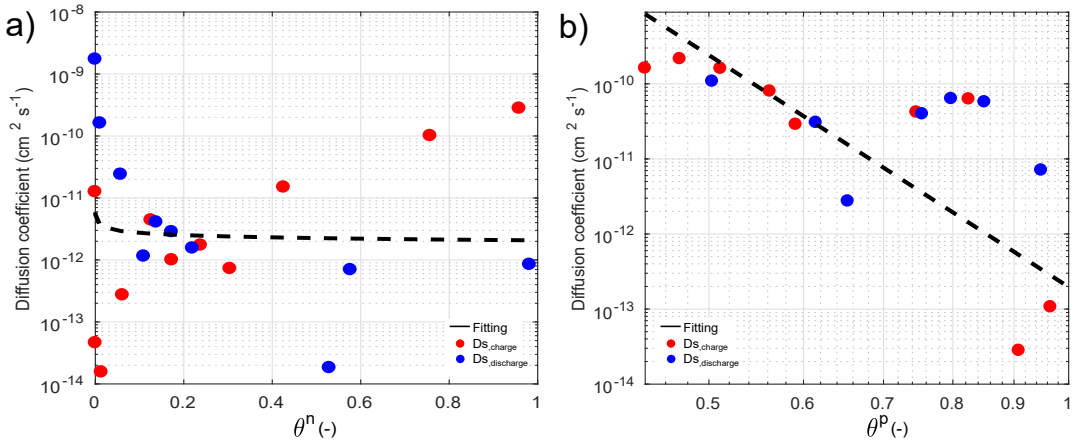

Figure 3.21: a) Solid diffusion coefficient for a) Negative electrode; b) Positive electrode.

3.5.4 Parameters related to porous structures and adjustable design parameters

The porous structure is defined during the mixing, coating, drying and calendering steps of the fabrication process of batteries, and changes during charge-discharge processes

due to the expansion/contraction of the materials [158]. In this subsection only the full-cell discharged state is characterised. First of all, the raw materials (NCA, LCO, graphite) shape and size were characterised. These properties are defined during the synthesis process and are critical when the porous structure of the electrodes is defined [159]. The effective particle diameter was calculated based on dynamic light scattering (DLS) measurements, and compared to SEM image processing results. In Figure 3.22 a) and b) the results obtained with DLS are presented. Samples were analysed in powder after a heat treatment to remove the binder. This technique was used to obtain a particle size distribution.

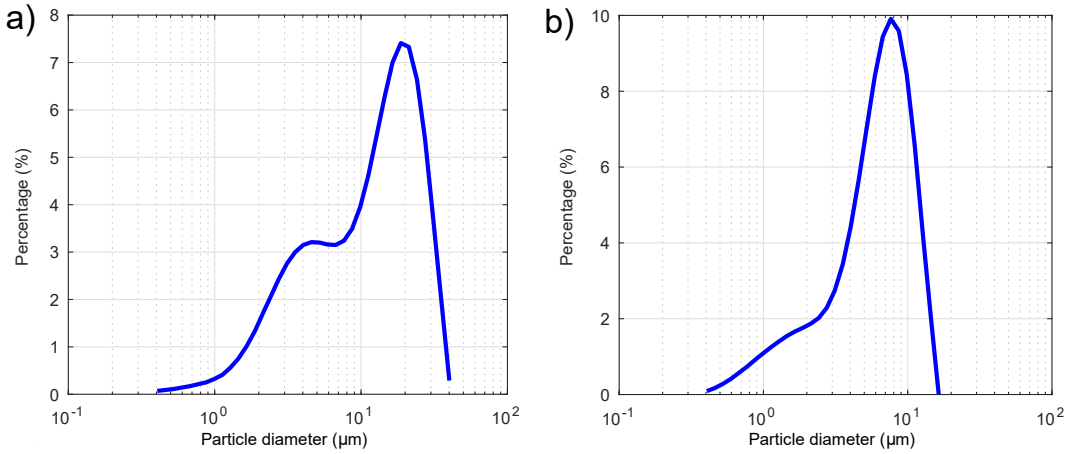

Figure 3.22: Particle size distribution with dynamic light scattering technique for a) Negative electrode; b) Positive electrode.

Moreover, SEM images were treated to obtain an average particle size of the electrodes and compared with the DLS measured effective particle diameter (see Figure 3.23).

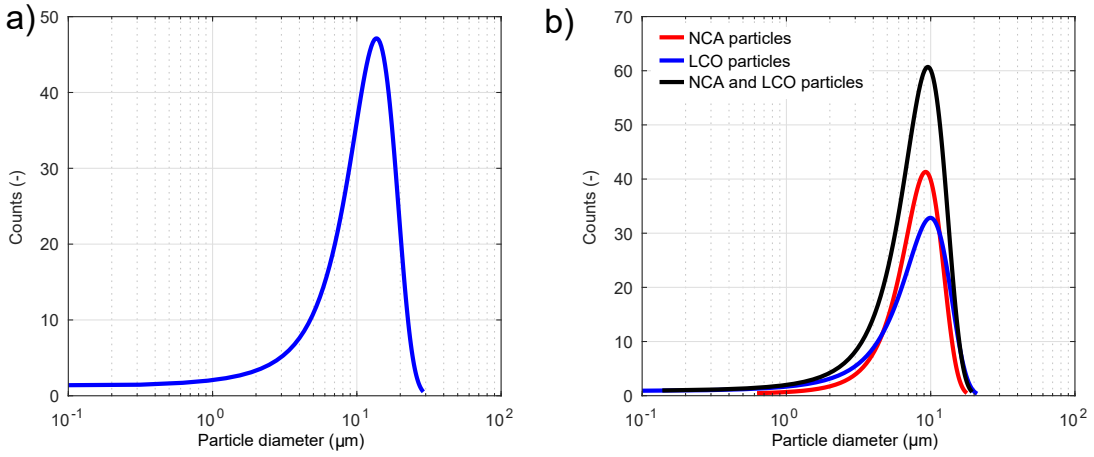

Figure 3.23: Particle size distribution calculated by SEM image processing for a) Negative electrode; b) Positive electrode.

The model assumes uniform sized and spherical particles in both electrodes, which affects the accuracy of the results. In DLS results, an effective particle diameter (Dv 50) of 13.1 ± 1.5 and 7.0 ± 0.6 µm for the negative and positive electrodes respectively, was calculated. With SEM analysis two different distributions corresponding to the previously identified blended material in the positive were measured in 2D electrode slices. The averaged particle diameter with SEM image post-processing were 13.7 µm for the graphite, 9.2 µm for the NCA, and 10.0 µm for the LCO active materials.

In Figure 3.24 a) the cross-section image of the negative electrode is presented, showing a flake-like shape (commonly seen in graphite electrodes). In Figures 3.14 and 3.24 b) the SEM images of the positive electrode are presented (spherical particle shape).

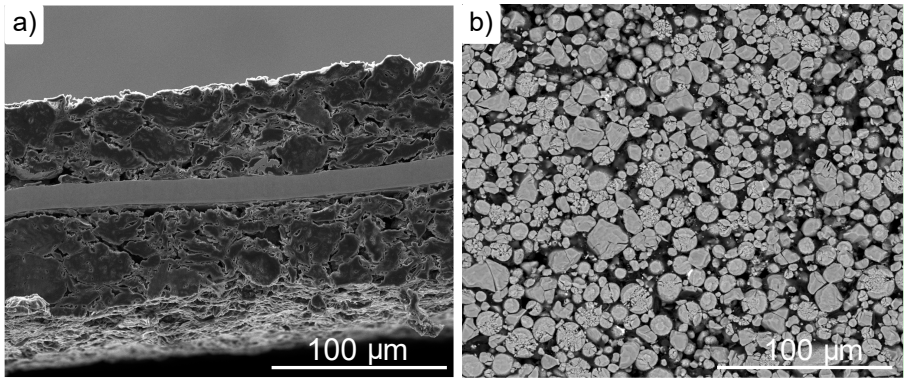

Figure 3.24: a) SEM cross-section image of the negative electrode (prepared by ion milling); b) SEM surface image of the positive electrode.

The geometrical parameters of this specific battery are given in Table 3.7. The thicknesses of the electrodes and the cross-sectional area (based on electrode width and length) are the parameters used in the P2D model. The cross-sectional area of the cell is 23.15 ± 0.1 cm^2, which corresponds to the positive electrode. The negative is larger than the positive electrode (1 cm^2 bigger) in order to ensure the whole positive electrode utilization, and reduce the dendrite formation risk [160]. In Figure 3.11 e) it is possible to assess visually the utilization area of the negative electrode. A dark colour can be distinguished around the borders, whereas the rest of the electrode is gold coloured.

Table 3.7: Geometrical parameters for the electrodes and separator.

Parameter	Positive electrode	Negative electrode	Separator
W (cm)	3.8 ± 0.1	3.9 ± 0.1	156.4 ± 0.1
H (cm)	6.1 ± 0.1	6.2 ± 0.1	6.5 ± 0.1
L (µm)*1	32.2 ± 0.5	49.8 ± 0.5	13.8 ± 0.5
Rs (µm)	6.55 ± 0.7	3.5 ± 0.3	-

*1 One side coating. Only the coated thickness is presented, without current collector.

The porous structure related parameters are defined during the electrode fabrication process (porosity, solid volume fraction, tortuosity and specific surface area) which affect to the final performance of the cell. In Figure 3.25 the different types of pores and densities studied in this chapter are illustrated.

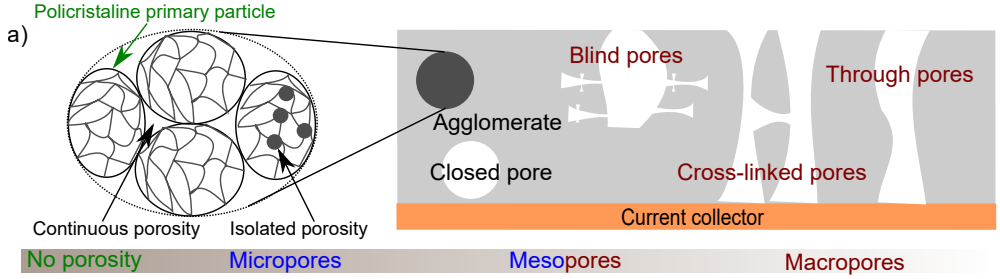

Figure 3.25: Different type of pores in a coated electrode. Based on [161] and [162].

In order to calculate the electrode coating porosity (ε_e) mercury porosimetry measurements were performed. In these experiments bulk and skeletal densities were calculated and corrected, so as to obtain the average porosity. As the P2D model does not account for pore size distribution, the average porosity value was used in the simulations (equation 3.45).

$$\varepsilon_{e,SA} = 100\left(1 - \frac{\rho_{bulk,SA}}{\rho_{ske,SA}}\right) \tag{3.45}$$

where $\rho_{bulk,SA}$ is the two sided coating mercury density (bulk density), and $\rho_{skeletal,SA}$ is the two sided coating mercury density (skeletal density).

The skeletal density and electrode coating bulk density were corrected in accordance with Froboese et al. [162] (equation 3.46) with the proposed correction by given sample area and mercury mass replacement.

$$\varepsilon_{e,SA} = \frac{(V_{p,HL} - V_{p,LL})\rho_{Hg}}{m_{pen,Hg} - [(m_{pen,Hg,sam} - m_{cc} + (\rho_{Hg} ML_{cc} A_{cc})/\rho_{cc}) - m_{coating}]} \tag{3.46}$$

where $V_{p,HL}$ is the maximum intruded mercury volume at the lowest considered pore diameter (0.01 nm), $V_{p,LL}$ is the minimum intruded mercury volume at the highest considered pore diameter (based on Dv90 of the DLS measurements), ρ_{Hg} is the mercury density, $m_{pen,Hg}$ is the weight of penetrometer and mercury, $m_{pen,Hg,sam}$ is the assembly weight (penetrometer, mercury and sample), ML_{cc} is the mass loading of the current collector, and A_{cc} is the area of the current collector.

In this case, bulk densities were 1.085 ± 0.001 g cm^{-3} and 2.468 ± 0.001 g cm^{-3} and skeletal densities were 1.489 ± 0.001 g cm^{-3} and 3.0454 ± 0.001 g cm^{-3} for the negative and positive electrodes, respectively. Combining both results, 27.095 ± 0.005 % porosity was defined for the negative electrode and 22.193 ± 0.005 % for the positive electrodes.

The pore size distributions obtained by mercury porosimetry for the coated samples are presented in Figure 3.26 a) and b), and are in good concordance with literature [61].

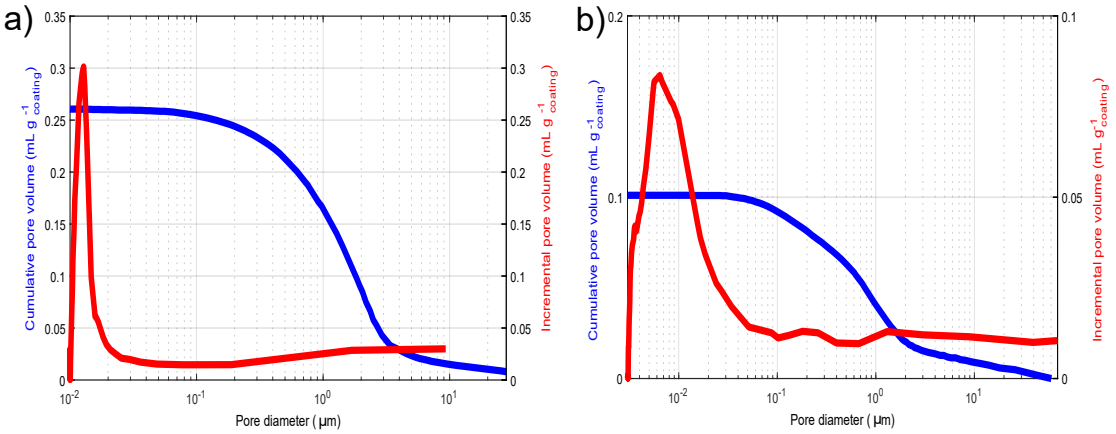

Figure 3.26: Mercury porosimetry results for a) Negative electrode; b) Positive electrode.

In addition to the liquid-volume fraction or coating porosity (ε_e) within the porous electrode, the solid-volume fraction (ε_s) needs to be defined. To this end, the inactive part of the electrodes (binder and additives) should be estimated. Apart from the inert

materials which form the composite solid matrix, some parts of the active material do not react and the solid volume fraction should be corrected adding the contribution of the non-electrochemically active volumes. Therefore, the solid-volume fraction of the material can be calculated as follows (equation 3.47):

$$\varepsilon_s = 1 - \varepsilon_e - \varepsilon_{non-act} \tag{3.47}$$

where $\varepsilon_{non-act}$ corresponds to the non-electrochemically active solid volumes (binder, additives, closed pores etc.).

To calculate the non-electrochemically active volume of the material, equations 3.36 and 3.47 should be combined (equation 3.48). This relationship is then used in the electrochemical model, allowing the coherence between experimentally obtained results and simulations.

$$\varepsilon_{non-act} = 1 - \varepsilon_e - \left(\frac{C_{pouch,\exp}}{C_{pouch,th}} \right) \tag{3.48}$$

The values used for the model are presented in Table 3.8.

Table 3.8: Porous structure parameters for the electrodes and separator.

Parameter	Positive electrode	Negative electrode	Separator
ε_e (-)	0.27095 ± 0.00005	0.22193 ± 0.00005	0.51 ± 0.00005
ε_s (-)	0.600 ± 0.00005	0.704 ± 0.00005	0.49 ± 0.00005
as (m^2 m^{-3})	5.11 ± 0.1 10^5	3.22 ± 0.1 10^5	-
brug	1.50 ± 0.001	1.46 ± 0.001	1.38 ± 0.001

Different methods to calculate the specific surface area between the active material and the electrolyte can be found in the literature [49, 50, 52, 158]. In all the cases, the assumption made during the experimental parameter measurement and simulations should be the same so as to have the ability to recalculate the area-related variables in the model [52]. Assuming uniform size and spherical particles, the approximation presented in equation 3.27 can be applied.

Moreover, the surface area (used for exchange current density and solid diffusion coefficient calculations) is calculated as in equation 3.49 [52] in which a value of 33.99 ± 0.1 and 10.01 ± 0.1 cm^2 were obtained for negative and positive electrodes, respectively.

$$S_{coin} = \frac{3V_{coin}\varepsilon_s}{R_s} = \frac{3A_{coin}L\varepsilon_s}{R_s} \tag{3.49}$$

Finally, the tortuosity of the electrodes is defined as in equations 3.22 and 3.23. The effective parameters for the model are defined in equations 3.24, 3.25 and 3.26.

In this research, the pore tortuosity was analysed by means of Carniglia's equation (equation 3.50 [163]), in which Fick's first law is used to describe fluid diffusion in cylindrical pores. The equation validity range for both electrodes was confirmed ($0.05 \leq V_{p,c}\rho_{coating,Hg} \leq 0.95$).

$$\tau = (2.23 - 1.13 V_{p,c}\rho_{coating,Hg}) \tag{3.50}$$

where $V_{p,c}$ is the intruded mercury volume per electrode coating mass.

The Bruggeman relationship is widely used in the literature to relate the tortuosity with the volume fraction (equation 3.51 [49, 57]). The extended Bruggeman relationship was applied and the results are given in Table 3.8.

$$brug = 1 - \log_{\varepsilon_e}(\tau) \tag{3.51}$$

In order to determine the separator parameters (porosity, tortuosity and Bruggeman exponent) the methodology that is explained in Arora et al. [142] was followed. In this method, the porosity of the sample is calculated based on the measured mass and geometrical volume of the separator compared to the true density of the separator (measured by helium pycnometry). The tortuosity of the separator was calculated by means of the difference between the electrolyte resistivity and the separator effective resistivity. Therefore, the resistivity of the separator sample impregnated in electrolyte using the reference 1 M LP50 electrolyte is measured (equation 3.52 [142]):

$$\frac{\rho^s}{\rho^e} = \frac{\tau^2}{\varepsilon_e} \tag{3.52}$$

where ρ^s is the specific resistivity of the separator saturated with electrolyte, and ρ^e is the specific resistivity of the electrolyte.

3.5.5 From components to full-cell: cell internal configuration and electrode balancing determination

The cell internal configuration is shown in Figure 3.27 a). It was assembled with 18 layers of double side coated negative electrodes, 17 layers of double side coated positive electrodes, and 2 single side coated positive electrodes. A Z-folding configuration was used to place the separator in between the electrodes and the cell was divided into two subcells.

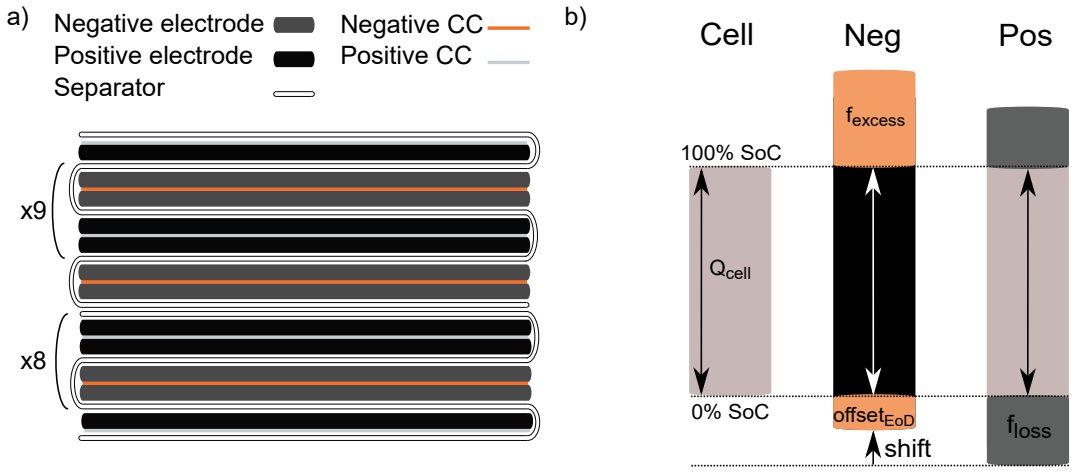

Figure 3.27: a) Cell internal configuration; b) Electrode utilization range.

The total mass of each component was calculated by multiplying the mass per unit area by the total area of each cell component. The electrolyte mass was estimated by subtracting the mass of the rest of the components from the mass of the cell before being opened. The obtained values were compared with the data provided by Kokam, as shown in Table 3.9.

Table 3.9: Mass of all cell components and comparison with the datasheet [140].

Total weight of cell	Units	Weight per unit (g)	Total weight (g)	Weight (%)	kokam datasheet (content %)
Negative electrode*1	18	0.35 ± 0.01	6.33 ± 0.01	19.20 ± 0.01	15 - 35
Copper foil	18	0.32 ± 0.01	6.10 ± 0.01	18.47 ± 0.01	3 - 12
Positive electrode*1	17 + 2	0.53 ± 0.01	9.55 ± 0.01	28.95 ± 0.01	20 - 50
Aluminium foil	17 + 2	0.13 ± 0.01	2.38 ± 0.01	7.20 ± 0.01	3 - 12
Separator	1	1.16 ± 0.01	1.16 ± 0.01	3.51 ± 0.01	< 8
Package*2	1	1.95 ± 0.01	1.95 ± 0.01	5.90 ± 0.01	< 5
Cell mass (calculation)			27.47 ± 0.01	83.23 ± 0.01	
Cell mass (before opening)				33.00 ± 0.01	100.00
Electrolyte			5.53 ± 0.01	16.77 ± 0.01	10 - 20

*1 AM, binder, additives; *2 Tabs included

The internal configuration is directly related to electrode balancing as the number and size of the electrodes determines the final cell capacity. Electrode balancing is a key process in the fabrication of batteries. After the step of cell assembly, formation cycles are performed to create the SEI layer and activate the cell. When the cell is charged for the first time, lithium ions are deinserted from the positive electrode and inserted in the negative electrode. In the first discharge process lithium ions are deinserted from the negative electrode and reinserted in the positive electrode. Note that after the first full cycle the positive electrode lithiation is y $<$ 1, due to the SEI formation and negative electrode irreversibility (lithium ions get trapped in the electrode structure, resulting in a decrease of the lithium inventory f_{loss}). One or more cycles need to be performed so as to form a stable SEI that provides the needed stability of the cell. In the case of commercial cells, the information of formation cycles was not available.

In the literature, different approaches for electrode balancing are found [52, 56, 61, 83, 137]. In all these cases half coin cell reconstruction is necessary to study negative and positive electrodes separately. In the next paragraphs, the methodology that was implemented for electrode balancing is presented. From the electrode balancing, the operational limits of the electrodes (θ_0^n, θ_{100}^n, θ_0^p and θ_{100}^p) as well as the excess of negative electrode (f_{excess}) and the loss of lithium inventory in the positive electrode (f_{loss}) due to the first formation cycles were obtained. A graphic explanation of the electrode balancing parameters and the interaction between them is presented in Figure 3.27 b).

In order to determine the full electrode balancing, in addition to electrode qOCVs (see subsection 3.5.2), qOCV curves at C/30 and 298.15 K from full coin and full pouch cells were experimentally obtained. First, the experimental qOCV tests were scaled from coin cell level to pouch cell level using $scale_{coinTOpouch}$ scaling factor (equation 3.53):

$$Q_{pouch} = Q_{coin,FC} scale_{coinTOpouch} \tag{3.53}$$

To correct the small experimental deviations that can arise due to the set up of the experiments, a correction factor was applied separately to each electrode. These correction factors are understood to be as a small variation of less than 10% of the real capacity, which could come from coin cell reconstruction process (see equation 3.54).

$$\begin{aligned} Q^n_{pouch} &= Q^n_{coin} scale_{coinTOpouch} scale^n_{corr} \\ Q^p_{pouch} &= Q^p_{coin} scale_{coinTOpouch} scale^p_{corr} \end{aligned} \tag{3.54}$$

Taking as a reference the maximum and minimum lithiation states of the materials (θ^n_{max}, θ^n_{min}, θ^p_{max} and θ^p_{min}) of subsection 3.5.2, the excess of negative electrode active material (f_{excess}) was determined by means of the following relationship (equation 3.55).

$$f_{excess} = 1 - (\theta^n_{max} - \theta^n_{min}) \left(\frac{\max(Q_{pouch})}{\max(Q_{coin,FC})} \right) scale_{coinTOpouch} scale_{neg,corr}) \tag{3.55}$$

Then, the negative electrode lithiation states at 0% and 100% of SoC of the pouch cell were calculated (equations 3.56 and 3.57). As an starting point, $offset_{EoD}$, which corresponds to the lithium trapped irreversibly in the negative electrode structure at low lithiation levels, was set to zero.

$$\theta^n_{100} = \theta^n_{max} - f_{excess} + offset_{EoD} \tag{3.56}$$

$$\theta^n_0 = \theta^n_{100} - (\theta^n_{max} - \theta^n_{min}) \left(\frac{\max(Q_{pouch})}{\max(Q_{coin,FC})} \right) scale_{coinTOpouch} scale_{neg,corr}) \tag{3.57}$$

Once the $offset_{EoD}$ was determined, the voltage difference between the full pouch cell and negative electrode at 100% SoC (θ^n_{100}) was used to first calculate the θ^p_{100} and thus, calculate the initial f_{loss} (equation 3.58). This parameter was updated iteratively during the electrode balancing process.

$$f_{loss} = 1 - (\theta^p_{100} + (\theta^p_{max} - \theta^p_{min}) \left(\frac{\max(Q_{pouch})}{\max(Q_{pos,coin})} \right) scale_{coinTOpouch} scale_{pos,corr}) \tag{3.58}$$

Finally, the lithiation states at 0% and 100% of SoC of the cell for the positive electrode are defined as (equations 3.59 and 3.60).

$$\theta^p_0 = \theta^p_{max} - f_{loss} \tag{3.59}$$

$$\theta^p_{100} = \theta^p_0 - ((\theta^p_{max} - \theta^p_{min}) \left(\frac{\max(Q_{pouch})}{\max(Q_{pos,coin})} \right) scale_{coinTOpouch} scale_{pos,corr}) \tag{3.60}$$

In Figure 3.28 a) the experimental and reconstructed cell voltage, the negative and positive electrode voltages and the error between the fitting and experimental voltage are presented. A maximum error of 10.75 mV or 0.36%, and a mean error of less than 5.69 mV or 0.15% is reported.

In Figure 3.28 b), the dVdQ plot of experimental and reconstructed curves is shown. A $scale^{p}_{corr}$ of 0.98 and $scale^{n}_{corr}$ of 0.93 were used to correct the reconstructed electrode balancing curves to fit experimental pouch cell data. In fact, the dVdQ peaks can be related to voltage plateaus of the graphite during coexisting phases and phase transitions. The positive electrode dVdQ are related to the material phase changes [136].

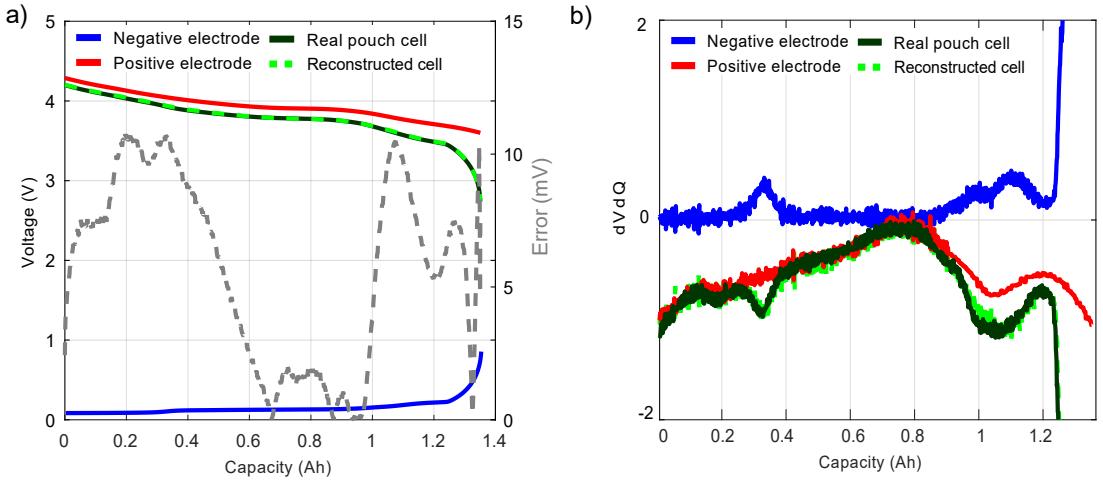

Figure 3.28: a) Pouch cell, reconstructed cell, negative and positive electrode voltage responses as a function of the cell capacity; b) dVdQ plot of the pouch cell, reconstructed cell, negative and positive electrodes.

Finally, the OCV curve as a function of the lithium content of the electrodes and the utilization range of the full-cell is shown in Figure 3.29 a) and b).

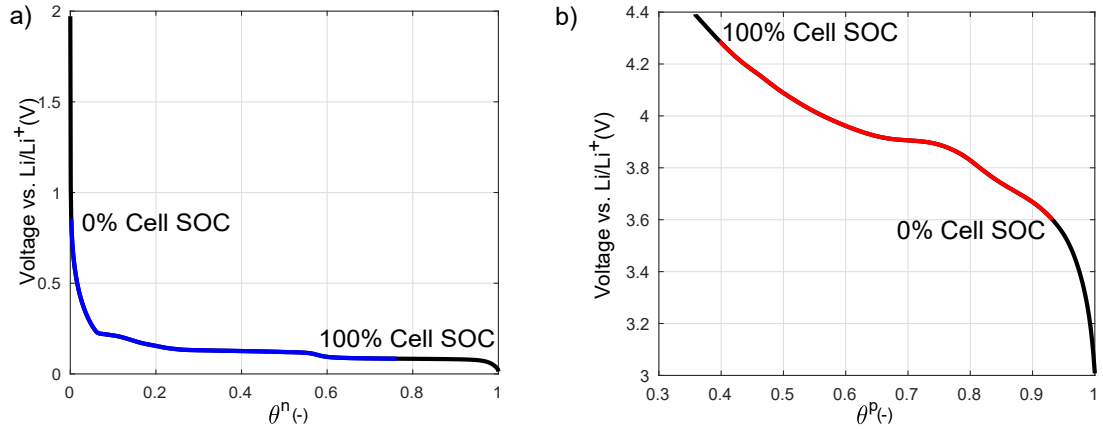

Figure 3.29: Equilibrium potential curve and electrode utilization range for a) Negative electrode (blue); b) Positive electrode (red).

The positive electrode utilization range is in between 0.40 and 0.93 SoL, and negative utilization range between 0.002 and 0.76 of SoL, which is in good concordance with the literature [52, 61, 137]. In addition, a f_{excess} of 0.24 and f_{loss} of 0.07 was obtained. It is worth mentioning that, as the positive electrode is a blended material composed of LCO and NCA, the x-axis of Figure 3.29 b) was obtained assuming a ratio between materials of 50% and assuming that the material dynamics of both materials are equal.

To help model prediction improvement, positive blend material decoupling is requiered[11]. In Figure 3.30, the methodology has been extended for the blend positive material composed of LCO and NCA.

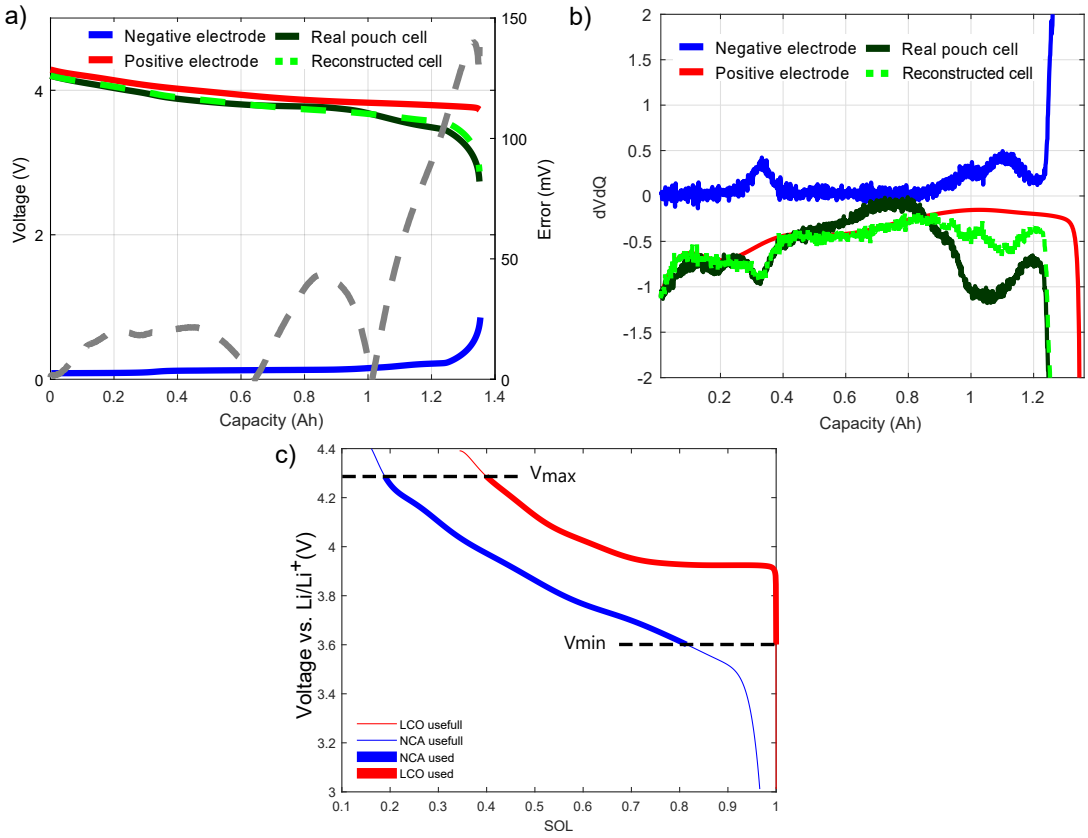

Figure 3.30: a) Pouch cell, reconstructed cell, negative and positive blended LCO/NCA electrodes voltage responses in function of the cell capacity; b) dVdQ plot of the pouch cell, reconstructed cell, negative and positive blend electrodes; c) Equilibrium potential curve and NCA-LCO utilization range in function of the stoichiometry.

In commercial cells, to separate OCV curves can not be experimentally tackled. Thus, knowing the exact contribution of each electrode is a challenge. However, a combination between previously proposed methodology and extra literature could be employed so as to include two materials into the electrochemical model [85, 164].

The experimental OCV curves used in this study were taken from Karthikeyan et al. [165]. In Figure 3.30 c) the decoupling of the OCV for the two positive materials is presented, showing the different lithiation ratios of the materials. Thermodynamic and transport parameters (presented in subsections 3.5.3 and 3.5.2) are properties related to the SoL of these materials. They should be characterised separately. However, in commercial cells those tests cannot be performed. Therefore, estimations or fittings could be performed to guess the aforementioned properties and improve model predictions. Therefore a mixed method between physico-chemical parameter measurement and computational identification methodologies could be used.

To experimentally measure the SoL of each active material, *ex-situ* XRD was performed (see Subsection 3.6.2).

[11]The implementation of the blend material methodology was carried out by Eneko Agirrezabala and the author.

3.6 MODEL VALIDATION

In order to evaluate the validity of the proposed experimental methodology, the measured parameters were implemented into a pseudo-two dimensional (P2D) model in Comsol Multiphysics® simulation software (version 5.5).

3.6.1 Non-invasive tests: Model response evaluation in pouch cells

The model response evaluation is used as a proof of the validity of the parameter measurement methodology. In this work, model responses in a wide operation range were compared against experimental measurements of the analysed device, giving a reliable view of the accuracy of the parameters. Validation tests at the full pouch cell level, which include galvanostatic charge-discharge cycles at different temperatures and currents, pulse tests (HPPC procedure) at different SoCs, and PEIS tests were performed.

3.6.1.1 *Different current rate and temperatures on galvanostatic cycles*

The time-domain model was used for electrode balancing verification and correct implementation of all the parameters (see Figure 3.31 a) and b). The maximum error obtained in the discharge curve C/30 and 25 °C was less than 1% of capacity.

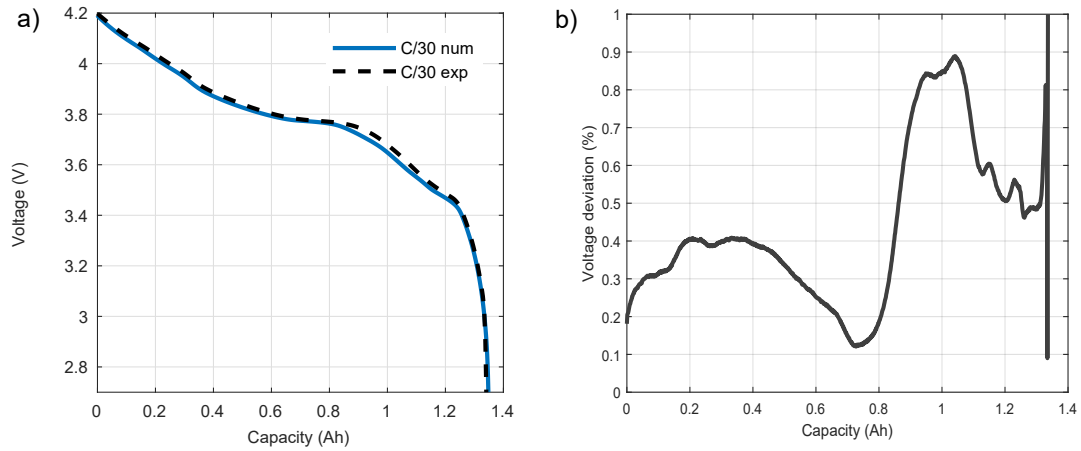

Figure 3.31: Experimental-simulation comparison for a) Experimental C/30 curve vs C/30 simulation at 25 °C; b) Voltage deviation between experimental and numerical C/30 curves at 25 °C.

Once the model parameters and responses were confirmed at low current rates at 25 °C, the dynamic response of the model needed to be assessed. First, galvanostatic cycles were checked as shown in Figure 3.32 a) and b)[12].

In Figure 3.32 c) and d) the lithium concentration inside particles and electrolyte are presented for a 1C discharge, respectively. These internal variables give an insight into whether the active materials or the electrolyte are the limiting factors of the discharges. At high rates, the solid diffusion coefficient and the reaction rate are key parameters, which limit the fast charging/discharging ability of electrodes. The initial concentration of the electrolyte is sufficient to prevent depletion of the lithium ions in the parts closest to the current collectors, in which the electrolyte concentration is lower.

[12]The post-process of the experimental results was carried out by Eneko Agirrezabala, experimental execution was performed by the author.

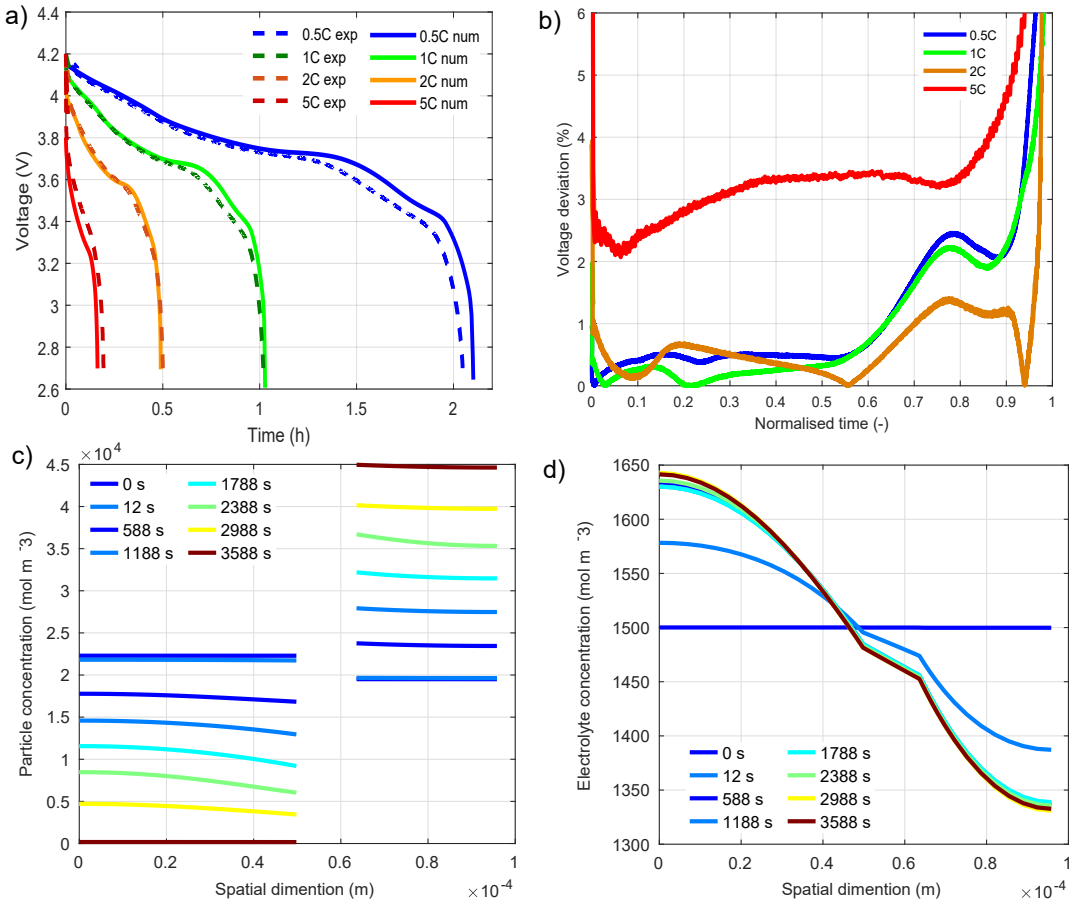

Figure 3.32: Experimental-simulation comparison for a) Galvanostatic discharges at different current rates at 25 °C; b) Voltage deviation between experimental and numerical galvanostatic discharge curves at 25 °C; c) State of lithiation of the electrodes for a 1C discharge at 25 °C; d) Electrolyte concentration for a 1C discharge at 25 °C.

In Table 3.10 the maximum capacity deviation for different conditions (5, 25 and 45 °C and galvanostatic charge and discharges) are presented.The maximum deviation was found at high current rates and high temperatures.

Table 3.10: Experimental and numerical maximum capacity deviations(%).

Temperature	5 °C		25 °C		45 °C	
C-rate	Discharge	Charge	Discharge	Charge	Discharge	Charge
0.5C	0.34	3.42	2.66	6.50	5.79	20.46
1C	0.92	0.55	1.05	4.88	7.23	25.53
2C	4.46	5.11	1.97	0.22	5.52	36.42
5C	19.26	-	15.39	-	5.41	-

3.6.1.2 *PEIS and HPPC tests*

Secondly, the impedance spectroscopy test showed greater deviations than galvanostatic cycles (Figure 3.33 a)) in which a second semi-circle is appreciable in the experimental curve. This can be attributed to the second phase of the positive material. Nevertheless, the other properties (i.e. average exchange current density, electronic conductivity) seems to be in good correlation with the literature (in terms of the order of magnitude).

The final step was to employ the HPPC test. A good correlation between the simulations and the experimental pulses are seen in Figure 3.33 b) for different SoCs. As was the case for the previous step, the main differences arising from this test could also be due to the blend positive material.

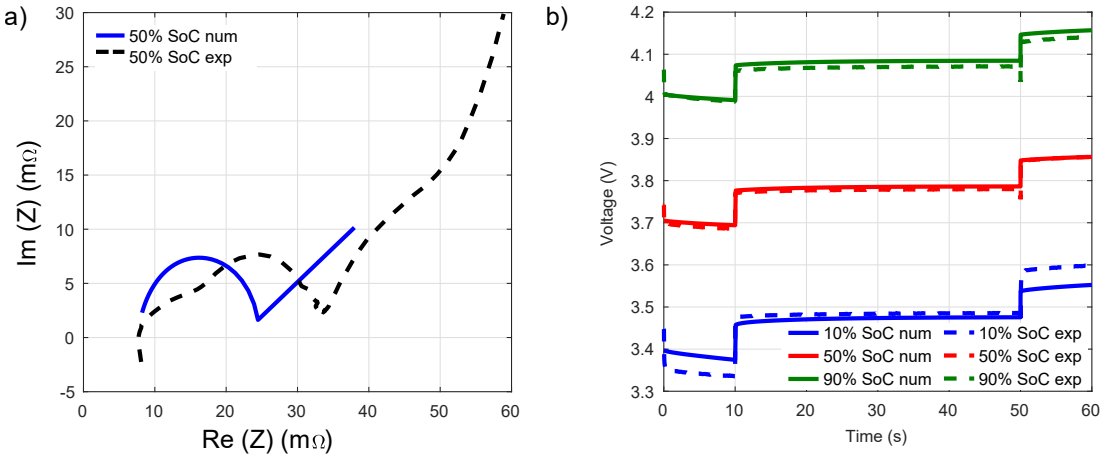

Figure 3.33: Experimental-simulation comparison for a) PEIS at 50% of SoC and 25 °C; b) HPPC pulses at different SoCs for 25 °C.

3.6.2 Invasive tests: Internal variable validation

Usually, the model validation ends with non-invasive test characterisation. However, invasive tests can provide relevant information about the lithiation state of the materials and electrode balancing.

3.6.2.1 *Three-electrode cell: positive and negative potential response*

A T-cell type three-electrode cell set-up is used for this purpose to evaluate the voltage evolution of each electrode separately. With this set-up, the voltage contribution of each electrode to the overall cell potential is experimentally obtained. In Figure 3.34 the experimental-numerical comparison of the electrodes potential is presented, showing good agreement between experimental T-cell electrode balancing and the methodology presented in subsection 3.5.5.

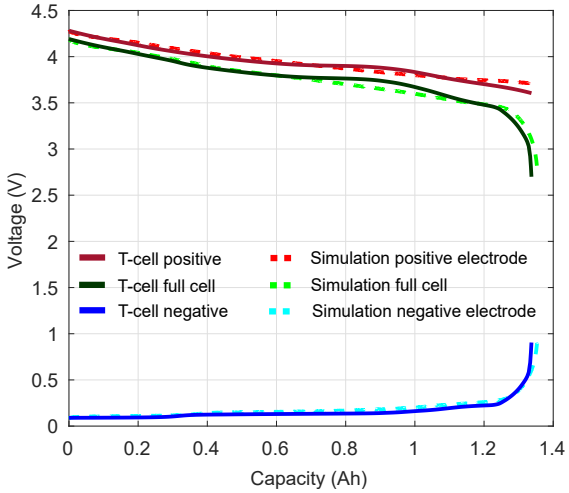

Figure 3.34: Comparison of the voltage evolution of the three electrode T-cell at 25 °C and C/10 and the P2D model.

The experimental capacity was extrapolated to the full cell capacity, based on the established half-full coin cell capacity relationships ($scale_{coinTOpouch}$, $scale^{n}_{corr}$ and $scale^{p}_{corr}$). Additionally, coin full-cell to coin T-cell scaling factor was applied. This could be related to the interaction of the lithium reference electrode as it is reported in the literature [123]. Those correction factors can be attributed to the cell set-up.

3.6.2.2 *XRD measurements at different lithiation levels: blend material ratios*

The solid lithium content of the negative electrode in the fully lithiation range is shown in Figure 3.35 to experimentally obtain the lithiation point at 0% and 100% SoC of the full cell. This information is complementary to the potential evolution presented in Figure 3.34 and helps to get insight into the electrode balancing of the cell, even if no information of the formation cycles is available. During the lithiation steps, intercalation compounds (LiC_6, LiC_{12}) were found. In addition, this experimental results could be compared to those obtained in Figure 3.31 c) for the particle concentration evolution during a discharge of the simulated cell. For a low C-rate discharge of Figure 3.31 a), the average state of lithiation of the electrode was plotted in Figure 3.35 c) to compare with experimental results. The XRD results are in good agreement with the simulation, which is an indicator that the electrode balancing estimation of subsection 3.5.5 was stated correctly. Negative utilization range between 0.002 and 0.76 of SoL were determined by means of the electrode balancing estimation in subsection 3.5.5.

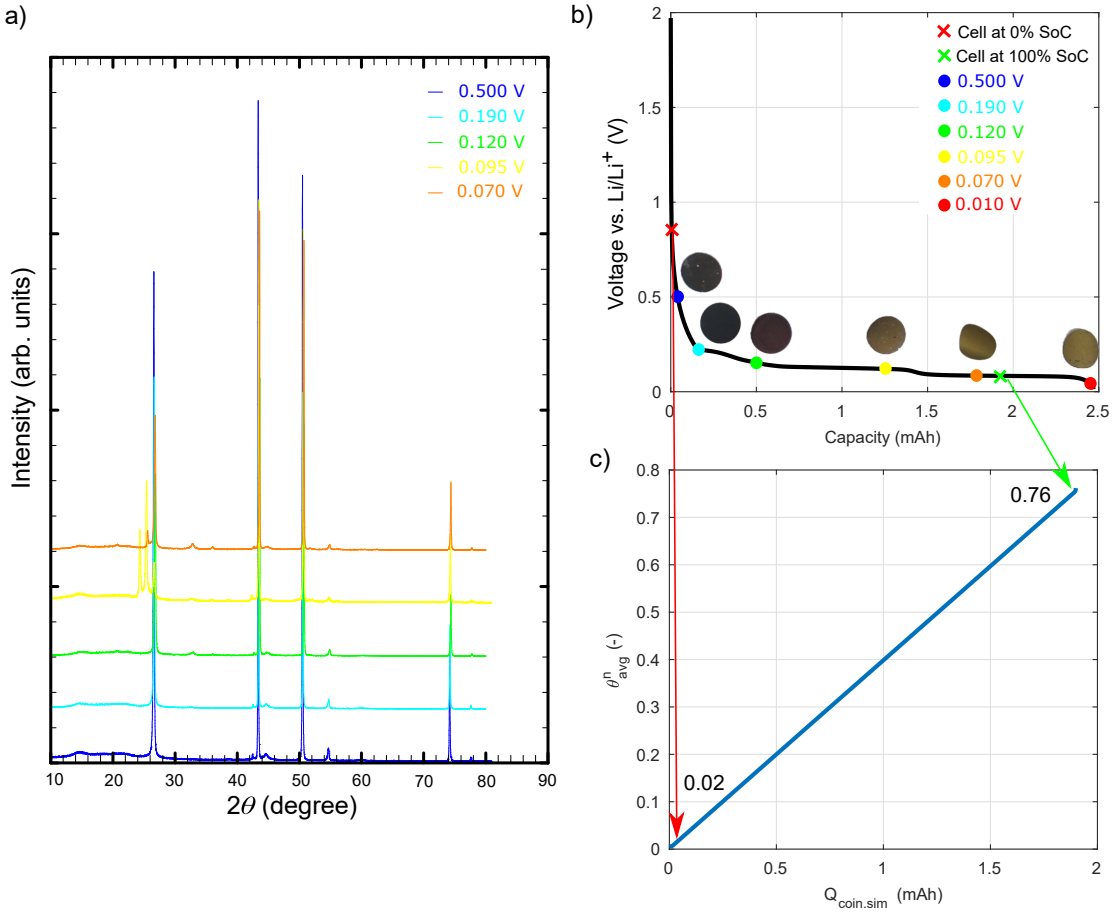

Figure 3.35: a) XRD diffractograms at different opening voltages for the negative electrode; b) Experimental C/30 curve at 25 °C showing the 0 and 100% of SoCs and the opening points and images taken after cell opening. c) Simulated negative average SoL vs coin cell capacity in a C/30 discharge at 25 °C.

Additionally, the solid lithium content of the positive active materials predicted by the electrode balancing estimation tool for the blend material decoupling were obtained experimentally by means of ex-situ XRD measurements at different electrode voltages (Figure 3.36 b)). A calibration curve (dots and lines) was determined to experimentally obtain the starting and ending SoLs (crosses) of the active materials based on the lattice parameters. At 100% of SoC, the lithiation level of LCO phase is almost 1, whereas the NCA phase is lower. The same tendency was observed in Figure 3.30 c). It is also in good correlation with literature [85]. Moreover, at 0% of SoC, the lattice parameters are closed to 4.3 V which is the expected results from Figure 3.34. This calibration curve could also be used for ageing mechanism study [136].

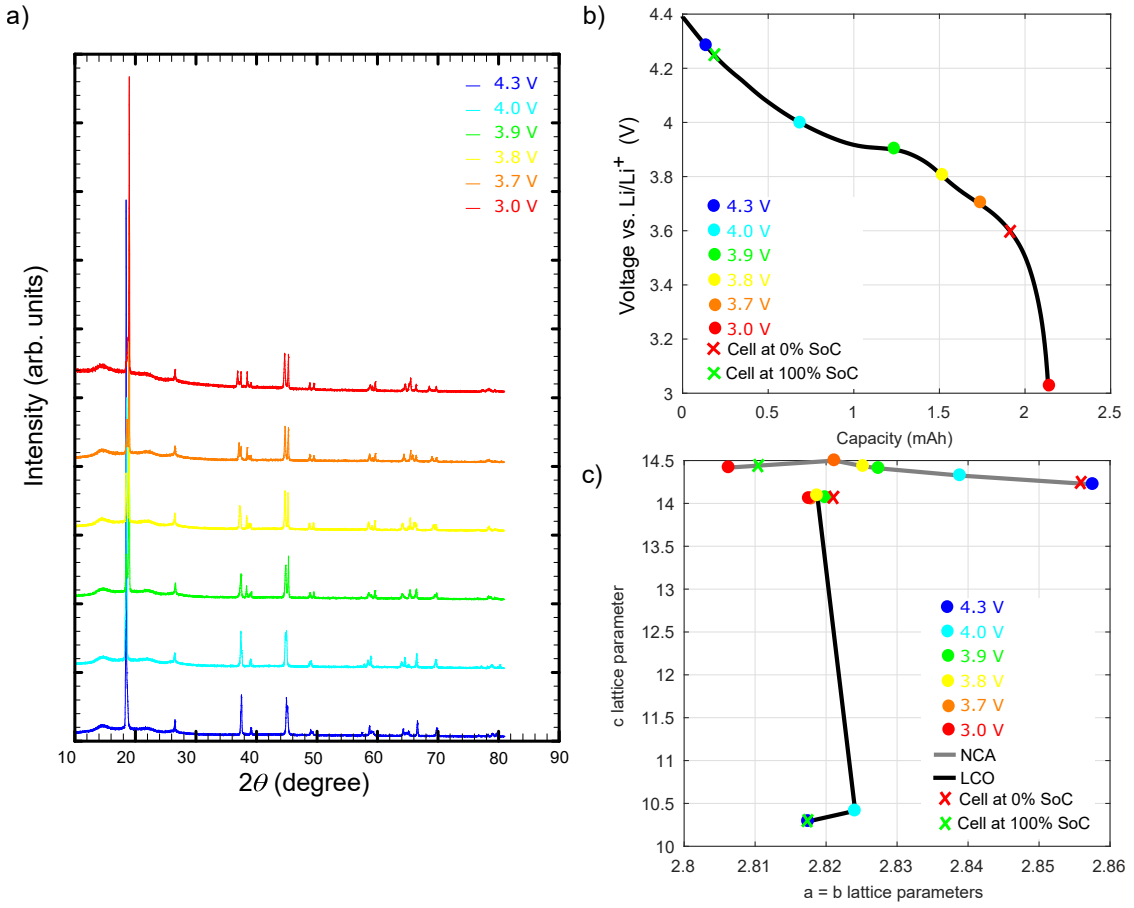

Figure 3.36: a) XRD diffractograms at different opening voltages for the positive electrode; b) Experimental C/30 curve at 25 °C showing the 0 and 100% of SoCs and the opening points; c) Lattice parameters of the positive electrode (two phase material) analysed with LeBail profile matching.

The consideration of uncertainty of model parameters in a real application is a non-trivial issue. Not only parameter uncertainty (cell-to-cell variability and measurement repeatability), but also assumptions taken from the electrochemical model itself (because equations does not describe the desired phenomena 100% accurately) should also be discussed. Due to these reasons when considering a real system, the uncertainties and inaccuracies need to be somehow handled. Different types of methods are reported in the literature, but Kalman filters are the most extensively used method [166]. These feedback-based algorithms seek to somehow tune the model to fit the observed behaviour, based on the assumption that the inaccuracies and uncertainties follow a statistic distribution. Thus, the errors introduced by the model (where both, parametric and model error) can be contemplated. These filters are able to give a more accurate prediction based on the

expectancy of the desired prediction, but more important, are able to give confidence boundaries. These boundaries will give insight on how precise the prediction could be, and allow to adopt conservative or optimistic predictions, based on use of those.

3.7 CONCLUSIONS

Obtaining a consistent set of parameters is essential to effectively evaluate battery performance by means of electrochemical modelling. Therefore, a complete physico-chemical methodology to measure all the necessary parameters for a pseudo-two-dimensional (P2D) electrochemical model is provided. In this work, a guideline for classifying and selection of the experimental techniques to measure model parameters is proposed. Several specific contributions were also proposed from the previous methodologies which are: 1) The identification of a blend positive electrode composed of LCO and NCA based on EDS mapping; 2) The ratio determination between LCO and NCA based on ICP-OES measurements; 3) The estimation of the formulation of both electrodes based on TGA measurements; 4) The electrolyte concentration estimation, even if no liquid was recovered, based on weighting and volume measurements; 5) The electrolyte composition determination based on GC-MS and NMR measurements; 6) The elucidation of the coherence between the experimental and simulated the specific surface area; 7) The measurement of separator properties; and 8) Electrode balancing determination based on reconstructed half and full cells and the commercial full-cell measurements.

The response to different tests performed in pouch cells were compared with model predictions in order to determine the accuracy of the parameter measurement methodology. This methodology was tested at the beginning of life of a commercial battery although it is also valid for ageing evolution analysis.

First, galvanostatic charge-discharge processes at low current rates and 25 ºC were selected for balancing proof determination. The composition and ratio of active materials was determined by means of XRD and TGA, which reduce the theoretical capacity calculation deviation and allowed us to identify that the positive electrode has a blend composition of LCO and NCA. Electrode balancing was assessed with a method accounting for lithium loss of the positive electrode during the SEI formation, and negative excess of capacity for lithium plating prevention. A maximum voltage deviation of 10.75 mV or 0.36% was reported for this methodology. The experimental-simulation comparison is in good agreement at low galvanostatic current rates.

Then, galvanostatic tests at different current rates and temperatures were compared to voltage predictions. The maximum voltage deviation was found at high current rates and high temperatures. Furthermore, to check the dynamic behaviour of the cells and the accuracy of thermodynamic, kinetic and transport parameters HPPC pulse testing and impedance spectroscopy tests were employed. Good correlation between experimental and numerical results were obtained in pulse tests. Larger deviations are presented in impedance spectra which could be attributed to the positive blend material, electrolyte uncertainty or oversimplification of the model. It is worth mentioning that, although real porous structures present particle and pore size distributions, the model only accounts for averaged porous properties. In addition, the model assumes spherical particles, although graphite is flake-shaped. The model accuracy could be enhanced adding complex 3D structures, but this leads to an increase in computational time.

Internal variables of the model (electrode potentials, electrolyte potential, electrolyte concentration and active material lithiation) provide valuable information about the limitations of the cell at the analysed conditions. At high rates, the solid diffusion coefficient and the reaction rate are key parameters, which limit the fast charging ability of electrodes. Moreover, at 1C discharge, the initial concentration of the electrolyte is sufficient to prevent depletion of the lithium ions in the parts closest to the current collectors, in which the electrolyte concentration is lower. The electrolyte salt and solvent ratio were determined by means of NMR and GC-MS, so as to perform all the characterisation tests with a similar electrolyte. However, the low amount of electrolyte of the commercial cells available for these tests hindered accurate electrolyte characterization, which could affect into the model predictions.

Finally, invasive tests (three electrode cell and *ex-situ* XRD measurements) were performed to provide more information about the internal variables of the cell. The three-electrode experimental cell is in good agreement with the numerical results of the cell. This validation confirms the model ability to monitor negative electrode potential (which is useful to study lithium plating). Moreover, a calibration curve of the lattice parameters of the positive active materials by means of *ex-situ* XRD allow us to decouple experimentally the contribution of each blend material phase at different analysed voltages. These calibration curves were used to place the cell maximum and minimum SoCs (0% SoC and 100% SoC of the pouch cells), and thus providing additional information of the lithiation evolution of both materials (LCO and NCA).

Parameters estimation uncertainty in terms of cell-to-cell variation, even if crucial to keep the estimations accuracy, is a difficult task to undertake due to the difficulty of measuring large sets of samples. Due to the laboratory time consuming experiments, from a practical point of view is not feasible to conduct such analysis to obtain a Gaussian distribution to assess the maximum parametric variability of cells. The maximum dispersion between tested cells at full cell level were found to be 1.328 ± 0.025 Ah and 38.8 ± 9 mΩ in capacity and resistance, respectively. Those variabilities in the effects of cell performance (capacity and internal resistance) can be linked to the contribution of each parameter, not only at the beginning of life of the batteries, but also during operation until the end of life. For that, Kalman filters are a good alternative to deal with cell-to-cell variation to take into account the parametric and model uncertainties. Prediction errors can be improved to some extent when applying these statistic-based algorithms. Furthermore, uncertainty boundaries are provided, so confidence boundaries can be obtained to cope with model inaccuracies, sensing errors and parameters induced uncertainties.

Moreover, to determine the variability of each parameter, the physico-chemical parameter measurement procedure proposed in this research could be combined with parameter identification methods. This mixed methods (combinations between experimental and optimisations) could give an insight about the parametric variability between cells and thus give the dispersion between cells.

Chapter 4

NCA AND GRAPHITE PROTOTYPED HALF-CELL MODELS ACCOUNTING FOR PROCESS RELATIONSHIPS

This chapter presents the methodology and validation followed to include process parameters into the electrochemical model. In Figure 4.1 the workflow of this chapter and the links with the full structure of the thesis is presented.

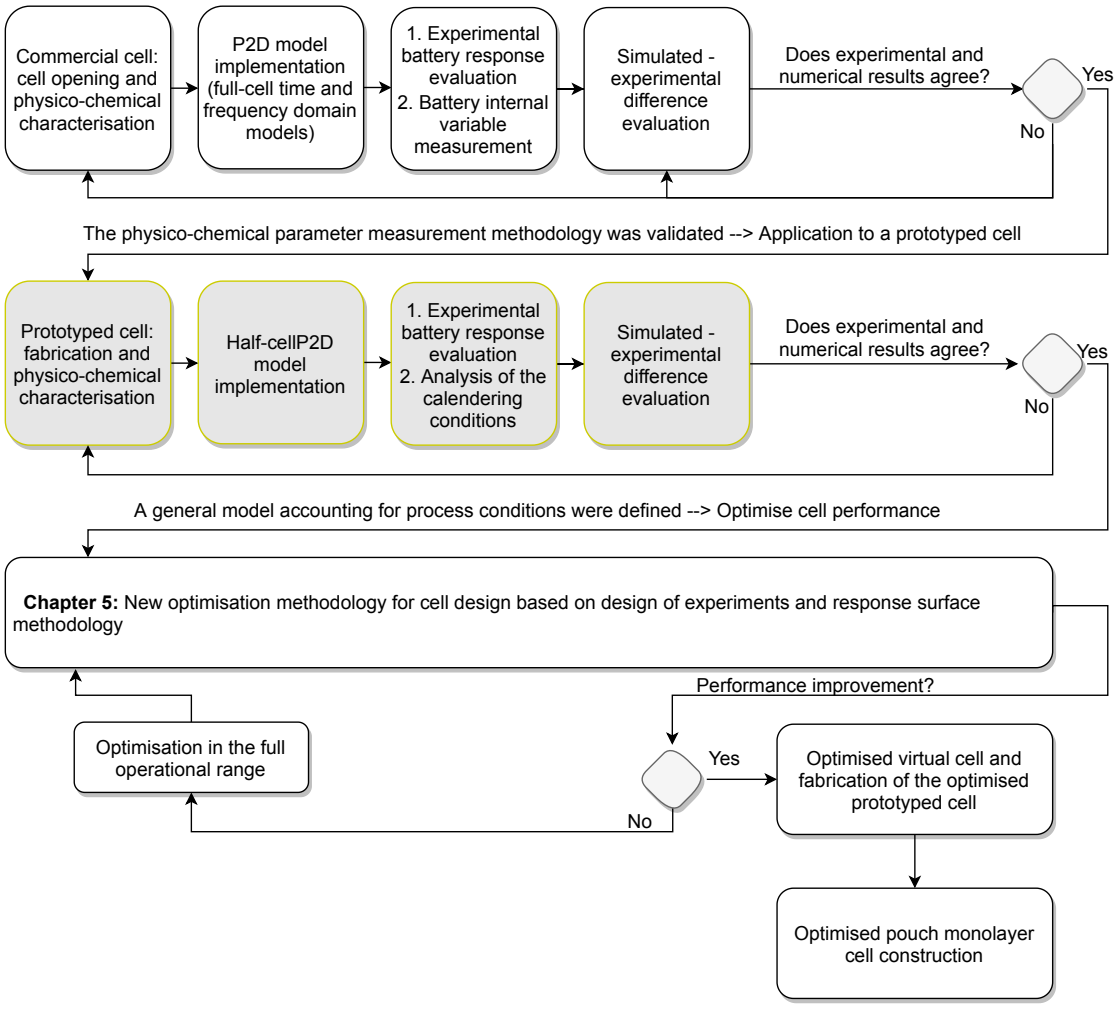

Figure 4.1: Main workflow of this research for Chapter 4.

4.1 STATE OF THE ART IN THE BATTERY FABRICATION PROCESS

In the following subsections a review of all the fabrication steps is set out, dividing the analysis into two: (1) Material processing stage before calendering step (subsection 4.1.1) and (2) Calendering step (subsection 4.1.2). The aim of this review is to identify the processing materials and techniques, the process parameters, the transformed or modified physical properties, and the characterisation techniques.

4.1.1 Material processing stage before calendering step

In Figure 4.2 the steps of the material processing stage are presented together with the input materials and their associated system level. In this subsection mixing, coating and drying processes are further explained.

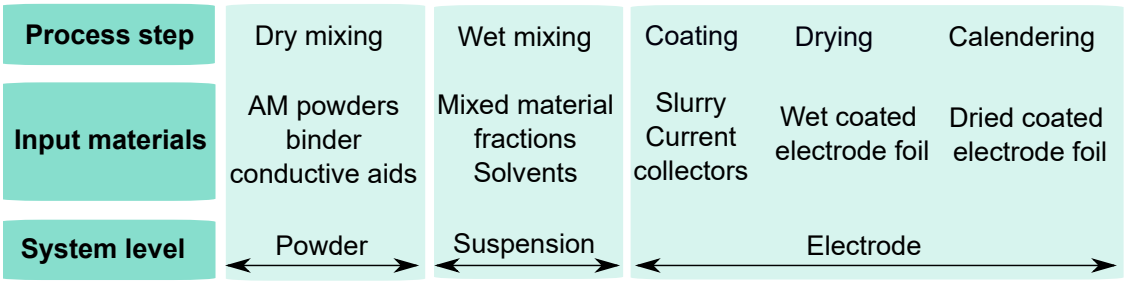

Figure 4.2: Material processing stage. Based on [47].

4.1.1.1 *Mixing step: from powder to slurry*

The objective of this step is to obtain a homogeneous slurry based on active material solid particles, conductive additives, binder, surfactant, and solvent. The main requirements are the deagglomeration of the components, the proper formation of an electrically conductive network (homogeneous morphology), and the proper slurry conditions for the next step of fabrication (coating) [167]. In Figure 4.3 a general schema of this process is summarised.

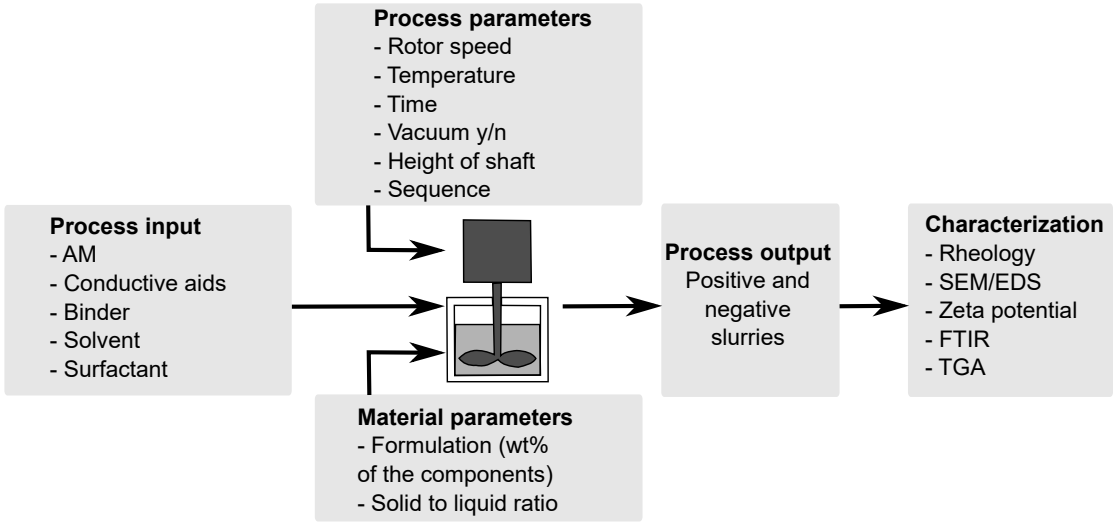

Figure 4.3: Mixing step.

The mixing step is dependent on the selected raw materials and ratios, process sequence (one or multi-step processing) and type of mixing devices. The raw materials are transformed from solid particles with inherent characteristics (particle size distribution, electronic conductivity of powders, bulk density, specific surface area, wettability, and flow behaviour etc.) into fluid suspension (slurry) [47]. In the case of lithium-ion battery electrodes, PVDF binder, NMP solvent and carbon black conductive additive are commonly used. However, with the aim of reducing environmental impact, water based binders (CMC and SBR) are becoming more common. Some of the widely used active materials are graphite or LTO for the negative electrode and LMO, LCO, NCA, LFP and NMC for the positive active material.

Different mixing and dispersion equipment is used in laboratories as compared to industry due to economies of scale. Ball milling and magnetic stirrers optionally followed by a sonication step are used for laboratory tests, whereas planetary ball milling, high-speed mixers, homogenizers, high intensity submersible horns, and high-shear rotor mixers are required for industry [168]. In order to determine the influence of the different equipment and sequences, several studies have been done. Liu et al. [168] compared and proposed a new machine for the mixing step, concluding that a good quality mixing process of negative electrodes could be achieved using a single turbine mixer. In contrast, in the positive electrode, a specific multi-stage mixing scheme in a three-dimensional mixer was selected as the best mixing option [168]. In fact, not only does the mixing device affect the final properties of the slurry, but also the mixing sequence has to be studied. So as to transform the solid particles into slurry, different formulations and mixing sequences have been proposed in the literature [169–171]. Ponrouch et al. [169] studied different slurry mixing procedures, concluding that ball milling can significantly modify AM microstructure, reducing cell electrochemical performance. They proposed a sonication step as a method to destroy agglomerates, thereby preserving the microstructure of the electrodes [169]. Bockholt et al. [171] analysed different dry mixing procedures while maintaining the same dispersing (wet mixing), coating, drying and calendering procedures to analyse the electrochemical properties of the cells. Kwade and Haselrieder [47] and Haselrieder et al. [170] also studied different mixing sequences with or without a dry mixing step.

Different operating parameters need to be defined depending on the device used. These are mainly rotor speed, temperature of the mixture, solid concentration, processing time, height of the shaft and vacuum. The final properties of the slurry are highly dependent on those parameters and the mixture sequence [93].

Once the mixing process step is finished, the transformed or modified physical properties are analysed by means of different techniques. If an inadequate mixing is selected, conductive additives are not homogeneously distributed and thus, agglomerates will reduce the final cell performance of the device. In a realistic case, deagglomeration and dispersion of the conducting additive phenomena occurs simultaneously. Ideally, a conductive additive film covers the entire surface of the active materials increasing the amount of primary electronic pathways, leading to a smaller porosity and higher homogeneity [167]. A homogeneous distribution of active material and conductive additive particles in the solvent is desired. However, some problems could arise such as coagulation or sedimentation [172]. Decreasing the solvent concentration, particle volume fraction and yield stress increases. However, below the optimal solvent quantity, the obtained slurry characteristics are poor (low discharge capacity and poor homogeneity) [172].

The final state of the slurry affects greatly the micro-structure of the final electrode and the following coating process. Therefore, the rheological behaviour of the slurry should be optimised to obtain a stable state without sedimentation, as well as a proper viscosity. The stability is increased with the increase of viscosity, as particle mobility is reduced. However, at high viscosities, low shear rates should be used to avoid coating defects [173]. Other studies are focused on the conductive additives and binder ratio as a critical parameter to optimise the interfacial resistance of the electrodes [174]. Overall, the concentration of the binder should be maintained as low as possible, while providing a good electrode integrity, as high binder concentrations may deteriorate the performance of the cell [168].

The quality of the slurry plays an important role as it directly impacts the remaining manufacturing steps. Different characterisation techniques can be found in the literature [47,173,175]. Some of the works present specific techniques for validation of the mixing step, whereas others use characterisation techniques in subsequent steps, maintaining the coating, drying and calendering processes parameters constant.

Slurries can be characterised using different techniques. One such technique is scanning electron microscopy coupled with EDS detector (SEM-EDS). As the samples are in suspension mode, cryogenic preparation must be conducted, in which samples should first be frozen in liquid nitrogen. Then, the EDS detector can be used to map the composition of the slurries [176]. On the other hand, rheological studies have been widely reported in the literature [168, 172, 173] and are used to investigate the particle dispersion and the different structures of the slurry. Rheological properties such as viscosity and shear stress as a function of shear rate are usually analysed for different mixing process conditions [47,176]. Moreover, the zeta potential as a function of the pH of the sample is presented as a good indicator of slurry stability, especially in aqueous slurries and as a technique for solvent selection [173]. Techniques such as TGA, FTIR and electronic conductivity measurements can also be used as methods for identifying the variation of slurries [176].

4.1.1.2 *Coating and drying: from slurry to dry electrode film*

Coating and drying steps consist of transforming the slurry of both electrodes into a dry electrode deposited on a current collector (see Figure 4.4).

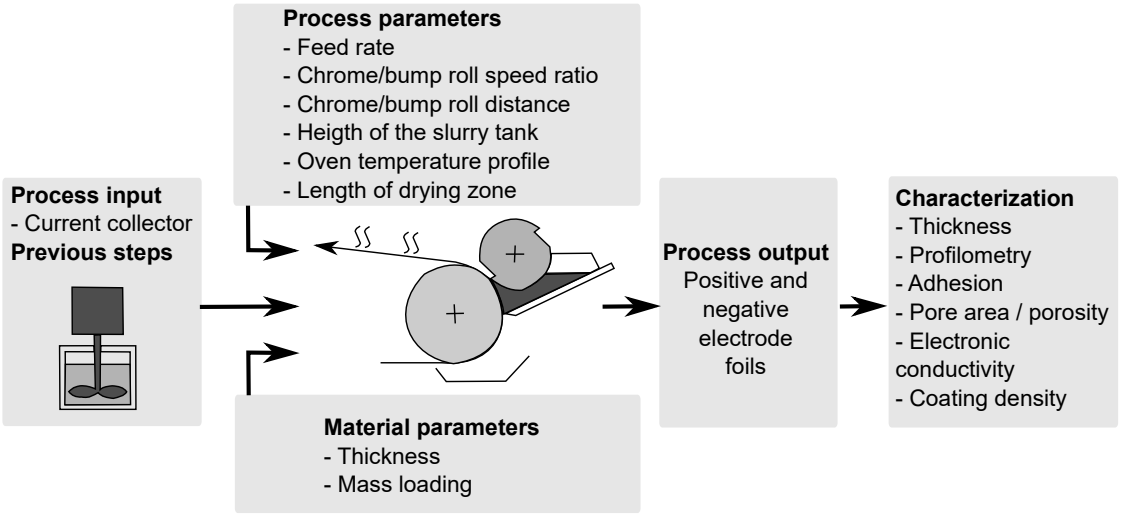

Figure 4.4: Electrode coating and drying steps.

The raw materials for the coating step consist of the slurry coming from the mixing step and current collector foils (copper or aluminium foils of 10 to 20 µm). In the drying step there is no additional raw material as the coated electrode is only transformed.

In the coating process, the slurry is deposited on the current collector and becomes a wet film layer. Defects such as pinholes, divots, agglomerates and ribbons can appear if the process parameters are not adjusted properly [173]. Different types of coating equipment can be found in the literature [47]. In Figure 4.5 the commonly used coating techniques at different scales are presented.

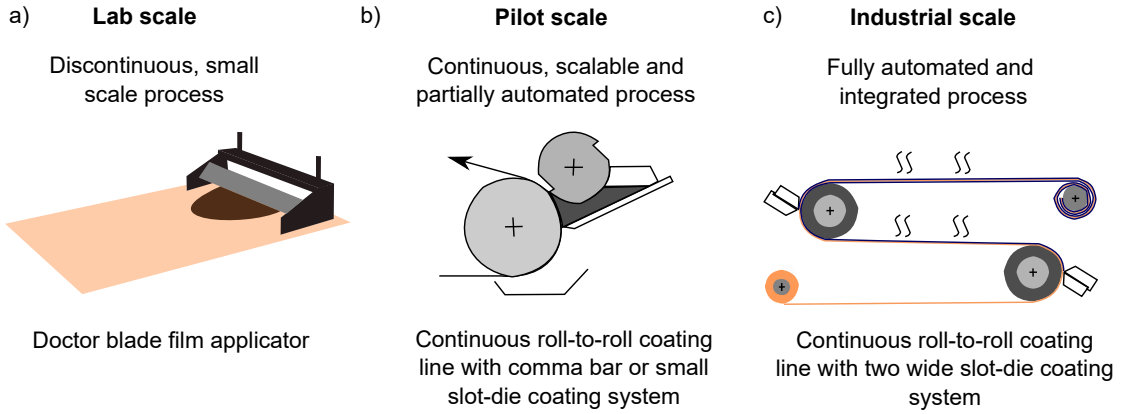

Figure 4.5: Coating step scalability: a) Laboratory scale; b) Pilot scale; c) Industrial scale. Based on [47].

At the laboratory scale (small scale) a micrometer adjustable film applicator is generally used, which is a discontinuous step. In this step a constant relative movement is applied to spread the slurry homogeneously on the current collector. Thin wet coating sheets are created with thicknesses from 20 to hundreds of microns [177]. In the pilot scale, systems such as continuous roll-to-roll coaters with comma bar or small slot-die coating systems are found, which are partially automated. In this step, the slurry is first poured into a container, and the current collector is placed in between all the metallic cylinders of the system. Then, the cylinders start to rotate. The gap between the container and the chrome-roll cylinder allows the deposition of the slurry onto the current collector. Afterwards, when the layer is in contact with the next cylinder, mass transference occurs [178]. Further information about different coating techniques can be found in [179]. At an industrial scale, completely automated and integrated systems are found. For this reason continuous systems which enable double-side coatings are implemented. However, simultaneous two-sided coating can lead to structural variations between the two coating layers, and thereby decrementing the capacity of the cell. Therefore, tandem coating is widely used in industry [47].

Slot-die coating systems have been investigated in depth, for example in the work of Schmitt [180], in which process windows and minimisation of edge effects to decrease defective rates and high-speed intermittent coatings are studied. The main operational parameters are the feed rate (defined for both coating and drying steps), chrome roll to bump roll speed ratio, chrome roll to bump roll distance, and height of the slurry tank.

During the drying process, the coated electrodes are passed through an oven of approximately 100 °C to evaporate the solvent. In Figure 4.6 the complete steps during drying process are presented. Starting from a homogeneous film (a), the solvent starts to evaporate, inducing film shrinkage of the initially wet layer (b). When the film shrinkage

terminates, the particles obtain their most dense packing (c). Then, the liquid phase recedes into the porous structure, (d) and when the solvent is completely evaporated the dry electrode is obtained (e) [181]. The main operational parameters of this process are oven temperature, length of the drying zone, and feed-rate (the same as the coating step).

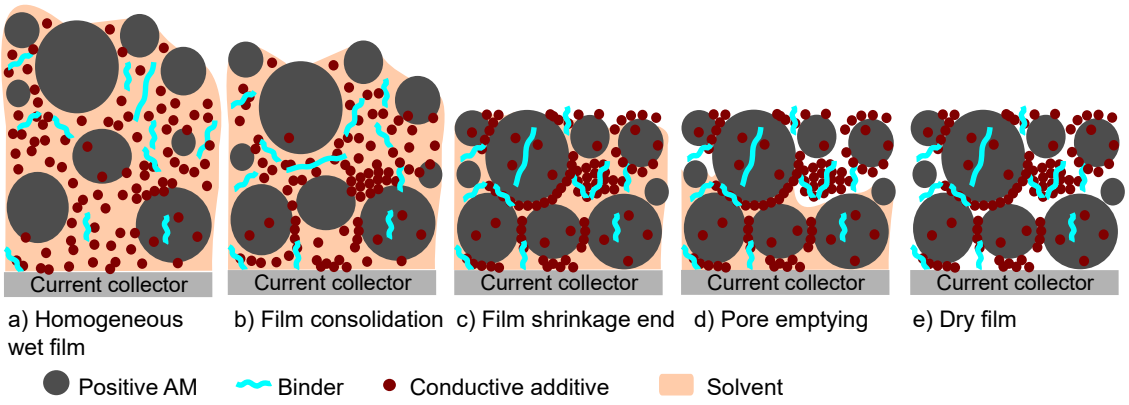

Figure 4.6: Schematic of drying phases from homogeneous wet film to dry film. Based on [181].

During those steps, material characteristics are modified, such as wet and dry thickness, adhesion strength, roughness, porosity, tortuosity, specific surface area, electronic conductivity and solid diffusivity. These parameters are classified into porous structure, and transport and kinetic parameters.

As regards, porous structure parameters, the topography of electrodes can be analysed to determine the homogeneity of the whole electrode [182]. Confocal profilometry can be used before and after the calendering process to determine the infuence of this step. Additionally, SEM techniques can provide an image of the homogeneity of the electrode [94]. Kwade et al. [47] studied five drying conditions and the adhesion strength for a graphite electrode. They concluded that, depending on the current collector supplier, the adhesion of slurry also varies leading to different electronic conductivity values [47]. Jaiser et al. [94] took a reference set of process parameters and tested some variations (increase in initial solvent volume fraction, dry film thickness, binder concentration, drying rate and decrease of graphite particle size) to study their influence on dry film porosity and void volume fraction. An increase of drying rate from 1.2 to 1.8 g m^{-2} s^{-1} led to an increase of the solvent volume fraction, and smaller graphite particles decreased both porosity (from 0.58-0.60 to 0.48) and void volume fractions, whereas the remaining variations had no influence [94]. They concluded that, for this specific case, only drying rate and particle radius affects the dry film porosity and void volume fraction. Additional characterisation can be performed to study the particle micro and nano structures (particle size distribution, pore size distribution, morphology of particles) which also influence the response of the cell and the coating and drying steps [47].

As for transport and kinetic parameters, e.g. electronic conductivity can be measured. This parameter is also influenced by the drying temperature and mass loading of the electrodes [183]. In order to reduce the drying zone (and drying time) electrodes should be thin (lower solvent mass, less time to dry) [94]. In that study, at low mass loadings of graphite electrode (3.5 and 5.4 mg cm^{-2}) the drying temperature has a minimal impact on the resistance due to the low solvent amount and the fast structure immobilization [183]. In contrast, in electrodes with high mass loadings (10.5 mg cm^{-2}), an increase of drying temperature results in a resistance increase [183]. Resistance increase can occur due to

the demixing of the electrode [184], the stress, and inhomogeneous distributions that are caused by the temperature increase during the drying process. Nevertheless, in industry it is difficult to reduce oven temperature as it decreases the efficiency of the whole process [173].

The step characterisation techniques which can be used after the coating and drying steps are the same as those used after the calendering process. A. Kwade and W. Haselrieder [47] provide a review of characterisation techniques for fabrication process validation. T. Waldmann et al. [141] presented an extended overview of post-mortem physico-chemical analysis techniques. The techniques that are generally used in the literature are set out in Figure 4.7. These techniques have been classified into three groups: physico-chemical, structural/mechanical, and electrical/electrochemical characterisation techniques. More detailed information about the different techniques can be found in [38,56,61,136,141,182].

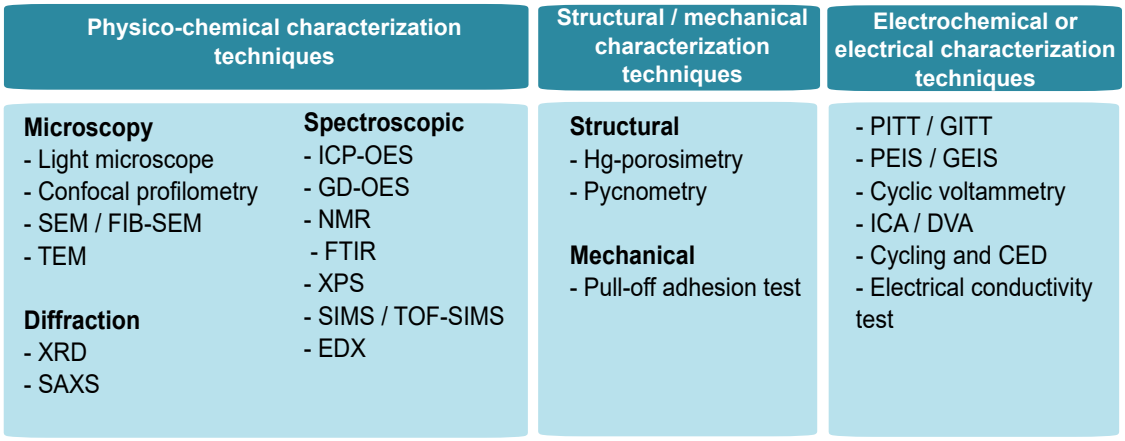

Figure 4.7: Electrode characterisation techniques. Based on [47, 141].

4.1.2 Calendering process

The battery manufacturing process continues with the electrode compaction. In Figure 4.8 the roll-pressing process is shown.

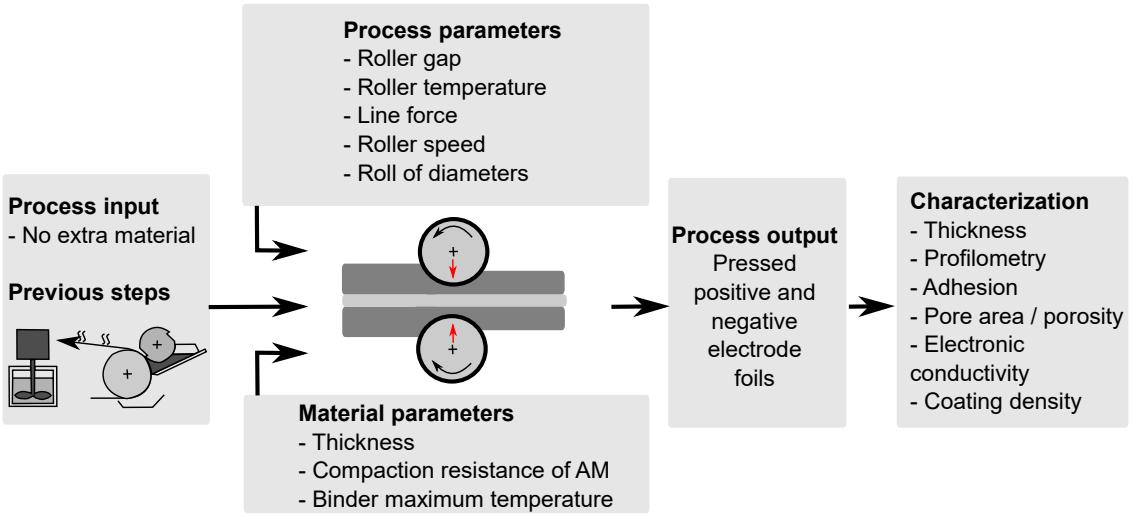

Figure 4.8: Calendering step.

The aim of this step is to reduce the inhomogeneities resulting from the previous steps, improve the electric contact (adhesion between active material and current collector), and find a good porosity value. As cathode materials are ceramic (LCO, LMO, NMC, LFP), which are hard and strong in compression, particles are maintained with a spherical shape. Nevertheless, graphite undergoes plastic deformation when pressure is applied deforming into particles of an elliptical shape. The process parameters of this step are the roller gap (thickness between cylinders), roller temperature, line force, roller speed and the repetitions in which the process is performed. If the pressure exceeds the operational limits, the electrode transport (ionic and electronic transport) will be reduced [47].

During the calendering step, different phases are identified (see Figure 4.9). From the non-calendered electrode (P0), a rearrangement of particles occurs (P1). Then, particles suffer from elastic and plastic deformation (P2). Finally, particle fragmentation occurs (P3). When the calendering induced force is removed, an increase in electrode porosity and thickness occurs due to elastic recovery (P4).

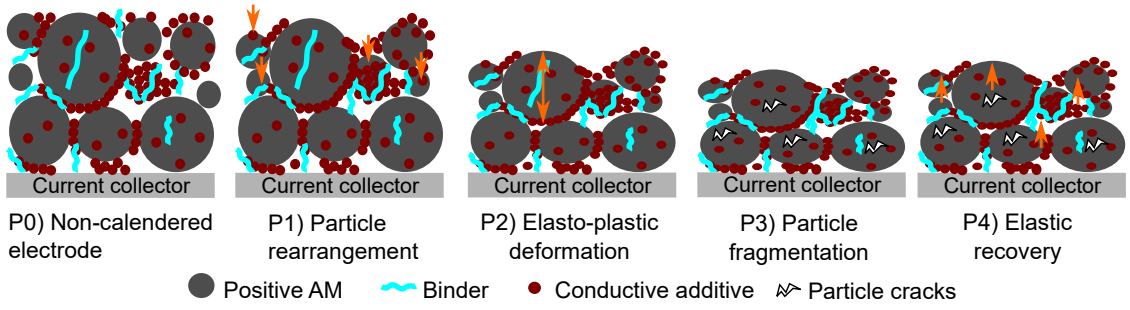

Figure 4.9: Calendering compression phases. Based on [185, 186].

The properties that are modified and the characterisation techniques used in this process are the same that can be used after the coating/drying process (see Figure 4.7).

An overview of the experimental and numerical optimisations that are available in the literature are analysed in the following subsections. At present, there are few studies that focus on calendering step optimisation using experimental and numerical approaches [93, 95, 185, 186].

4.1.2.1 *Experimental studies of the calendering process*

Nowadays, widespread trial-error experiments are used to define material and process limits, and determine the optimal solution for specific materials and process conditions. This is a critical step which established the relationships between cell and process parameters. However, only a finite number of experiments can be done, as this process is costly and time consuming.

This review helps to define the target electrode properties that are normally searched, the control variables, the main constraints of the process or materials, and the characterisation techniques that can be used for verification. The calendering step is affected by the preceding steps (mixing, coating and drying), as well as the raw material used (type of active materials, binder and additives). In addition, process constraints need to be considered (available equipment, adjustable process parameters etc.).

First of all, the differences between acceptable and rejected calendered electrodes should be defined. Some of the process outputs can be defective due to excessive applied pressure,

the previous steps, or the materials used [185]. These should be identified and classified in order to gain insight into the calendering process. Understanding the cause of these defects it is of great importance, because they can have detrimental effects on the final performance or the cell. The main defects of the calendering process are identified by Gunter et al. [185] and presented in Figure 4.10.

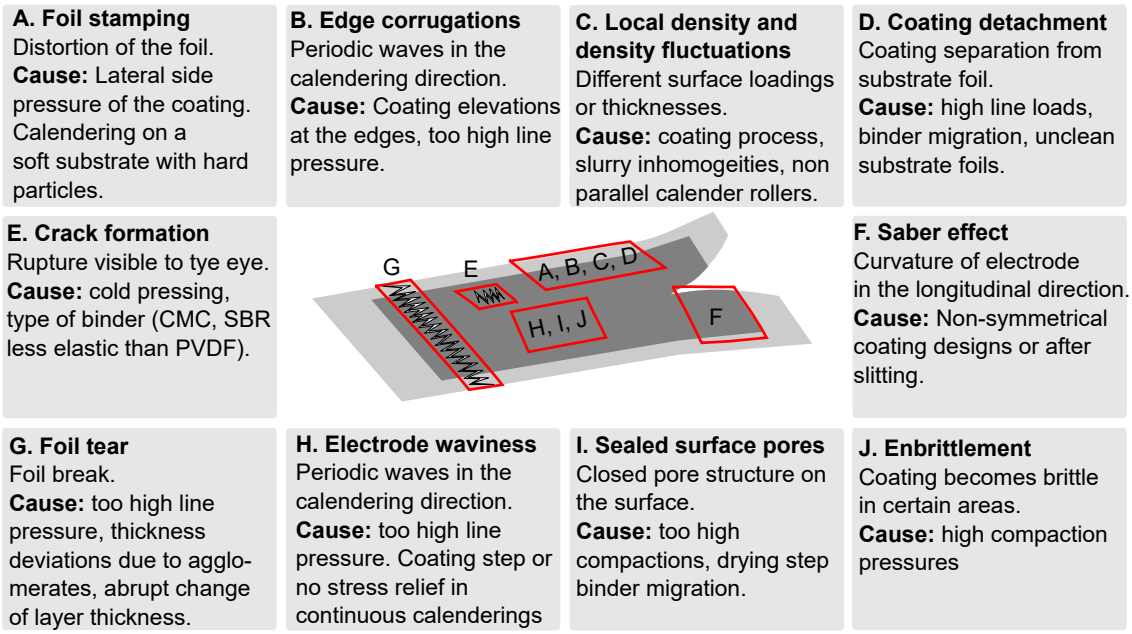

Figure 4.10: Main defects of the calendering step. Based on [185].

Even if the calendering step is defect free, the electrodes may still not have optimum properties. Thus, there is a need to adapt the process parameters to each material, formulation, mass loading etc. to obtain the best cell performance.

An example of property modification due to calendering is presented by Kwade et al. for an NMC positive electrode [47]. They analysed the particle distribution change due to the different compression ratios, and found a bimodal distribution of particles, and a shift to small pore and void volumes in both peaks when the compression rate increased. They observed that if the porosity is too high, the electronic conductivity decreases. In contrast, if the porosity is too low, the electrolyte cannot wet all the electrode, and thus the electrochemical reaction does not take part in that area (lower surface area). They also found an operating range between 5 to 10 rate of compression (which corresponds to 50 to 150 N mm^{-1} of line distributed load, for those studied conditions), in which an optimal porosity is obtained to reduce the electron and ion transport limitations. They concluded that diffusion limitations occurred due to porosity reduction [47]. Changing the structure of the electrodes modifies ion and electron transport through the electrodes which affects to the final cell performance.

For the negative electrode, Froboese et al. [162] studied different calendering conditions for 90 wt% of graphite (C-Nergy KS6L), 5 wt% of CMC, and 5 wt% of conductive carbon black (C-energy Super C65). Five compression rates were presented in which from 20% to 31% the entire pore structure was compacted without particle cracking. In Figure 4.11 common raw materials for lithium-ion batteries, process parameters and expected best performance conditions are presented.

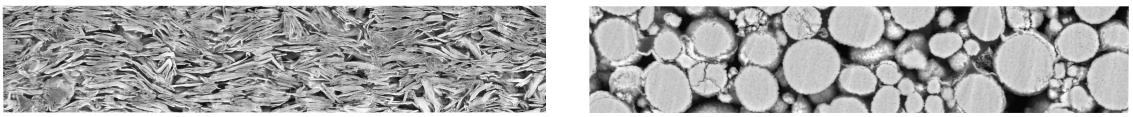

Raw materials: graphite with PVDF, SBR, CMC, C45, C65

Raw materials: LPF, NMC111, NMC622, NMC811, NCA, blended materials, LMO with PVDF, C65

Process parameters: Line load max. depending on the machine up to 1500 N mm^{-1}, T_{roll} = 25 - 150 ºC, roller gap depending on the AM compresion resistance and mass loading, roller speed (2 - 5 m min^{-1})

Performance: higher compression rates than 31% particle crack appear

Performance: compression rates between 5 to 10% decrease transport limitations

Figure 4.11: Positive and negative calendering step: Common raw materials, process parameters and expected best performance conditions. Based on [47, 86, 96, 97, 162].

In order to optimise experimentally the calendering process, Halselrieder [93] and Meyer et al. [86, 95–97] presented an exponential relationship to relate the pressure needed to plastically deform the coating with the process conditions (roller temperature and gap) and the obtained density or porosity after the calendering step. Different active materials were analysed and their compaction resistance characterised. Moreover, the roller speed was found to have little influence. The obtained relationship is (equation 4.1):

$$\varepsilon_{e,cal} = \varepsilon_{e,min} + (\varepsilon_{e,dry} - \varepsilon_{e,min}))e^{\frac{-q_L}{(\mu_0 - \xi T_{roll})M_{L,dry}}} \tag{4.1}$$

where $\varepsilon_{e,cal}$ is the calendered coating porosity, $\varepsilon_{e,min}$ is the minimum achievable porosity, $\varepsilon_{e,dry}$ is the initial (dry) coating porosity, q_L is the applied line load (which is calculated dividing the rolling force (F_N) by the coating width (L)), μ_0 is the compaction resistance at 0 °C, ξ is the temperature correction factor, T_{roll} is the applied roller temperature, and $M_{L,dry}$ is the mass loading of the electrode.

Additionally, Schreiner et al. [98] proposed a correlation between machine, material, process and structure.

4.1.2.2 *Simulated aided optimisation of the calendering process*

With aim of reducing the time and costs associated with experimental procedures, the Battery 2023+ Roadmap, has identified multiphysic and multiscale model enhancements to perform inverse cell design. A further benefit of modelling is that it provides additional information for electrode optimisation [186]. Two different approaches can be followed to model the calendering process: virtual cell design including cell to process relationship, or virtual manufacturing (simulating the process itself).

On the one hand, in the virtual cell design approach, some works have been proposed. Lenze et al. [89] introduced a P2D model to study cell performance differences between a non-calendered and 22% calendered positive electrode. They combined experimental characterisation methods with simulations for that purpose. They included the calendering influence with a calendering dependent factor in the specific surface area (equation 4.2).

$$a_{s,cal} = a_s \lambda_{cal} \tag{4.2}$$

where $a_{s,cal}$ is the specific surface area accounting for calendering variations, a_s is the original specific surface area, and λ_{cal} is the calendering dependent factor.

Moreover, they established two parameter groups: calendering dependent and independent. The calendering dependent parameters were measured (electrode thickness), calculated (porosity and solid volume fractions) or fitted (electronic conductivity, ionic conductivity and the calendering dependent factor) for each calendering condition. The model was validated against galvanostatic discharge curves at different current rates. To our knowledge, is the first model considering calendering effects in the final cell performance, fitting of a certain calendering condition was performed. However, a direct engineering problem was stated as some parameters are obtained by model fitting. In order to enhance the models, cell to process parameter relationships should be included so as to gain insight into the optimal process parameters to apply for the targeted electrode properties. Experimental relationships as proposed by Meyer et al. [86, 95–97] could be included in the model to establish a calendering to cell relationship. Mixing, coating, drying and calendering relationships have been included by Schmidt et al [99] to study the uncertainties of the fabrication process of batteries. Moreover, the work of Lenze et al. [89] has been improved by modifying the P2D original microscale model to represent carbon black and binder effect [18, 187].

On the other hand, the virtual manufacturing approach aims to simulate the calendering process itself. The compressibility of the electrodes has been studied by some authors [186, 188–190]. Wang et al. [188] studied the compressibility of lithium-ion negative electrodes (graphite particles). Then, Ott et al. [189] investigated porous electrode structures with two types of particles: spherical particles (describing AM particles) and small particles (for carbon black particles). Discrete element modelling (DEM) was used to densify the microstructure of the electrodes using the Hertz contact model. Kespe et al. [190] developed a three dimensional microscale half-cell model to describe spherical AM particles under different compressions. Sangros et al. [186] modelled the calendering process with FEM to see the effect of elastic recovery (which cannot be determined experimentally).

4.2 PROTOTYPED CELL FABRICATION PROCESS

In this thesis, CIC energiGUNE centre facilities were used for the experimental research of energy storage systems. The electrode fabrication process is shown in Figure 4.12[1].

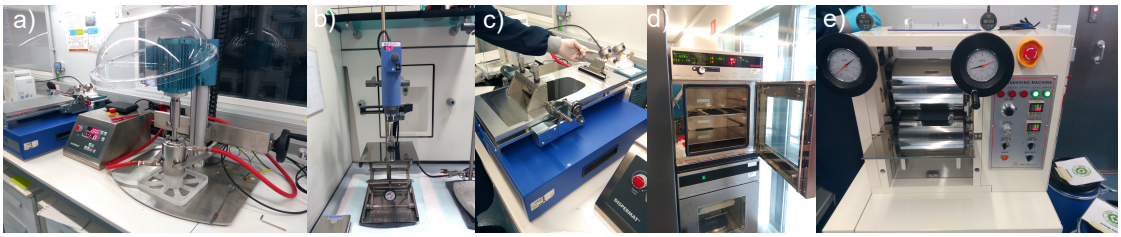

Figure 4.12: Equipment and fabrication process: a) Mixing equipment used for the positive electrode; b) Mixing equipment used for the negative electrode; c) Coater; d) Vacuum oven; e) Calendering machine.

The positive electrode[2] was fabricated inside a dry room as the formulation selected is non-aqueous. In the mixing step Dissolver DISPERMAT® LC30 (VMA Getzmann) was employed (see Figure 4.12 a)). The negative electrode[3] formulation is aqueous. The mixing

[1] The formulation of both electrodes and fabrication procedure was provided by CIC energiGUNE.
[2] Positive electrode fabrication was conducted by Guillermo Liendo.
[3] Negative electrode fabrication was carried out by the author with help of Silvia Martín and Alvaro Herrán.

equipment used was IKA stirrer T25 Ultra Turrax shown in Figure 4.12 b). The coating was performed with a K Control Coater (RK PrintCoat Instruments) coupled to a micrometer adjustable film applicator (see Figure 4.12 c)). All the coatings were dried in a vacuum oven (see Figure 4.12 d)). Finally, the Mediatech calender machine was employed for electrode pressing (see Figure 4.12 e)).

The raw materials used for this thesis are listed in Table 4.1. The same electrolyte and separator used for coin cell reconstruction of the commercial cell were used for the prototyped cells. A trilayer (PP/PE/PP) separator was used for the pouch monolayer cells in Chapter 5.

Table 4.1: Raw materials of the prototyped cells.

Raw material	Purpose	Brand and reference
NCA powder	AM	Targray
Graphite powder	AM	SFG-15L
Graphite powder	Conductive aid	KS-6L
Carbon black powder	Conductive aid	C45 Imerys
PVDF	Binder	Solvay Solef 5130
CMC	Binder	Solvay
SBR	Binder	Solvay
Glass fibre separator	Separator	Whatman (Grade GF/D)
PP/PE/PP separator	Separator	Celgard 2325
1M $LiPF_6$ in EC:EMC (50:50 v%)	Electrolyte	LP50 (Sigma Aldrich)

In Figure 4.13 the reference sequence for this thesis is presented. There are some process parameters that are highlighted with blue, which represents the variations performed during the process characterisation and optimisation in Chapter 5. In addition to the sequence, the formulation is shown in Figure 4.13.

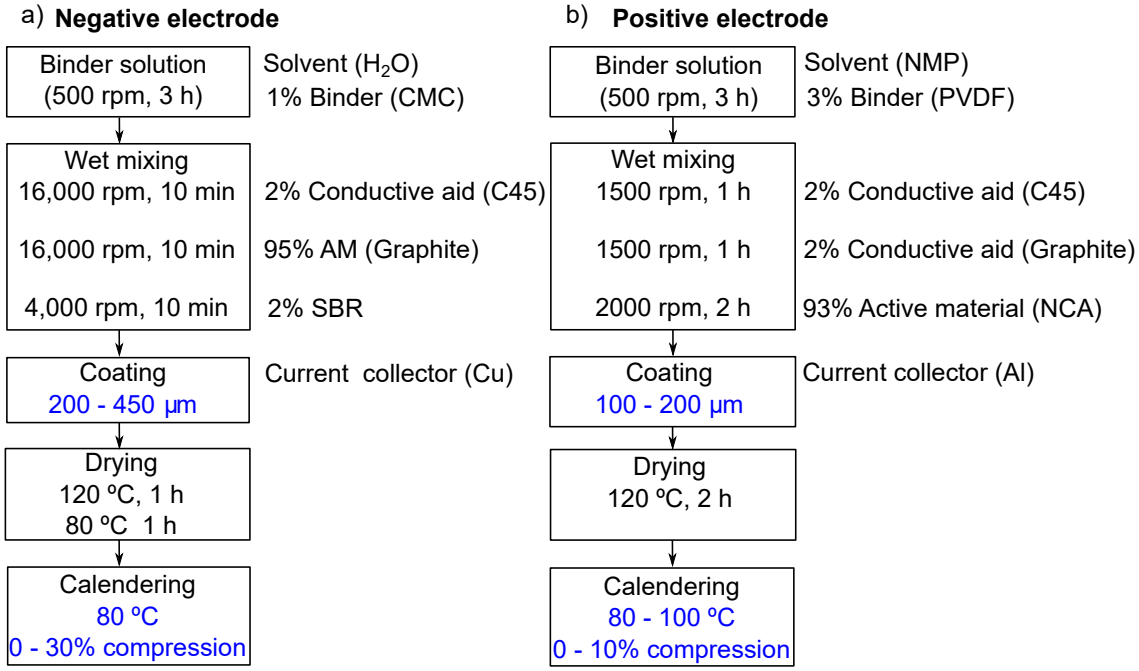

Figure 4.13: Fabrication mixing sequence for a) Negative; b) Positive.

The process parameter ranges are presented in Table 4.2 for the equipment used. Mixing, coating and drying equipment are laboratory scale machines but can be used to obtain material-process-model relationships.

Table 4.2: Equipment process parameter limits.

Equipment	Process parameter		Unit
Dissolver DISPERMAT®	Speed	0 - 20000	rpm
LC30 coupled to a	Tank volume	50 - 1000	ml
temperature control	Dissolver disc	30	mm
bath	Temperature	296.15	K
	Speed	3000 - 25000	rpm
IKA® stirrer T25	Tank volume	10	ml
Ultra Turrax	Dissolver accesory	S 25 N - 10 G	
	Temperature	RT	K
K Control Coater	Coater speed	2 - 15	m min^{-1}
coupled to a	Blade width	100	mm
film applicator	Blade gap	0 - 10	mm (Δ = 10 µm)
	Roller temperature	RT - 423.15	K
Mediatech® calender	Roller diameter	200	mm
machine	Roller speed	0.3 - 2	m min^{-1}
	Max. pressure	50	Tn total $width^{-1}$
	Working width	50 - 150	mm
	Working thickness	50 - 300	µm

4.3 METHODOLOGY AND SAMPLE PREPARATION

Different types of analyses were performed in prototyped cells at powder, suspension, electrode and cell level. An analogue methodology used in the commercial cell of Chapter 3 was employed (see Figure 3.10). The main difference lies in the component composition identification procedure. While in the commercial cells no previous information of components was presented, in the prototyped cells those properties were known. Therefore, techniques that were used in Chapter 3 for component composition identification (SEM-EDX, ICP-OES, TGA, GC-MS, NMR, FTIR) were not necessary. Nevertheless, there are some process characterisation techniques that were included to analyse the materials during the fabrication process of the prototypes (rheology, profilometry and formation cycles).

The viscosity and shear rate of the studied slurries are 51.94 and 1.116 Pa s (measured at 1 shear rate (1 s^{-1}). The viscosity and shear rate affect the deposition of the slurry onto the current collector. In order to prevent dispersions in the mixing process, the same slurry batch was used for all the experiments presented in this chapter. Equation 4.3 describes the solid to liquid ratio (R_{SL}) of the slurry:

$$R_{SL} = \left(\frac{m_{solid}}{m_{solid} + m_{solvent}} \right) 100 \tag{4.3}$$

where m_{solid} represents all the solid materials involved in the mixing process (AM, binder and additives), and $m_{solvent}$ is the solvent weight.

In Table 4.3 the experimental matrix studied in this thesis, based on DOE methodology, is shown, in which different calendering conditions are presented.

Table 4.3: Analysed process conditions of positive and negative materials.

Electrode	AM_{per} (%) (± 0.2)	R_{SL} (%) (± 2)	δ_{blade} (µm) (± 5)	T_{roll} (K) (± 3)	G_{roll} (µm) (± 1)
Positive	93	73.81	200	-	-
	93	73.81	200	80	7
	93	73.81	200	100	7
	93	73.81	200	80	37
	93	73.81	200	100	37
	93	73.81	200	80	57
Negative	95	27.19	450	-	-
	95	27.19	450	80	63.9

In the positive electrode, calendering related parameters (roller gap (G_{roll}) and roller temperature (T_{roll}) were varied. The roller speed was maintained constant throughout this study because it affects the time that the pressure is applied in a determined area. Two factors (G_{roll} and T_{roll}) were studied in a two level full-factorial design to determine interactions between those two parameters. Two additional conditions (non-calendered and minimum gap condition) were studied to provide the initial state and validate the material-process-model relationships. A reference negative electrode was fabricated for full-cell level study. The physico-chemical properties of the abovementioned conditions and the relationships necessary to include process parameters in the model are studied in sections 4.4 and 4.5.

4.4 PHYSICO-CHEMICAL CHARACTERISATION

This section sets out all the parameters that were employed to build the electrochemical model with process variations.

4.4.1 Component composition

In Figure 4.14 a) the negative active powder XRD pattern is shown. The active material powder graphite SFG-15L was employed and compared with the graphite diffraction pattern of the ICSD database. The positive XRD pattern (see Figure 4.14 b)) fit with the cell parameters of $Li_yNi_{0.8}Co_{0.15}Al_{0.05}O_2$ (NCA) [143], as was expected. The active material composition of the prototyped cells was close to the materials shown in Chapter 3 for the commercial cell (graphite-NCA/LCO for commercial cell and graphite-NCA for prototype cells). Moreover, the selected formulation was also similar, containing 93% and 95% of active material in the positive and negative electrodes, respectively.

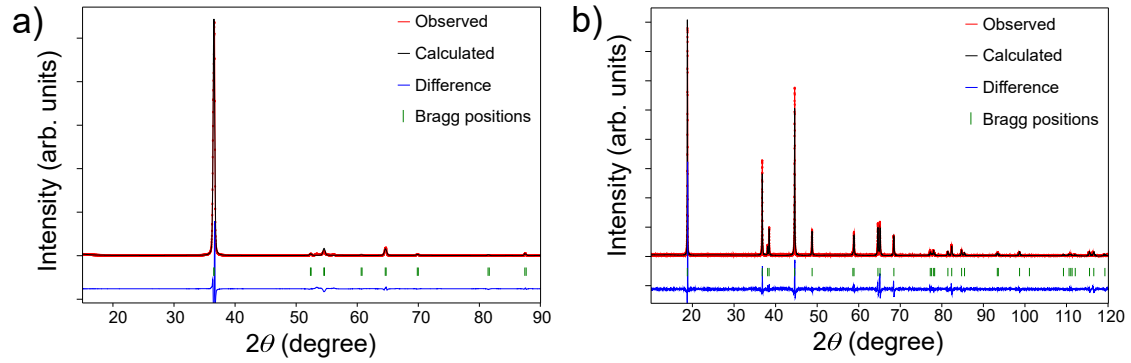

Figure 4.14: XRD patterns and Rietveld refinement of the a) AM powder of negative electrode (SFG15L); b) AM powder of positive electrode (NCA).

4.4.2 Thermodynamic, kinetic and transport properties

The qOCV curves were obtained following the same procedure as the commercial cell of Chapter 3, and are presented in Figure 4.15. This curve was obtained averaging all the C/30 charge and discharge curves of the studied conditions. The shadow represents the maximum deviation from the averaged curves.

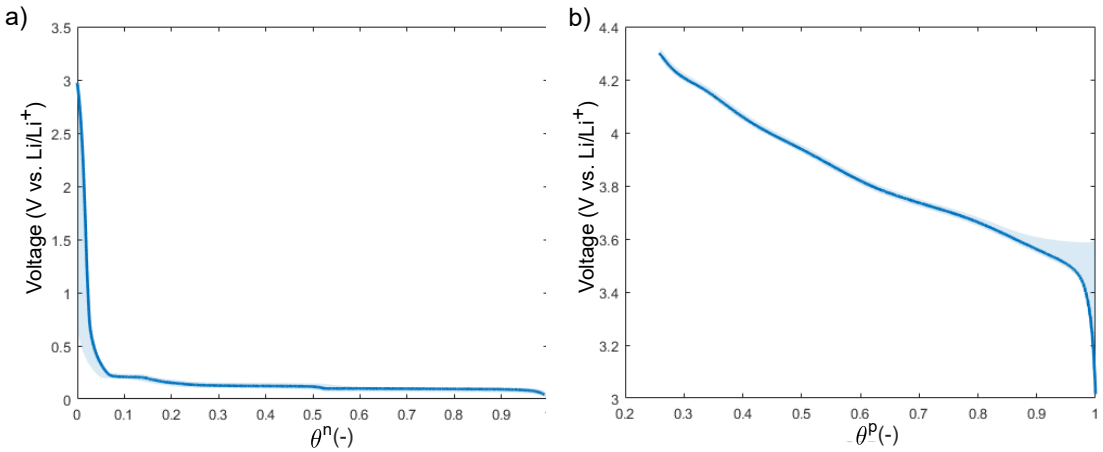

Figure 4.15: OCV curve as a function of SoL a) Negative electrode; b) Positive electrode.

PEIS technique was used to determine the film resistance, charge transfer resistance, and the double layer capacitance of both electrodes, as in subsection 3.5.2. The experiments were performed in half-coin cells at six different SoLs and 25 °C. Half-coin cells with a maximum voltage amplitude of 10 mV and a frequency range between 11 mHz and 1 MHz were selected. The methodology followed for the analysis is explained in subsection 3.5.2, and equations 3.37 to 3.41 were used for the post-processing of the results. The exchange current density results obtained with this procedure are shown in Figure 4.16 a) and b).

The effective surface area (S) for the different conditions was calculated with the procedure explained in subsection 3.5.4, and applied to the prototyped conditions of this chapter in subsection 4.4.3. The obtained exchange current density values were in the same order of magnitude of the commercial cell. In the negative electrode, the calendering steps improved the exchange current density of the electrode. In the positive electrode only slight differences were found between different conditions except from the most calendered condition (373 K and 55 µm), in which the exchange current density decreased consider-

ably, which could indicate that at those process conditions the electrode behaviour is not optimal because of a large compression ratio.

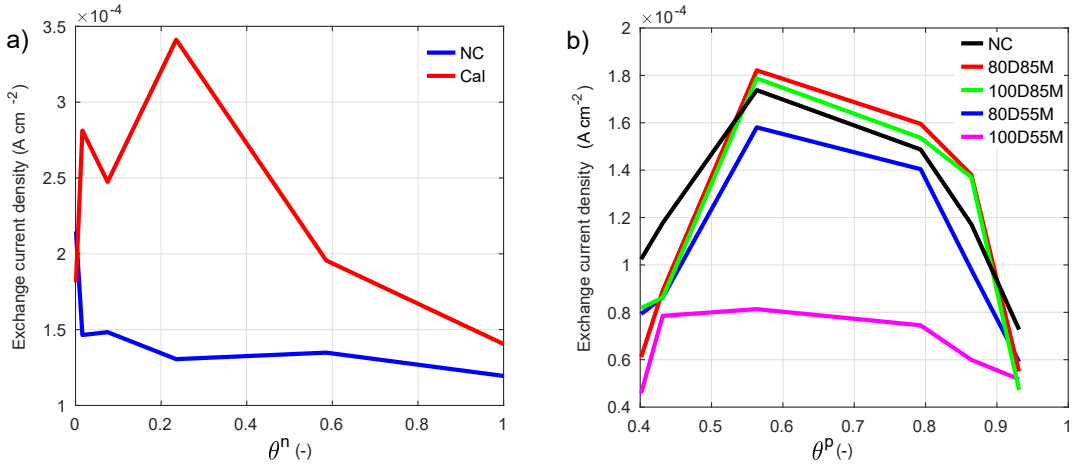

Figure 4.16: Exchange current density for a) Negative electrode; b) Positive electrode.

Moreover, the average values of the double layer capacitance were 0.0315 F m^{-2} and 0.2051 F m^{-2}, and the average film resistances were 0.0348 Ω m^2 and 0.0193 Ω m^2 for the negative and positive electrodes, respectively.

Solution-phase properties (the ionic conductivity, the diffusivity, the activity coefficient, and the transport number) are described in subsection 3.5.3. The same commercial electrolyte for the prototyped cells was used (1M $LiPF_6$ EC:EMC (50:50 v%)).

In the solid-phase, electronic conductivity and solid diffusion coefficient were determined following the same procedure as in subsection 3.5.3. The solid diffusion coefficient (D_s) was measured using a combination of PITT and PEIS at 25 °C for the non-calendered electrode. The diffusion coeficient is a material property, thus, it does not change with the calendering. Due to the nature of the experimental procedure (the experiment is conducted in electrodes), the value obtained is the effective diffusion coefficient. In the model, the active material particles are described in the pseudo-dimension, in which the bulk diffusion coefficient is required. That is why the morphological factor is included when calculating the final diffusivity value.

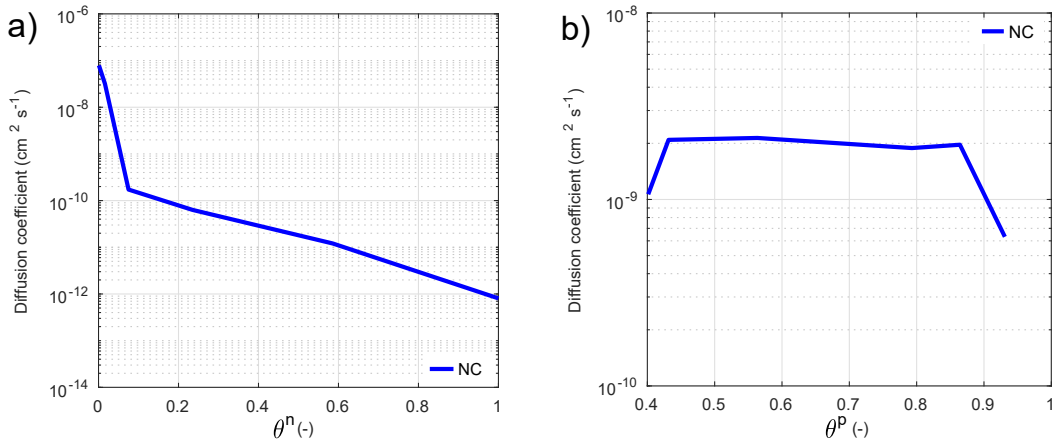

Figure 4.17: Solid diffusion coefficient for a) Negative electrode; b) Positive electrode.

The electronic conductivity characterisation was performed in a pristine state, before cycling. A value of 5 S m^{-1} and 1.18 S m^{-1} was measured for bulk negative and positive active material electronic conductivity, respectively (no binder or conductive additives were added to the measurements). The pycnometry powder density (2.1576 g cm^{-3} and 4.6641 g cm^{-3} for negative and positive electrodes, respectively) was measured to calculate the average thickness of the analysed powder.

4.4.3 Parameters related to porous structures

In Figure 4.18 a representation of parameter changes related to porous structure occurring during the calendering process are presented. The porous structure was analysed in pristine electrodes (prior to cycling) and one side coated electrodes which differs from the state studied in the commercial cell. Therefore, special care was taken while comparing both cells.

As the electrode is compressed, the thickness is expected to reduce with an increase of surface homogeneity. The density is expected to increase while decreasing the porosity of the coating [47, 93, 95]. The results vary depending on the active material (compaction resistance, particle shape and size), formulation (ratio between solid materials), mass loading, applied roller temperature, and roller gap.

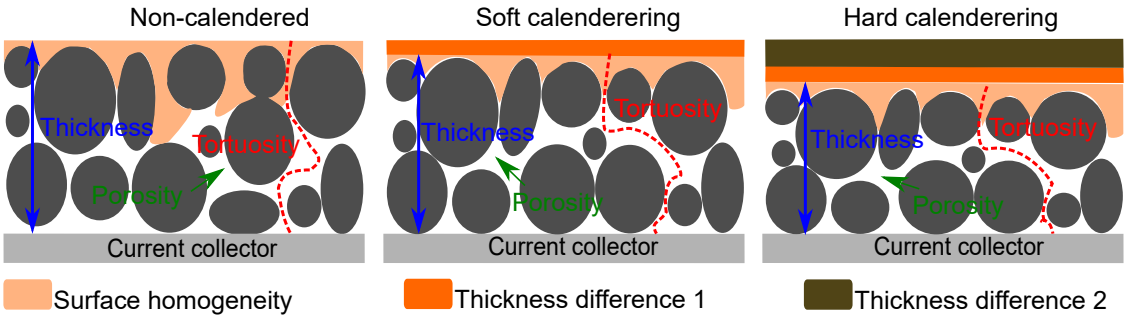

Figure 4.18: Different calendering conditions.

The general compression rate (Π_c) equation was used to determine the relationship between the initial and final thickness (see equation 4.4).

$$\Pi_c = \left(1 - \left(\frac{\delta_{cal}}{\delta_{dry}}\right)\right) 100 \tag{4.4}$$

Between the established thickness between rollers (roller gap) and the final thickness of the laminate, the materials undergo an elastic recovery (ER) defined as equation 4.5, which depends on the elasto-plastic properties of the pressed materials.

$$E_R = \frac{\delta_{cal} - G_{roll}}{\delta_{dry}} \tag{4.5}$$

The parameters after the coating, drying and calendering steps for the studied conditions are shown in Table 4.4. The dry thickness shows that deviations between measurements up to 1-2 µm (measurement error) and to approximately 10 µm (process variation) could occur with lab scale equipment as the process is less automatised than at industrial level. The compression rate takes into account the initial thickness of each laminate so as to normalise the results. When the roller gap was decreased, higher compression rates were obtained (see Table 4.4) until the maximum applied force of the machine. Moreover, with higher roller temperatures, a slightly higher compression rate was obtained which is

in good correlation with the literature [93, 97]. Thickness homogeneity of the laminates was also improved at higher compression rates, as we can observed in Table 4.4. In this case, prototyped electrodes were thicker compared to the commercial cell of Chapter 3 (approximately 50% thicker). This could increase the energy density of the cell, as less current collectors are needed. However, the higher coating thicknesses could also decrease the power density resulting in lower performance at higher current rates [191].

Table 4.4: Thickness related measurements during coating, drying and calendering steps.

	T_{roll} (K) (± 3)	G_{roll} (µm) (± 1)	δ_{blade} *1 (µm) (± 5)	δ_{dry} *1 (µm) (± 2)	δ_{cal} *1 (µm) (± 1)	δ_{rough} (µm)	$\delta_{cal-dry}$ (µm)	Π_c (%)	E_R (%)
+	-	-	200	93.67	93.67	5.60	-	-	-
	353	7	200	90.00	88.88	4.70	1.13	1.25	4.31
	373	7	200	92.13	90.71	4.20	1.41	1.53	6.20
	353	37	200	91.20	83.89	3.20	7.31	8.02	31.68
	373	37	200	92.50	84.70	3.40	7.80	8.43	32.11
	353	57	200	91.90	82.57	-	9.33	10.15	51.77
-	-	-	450	213	213	-	-	-	-
	353	63.9	450	213	133	-	80.00	37.56	32.44

*1 One side coating with current collector (Al foil: 16 µm and Cu foil: 18 µm).
δ_{blade} is the coater blade thickness (gap); δ_{dry} is the dry thickness of the electrode; δ_{cal} is the calendered thickness; δ_{rough} is the surface roughness.

In Figure 4.19 a) and b) the particle diameter distribution using dynamic light scattering is presented. An effective negative and positive particle diameter (D_v 50) of 16.02 and 9.61 µm, respectively were obtained (assuming spherical particles). The particle diameters of the prototyped active materials were 18% and 28% larger than those of the analysed commercial cell (Chapter 3). This could likely affect the solid mass transport through the particles.

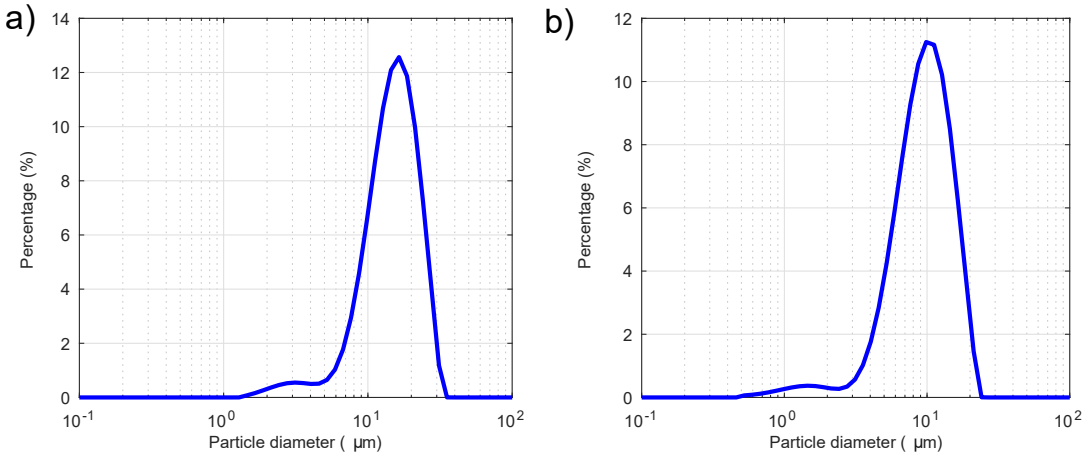

Figure 4.19: Particle size distribution with dynamic light scattering technique for a) Negative electrode; b) Positive electrode.

In Figure 4.20 SEM images present the particle shapes as well as the microstructure in non-calendered electrodes. As in the case of the commercial cell, a flake-like graphite

shape and spherical NCA particles were observed. The shape and size of active materials affects the final properties of the laminate (i.e. the tortuosity, porosity and specific surface area of the electrodes). Mixing, coating and drying steps are affected by the raw materials. Moreover, size, shape and AM affects the compaction resistance during the calendering process [96]. These properties could be changed in the optimisation process of the cell, but that would require changing the synthesis process of the raw materials [192–194]. In this thesis, the same active materials were used for all the experiments. In the commercial cell of Chapter 3 a combination of different AM in the same electrode (blend electrode) was employed, which had different particle size distributions.

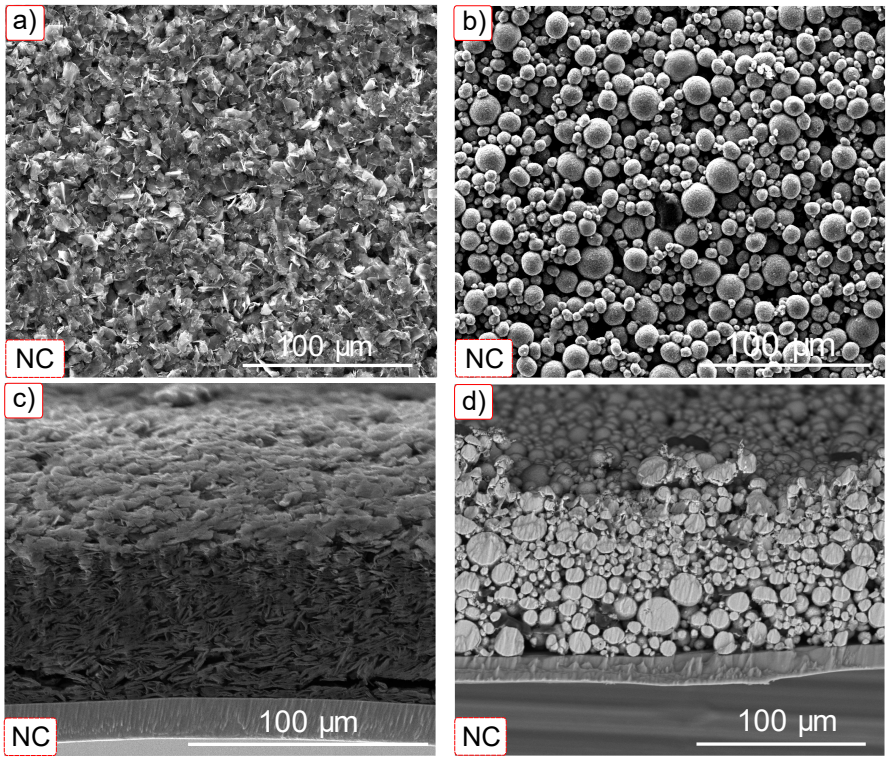

Figure 4.20: Particle shape in non-calendered electrodes. SEM surface image: a) Negative; b) Positive electrode; SEM cross-section image c) Negative and d) Positive electrode.

Different methods for giving porous structure parameters were identified in the literature. Three different groups are discussed in the following lines:(1) Mass and thickness based calculations; (2) Mercury porosimetry and Helium pycnometry measurements; (3) Scanning electron microscopy image post-processing.

4.4.3.1 *Mass and thickness based calculations*

The measured mass loadings, tapped densities and porosities before and after the calendering process are presented in Table 4.5. The mass loading measurements were taken after the calendering step. Helium pycnometry was used to determine the true density of the materials, and the powder density of the solid part $\rho_{solid,\max}$ was calculated with equation 4.6.

$$\rho_{solid,\max}(g\ cm^{-3}) = \frac{m_{solid}}{\left(\frac{m_{AM}}{\rho_{AM}}\right) + \left(\frac{m_{add}}{\rho_{add}}\right) + \left(\frac{m_{binder}}{\rho_{binder}}\right)} \tag{4.6}$$

where m_{AM} and ρ_{AM} are the weight and density of the active material, m_{add} and ρ_{add} are the weight and density of the conductive additives, and m_{binder}, and ρ_{binder} are the

weight and density of the binder used.

Coated porosities before ($\varepsilon_{e,dry}$) and after ($\varepsilon_{e,cal}$) the calendering process were calculated by equation 4.7. $\rho_{e,diff}$ and $\varepsilon_{e,diff}$ represent the normalised increased percentage of density and porosity throughout the calendering process, respectively.

$$\varepsilon_e = (1 - (\rho_{AM} / \rho_{solid,\max}))100 \tag{4.7}$$

In Table 4.5 slight differences in the mass loading of electrodes can be observed. This likely corresponds to the dispersion between laminates of the same batch at laboratory scale (coater film applicator was used in this thesis).

Table 4.5: Mass loading, tapped density and calculated porosity before and after calendering.

	T_{roll} (K)	G_{roll} (µm)	$M_{L,dry}$ (kg m^{-2})	ρ_{dry} (kg m^{-3})	$\varepsilon_{e,dry}$ (%)	ρ_{cal} (kg m^{-3})	$\varepsilon_{e,cal}$ (%)	ρ_{diff} (%)	$\varepsilon_{e,diff}$ (%)
+	-	-	0.19	2183	48.29	-	-	-	-
	353	7	0.16	2351	44.31	2387	43.45	1.52	1.94
	373	7	0.15	2184	48.26	2225	47.28	1.85	2.02
	353	37	0.15	2193	48.04	2429	42.45	9.72	11.65
	373	37	0.15	2165	48.71	2411	42.88	10.20	11.96
	353	57	0.17	2354	44.23	2668	36.79	11.77	16.83
-	-	-	0.10	491	76.48	-	-	-	-
	353	63.9	0.09	424	79.72	840	59.77	49.60	25.03

4.4.3.2 *Mercury porosimetry and Helium pycnometry measurements*

In order to study the dispersion between electrodes, two positive laminates were studied with mercury porosimetry before the calendering step. In Figure 4.21 the pore size distribution is presented for the positive non-calendered electrode.

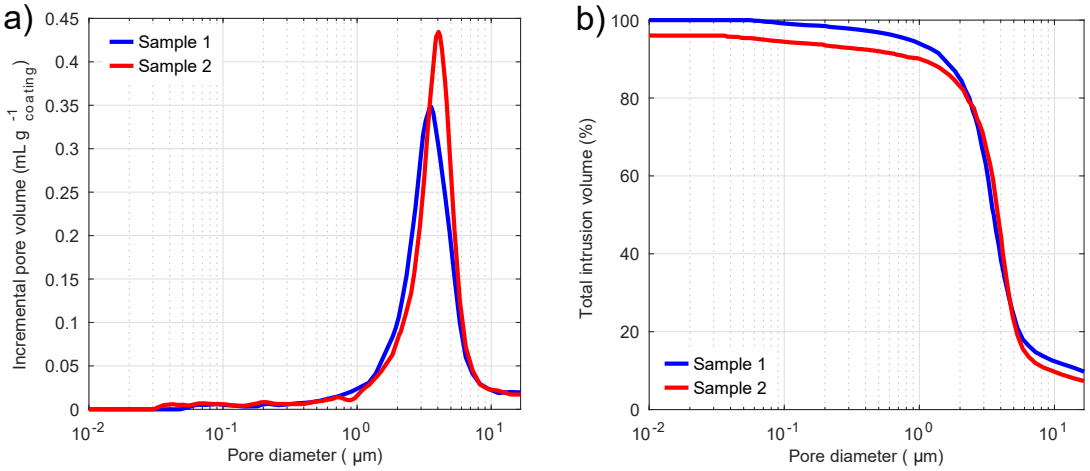

Figure 4.21: Mercury porosimetry results of the non-calendered positive electrode a) Incremental pore size distribution; b) Total intrusion volume.

The pore size range was corrected according to [162] (see Equation 3.46) in which the lowest considered pore diameter was 0.01 nm, and the highest considered pore diameter was based on Dv90 of the DLS measurements. A Dv90 value of 16.56 µm for NCA AM was measured. The incremental pore volume results obtained from the equipment was

corrected by subtracting the current collector weight from the sample weight. A noticeable dispersion was found between laminates at laboratory scale. For that reason, results were carefully analysed to assess the influence of the calendering step on the pore size reduction. In Figure 4.22 the results for the different calendering step conditions are plotted. Four different laminates were used for the analysis: (i) Non-calendered (NC); (ii) Second non-calendered electrode NC2 and 373 K with 35 µm (80D35M) roller gap; (iii) 353 K with 85 and 55 µm roller gap (80D85M and 80D55M), and (iv) 373 K with 85 and 55 µm roller gap (100D85M and 100D55M).

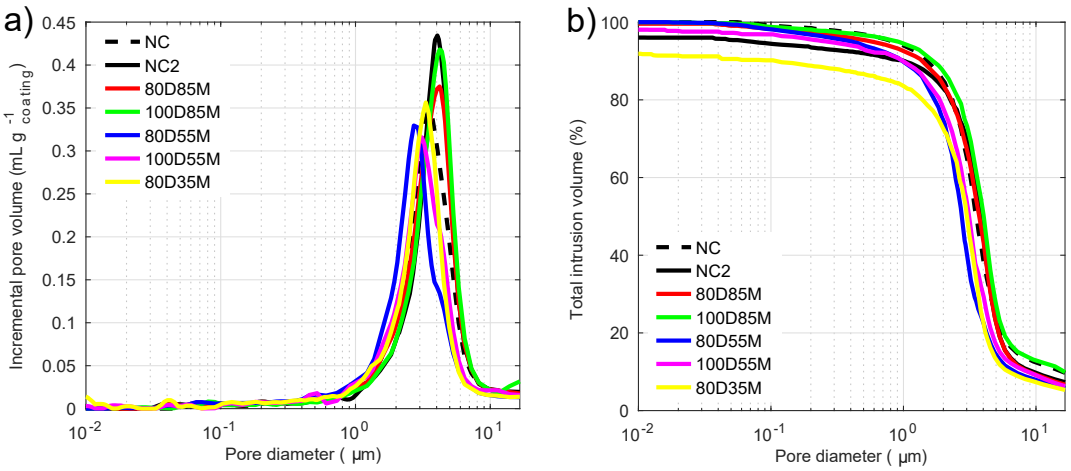

Figure 4.22: Mercury porosimetry results for the positive electrode at different calendered conditions: a) Incremental pore size distribution and b) Total intrusion volume.

In Figure 4.23 some particle cracks at high compression rates can be observed, which could also be attributed to the volume increase at lower pore diameters.

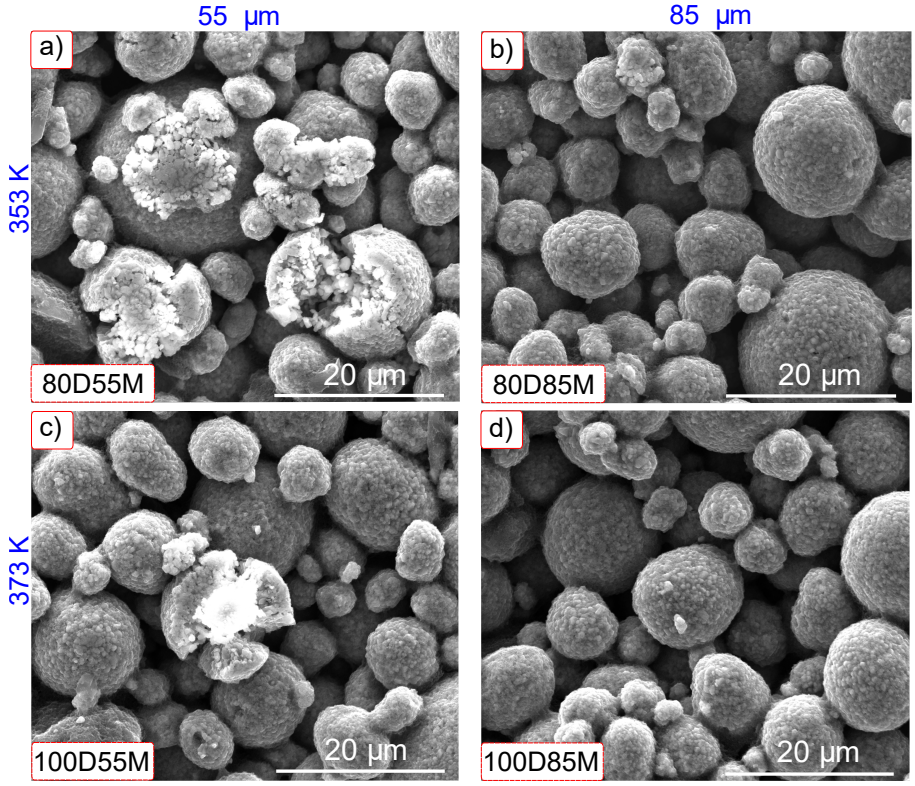

Figure 4.23: Positive electrode SEM surface images for different calendering conditions.

As was expected, with higher roller gaps, the peak size decreases in the pore size distribution graph and shifts to the left moving to smaller pores. This is particularly evident when the same laminates are compared. Moreover, with a temperature rise higher compression rates were obtained although the influence of temperature was inferior to that of the roller gap. At small roller gaps only small differences (compression rates of 1.25 and 1.53%) from the non-calendered electrode were obtained. Moreover, the dispersion between laminates arising from the coating step of the fabrication process seem to be higher than the effect of the calendering on the laminates.

In Figure 4.24 a) and b), the non-calendered and calendered pore size distribution and specific pore volume are presented for the negative reference electrode. A Dv90 value of 25.50 µm for negative active material was measured with DLS. As was expected, the pore volume decreased when a compression force was applied. The electrode underwent a plastic deformation in which particle movement occurred to close the voids inside the structure. At low compression rates and similar materials (0 - 10%) Froboese et al. [162] presented that only the surface of the electrode was compressed. The compression rate of this calendered electrode is 37.56% as it is shown in Table 4.4.

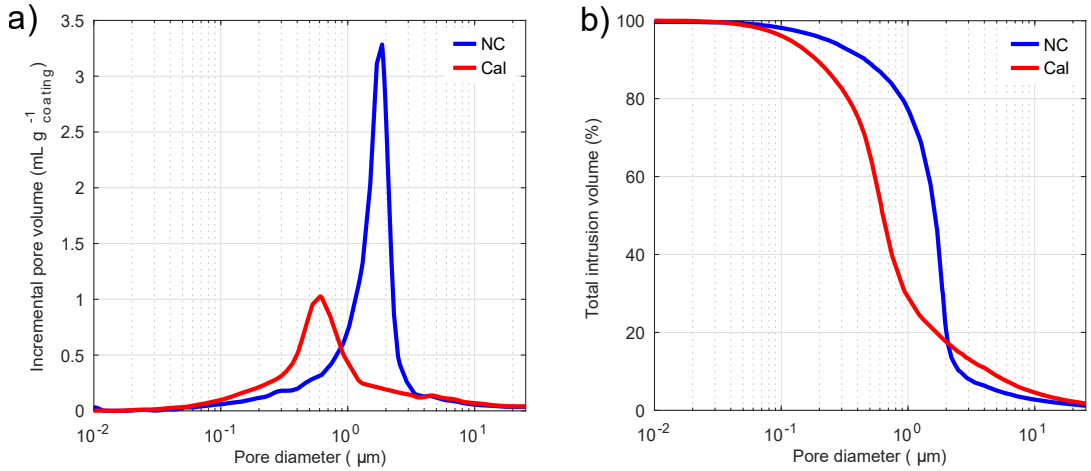

Figure 4.24: Mercury porosimetry results of the negative electrode a) Pore size distribution; b) Specific pore volume.

For further calculation regarding the coating density, coating porosity and tortuosity, the three methods proposed by Froboese et al. [162] for current collector correction were conducted. Corrections by means of the sample thickness (CT), sample area (SA) and mass loading (ML). In addition to that post-process, in order to get the total porosity of the samples (from micro to macroporosity), helium pycnometry measurements were performed and the equation 4.8 was applied for total porosity calculation (combining mercury porosimetry and helium pycnometry).

$$\varepsilon_e = (1 - (\rho_{Hg}/\rho_{He}))100 \tag{4.8}$$

4.4.3.3 *Scanning electron microscopy image post-processing*

Cross-sectional SEM images prepared by ion-milling were also employed for the porosity estimation (Fiji software) (see Figure 4.25).

These results are also compared with Hg and He porosimetries in Figure 4.29 b) and are in the same order of magnitude as the results obtained with mercury porosimetry, although the dispersion between samples is high.

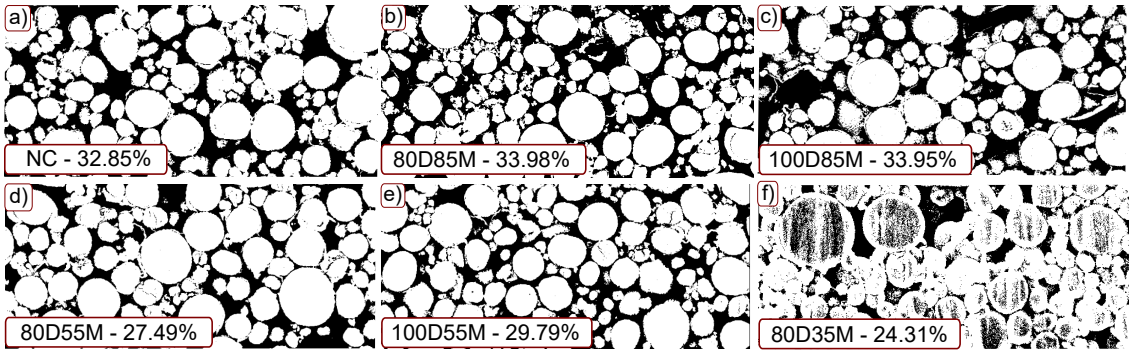

Figure 4.25: Positive electrode porosity estimation by SEM cross-section image and Fiji software.

Figure 4.26 show that particles which are not on the surface were not cracked which could be attributed to the applied moderate compression rate (up to 10.15%) which is in good correlation with Figure 4.22.

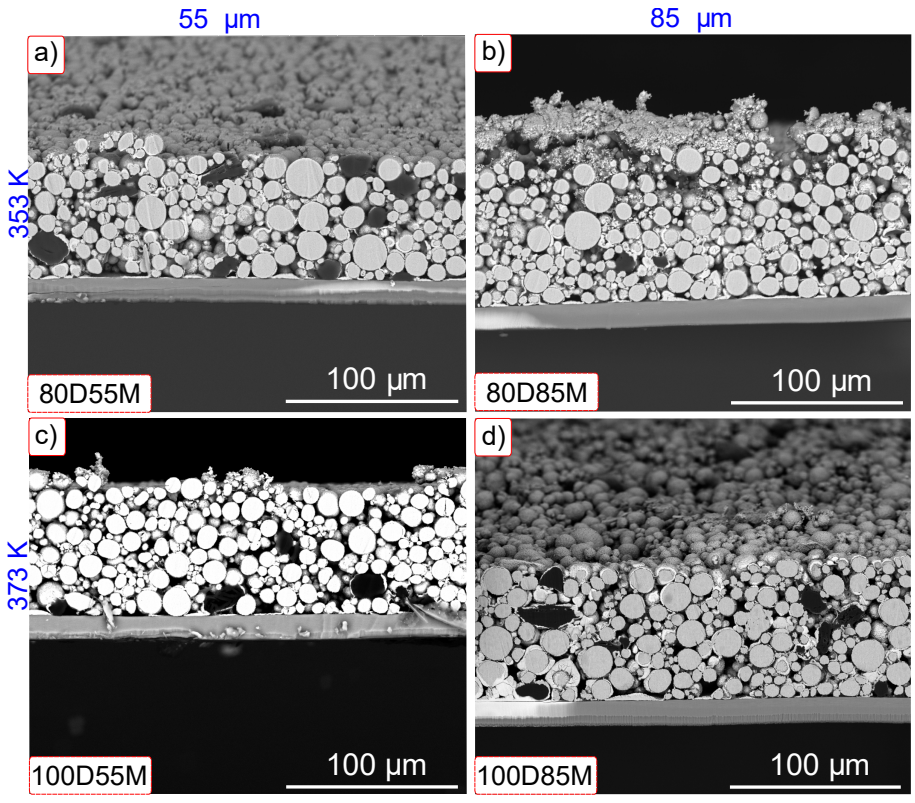

Figure 4.26: Cross section SEM images for different calendering conditions of the positive electrode.

Moreover, surface and cross-section SEM images of the negative electrode were analysed as shown in Figure 4.27 a) and b). In Figure 4.27 b) delamination of the coated electrode close to the current collector is observed. This issue can be attributed to the preparation of thick electrodes or to the SEM sample preparation process and the ion milling step, although additional adhesion tests were not conducted for confirmation.

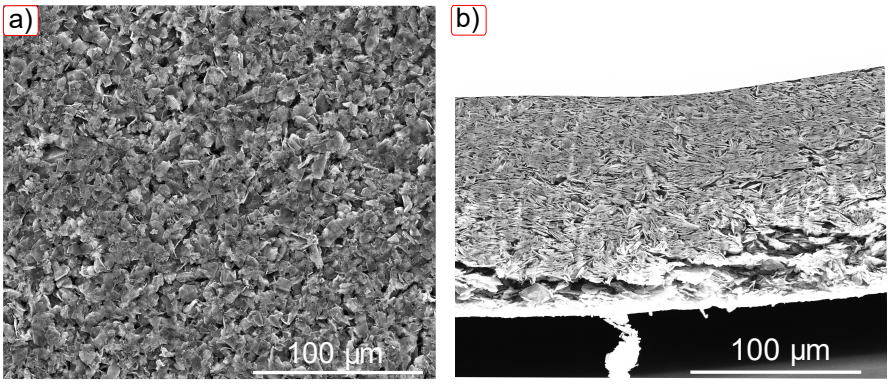

Figure 4.27: Calendered negative electrode: a) SEM surface image; b) SEM cross-section image.

Figure 4.28 a) and b) shows the porous estimation procedure using the Fiji program for the negative electrode.

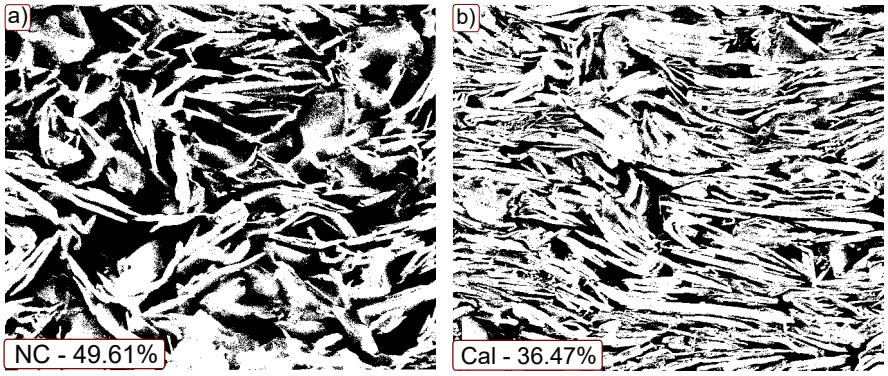

Figure 4.28: a) Non-calendered negative SEM binary image showing pores in black; b) Calendered negative SEM binary image showing pores in black.

4.4.3.4 *Comparison between techniques*

In Figure 4.29 a) and b) a comparison between densities and porosities obtained with different methods are shown.

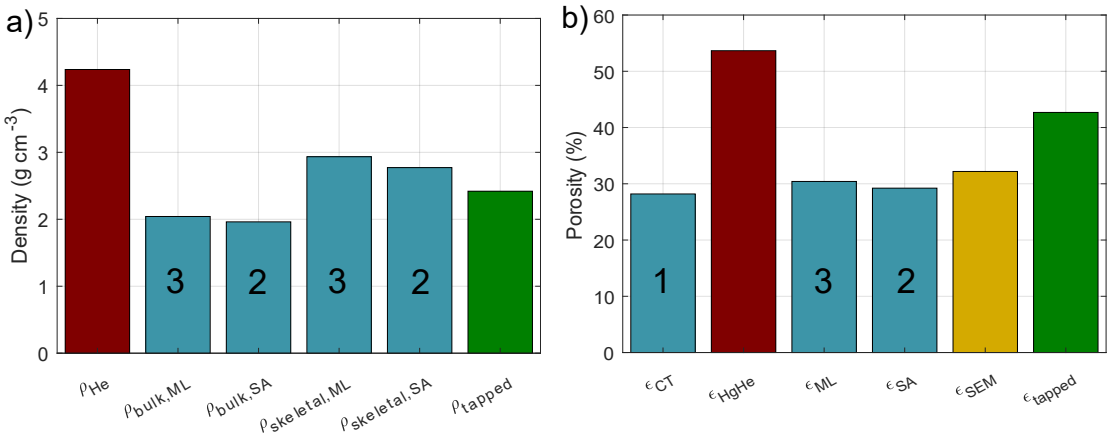

Figure 4.29: Non-calendered averaged electrode. a) Measured coated densities calculated with different methods; b) Measured coated porosities calculated with different methods. Where red represents helium pycnometry, blue represents mercury porosimetry, green represents mass and thickness based measurements and yellow represents SEM based post-process.

Those results compare six different density values: helium pycnometry density, tapped density and mercury porosimetry densities (bulk and skeletal). The mercury porosimetry results were corrected using different methods to eliminate the current collector error according to the the sample area (SA -method 2) and mass loading (ML - method 3) [162]. These density values presented in Figure 4.29 a) serve to calculate the average coating porosity of the electrode. In Figure 4.29 b) porosity calculated with different methods are shown for the non-calendered electrode. Porosities calculated by mercury porosimetry corrected given the coating thickness ($\varepsilon_{e,CT}$ - method 1), the sample area ($\varepsilon_{e,SA}$ - method 2) and the mass loading ($\varepsilon_{e,ML}$ - method 3) according to the methodology of Froboese et al. [162] where compared with the results obtained from SEM image processing ($\varepsilon_{e,SEM}$), tapped density ($\varepsilon_{e,tapped}$) and a combination between helium pycnometry and mercury porosimetry ($\varepsilon_{e,HgHe}$).

Between the methods compared in Figure 4.29, the density obtained from mercury porosimetry and corrected with sample area was selected as the most representative. This is because of the method of mercury replacement when the current collector correction is performed. Properties measured in a large volume are more representative than those measured by indirect properties (tapped density) due to the variations expected in those magnitudes. However, when other technologies are studied (such as solid state batteries), mercury and helium pycnometry measurements are not able to study close pores. Thus, image processing techniques could be more suitable. In addition, SEM is a widespread and fast technique that could also give information about composition (if EDS detector is used etc.). A combination of helium pycnometry and mercury porosimetry is also proposed to give a general value of porosity, as it takes into account from the microstructure to the macrostructure. In Figure 4.30 the results for the different positive electrode calendering conditions are summarised.

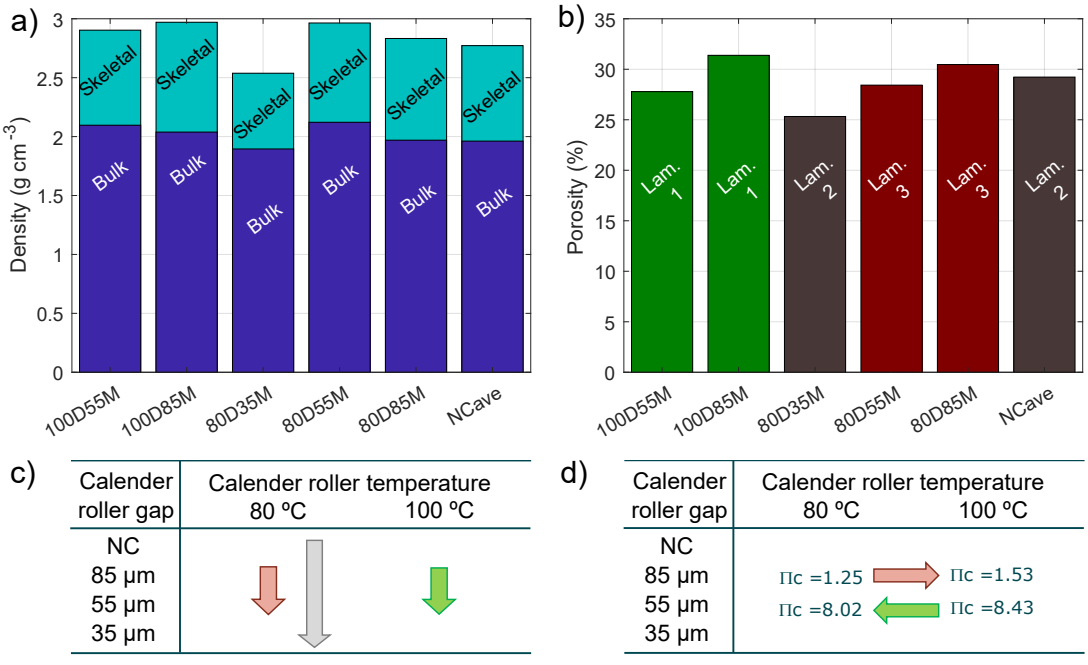

Figure 4.30: Different calendering conditions. a) Measured coated densities calculated with different methods; b) Measured coated porosities calculated with different methods; c) Effect analysis when the calender roller gap is varied; d) Effect analysis when the calender roller temperature is varied.

In Figure 4.30 c), the calender roller gap influence is plotted. There, three different results are available: at 80°C, 100°C and an additional condition between non-calendered and the minimum roller gap of 35 µm. As was expected, with higher roller gaps, the porosity decreases. In Figure 4.30 d), the influence of the calender roller temperature for 80°C and 100°C for different calender roller gaps were analysed. An opposite response was found. With a temperature rise of 20°C, slightly higher compression rates were obtained, leading to the conclusion that the influence of temperature was inferior to that of the roller gap. Moreover, the dispersion between laminates arising from the coating step seem to be higher than the effect of the calendering temperature on the laminates. The different laminates used in this analysis are presented with different bar colors: green, grey and red. The non calendered porosity, is slightly inferior to that of the red and green laminates, thus, the 1% of variation in compression rate is inside the experimental error.

A summary of the results for all the analysed conditions are presented in Table 4.6. In Table 4.6, the experimental specific surface area is presented. However, the entire surface area in contact with the electrolyte does not react when the cell is cycled.

Table 4.6: Helium pycnometry and mercury porosimetry experimental results.

	T_{roll} (K)	G_{roll} (µm)	$\rho_{ske,SA}$ (kg m^{-3})	$\rho_{bulk,SA}$ (kg m^{-3})	ρ_{He} (kg m^{-3})	$\varepsilon_{e,SA}$ (%)	$\varepsilon_{e,HgHe}$ (%)	$a_{s,Hg}$ (m^2 m^{-3})	τ (-)
+	-	-	2772	1962	4237	29.22	53.66	2.11 10^6	1.90
	353	7	2833	1970	4107	30.47	52.04	5.12 10^6	1.89
	373	7	2970	2038	4123	31.38	50.56	2.47 10^6	1.88
	353	37	2964	2122	4153	28.43	48.92	3.68 10^6	1.91
	373	37	2903	2097	4089	27.78	48.73	2.12 10^7	1.92
	353	57	2538	1895	4219	25.32	55.08	8.29 10^7	1.94
-	-	-	2285	675	2289	70.48	70.53	6.20 10^6	1.43
	353	63.9	1713	803	3045	53.09	73.61	1.02 10^7	1.63

In Table 4.7 the calculated specific surface area and coin cell effective surface area are presented.

Table 4.7: Effective surface area and solid volume fraction calculation.

	T_{roll} (K)	G_{roll} (µm)	ε_e (%)	$\varepsilon_{non-act}$ (%)	ε_s (%)	R_s (µm)	δ_{cal} (µm)	S_{coin} (m^2)	a_s (m^2 m^{-3})
+	-	-	29.22	31.87	38.91	4.81	93.67	2.57 10^{-3}	2.43 10^5
	353	7	30.47	19.19	50.34		88.88	3.16 10^{-3}	3.14 10^5
	373	7	31.38	20.20	48.42		90.71	3.10 10^{-3}	3.02 10^5
	353	37	28.43	12.52	59.05		83.89	3.50 10^{-3}	3.69 10^5
	373	37	27.78	10.90	61.32		84.70	3.67 10^{-3}	3.83 10^5
	353	57	25.32	1.92	72.76		82.57	4.24 10^{-3}	4.54 10^5
-	-	-	70.48	0.00	29.52	8.01	213.00	2.66 10^{-3}	1.11 10^5
	353	63.9	53.09	13.81	33.10		133.00	1.86 10^{-3}	1.24 10^5

The calculated specific surface area and coin cell effective surface area are necessary for exchange current density, film resistance, capacitance and solid diffusion coefficient calculations. The calculated real specific surface area results were in good agreement with the values obtained from mercury porosimetry (both methods followed the same ascendant tendency increasing the compression rate). $\varepsilon_{non-act}$ calculation is based on electrochemical measurement on half-coin cells in which the theoretical and the experimental capacities are compared as an approximation of the non electrochemically active area.

4.5 MATERIAL-PROCESS-MODEL RELATIONSHIPS

The material properties which can be varied and controlled throughout the material processing stage of the fabrication process are described in Figure 4.31. These material parameters represent the link between the fabrication process and the model. The fabrication steps and their inclusion in the P2D model are calculated as follows.

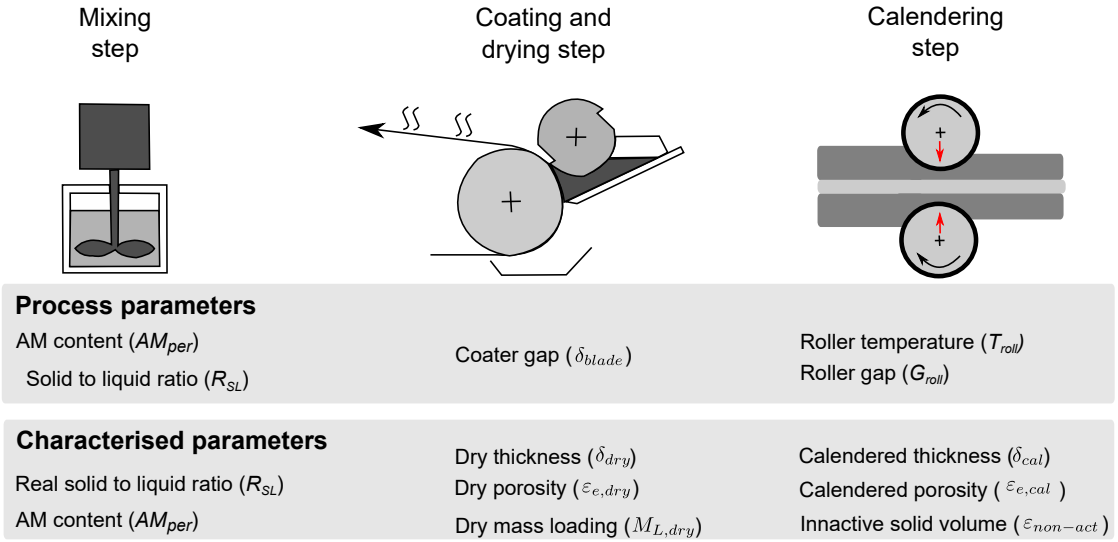

Figure 4.31: Model parameters and their relationship with electrochemical model parameters.

The optimisation of the mixing process is out of the scope of this thesis, however, the variations between different batches within the same fabrication process were included into the model with the solid-liquid ratio (R_{SL}) parameter. This allows the decoupling of the mixing process variations from the subsequent fabrication steps. The slurry density ρ_{slurry} after the mixing process is calculated by equation 4.9:

$$\rho_{slurry}(g\ cm^{-3}) = \frac{m_{solid} + m_{solvent}}{\left(\frac{m_{solid}}{\rho_{solid,\max}}\right) + \left(\frac{m_{solvent}}{\rho_{solvent}}\right)} = \\ = \frac{m_{solid} + m_{solvent}}{\left(\frac{R_{SL}(m_{solid} + m_{solvent})/100}{\rho_{solid,\max}}\right) + \left(\frac{(1 - R_{SL})(m_{solid} + m_{solvent})/100}{\rho_{solvent}}\right)} \tag{4.9}$$

The material is deposited onto a copper or aluminium foil with a predefined gap δ_{blade}. The mass loading of the slurry $M_{L,wet}$ is defined with equation 4.10:

$$M_{L,wet}(g\ cm^{-2}) = \rho_{slurry}\delta_{wet} \tag{4.10}$$

where δ_{wet} is the final wet thickness when δ_{blade} is set in the film applicator for a certain coating speed. The differences between δ_{blade} and δ_{wet} arise from the deviations that may

occur during the electrode fabrication process. The final mass loading ($M_{L,wet}$ is known in studied samples).

Then, the properties after the drying step are calculated. These properties corresponds to the non calendered electrode. The maximum achievable theoretical mass loading $M_{L,solid,\max}$ is calculated using equation 4.11:

$$M_{solid,\max}(g\ cm^{-2}) = \rho_{solid,\max}\delta_{wet} \tag{4.11}$$

In order to calculate the real mass loading $M_{L,solid,real}$, the porosity ε_{dry} must be included to account for the pores that are not filled by solid materials after solvent evaporation, which can be calculated with $\rho_{dry}/\rho_{solid,\max}$ (equation 4.12).

$$\begin{aligned} M_{L,solid,real}(g\ cm^{-2}) &= \rho_{solid,\max}\delta_{wet}(1-\rho_{dry}/\rho_{solid,\max}) = \\ &= \rho_{solid,\max}\delta_{wet}\left(1-\frac{\left((\rho_{slurry}m_{solid})/(m_{solid}+m_{solvent})\right)}{\rho_{solid,\max}}\right) \end{aligned} \tag{4.12}$$

where ρ_{dry} is the dried thickness before the calendering step.

Finally, the thickness of the dried sample (δ_{dry}) can be calculated with equation 4.13.

$$\delta_{dry} = \frac{M_{L,solid,real}}{\rho_{dry}} = \frac{\rho_{solid,\max}\delta_{wet}}{\rho_{dry}} - \delta_{wet} \tag{4.13}$$

Table 4.8: Calculated mixing, coating and drying parameters.

	R_{SL} (%)	ρ_{slurry} (kg m^{-3})	δ_{blade} (µm)	δ_{wet} (µm)	$M_{L,wet}$ (kg m^{-2})	δ_{dry} (µm)	ρ_{dry} (kg m^{-3})	$M_{L,dry}$ (kg m^{-2})	$\varepsilon_{e,dry}$ (%)
+	73.81	2352	200	150.0	0.35	92.0	2183	0.20	48.28
-	27.19	1165	450	409.5	0.48	211.5	499	0.11	76.15

The calendering relationships were based on experimental measurements of the active materials described in this chapter. A relationship taking into account electrode mass loading, calender roller temperature and calender roller gap was performed for calendered density, electrode tortuosity and the solid inactive part of the electrode (see equations 4.14, 4.15 and 4.16). The coefficients for those relationships are presented in Table 4.9.

$$\rho^p_{cal}(T^p_{roll}, G^p_{roll}) = \rho^p_{dry}(1 + (p_{00} + p_{10}T^p_{roll} + p_{01}G^p_{roll}))M_L{}^p \tag{4.14}$$

$$\varepsilon^p_{non-act}(T^p_{roll}, G^p_{roll}) = \varepsilon^p_{non-act,dry} + (p_{00} + p_{10}T^p_{roll} + p_{01}G^p_{roll})M_L{}^p \tag{4.15}$$

$$\tau^p(T^p_{roll}, G^p_{roll}) = \tau^p_{dry} + (p_{00} + p_{10}T^p_{roll} + p_{01}G^p_{roll})M_L{}^p \tag{4.16}$$

The thickness after the calendering process can be estimated with equation 4.17. This approach assumes that the mass loading of the non-calendered and calendered electrode are the same, which means that no elongation in the calendering or lateral direction is taken into account.

$$\delta_{cal} = \frac{M_{solid,real}}{\rho_{cal}} \tag{4.17}$$

The solid diffusion coefficient and exchange current density were corrected considering that the specific surface area changes with calendering, and using equations 3.41 and 3.44.

Table 4.9: Calendering relationship coefficients for calendering density, non-active solid volume fraction and tortuosity (with 95% confidence bounds) for positive electrode.

Coefficients	p_{00}	p_{10}	p_{01}	R^2
ρ^p_{cal}	-17.9 (-77.56, 41.77)	0.05069 (-0.1147, 0.2161)	0.2281 (0.1529, 0.3033)	0.9688
$\varepsilon^p_{non-act}$	176.3 (-932.4, 1285)	-0.5701 (-3.643, 2.503)	-2.193 (-3.59, -0.7959)	0.8929
τ^p	0.6044 (-2.246, 3.455)	-0.001879 (-0.009781, 0.006023)	0.00438 (0.0007883, 0.007973)	0.8434

The adjusted coefficients for the negative electrode are presented in Table 4.10. A constant roller temperature of 353 K was used for all the calendered conditions. Nevertheless, in order to find a good electrode balancing condition, those relationships were done accounting different coating blade gaps and calendering roller gaps as presented in equations 4.18, 4.19 and 4.20.

$$\rho^n_{cal}(\delta^n_{wet}, G^n_{roll}) = \rho^n_{dry}(1 + (p_{00} + p_{10}\delta^n_{wet} + p_{01}G^n_{roll}))M^n_L \tag{4.18}$$

$$\varepsilon^n_{non-act}(\delta^n_{wet}, G^n_{roll}) = \varepsilon^n_{non-act,dry} + (p_{00} + p_{10}\delta^n_{wet} + p_{01}G^n_{roll})M^n_L \tag{4.19}$$

$$\tau^n(\delta^n_{wet}, G^n_{roll}) = (p_{00} + p_{10}\delta^n_{wet} + p_{01}G^n_{roll}){M_L}^n \tag{4.20}$$

Table 4.10: Calendering relationship coefficients for calendering density, non-active solid volume fraction and tortuosity (with 95% confidence bounds) for negative electrode.

Coefficients	p_{00}	p_{10}	p_{01}	R^2
ρ^n_{cal}	6.93 (-81.13, 94.99)	-0.01723 (-0.2399, 0.2054)	1.183 (0.756, 1.609)	0.9976
$\varepsilon^n_{non-act}$	406.5 (-2103, 2916)	-0.8512 (-7.198, 5.496)	1.317 (-10.84, 13.47)	0.4298
τ^n	34.79 (25.24, 44.34)	-0.04696 (-0.07111, - 0.02281)	0.0269 (-0.01935, 0.07316)	0.9952

The experimental-numerical correlations were corrected to minimise the difference between experimental and numerical curves. To that end, three parameters were adjusted for all the curves, which corresponds to the more sensitive parameters: exchange current density, solid diffusion coefficient and the inactive part of the solid volume (which affects

to the specific surface area calculation). The variation between different calendering conditions was only due to the specific surface area before including these new relationships (equations 4.21, 4.22 and 4.23).

$$i_0(T^p_{roll}, G^p_{roll}, SoL^p) = i^p_{0,dry} S^p + \\ +(p_{00} + p_{10}T^p_{roll} + p_{01}G^p_{roll} + p_{11}T^p_{roll}G^p_{roll} + p_{02}T^{p2}_{roll}) \tag{4.21}$$

$$D_s{}^p(T^p_{roll}, G^p_{roll}, SoL^p) = D^p_{s,dry} S^p + \\ +(p_{00} + p_{10}T^p_{roll} + p_{01}G^p_{roll} + p_{11}T^p_{roll}G^p_{roll} + p_{02}T^{p2}_{roll}) \tag{4.22}$$

$$\varepsilon^p_{non,act}(T^p_{roll}, G^p_{roll}) = \varepsilon^p_{non,act} S^p + \\ +(p_{00} + p_{10}T^p_{roll} + p_{01}G^p_{roll} + p_{11}T^p_{roll}G^p_{roll} + p_{02}T^{p2}_{roll}) \tag{4.23}$$

The final coefficients for the general model are shown in Table 4.11.

Table 4.11: Final calendering relationship coefficients for exchange current density, solid diffusion coefficient and non-active solid volume fraction (with 95% confidence bounds).

Coefficients	p_{00}	p_{10}	p_{01}	p_{11}	p_{02}	R^2
i^p_0	-3.118	0.01167	1.262	-0.001667	-0.01454	1
D^p_s	-0.02118	0.0001167	0.00582	-1.67 10^{-5}	9.01 10^{-6}	1
$\varepsilon^p_{non,act}$	-116.9	0.3	-0.296	9.11 10^{-18}	0.02188	1

In Table 4.12 the estimated parameters are presented. The relationships were employed in the inverse cell design when no experimental information was available.

Table 4.12: Estimated model parameters with the calendering relationships of this section.

	T_{roll} (K)	G_{roll} (µm)	ρ_{cal} (kg m^{-3})	δ_{cal} (µm)	$\varepsilon_{e,cal}$ (%)	τ (-)	$\varepsilon_{non-act}$ (%)	ε_s (%)	a_s (m^2 m^{-3})
	-	-	2499	93.28	30.01	1.89	27.04	42.95	2.68 10^5
	353	7.0	2539	92.06	29.21	1.89	24.07	46.72	2.92 10^5
	373	7.0	2564	91.31	28.70	1.89	21.87	49.42	3.09 10^5
+	353	37.0	2710	87.26	25.86	1.92	11.37	62.78	3.92 10^5
	373	37.0	2735	86.60	25.37	1.91	9.17	65.46	4.09 10^5
	353	57.0	2824	84.39	23.69	1.94	2.90	73.41	4.58 10^5
	-	-	531	201	74	1.32	2.2	23.5	0.87 10^5
-	353	63.9	922	112	55.89	1.49	10.26	42.3	1.27 10^5

4.6 HALF-CELL MODEL VALIDATION

Before cell performance evaluation, formation cycles of the cell were performed in order to properly form the SEI layer. In Figure 4.32 the irreversible capacities are shown.

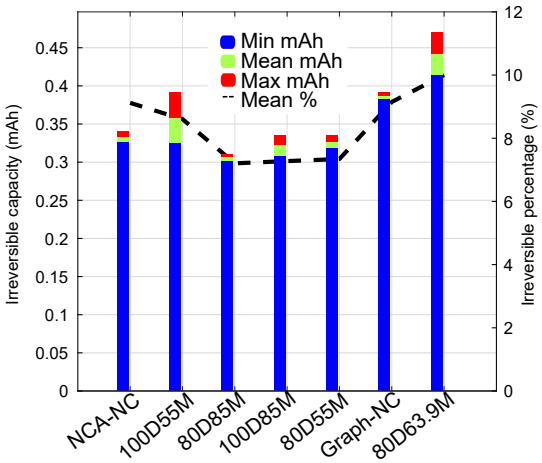

Figure 4.32: Irreversible capacity of the formation cycles of positive and negative half-cells.

Irreversible capacity in the first formation cycle is almost constant for positive (8%) and negative (9 - 10%) cells. The galvanostatic discharge performances for positive and negative non-calendered electrodes are shown in Figure 4.33 [4]. The cell voltage is presented as a function of specific cell capacity (mAh g^{-1}). The simulated cell responses are in good agreement with the experimental results. For high current rates (1C and 2C) performance loss was observed in the experimental cells, specially in the negative electrode. Moreover, after the calendering process the cell performance was improved.

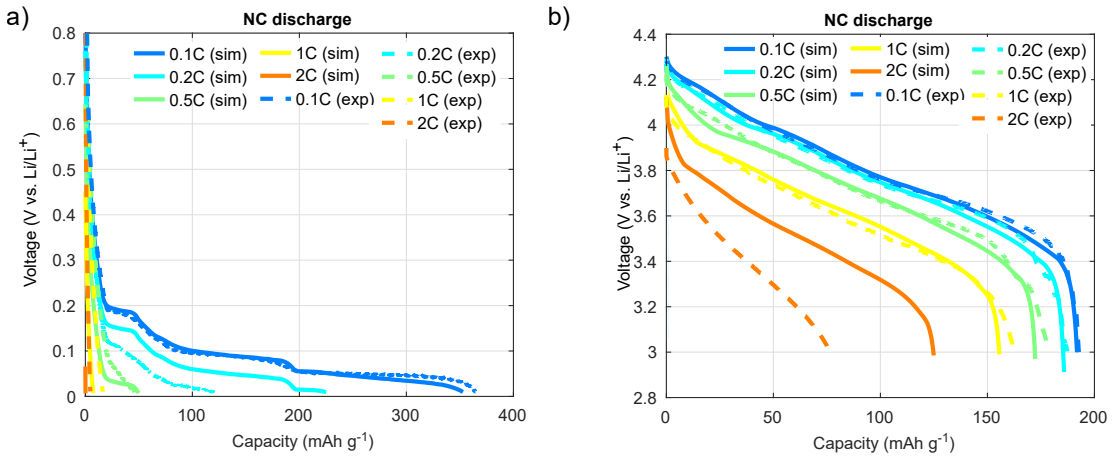

Figure 4.33: Half-cell experimental and simulation comparison of non-calendered electrodes. a) Negative electrode; b) Positive electrode.

The galvanostatic discharge performances for the different calendering conditions of the positive electrode are shown in Figure 4.34. The simulations present the same tendency.

[4] The post-process of the experimental measurements for different positive and negative calendering conditions was carried out by Eneko Agirrezabala, experimental execution and simulations was performed by the author.

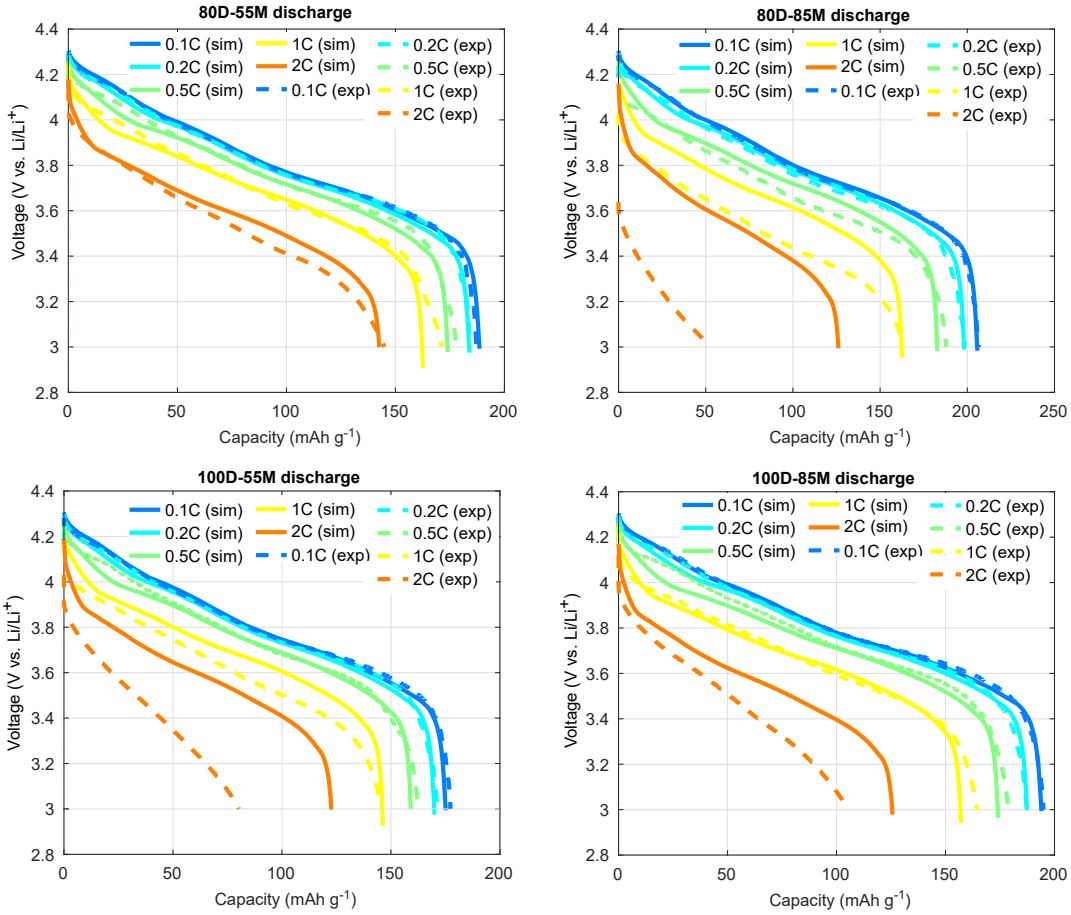

Figure 4.34: Half-cell model validation: a) 80D85M; b) 100D85M; c) 80D55M; d) 100D55M.

Experimental and numerical voltage percentage deviations are shown in Table 4.13 for all the studied conditions. At low discharge rates, the experimental numerical deviations are less than 1%. At higher current rates (1C and 2C) the deviations increase. Regarding the negative electrode, higher deviations are found between experimental and numerical study. This could be attributed to higher dispersions in the electrode fabrication process due to high mass loadings resulting in higher dispersion between the analysed cells. It is worth noting that, as far as those relationships are built with more experimental data, the process-model-cell characteristics will be more accurate.

Table 4.13: Experimental and numerical voltage percentage deviations.

C-Rate	Pos NC	Pos 80D85M	Pos 100D85M	Pos 80D55M	Pos 100D55M	Neg NC
0.1C	0.41	0.02	0.13	-0.29	0.32	-42.52
0.2C	0.21	0.27	0.62	-0.10	0.30	17.33
0.5C	0.96	-0.12	1.61	0.61	1.08	34.47
1C	2.84	0.96	2.71	0.77	2.25	39.99
2C	5.79	3.60	5.28	-0.59	4.60	-42.52

4.7 CONCLUSIONS

In this chapter, half-cell models of lithium-graphite and lithium-NCA were studied. Material-process-model relationships were implemented for the material processing stage of the battery manufacturing process. These relationships were validated against experimental results and a good correlation was obtained. Therefore, the model and relationships are valid for inverse cell design.

The graphite electrode showed less current rate performance than the positive electrode for a similar mass loading (aprox. 4 mAh cm^{-2}). In order to improve the current rate performance of the negative electrode, spherical graphite active material could be employed to decrease the tortuosity of the electrode and enhance the solid diffusion inside the particles. Moreover, a decrease in electrode mass loading would reduce the energy density of the cell, but would increase the power density. In chapter 5 the interaction between both electrodes and the balance between energy and power density are discussed.

The parameters of the material processing stage (solid to liquid ratio, active material percentage, coater blade gap, calender roller temperature, and calender roller gap) were accounted for in the P2D model. To improve the accuracy of the model, rheology results and shrinkage factor in the drying step could be measured and employed. In order to get more accurate results, cells could be modelled taking into account the specific measurements for each cell, instead of taking the averaged value or the property calculated by the material-process-model relationships. However, this approach is not valid for optimisation, as no inverse cell design is possible with this approach.

A limited number of experiments were performed, which was designed in purpose, as usually the number of experiments are limited. Only six positive electrode conditions and two negative electrode conditions were studied. Those conditions were studied taking the relationships to build one general model. The model was calibrated according to the experimental-numerical cell performance to fit the results by the variation of the non-active volume fraction, exchange current density and solid diffusion coefficients. In general, the objective of using electrochemical models is to reduce the number of experiments to be done, therefore, if the same or more experiments are required for this methodology, the developed tool would not be practical. In summary, the half-cell models of lithium-graphite and lithium-NCA are able to predict the voltage response under different constant current rates. In addition, internal variables such as lithium concentration of the electrolyte and the solid lithium content of the electrodes can be analysed. Thus, the models built in this chapter were used for inverse cell design as set out in Chapter 5.

Chapter 5

MODEL-BASED DESIGN TOOL DEVELOPMENT AND VALIDATION WITH AN OPTIMISED EXPERIMENTAL CELL

This chapter presents the methodology for inverse battery design of a graphite-NCA cell. The general schema of the methodology linked to the previous chapters is presented in Figure 5.1.

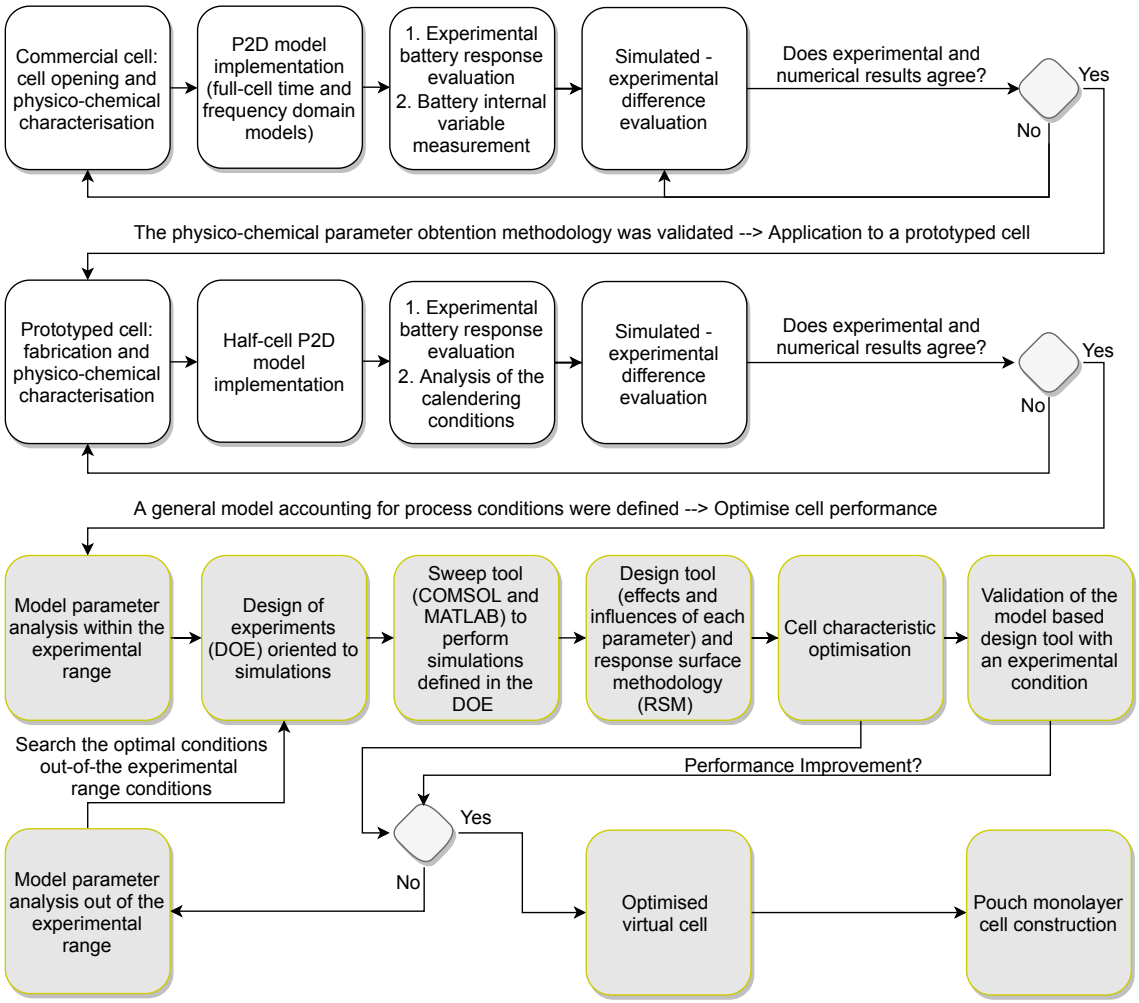

Figure 5.1: Main workflow of this research highlighting Chapter 5.

5.1 STATE OF THE ART IN BATTERY OPTIMISATION

Experimental examples for a wide range of optimisation purposes related to lithium-ion batteries are present in the literature. To cite some, Mathieu et al. [195] studied the cycling and calendar ageing processes with accelerated ageing using a DOE matrix, resulting in a double quadratic model to study the interaction effects and reduce the experimental cost. In another study, Yun et al. [196] analysed the relationship between capacity, applied stress and OCV of batteries. Furthermore, Rynne et al. [197] proposed a DOE to optimise the electrode formulation. These studies show that the use of DOE significantly reduce the amount of experiments and helps battery optimisation.

The numerical analysis of batteries has also been proposed in recent years, with early studies focusing on sensitivity analysis of lithium-ion cells [81,198]. It is important to note that this method could differ significantly if values are far from the studied case [81].

In later works, the main effects and interactions between parameter studies were developed following the DOE methodology. There is however, few numerical study which has used statistical analysis of design variables applied to electrochemical models for lithium-ion batteries [199,200]. In the work of Hosseinzadeh et al., they analysed an LFP/graphite battery with parameters taken from the literature. They varied four parameters (R_s, L^p, ε_s^p and C-rate) over three different levels with a study range selected from the literature. They performed a 3-level full factorial design, analysing the energy and power density responses of the cell. Their results included the main effects, interaction plots and contour plots. Nevertheless, they analysed only four positive electrode parameters in an arbitrary selected design space, and further work is needed to find a complete method to analyse and optimise cells. A similar approach was followed by Kim et al. [200]. In this case, eight parameters were varied (R_s^p, L^p, ε_s^p, R_s^n, L^n, ε_s^n, L^s, ε_s^s). However, none of the cases took into account process relationships and parameter feasibility into a prototyping line.

In other studies, design of experiments have been applied and optimisations based on neural networks have been proposed [191,201–203]. Nevertheless the results have not been experimentally validated. In addition, process constraints were not considered in any of the cases, thus further research should be conducted in this field.

Artificial intelligence and multiscale simulations are also becoming the subject of increased study. Those works apply AI to battery design from atomistic simulations to continuum cell level, and are currently under development [204,205].

5.2 STATE OF THE ART OF CELL ASSEMBLY, ELECTRODE BALANCING AND CELL FINAL VALIDATION

The aim of the cell assembly stage is to produce a functional battery in which good performance is obtained. In this stage, electrode notching, stacking, tab welding, cell housing, electrolyte filling, forming cycles, degassing, and final sealing steps are conducted. In Figure 5.2 the main schema of the remaining steps of the battery manufacturing process are presented.

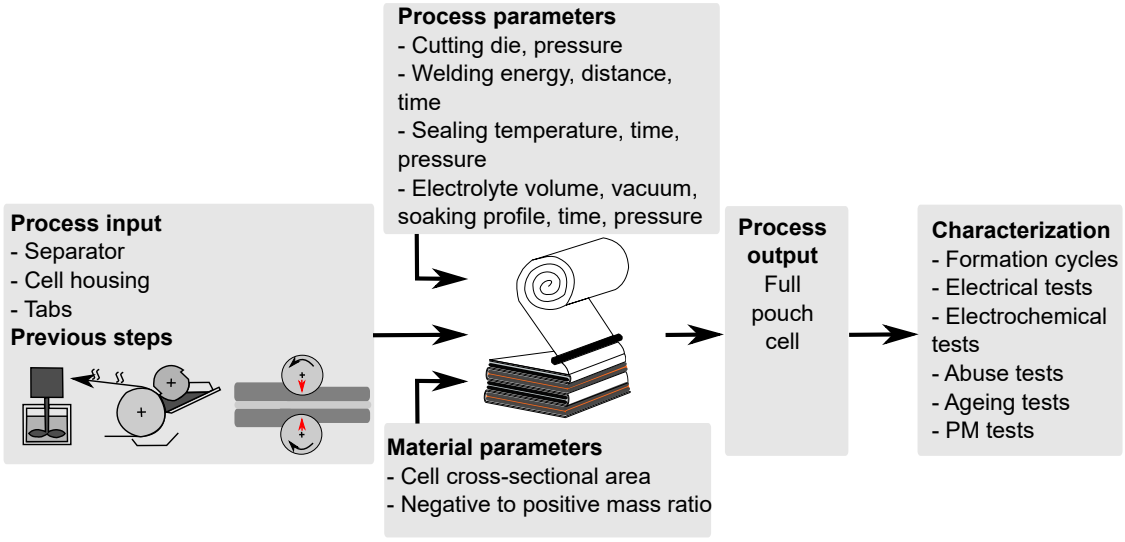

Figure 5.2: Cell assembly.

In addition to the inactive materials that take part in the electrode level (binder, conductive additives and current collectors), at the cell level, separators, cell housing and tabs are included for the proper working of the battery. These materials correspond to the additional raw materials that are needed in this stage. As they negatively affect the final specific energy and power of the device, they should be reduced to the minimum.

As the procedure for cell assembly also affects the final performance of the cell, many studies have been conducted [160, 206–209]. In the electrode notching step, the final electrode geometry (length and width) of the cell is defined. In this step, the laser cutting technique can be used to minimise the cutting edges, which deform the electrode and decrease cell performance [206].

The electrode stacking step can be performed using winding, stacking or folding methods [207], depending on whether the material provision (separator and electrodes) is continuous and/or discrete. If the electrodes are not aligned, this will result in an increase of the internal resistance, fast ageing and lower capacity retention [207]. Moreover, tab welding is required to join multiple sheets of electrodes. Different materials (copper, aluminium, nickel) and welding processes (resistance, laser, ultrasonic and mechanical welding) can be used [208].

Once the cell has three sealed sides, the filling of the electrolyte is accomplished. Sheng [209] concluded that the wetting rate of the electrolyte changes with pore structure, confirming the importance of calendering in the final cell performance. Finally, formation cycles, degassing and final sealing steps are executed. Chhor [210] studied the interface between the electrode and electrolyte, and the different formation protocols that could be used to obtain the maximum cell performance showing the importance of this step optimisation.

There are some characterisation techniques that can be used to finish the complete physico-chemical characterisation process of a cell. During assembly, techniques such as SEM can be used for the inspection of the separator elongation during the stacking process, the electrode cutting quality or the tab welding process [47]. In order to determine the ionic conductivity of the electrolyte, impedance spectroscopy can be employed.

When the cell assembly is finished, cycling behaviour of the cells is tested for cell evaluation and redesign. Researchers usually perform preliminary tests on coin cell formats, which are said to have the same tendencies as pouch cells [211]. Normally, several activation or formation cycles are performed, then performance in the short and long terms are evaluated. Pouch cells are constructed for final validations in which different electric and electrochemical tests could be performed. Three-electrode cells can be constructed to verify the electrode balancing correctness and provide insight into the cell formation cycles.

There are additional considerations to be taken into account when passing from electrode to full cell. The negative to positive electrode ratio should be determined (electrode balancing), as it is a critical aspect of optimisation and cell design. Even if the manufacturing process in all the steps is well controlled and executed, if the electrode balancing is not adequate the cell will not achieve optimal performance. Electrode balancing has been widely studied experimentally [42, 212, 213], and in Figure 5.3 an overview of the different approaches found in the literature are presented.

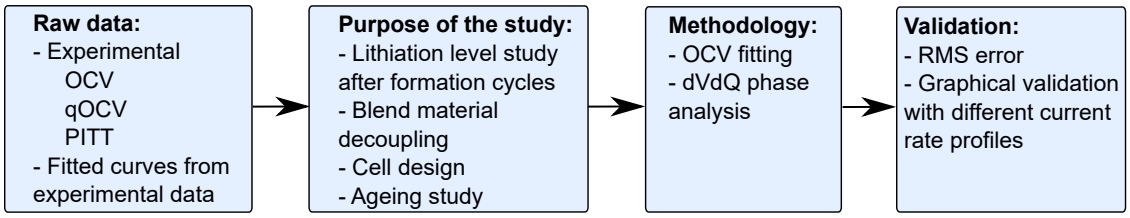

Figure 5.3: Electrode balancing review.

Open circuit potential data from both electrodes is necessary for electrode balancing analysis. This can be introduced into the analysis as a lookup table with the results obtained directly from experiments (OCV [50, 52, 83, 214], qOCV [50, 52, 56, 83, 136, 164] or PITT [137] techniques), or as a fitting function of the experimental data (a well known equation is the Redlich–Kister expansion [54, 165]).

Electrode balancing analysis is performed for different purposes, but most commonly, to assess the lithiation levels of the electrodes at a certain SoC when no information of formation cycles is available (usually in commercial cells) [50, 52, 56, 83, 214]. In addition, Mayur et al. [85] used fitting functions obtained from the literature to decouple the contribution of positive blend materials (NCA/LCO) from the performance of the cell. Rodriguez et al. [164] also took a blend positive material into account in their electrical model. Electrode balancing analysis could be used to study ageing [136, 137, 214], to determine the degradation causes of the cell. It could also be employed for electrode balancing improvements in the fabrication process of batteries, thereby preventing excessive deadweight [42] or limiting lithium plating.

Generally, two types of methodologies are employed in the literature to correlate the full cell OCV curve with the electrode OCV curves: optimisation routines and dVdQ analysis. Optimisation routines use a cost function to search the minimum RMS error of the cell voltage curve to assess the lithium content of the electrodes as a function of the SoC of the cell [83] (equation 5.1). However, this type of analysis is not always the best solution as the lithiation phases might not be well positioned. In order to ensure that the phases are well located, phase transitions of the materials by means of dVdQ analysis is needed [137]. The electrode balancing process is graphically validated with different galvanostatic profiles [50, 52, 56, 83, 85, 137, 214].

$$J = (U^{c}_{ocp,FC} - (U^{p}_{ocp} - U^{n}_{ocp}))^2 \tag{5.1}$$

Short-term performance tests are designed to determine the behaviour of the devices at the beginning of life (without ageing) under different conditions. Performance is commonly evaluated with charge and discharge pulses at a nominal current rate and different SoCs, and charge and discharge cycles at different current rates. Ageing tests on the other hand, are designed to evaluate the evolution of device performance during its cycle life. To quantify loss of performance, periodic check-up tests (CU) are performed. A complementary post-mortem analysis of all the tests is often carried out as it provides information about the degradation mechanisms that occur when certain current rate, temperatures or abuse tests are applied [136, 141]. Electrolyte degradation is commonly tested with NMR and gas chromatography-mass spectrometry (GS-MS) [141]. Other techniques include cyclic voltammetry, impedance spectroscopy and couloumbic efficiency determination tests. Moreover, thermal characterisation, abuse tests or specific tests (ultrasound characterisation, heat flux sensors) are also used to obtain further information about cell performance.

5.3 FULL CELL MODEL DEVELOPMENT AND VALIDATION

The electrode balancing was performed with average half-cell and full-cell curves, as the mass loading was equal for all the conditions. The results are plotted in Figure 5.4. 12 mm electrode discs (coin-full-cell and T-cell formats) were used for electrode balancing of the calendered graphite and NCA fabricated in the previous chapter in addition to half-cell data. C/30 galvanostatic discharge curves were selected as input data in all the cases.

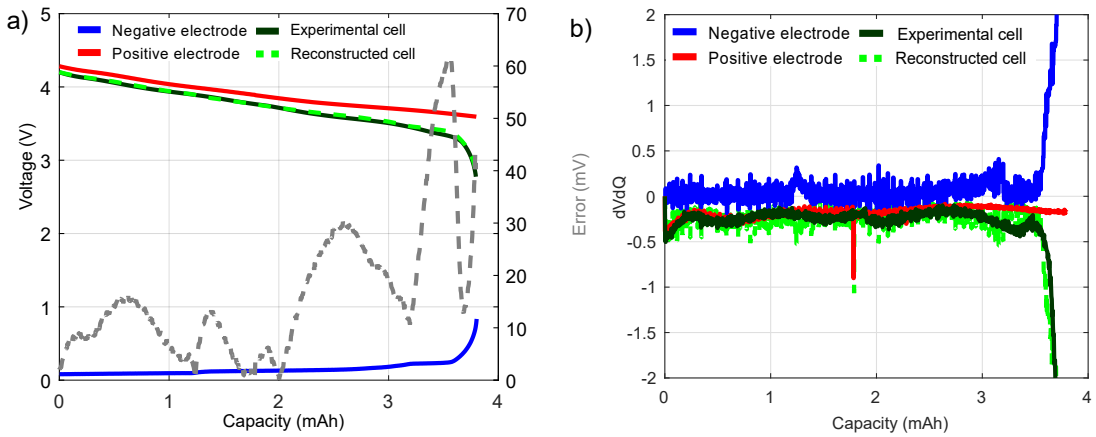

Figure 5.4: a) Experimental cell, reconstructed cell, negative and positive electrode voltage responses as a function of the cell capacity; b) dVdQ plot of the coin cell, reconstructed cell, negative and positive electrodes.

The maximum voltage error was found at the end of the discharge of the full-cell. Compared to the results obtained with the commercial cell, this error was slightly higher. This could be because different cells were used in the procedure, which could lead to higher deviations. Moreover, the commercial cell samples were taken from the same cell. Mass balance is defined with Faraday's law which relates mass loading with cell theoretical capacity (equation 5.2). Reversible capacities after formation cycles are used for electrode balancing determination.

$$(N:P)_Q = \frac{Q^{n}_{rev}}{Q^{p}_{rev}} = \frac{(\mathrm{nF})/(3600\mathrm{M}^{n}_{\mathrm{w}})\mathrm{m}^{n}_{AM} - Q^{n}_{irrev}}{(\mathrm{nF})/(3600\mathrm{M}^{p}_{\mathrm{w}})\mathrm{m}^{p}_{AM} - Q^{p}_{irrev}} \tag{5.2}$$

The OCV curve as a function of the lithium content of the electrodes and the utilization range of the full-cell is shown in Figure 5.5 a) and b).

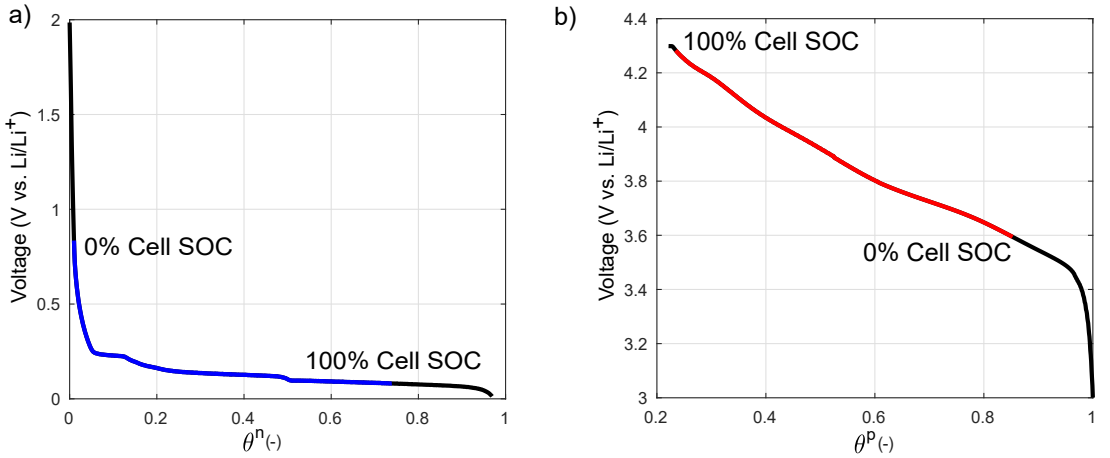

Figure 5.5: Equilibrium potential curve and electrode utilisation range for a) Negative electrode (blue); b) Positive electrode (red).

Electrode balancing is key to producing good quality and long lasting cells. Therefore, the interaction between electrodes was also studied so as to determine if the cell was well balanced. A negative to positive mass ratio of 1.1 - 1.2 is desirable (to prevent lithium plating on the negative electrode without increasing deadweight) [213]. The positive electrode utilisation range was between 0.8536 and 0.2354 of SoL, and the negative utilisation range between 0.7390 and 0.0098 of SoL. In addition, a f_{excess} of 0.2408 and f_{loss} of 0.1464 were obtained. An approximate excess of 24% in the negative electrode was calculated for this averaged cell, which was in between the targeted value.

In Figure 5.6 a) and b) the cell performance at different current rates for the studied conditions of Chapter 4 are presented.

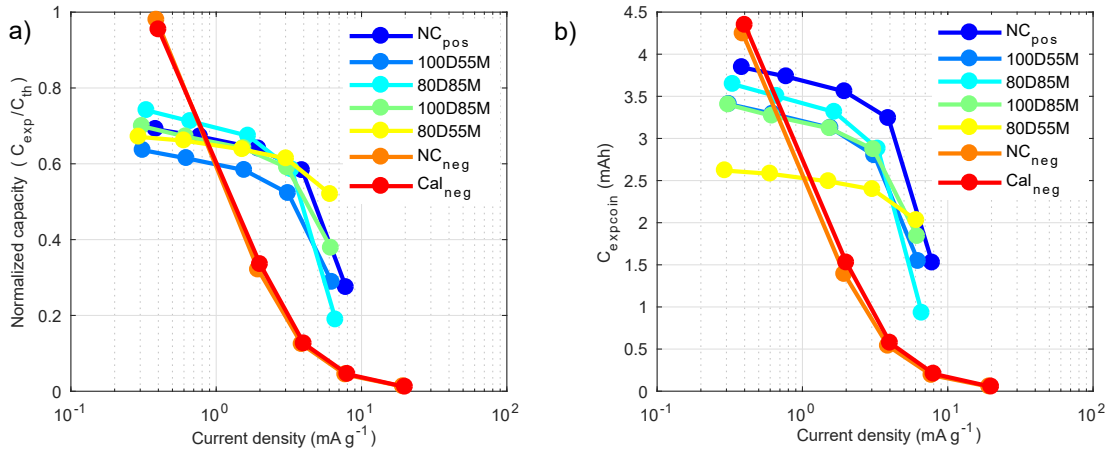

Figure 5.6: Rate capability performance comparison of both electrodes a) Normalised capacity by weight and theoretical capacity; b) Non-normalised capacity.

Of all the studied conditions of Chapter 4, the roller temperature of 353 K and roller gap of 55 µm presented the best capacity performance over the current rate when the cell is normalised by weight and theoretical capacity, although slightly inferior capacity was obtained at low current rates. A sharp capacity depletion in the negative electrode is shown in Figure 5.6 which particularly has an effect at high current rates. The non-calendered

and calendered negative electrodes were close to each other even when a compression rate of 37.56% was applied. The electronic conductivity and adhesion strength should have improved the performance, but the pore size was decreased considerably and particle cracks might have appeared with a detrimental effect on the electrode capacity [162].

In Figure 5.6 b) the non-normalised coin half-cell capacity is plotted showing that the weight normalisation plays an important role in data analysis and modelling. The specific weight of the analysed experimental cell determines the experimental mass loading for each electrode and electrode balancing. In the averaged model, these weight differences were not taken into account (nor in the optimisation procedure), as those experimental values were not available when inverse cell design was performed. However, when directly comparing experimental and numerical, the experimental factors should be considered, thus, modifying certain parameters slightly.

The full-cell model to check the electrode balancing assessment was performed for 353 K and roller gap of 55 µm, in which an experimental 1.11-1.2 capacity ratio was calculated based on equation 5.2. In Figure 5.7 a) the comparison between experimental and simulated galvanostatic discharge performance at different current rates is presented.

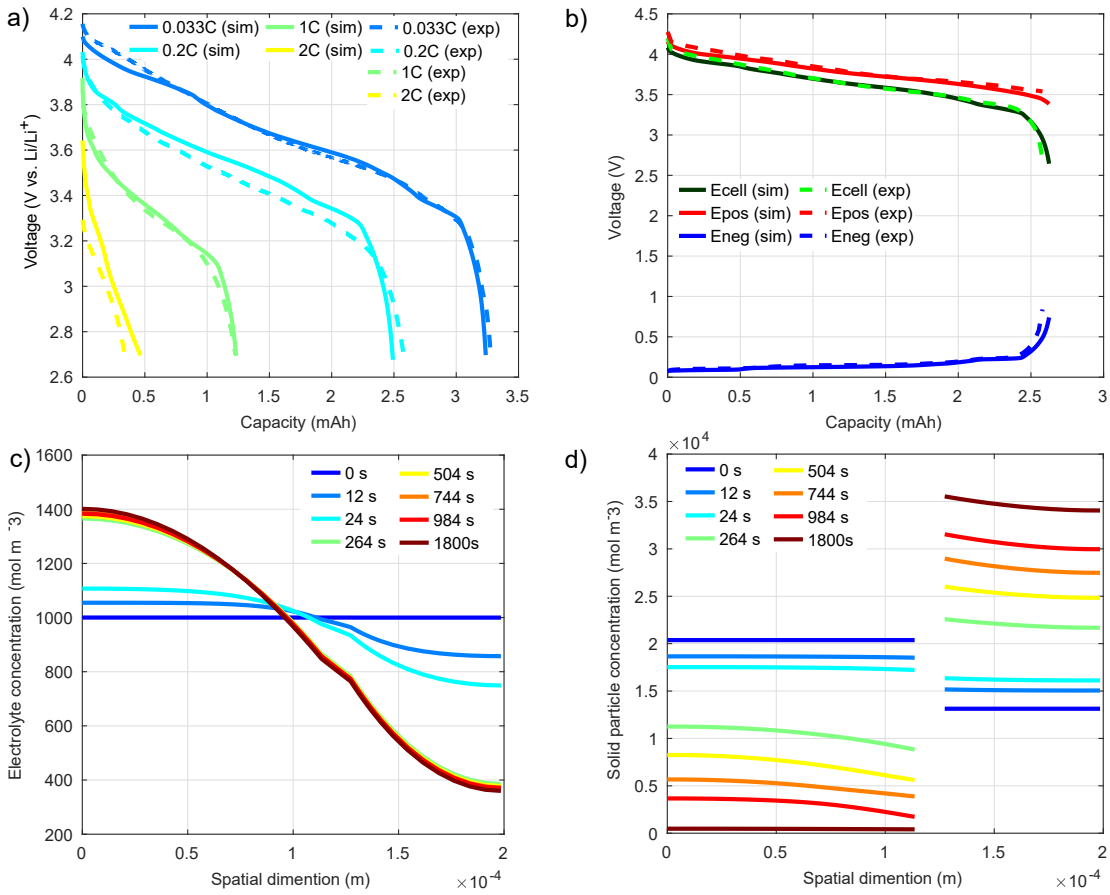

Figure 5.7: a) Comparison of the experimental and simulated rate capability at 298 K for the 80D55M positive and calendered negative cell; b) Voltage evolution of a three electrode experimental T-cell at 298 K and the comparison with the simulated responses at C/10; c) Spatial and time evolution of the state of lithiation of electrolyte concentration for 1C constant current discharge at 298 K; d) Spatial and time evolution of the state of lithiation of the active materials for 2C constant current discharge at 298 K.

In Figure 5.7 b) the experimental electrode balancing in the T-cell configuration at C/10 on discharge is shown. The same methodology of correction factors used in Chapter

3 was applied to the capacity deviations (the capacity ratio between coin full cell and Tcell was set to 1:0.85). Usually, electrode balancing is assessed at low current rates, in which the transport and kinetic limitations of the electrodes are assumed to be negligible. However the cell could be unbalanced at higher current rates. In the present research, the negative electrode performance in a 1C discharge for a half-cell configuration was lower than the capacity of the positive electrode.

In Figure 5.7 c) and d) the evolution of electrolyte concentration and lithium inside particles as a function of discharge time at 1C is shown. When the lithium concentration inside the negative active material reaches almost zero, the electrochemical reaction stops. In the scenario of Chapter 4 the negative electrode limitations were visible, which were then reproduced in full-cell configuration. These limitations of the negative directly affect the final cell performance, therefore, even if the positive electrode calendering process is optimised, no performance improvement will be noticed. The limitations of the negative electrode lead to slow intercalation kinetics and lithium transport inside particles [150]. These could be attributed to high mass loadings, its porous structure, and physical properties. In the next section, different options for cell improvement are presented.

5.4 MODEL-BASED DESIGN TOOL

In this section the model-based design tool is presented for different battery design strategies. The aim of this methodology is to provide a versatile and fast design tool in which design parameters are varied to find a tailored power to energy ratio.

5.4.1 Methodology implementation and battery design strategies

In Figure 5.8 the model-based design tool workflow is presented.

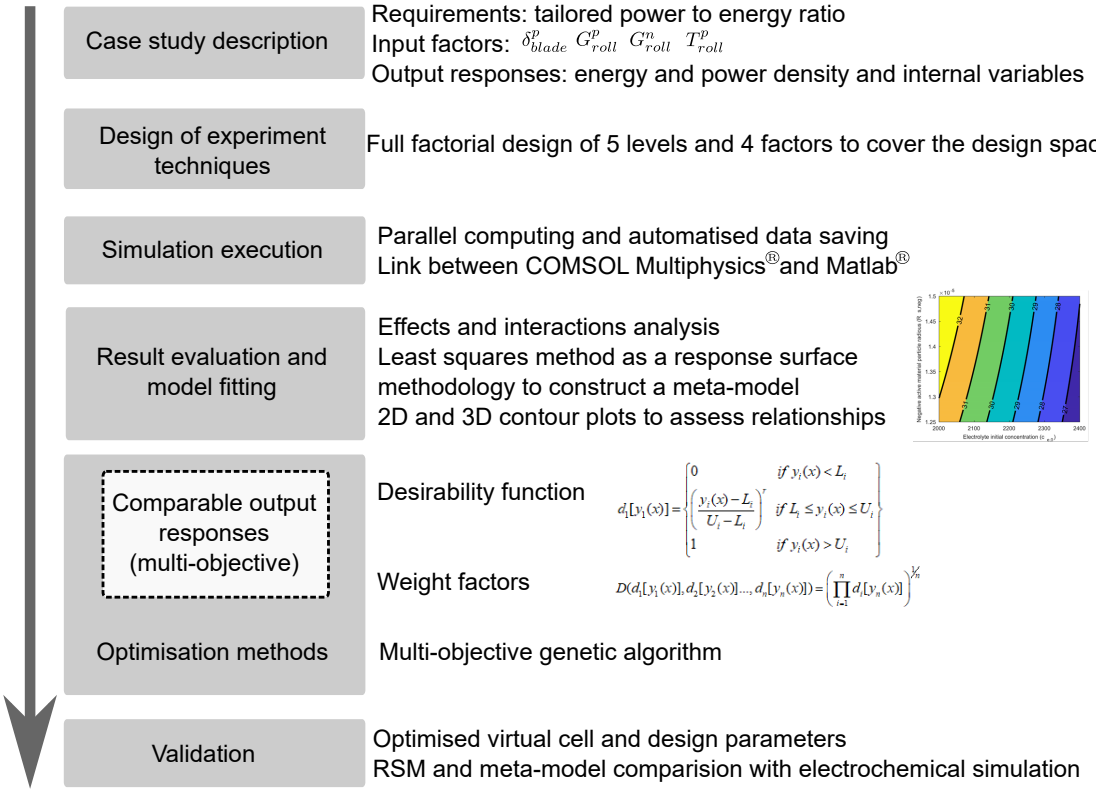

Figure 5.8: Optimisation methodology for the selected case study.

This methodology (design of experiments, sweep tool, design tool and optimisation) was presented in the COMSOL conference in Lausanne as a poster and paper contribution (conference paper C4). In that conference, model parameters were taken from the Doyle cell [49] and the specific energy response was presented with a three-level full factorial design with 3D surface plot, 2D contour plots, main effects and interaction effects.

This methodology is divided into five parts: (i) Case study description depending on the design strategy; (ii) Design of experiment technique selection; (iii) Simulation execution; (iv) Model fitting, comparable output responses and multi-objective optimisation; (v) Optimised virtual cell evaluation and design parameters. The electrochemical model was kept simple with the intention of limiting the computational cost of each simulation.

5.4.1.1 *Case study description depending on the design strategy*

The cell could be optimised to give the highest energy, the highest power or a tailored energy to power balance. The different strategies and main differences between energy, energy-power balanced and power cells are presented in Figure 5.9.

Three different case studies were defined. The first one is related to the optimisation in the same range of the experimental analysis of Chapter 4. The second case study extrapolate the obtained results of the case study 1 for a different design scenario (out of range of the experimentally measured conditions). Finally, in the third case study further design strategies that could improve cell performance but that were not tested experimentally are discussed.

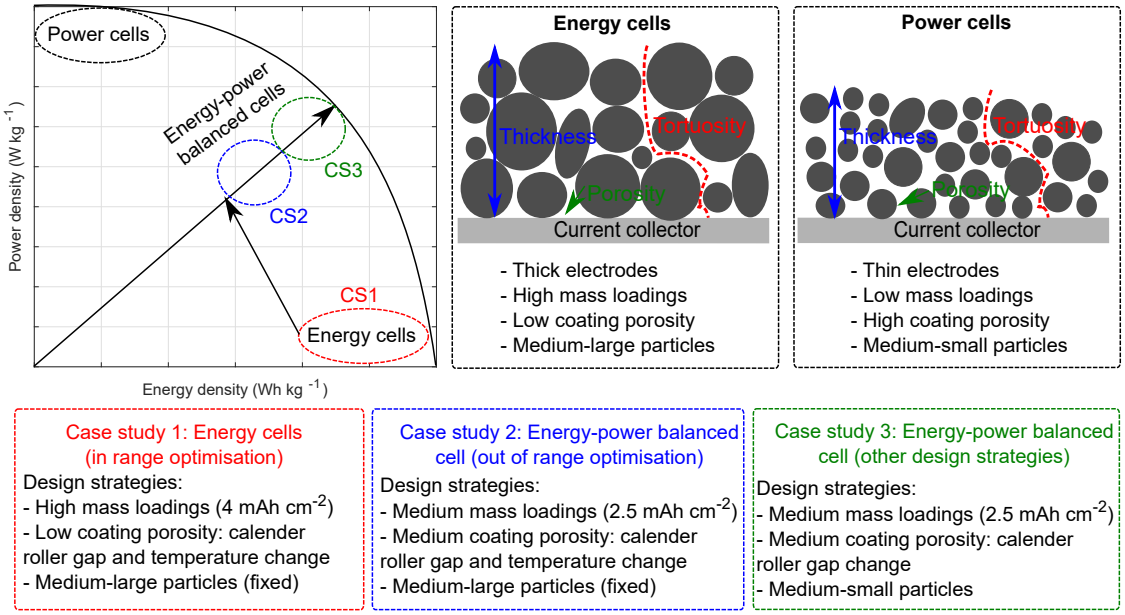

Figure 5.9: Battery design strategies and relationship with design parameters.

In the first case study (CS1), an analysis of the best option in the range of Chapter 4 conditions are presented. The cell is optimised in specific energy with mass loadings of approximately 4 mAh cm^{-2}. Between cells with the same loading, different calendering conditions were simulated to find a compromise between lowering electrode porosity and increasing accessible electroactive area. When a high energy is required, the active material content per electrode should be increased to the maximum. To achieve that, thicker electrodes with high mass loadings are fabricated, and medium to large particles are used. In addition, to increase the density of the electrodes, low porosities are searched. In thick

electrodes, the mass transport becomes limiting due to the difficulty of lithium ions to diffuse throughout the thickness of the electrode.

In the second case study, an energy-power balanced cell was proposed (CS2). To achieve that, process relationships extrapolation are required and their validity out of the experimentally characterised range was evaluated. In this thesis, the used active material was not changed, therefore, smaller particles could not be used to obtain a power cell.

In the third case study (CS3), design strategies are proposed in a numerical environment to analyse the influence of different parameters (thin electrodes and particle size). Power cells could provide high specific power but store lower energy. This could be achieved decreasing the thickness of the electrodes and, therefore, the mass loading. Moreover, the increase of conductive additives could be beneficial, allowing faster kinetics. Higher porosities than for the energy cell are required to allow lithium ions to diffuse correctly.

The interrelations between Chapter 4 and the case studies of Chapter 5 are defined in Figure 5.10, in which the scale up of the prototype cells is given (starting from half-cells to pouch monolayer cells).

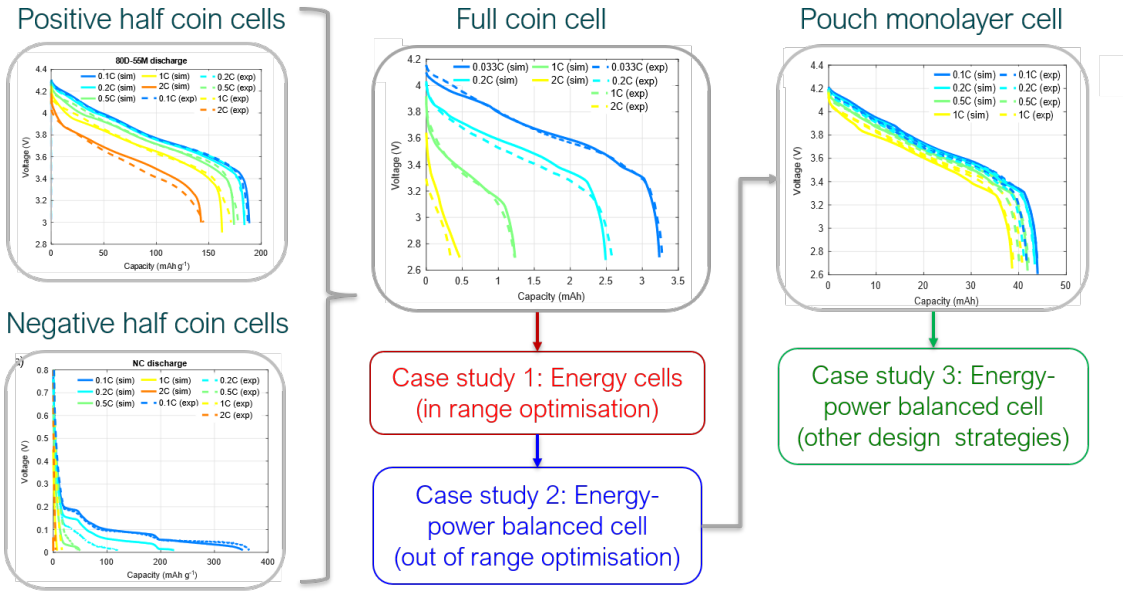

Figure 5.10: Scaling up schema and relationship with the case studies of this Chapter.

In Figure 5.11 the case study definition workflow is shown. First of all independent factors were selected, then the study space was assessed taking into account material and process constraints. Finally output responses with the sufficient degree of sensitivity were selected.

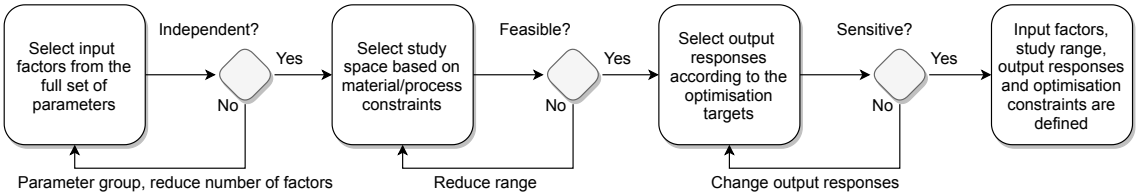

Figure 5.11: Case study definition workflow.

In Table 5.1 the varied parameters in each study, the range of study and the criteria for upper and lower bound selection are described.

Table 5.1: Parameter, range and criteria for each case study.

Parameter	CS1	CS2	CS3	Criteria
δ^p_{blade} (µm)	200 ± 10	100 ± 10	70	$\pm$ 10 (µm) variation is considered as the maximum expected variability in production[*1]
T^p_{roll} (K)	363.15 ± 10	363.15 ± 10	353.15	The parameter has studied within the experimental range[*2]
G^p_{roll}[*3] (µm)	$(30 \pm 10)\%\ \delta^p_{dry}$	$(30 \pm 10)\%\ \delta^p_{dry}$	$(20 \pm 20)\%\ \delta^p_{dry}$	CS1 and CS2: variation in the expected optimal range; CS3: full variation range[*4]
G^n_{roll}[*3] (µm)	$(30 \pm 10)\%\ \delta^n_{dry}$	$(30 \pm 10)\%\ \delta^n_{dry}$	$(20 \pm 20)\%\ \delta^n_{dry}$	CS1 and CS2: variation in the expected optimal range; CS3: full variation range[*4]
R^p_s (µm)	N.A.	N.A.	5 ± 2	Based on [216]
R^n_s (µm)	N.A.	N.A.	6 ± 2	Based on [216]

[*1] We expect this parameter to impact directly to cell capacity. Literature reports xxxx value for similar electrodes when semi-automated equipments are used.
[*2] No much influence was found after the experimental analysis when 20 K are varied.
[*3] The roller gaps are defined according to a percentage reduction of the dry thickness of the electrode ($G_{roll,per}$) (removing first the current collector thickness).
[*4] The variation optimal range (CS1 and CS2) was set according to Chapter 4 results, in which the optimal range is not expected to happen at very low compression rates.
N.A.: Not applicable.

5.4.1.2 *Design of experiment technique selection*

Statistical-based and space filling techniques were selected as the design of experiment technique in order to study the effects and interaction between the studied parameters. A full factorial design of 5 levels and 4 factors was defined (625 simulations).

5.4.1.3 *Simulation execution*

The simulation execution should have a plan to collect the representative data for further analysis. In Figure 5.12 the program structure and interactions between Comsol Multiphysics® and Matlab® to run the simulations is presented.

First of all, the parameters were loaded and the DOE was constructed. Then, a number of Comsol Multiphysics® ports were opened to establish the link between programs. Finally, parallel computing was used to reduce computational time, thereby achieving faster results. All the output responses were saved for data analysis, meta-model building and optimisation.

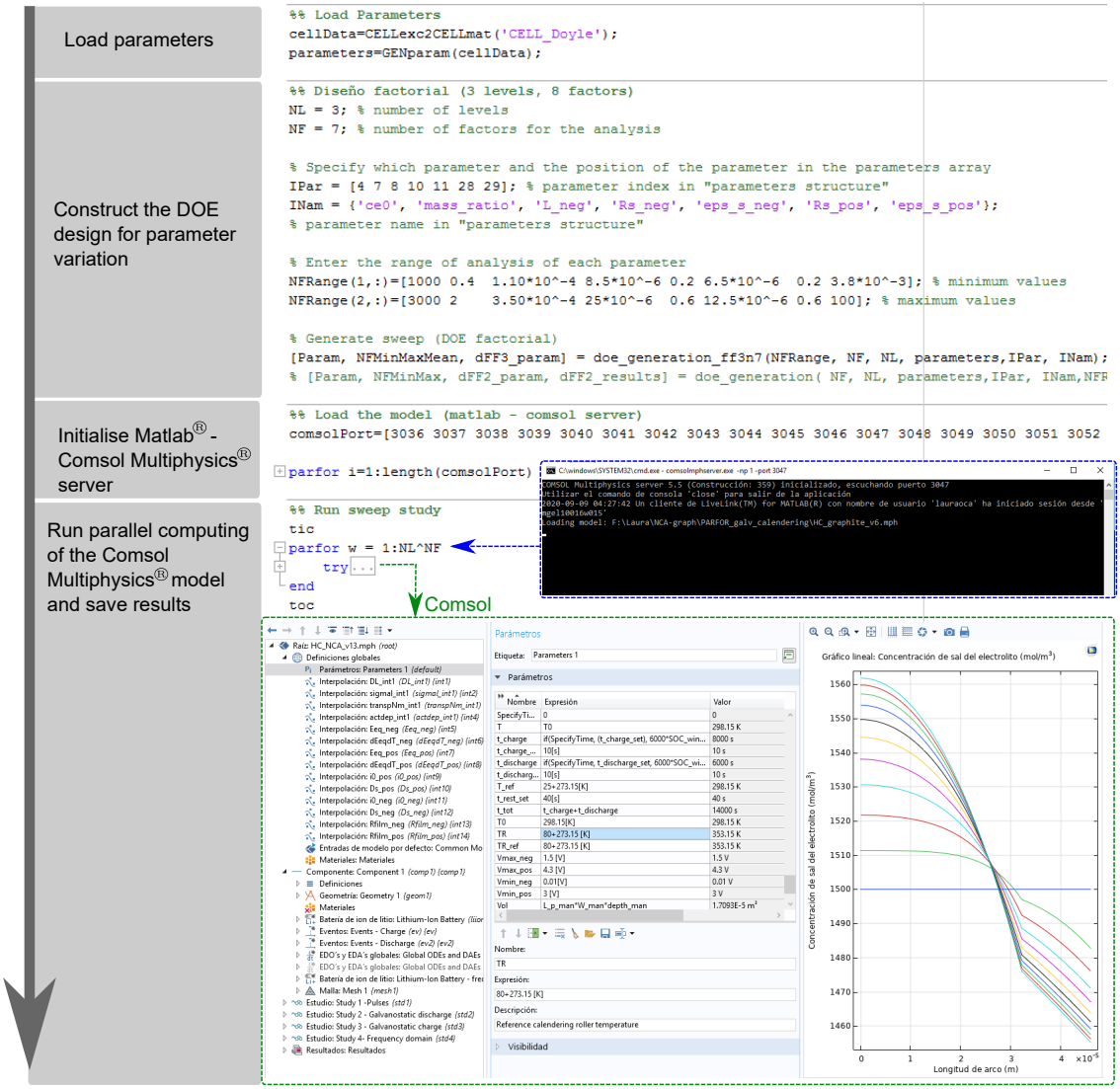

Figure 5.12: Design of experiment program structure in Matlab® and link with Comsol Multiphysics®.

Figure 5.13 presents an example in which several simulations are performed with the same model to quantify the computational time required, depending upon whether 1 or 20 workers are used to solve 1, 20 or 100 simulations. The graph clearly shows that the use of 20 workers in every batch of simulations achieves considerable time saving.

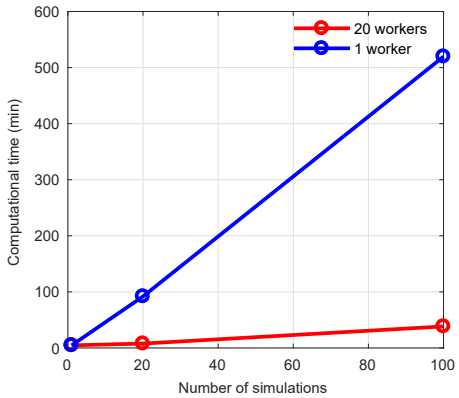

Figure 5.13: Computational time as a function of the number of workers and simulations.

5.4.1.4 *Model fitting, comparable output responses and multi-objective optimisation*

The analysis of variance was performed to confirm that the selected factors are significant for the selected responses (specific energy and power). In this research, all the p-values of the main factors and interactions were close to zero for the plotted results, which means that the factors are significant. A second order model was employed for data fitting of the output responses according to equation 5.3 [100, 101]. The analysis of variance results of both responses and the fitting coefficients of the model are presented in Appendix B.

$$y = \beta_0 + \sum_{i=1}^{k} \beta_i x_i + \sum \sum_{i<j} \beta_{ij} x_i x_j + \sum_{i=1}^{k} \beta_{ii} {x_i}^2 + error \tag{5.3}$$

where y is the response, x_i are the design factors, k is the number of factors, and β the terms which correspond to the fitting coefficients.

Once the meta-model is obtained, in order to reach an optimal design, the output responses should be combined and analysed together. If multiple responses need to be optimized simultaneously, desirability function could be used to obtain comparable output responses. The desirability function $d_i(y_i)$ approach has been used to transform each output response (y_i) into a 0 to 1 response in order to perform the maximization of the aggregate desirability value. With this approach comparable magnitude that goes from zero to one are obtained. The desirability function is calculated as [101]:

$$d_1[y_1(x)] = \left\{ \begin{array}{ll} 0 & if\ y_i(x) < L_i \\ \left(\frac{y_i(x)-L_i}{U_i-L_i}\right)^r & if\ L_i \leq y_i(x) \leq U_i \\ 1 & if\ y_i(x) > U_i \end{array} \right\} \tag{5.4}$$

where L_i and U_i are the low and up values of the response and r is a weight factor.

Moreover, different weights could be applied to establish the priority of the optimization. Then, the objective function is built as:

$$D(d_1[y_1(x)], d_2[y_2(x)]..., d_n[y_n(x)]) = \left(\prod_{i=1}^{n} d_i[y_n(x)]\right)^{1/n} \tag{5.5}$$

where D is the aggregate desirability value.

Genetic algorithms were used for optimising the output responses. Genetic algorithms try to mimic the evolution of species. First of all, the initial population is randomly generated. Then, the fitness function (or objective function) is evaluated. If the stop criteria is fulfilled, then the optimisation problem is finished with a new optimal solution. Sometimes the number of iterations exceeds the specified limit, and therefore the optimisation is not successful. If the stop criteria is not reached, a new set of designs is created (new population), which improves the average fitness value of the previous population. To this end: reproduction, crossover and mutation steps are accomplished [215]. If multi-objective optimisation is desired, a multi-objective genetic algorithm (MOGA) can be used, which is a variation of GA [100].

5.4.1.5 *Optimised virtual cell evaluation and design parameters*

The results obtained with RSM are based on a quadratic model which is useful to obtain faster optimisation results. Nevertheless, the electrochemical model responses should be check to confirm that the surrogate model of the RSM methodology is suitable.

5.4.2 Case study 1: Energy cell

This case study was defined to determine the best calendering condition between the analysed experimental range. High mass loadings of about 4 mAh cm^{-2} were simulated. Additionally, a small variation of the coating thickness were assessed to observe the uncertainties of the process.

5.4.2.1 *Case study description*

In the present study, parameters related to electrode manufacturing were selected, which could easily be set in the prototyping line. The parameters and the studied space are presented in Table 5.2 and represent the coater gap thickness of the positive electrode (δ^p_{blade}), the calender roller gap of positive (G^p_{roll}) and negative electrodes (G^n_{roll}) and calender roller temperature of the positive electrode (T^p_{roll}). The roller gaps were varied according to a percentage variation of the dry thickness of the electrode. Therefore, the factors that are varied in the DOE are $G^p_{roll,per}$ and $G^n_{roll,per}$ which impacts in the calender roller gap as presented in Table 5.2.

The sampling technique was defined according to factor sensitivities. For example, a three level full factorial design would not be enough to describe the behaviour of output responses, therefore, a five level design should be selected. The studied point variation is a compromise between detecting a significant change in the response while maintaining its linearity. Therefore, the levels of the study should be defined accordingly. Once the parameters and the maximum variation range were assessed, the model responses were selected. In this case study, not only specific energy (E_m), but also specific power (P_m) was selected for optimisation. Discharges at low (C/30) and high current (1C) rates were analysed.

Table 5.2: CS1: Input factors, design space and selected variations.

Parameter	Low (-2)	Low (-1)	Mean (0)	High (+1)	High (+2)
δ^p_{blade} (µm)	190	195	200	205	210
T^p_{roll} (K)	353.15	358.15	363.15	368.15	373.15
${G^p_{roll}}^{*1}$ (µm)	20% δ^p_{dry}	25% δ^p_{dry}	30% δ^p_{dry}	35% δ^p_{dry}	40% δ^p_{dry}
${G^n_{roll}}^{*1}$ (µm)	20% δ^n_{dry}	25% δ^n_{dry}	30% δ^n_{dry}	35 % δ^n_{dry}	40% δ^n_{dry}

^{*1} The roller gaps are defined according to a percentage reduction of the dry thickness of the electrode ($G_{roll,per}$) (removing first the current collector thickness).

5.4.2.2 *Output response evaluation and multi-objective optimisation*

In Figure 5.14 a) the main effect of the positive blade thickness for the specific energy is presented for a C/30 discharge. At very low current rates, the differences between different calendering conditions are not significant as the mass transport is not the predominant limiting mechanism. When positive blade thickness is varied (or mass loading) due to the uncertainties of the fabrication process, cell capacity is changed, and therefore, a small variations of specific energy and power could be noticed. Additional information about the analysis of variance, the obtained regression parameters and the pareto front of all the simulations can be found in the Appendix B in which five different clusters could be distinguished, corresponding to positive blade variations.

When higher rates (1C) are analysed, the specific energy decreased as the mass transport limitations start to appear. In such case, higher dispersion between calendering conditions could be found. In Figure 5.14 b) the main effect for the negative electrode calender roller gap percentage at 1C is presented. Based on those results, a higher electrode thickness and a moderate compression rate of the negative electrode (0.2% corresponds to 49 µm in this case) should increase the cell performance in terms of specific energy.

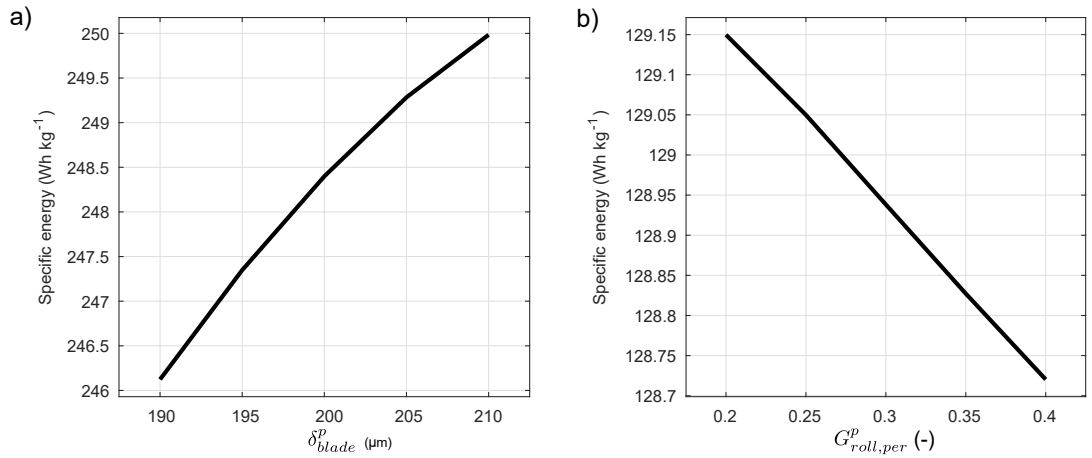

Figure 5.14: CS1: Main effect for specific energy (Wh kg^{-1}) for a) a C/30 galvanostatic discharge of the δ^p_{blade} parameter; b) 1C galvanostatic discharge of the $G^n_{roll,per}$.

The interaction plots of specific energy at 1C are shown in Figure 5.15. The interaction plots confirm that high levels of positive electrode roller gaps (calendering effect) are desirable to maximise specific energy, which are in good concordance with the literature.

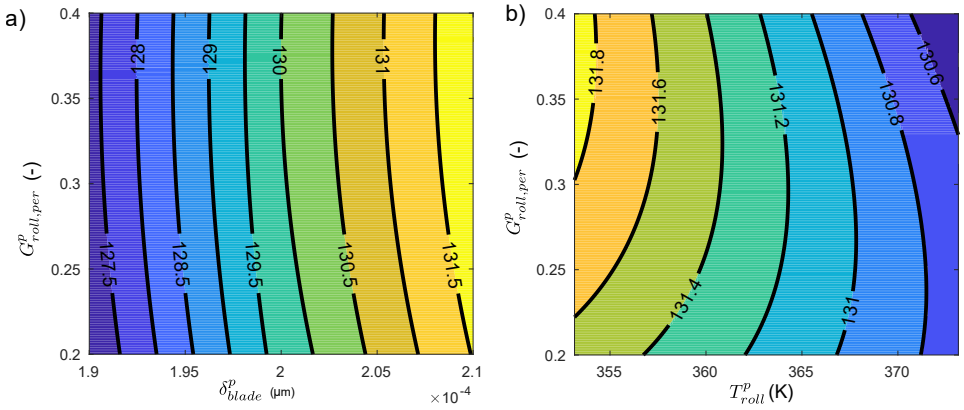

Figure 5.15: CS1: Interaction effects for specific energy (Wh kg^{-1}) for a 1C galvanostatic discharge: a) $\delta^p_{blade} : GR^p_{diff,per}$; b) $T^p_{roll} : G^p_{roll,per}$.

In Figure 5.16 a 3D contour plot comparing the obtained response with the RSM and electrochemical model are presented for $\delta^p_{blade} : G^p_{roll,per}$ interaction. A good correlation is found for the selected parameters and studied range.

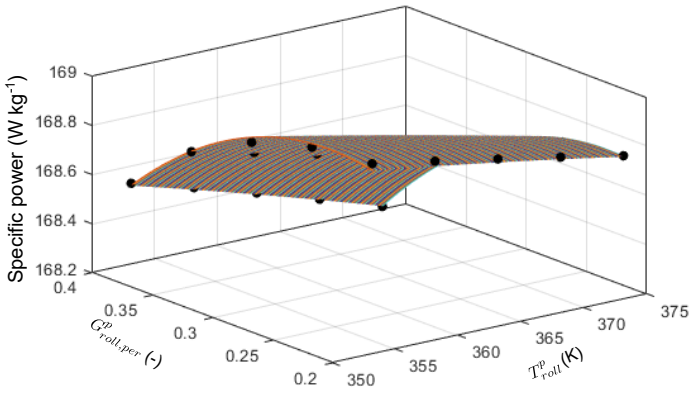

Figure 5.16: Comparison between the metamodel (surface) and the electrochemical model (dots) for $\delta^p_{blade} : G^p_{roll,per}$ interaction for specific power at 1C discharge.

Moreover, as it was expected, the maximum specific power was obtained with low level values of coater blade thickness of the positive electrode (Figure 5.17). The temperature had less influence in the power and energy performance than the rest of the parameters. The experimental results also showed a slow increase in performance with 20 K decrease of roller temperature.

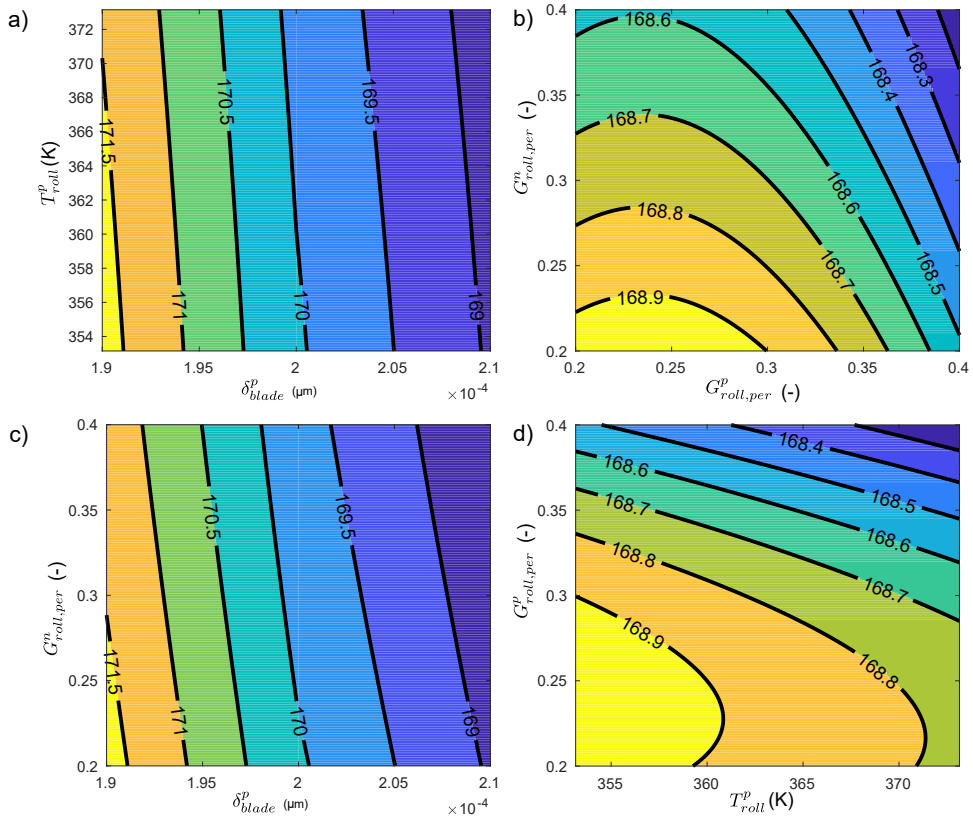

Figure 5.17: CS1: Specific power (W kg^{-1}) interaction effects (1C discharge): a) $\delta^p_{blade} : T^p_{roll}$; b) $G^p_{roll,per} : G^n_{roll,per}$; c) $\delta^p_{blade} : G^n_{roll,per}$; d) $T^p_{roll} : G^p_{roll,per}$.

Based on the optimisation analysis, in Table 5.3 the optimal ranges of the parameters are highlighted in green. In the Appendix B.1 the results of the optimisation is plotted. Between the studied range, 200 µm of positive electrode blade thickness was found to maximise specific energy and power. The influence of thickness variations (lower mass loadings) are discussed in case studies 2 - 3.

Table 5.3: CS1: Optimal design parameter range.

Parameter	Low (-2)	Low (-1)	Mean (0)	High (+1)	High (+2)
δ^p_{blade} (µm)	190	195	200	205	210
T^p_{roll} (K)	353.15	358.15	363.15	368.15	373.15
G^p_{roll} (µm)	20% δ^p_{dry}	25% δ^p_{dry}	30% δ^p_{dry}	35% δ^p_{dry}	40% δ^p_{dry}
G^n_{roll} (µm)	20% δ^n_{dry}	25% δ^n_{dry}	30% δ^n_{dry}	35% δ^n_{dry}	40% δ^n_{dry}

As regards to calendering process parameters, the interaction plots shows that lower roller temperatures could be beneficial for the performance. Moreover, a temperature increase of 20 K does not change strongly the performance, thus, from a fabrication point of view, the low temperature level is commonly desired, as the energy consumption of the process would be reduced. Experimentally, 7 (µm) and 55 (µm) roller gaps were studied. In simulation, a middle optimal point was found at 23 (µm) ($G^p_{roll,per}$ 0.25). A calender roller gap of 39 (µm) ($G_{roll,neg} = 0.2$) was determined as the best solution for the negative electrode. That value was found to be in between the non-calendered and calendered negative electrode of reference (63.9 (µm) or $G^n_{roll} = 0.33$).

As important as these parameter changes is the electrode balancing and electrolyte and active material limitations. This case study was performed with an ideal mass balance of 1.1:1. When electrode balance tends to the ideal case, the loss of lithium inventory of the positive electrode is maintained to the minimum possible to form the SEI layer and the graphite electrode is not oversized. The electrolyte and active material concentrations during 1C discharge for the optimised virtual cell is presented in Figure 5.18. The simulations presents a similar behaviour of experimental conditions, in which the negative electrode is the limiting factor of the cell.

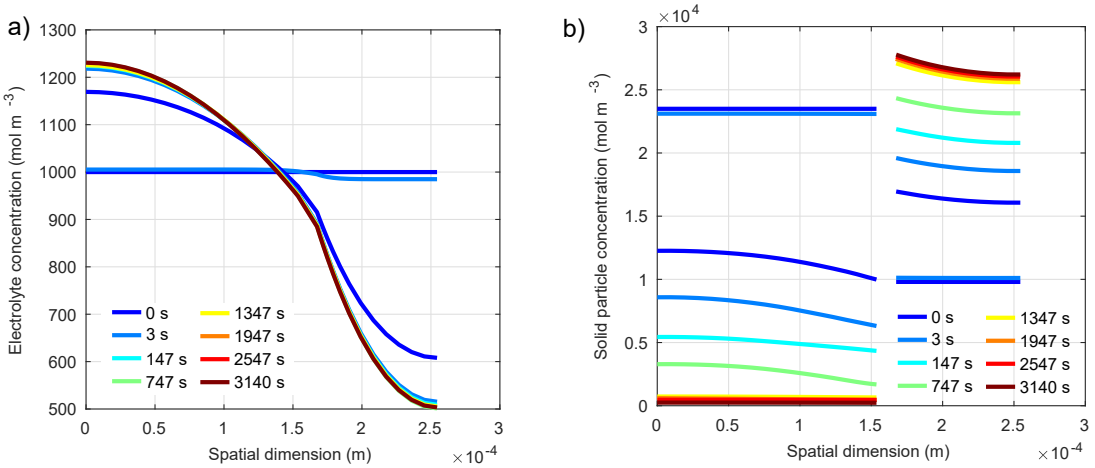

Figure 5.18: a) Spatial and time evolution of the state of lithiation of electrolyte concentration for 1C constant current discharge at 298 K ; b) Spatial and time evolution of the state of lithiation of the active materials for 1C constant current discharge at 298 K.

5.4.2.3 *Optimised virtual cell evaluation and design parameters*

As the optimisation is based on the second order regression model, the accuracy of the predicted values could differ from the obtained electrochemical model responses. To conclude the analysis, the optimised design factors were run in COMSOL Multiphysics® software and the results were compared with the RSM results. The design parameters used and their output responses are shown in Table 5.4. The RSM results are in good

agreement with the electrochemical responses, therefore, the factor variation range and selected regression model are suitable for this analysis.

Table 5.4: RSM model and P2D model output responses.

	RSM	P2D
δ^p_{blade} (µm)	195	195
T^p_{roll} (K)	353.15	353.15
$G^p_{roll}{}^{*1}$ (µm)	0.25	0.25
$G^n_{roll}{}^{*1}$ (µm)	0.20	0.20
E_m (Wh kg^{-1})	128.78	129.2
P_m (W kg^{-1})	170.78	169.8

5.4.3 Case study 2: Energy-power balanced cell

The second case study is defined as an approach to balance the cell not only at low current rates, but also at moderate-high rates (1C). In order to obtain faster kinetics with the negative electrode, the mass loading of the electrodes were set to approximately 2.5 mAh cm^{-2}. For that, the positive and negative coater gap were decreased. Based on the experience of CIC energiGUNE prototyping line, 100 µm of positive electrode coater blade thickness was selected. In such conditions, different coating densities were analysed with the optimisation tool to set the optimal conditions for cell fabrication.

5.4.3.1 *Case study description*

The same procedure of case study 1 was applied for the parameters and ranges listed in Table 5.5. The unique difference between both case studies was the mass loading of the electrodes, which is defined when the positive electrode coater blade thickness is varied.

Table 5.5: CS2: Input factors, design space and selected variations.

Parameter	Low (-2)	Low (-1)	Mean (0)	High (+1)	High (+2)
δ^p_{blade} (µm)	90	95	100	105	110
T^p_{roll} (K)	353.15	358.15	363.15	368.15	373.15
G^p_{roll} (µm)	20% δ^p_{dry}	25% δ^p_{dry}	30% δ^p_{dry}	35% δ^p_{dry}	40% δ^p_{dry}
G^n_{roll} (µm)	20% δ^n_{dry}	25% δ^n_{dry}	30% δ^n_{dry}	35% δ^n_{dry}	40% δ^n_{dry}

5.4.3.2 *Process relationship extrapolation*

Different considerations before using the model-based design tool were required to generalise the model. The following assumptions were assessed to extrapolate the obtained relationships in the non-studied conditions:

- For the positive electrode, the differences between δ_{wet} and δ_{blade} and shrinkage factor were related with a percentage that is proportional to the δ_{wet} variation with respect to the reference δ_{wet} at 200 µm (see equations 5.6 and 5.7).

$$\delta_{blade-wet} = \delta_{blade-wet,ref}\left(\frac{\delta_{blade}}{\delta_{blade,ref}}\right) \tag{5.6}$$

$$Schrinkage = Schrinkage_{ref} \left(\frac{\delta_{blade}}{\delta_{blade,ref}} \right) \tag{5.7}$$

- An additional coating gap for the negative electrode (250 µm) was experimentally fabricated to improve the empirical relationship of this electrode.
- The corrections applied after the numerical-experimental comparisons of Chapter 4 were used as calibrated data, as they are assumed to be more representative that the original values. This directly affects the exchange current density, solid diffusion coefficient and inactive part of the solid volume fraction.
- The electrode balancing was maintained constant to 1.1:1 to prevent lithium plating and avoid excessive deadweight of the negative electrode. This relationship was set considering the reversible capacities of both electrodes (equation 5.2). A reversible capacity of 350 mAh g^{-1} and 200 mAh g^{-1} for negative and positive electrodes respectively were used for the calculations. These values were taken based on the half-cell experiments of Chapter 4. The negative electrode thickness was fixed based on the positive electrode thickness and the electrode balancing. The maximum achievable loading capacity for the negative electrode was set to > 0.12 kg m^{-2} which corresponds to 4.5 10^{-4} m of coater gap thickness, according to experimental results of Chapter 4.
- The cross-sectional area was set to the positive electrode area of the pouch monolayer cell (0.02025 m^2) to allow comparisons with the experimental validation.

5.4.3.3 *Fabrication limitations of this thesis*

In addition to process-model relationships, the following process limits were included:

- The minimum achievable porosity was fixed to the maximum compaction factor between the simple cubic packing (47.64%) and the cubic close packing (25.95%), according to the assumption made by [86].
- In the calender machine, a maximum line load of 1000 N mm^{-1} was considered. The applied line load for different calendering conditions was calculated according to Meyer [95] in which a compaction resistance of 126 N mm^{-1} for the negative, and a mass dependency factor of 1.40 ± 0.11 for the NCA were experimentally obtained by that author.
- The minimum calender roller gap was fixed to 35 µm as it is the limit of the experimental equipment used in this thesis.

5.4.3.4 *Simulated optimal condition*

Analogue to case study 1 higher specific energies were obtained increasing positive electrode coater thickness but with a detrimental effect in specific power. In the positive electrode, lower compression rates than for the case study 1 were obtained from the optimisations, which is in good agreement with the literature [216]. Slightly higher performance was obtained with 353.15 K roller temperature. The effect of negative calendering gap did not affect significantly to the analysed responses. That effect could be due to the poor diffusion coefficient that was obtained experimentally for thick electrodes.

Based on the optimisation analysis, in Table 5.6 the optimal ranges of the parameters are highlighted in green. The analysis of variance, interaction plots and results of the desirability function maximisation are summarised in Appendix B.2.1.

Table 5.6: CS2: Optimal design parameter range.

Parameter	Low (-2)	Low (-1)	Mean (0)	High (+1)	High (+2)
δ^p_{blade} (µm)	90	95	100	105	110
$T_{roll,pos}$ (K)	353.15	358.15	363.15	368.15	373.15
G^p_{roll} (µm)	20% δ^p_{dry}	25% δ^p_{dry}	30% δ^p_{dry}	35% δ^p_{dry}	40% δ^p_{dry}
G^n_{roll} (µm)	20% δ^n_{dry}	25% δ^n_{dry}	30% δ^n_{dry}	35% δ^n_{dry}	40% δ^n_{dry}

5.4.3.5 *Fabrication and characterisation*

In this section the experimental validation of the virtual optimised cell is performed. To this end, the virtual cell obtained with the model-based design tool was fabricated. In this section physico-chemical characterisation of the electrodes and cell and pouch monolayer cell fabrication is explained.

Following the same procedure as Chapter 4, the electrode properties and cell balancing were assessed. First of all, new slurries for positive and negative electrodes were fabricated, as different coating thicknesses were proposed with the model-based design tool. Thus, different mass loadings of Chapter 4 were used and proved for out-of-range validation. The fabricated conditions are summarised in Table 5.7.

Table 5.7: Analysed process conditions of positive and negative materials for the pouch cell.

Electrode	AM_{per} (%)	R_{SL} (%)	AM_{per} (%) (± 0.2)	R_{SL} (%) (± 2)	δ_{blade} (µm) (± 5)	T_{roll} (K) (± 3)	G_{roll} (µm) (± 1)
Positive	93	74.15	100	-	0		
			93	74.15	100	80	22
Negative	95	27.04	340	-	0		
			95	27.04	340	80	49

In Table 5.8 the thickness related measurements of the pouch cell are presented.

Table 5.8: Thickness related measurements during material processing stage for the pouch cell.

	T_{roll} (K) (± 3)	G_{roll} (µm) (± 1)	δ_{blade} [*1] (µm) (± 5)	δ_{dry} [*1] (µm) (± 2)	δ_{cal} [*1] (µm) (± 1)	$\delta_{cal-dry}$ (µm)	Π_c (%)	E_R (%)
+	353	22	100	80.14	66.50	13.64	17.02	55.53
-	353	49	340	151.40	115.00	35.40	23.38	76.62

[*1] One side coating with current collector (Al foil: 16 µm and Cu foil: 18 µm).

Five different laminates were manufactured for the positive electrode and all of them were tested with helium pycnometry as a fast method to select the electrodes for pouch cell fabrication. Coating density was found to be 4263 ± 59 kg m^{-3}. Moreover, the calculated properties are presented in Table 5.9.

Table 5.9: Mass loading, tapped density and calculated porosity before and after the calendering step for the pouch cell.

	δ^p_{blade} (µm)	T_{roll} (K)	G_{roll} (µm)	$M_{L,dry}$ (kg m^{-2})	ρ_{dry} (kg m^{-3})	ε_{dry} (%)	ρ_{cal} (kg m^{-3})	ε_{cal} (%)	ρ_{diff} (%)	ε_{diff} (%)
+	100	353	22.0	0.12	2199	47.91	2712	35.76	18.92	25.37
-	340	353	49.0	0.08	572	72.64	834	60.09	31.43	17.27

Non-calendered and calendered electrodes of the same laminates were measured by mercury porosimetry. In Figure 5.8 the pore size distribution and specific pore volume graphs are shown. As was expected, the pore size decreases when the electrodes are pressed.

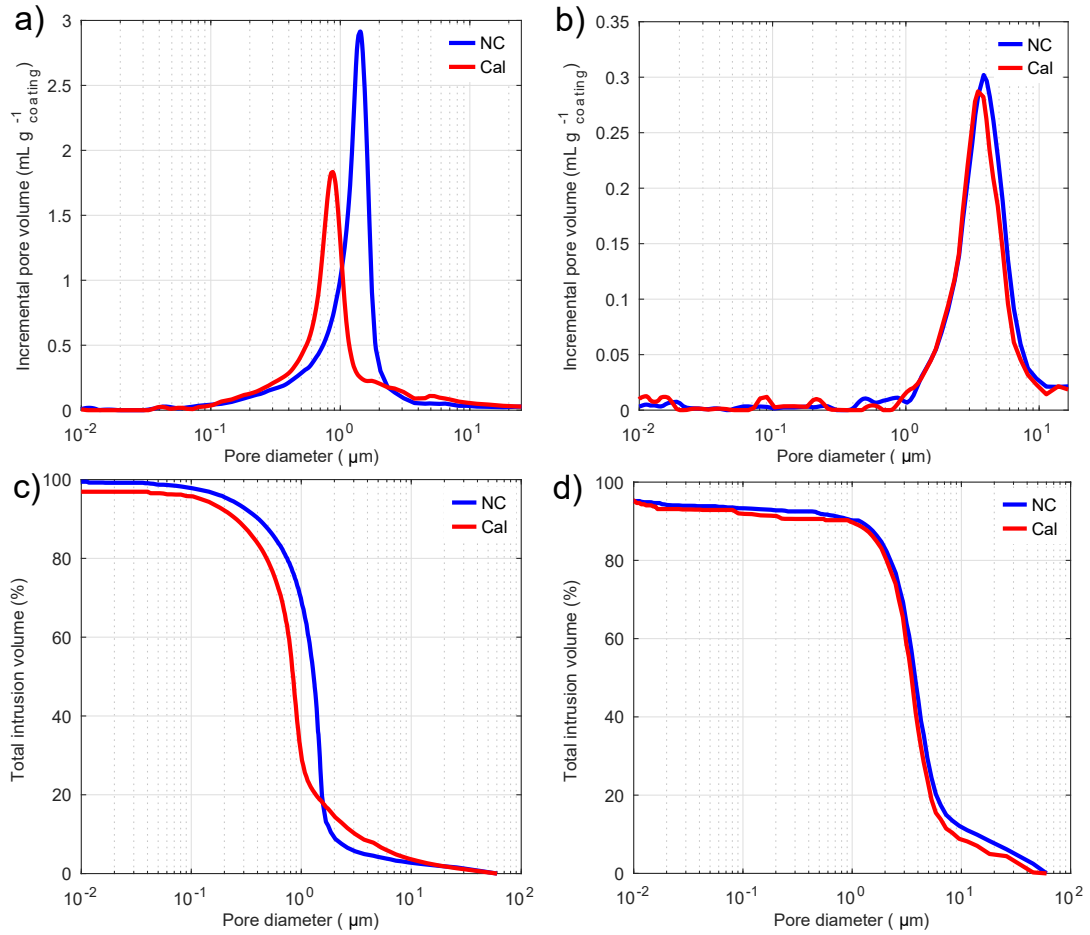

Figure 5.19: Mercury porosimetry results: a) Pore size distribution; c) Specific pore volume of the negative electrode; b) Pore size distribution; d) Specific pore volume of the positive electrode.

The electrode morphology in the cross-sectional view and surface view is shown in 5.20. Compared to Chapter 4 the electrodes are thinner. The negative electrode adhesion appears to have improved, as no delamination was observed.

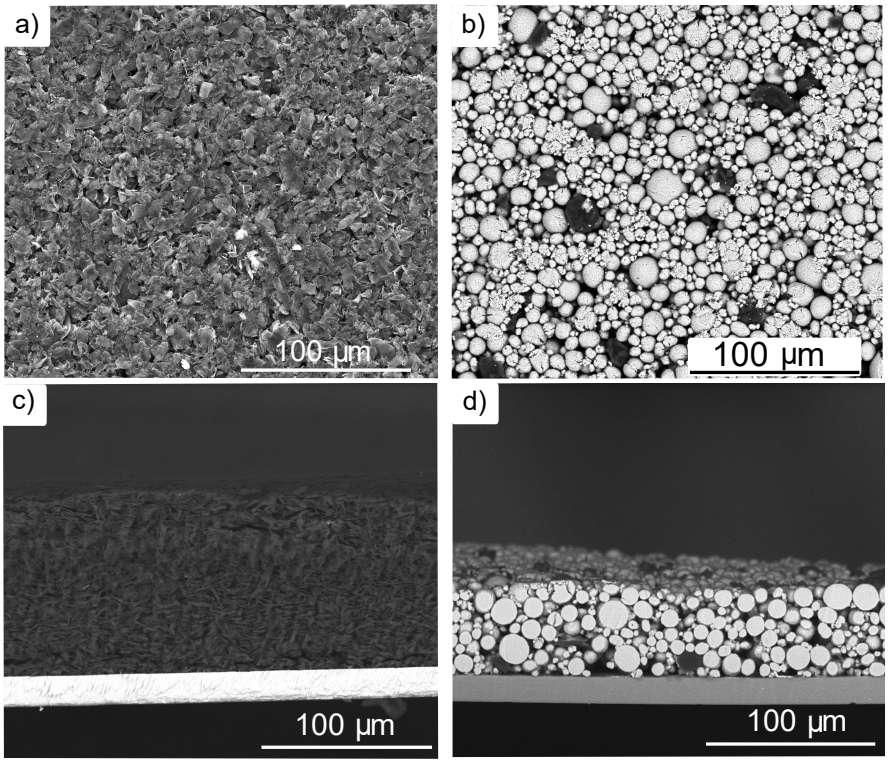

Figure 5.20: Particle shape in the calendered electrodes used in pouch cells. SEM surface image a) Negative and b) Positive; SEM cross-section image c) Negative and d) Positive.

In Table 5.10, the experimental properties of the electrodes are shown.

Table 5.10: Helium pycnometry and mercury porosimetry experimental results for the pouch cell.

	T_{roll} (K)	G_{roll} (µm)	$\rho_{ske,SA}$ (kg m^{-3})	$\rho_{bulk,SA}$ (kg m^{-3})	ρ_{He} (kg m^{-3})	ε_{SA} (%)	ε_{HgHe} (%)	a_s (m^2 m^{-3})	τ (-)
+	-	-	2399	1820	4223	24.14	56.91	5.56 10^7	1.96
	353	22	2254	1765	4301	21.67	58.96	6.96 10^7	1.99
-	-	-	1696	700	2449	58.76	71.43	1.23 10^7	1.57
	353	49	1511	748	2597	50.48	71.19	3.48 10^7	1.66

Finally, the parameters related to the electroactive area of the electrode are presented in Table 5.11.

Table 5.11: Effective surface area and solid volume fraction calculation.

	T_{roll} (K)	G_{roll} (µm)	ε_e (%)	$\varepsilon_{non-act}$ (%)	ε_s (%)	R_s (µm)	δ_{cal} (µm)	S_{coin} (m^2)	a_s (m^2 m^{-3})
+	-	-	24.14	32.86	43.00	9.61	80.14	1.95 10^{-3}	2.68 10^5
	353	22	21.67	23.33	55.00		66.50	1.96 10^{-3}	3.43 10^5
-	-	-	58.76	12.24	29.00	16.02	151.40	2.77 10^{-3}	1.81 10^5
	353	49	50.48	12.52	37.00		115.00	2.59 10^{-3}	2.31 10^5

Once the electrodes are fabricated and the electrode balancing is assessed, the final step of the fabrication process of a battery is the pouch cell fabrication process. To achieve this,

the steps presented in Figure 5.21 are necessary.

First of all the electrode notching was used to cut the electrodes to a fixed area. In Figure 5.22 a) and b) the negative and positive electrode cut patterns are presented. Then, after the electrodes were stacked between separator films, the tabs were welded to the electrodes using an ultrasonic welding machine (see Figure 5.21 b). Then, the stack was introduced and three side sealing was performed (see Figure 5.21 c). The pouch cell was left in a vacuum oven at 80 °C overnight before the electrolyte filling process (Figure 5.21 d)).

Figure 5.21: Pouch cell fabrication process equipment: a) Electrode notching machine and cut electrodes; b) Ultrasonic welding equipment; c) Three side sealing equipment; d) Electrolyte filling equipment; e) Cell degassing and final sealing equipment.

The finished pouch cell before degassing is shown in Figure 5.22 d). Then, five formation cycles at C/10 rate were carried out at 25 °C. Afterwards, the cell degassing and final sealing was performed and the cell was cycled again to conduct the electrical and electrochemical characterisation tests.

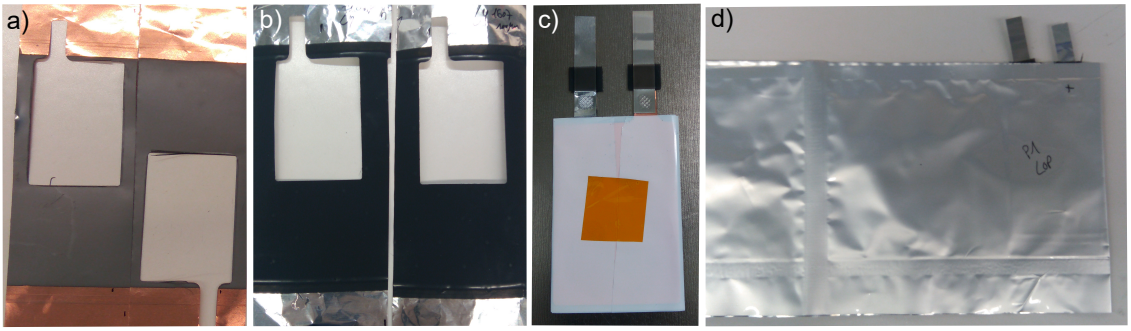

Figure 5.22: Pouch cell during fabrication: a) Negative electrode notching; b) Positive electrode notching; c) Cell stacking; d) Finished pouch cell before degassing.

A capacity between the 45.24 and 47.64 mAh for positive electrode, and 51.34 and 52.10 mAh for the negative electrode were calculated based on weight measurements. The experimental mass balance was 1.09 - 1.12 for the analysed pouch monolayer cells.

5.4.3.6 *Experimental-numerical correlation*

In Figure 5.23 the Ragone plot for the case studies 1 and 2 are presented. The measured specific energy and power of both fabricated pouch cells were added to the graph to compare model predictions with experimental values for 1C discharge. Large differences between the simulation and experimental conditions are presented due to the out-of-range extrapolation of the experimentally measured conditions for energy cells. The active material diffusion coefficient was characterised for thick electrodes, which was observed to be underestimated for thinner electrodes. In order to enhance the model predictions, the characterised conditions of the pouch cell were included.

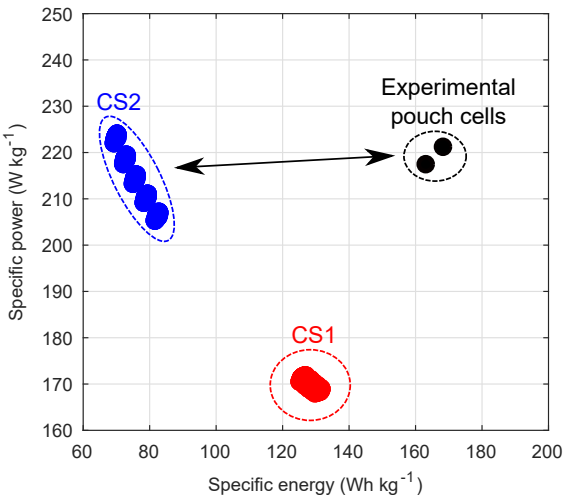

Figure 5.23: CS2: Ragone plot of the simulated and fabricated conditions.

5.4.3.7 *Process-model relationships enhancement*

The optimisation point was out of the studied experimental range (out-of-range optimisation). For this reason, the model was not able to completely adapt to the new prototype cell as no study points were available at lower mass loadings. After the pouch monolayer cell was constructed and characterised, more information of different design space points became available. Therefore, it was necessary to update the process-model relationships which provided more reliable results. The following modifications were made in the model to account for the differences between this chapter and Chapter 4 experimental characterisations:

- The calendered density is affected by the mass loading. Meyer et al. [96] demonstrated that the compaction resistance value increases linearly with the increase of mass loading, thus affecting the obtained calendering density. For the positive electrode relationship, a mass loading factor was included to account for that change.
- The solid diffusion coefficient of both electrodes significantly affects the final performance of the cell and improves when thinner electrodes are fabricated. A mass loading dependency for both electrodes was included.
- Model-process relationships defined on Chapter 4 were updated with the information obtained from pouch cell characterisation.

5.4.3.8 *Simulated fabricated condition*

The analysis conducted for the simulated results including the characterisation presented in the previous section is summarised in Appendix B.2.2. The results are presented in Table 5.12. Introducing the enhancements of the process-model relationships a different optimal solution was obtained. Values of 0.27 and 0.33 for G^{p}_{roll} and G^{n}_{roll} were experimentally measured in the fabricated pouch cell. The positive electrode calendering gap was close to the optimal solution of the design tool. Nevertheless, lower compression rates for the negative electrode were identified as a more optimum point. This could lead to the conclusion that, when thinner electrodes are fabricated, higher porosities (lower compressions) are required for the negative electrode.

Table 5.12: CS2$^+$: Optimal design parameter range.

Parameter	Low (-2)	Low (-1)	Mean (0)	High (+1)	High (+2)
δ^p_{blade} (µm)	90	95	100	105	110
$T_{roll,pos}$ (K)	353.15	358.15	363.15	368.15	373.15
G^p_{roll} (µm)	20% δ^p_{dry}	25% δ^p_{dry}	30% δ^p_{dry}	35% δ^p_{dry}	40% δ^p_{dry}
G^n_{roll} (µm)	20% δ^n_{dry}	25% δ^n_{dry}	30% δ^n_{dry}	35% δ^n_{dry}	40% δ^n_{dry}

5.4.3.9 *Experimental-numerical correlation*

Once the process-model relationships were updated, the case study 2 was executed again. The interaction plots for specific energy and power can be found in Appendix B. The model and experimental results are in good agreement as it is shown in Figure 5.24.

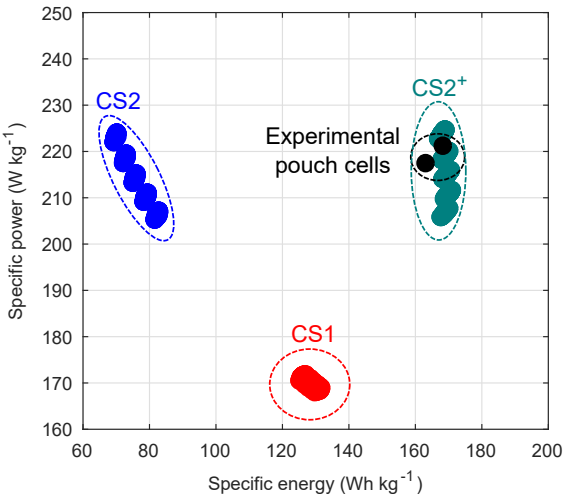

Figure 5.24: CS2$^+$:Ragone plot of the simulated conditions.

In addition to Ragone plot, in Figure 5.25 a) the galvanostatic discharge performance of the pouch cell is presented. The discharge curves show a good correlation between experimental and numerical analysis.

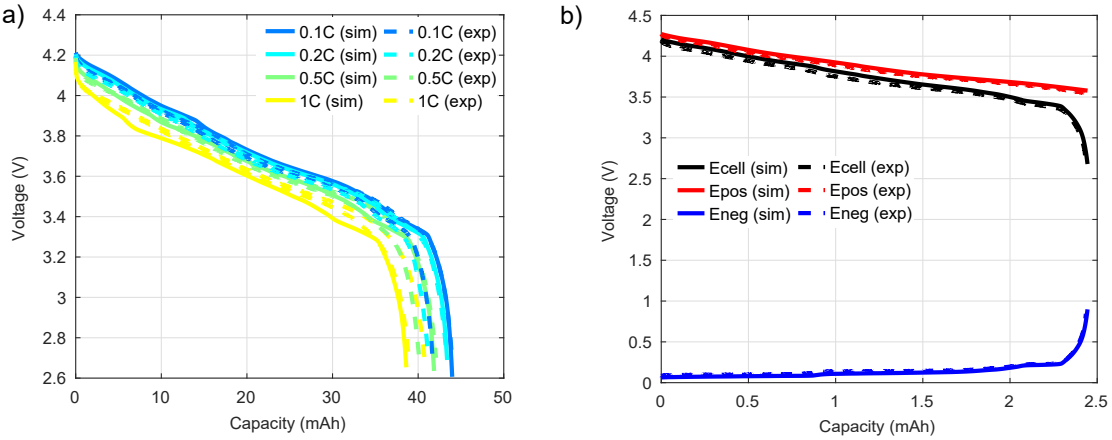

Figure 5.25: a) Comparison of the experimental and simulated rate capability at 298 K for the pouch cell; b) Voltage evolution of a three electrode experimental T-cell at 298 K and the comparison with the simulated responses at C/10.

Moreover, a three electrode T-cell was built to check that the cell was well balanced. In Figure 5.25 b) formation cycles at C/10 were performed to check the electrode balancing and compared with the simulated results. An experimental negative to positive reversible capacity ratio of 1.12:1 was observed. The commercial cell studied in Chapter 3 presented similar electrode balance (1.15:1) and mass loadings, 0.07 kg m^{-2} and 0.11 kg m^{-2} for the negative and positive electrodes, respectively. The optimised prototyped cell mass loadings were slightly higher than the commercial cells which could lead to increased energy performance.

5.4.4 Case study 3: Further design strategies

The third case study is defined to study different scenarios that could be followed in further optimisations. In Figure 5.9 the importance of particle radius and different design strategies were described. In this thesis, the AM were kept constant, therefore, this section was not implemented experimentally.

5.4.4.1 *Case study description*

In this case study, variation of AM particle radius and calender roller gap for both electrodes with a positive coater blade gap of 70 (µm) was studied. The parameters and ranges listed in Table 5.13 were varied. This strategy could be used as an approach to maximise specific power of the cell.

Table 5.13: CS3: Input factors, design space and selected variations.

Parameter	Low (-2)	Low (-1)	Mean (0)	High (+1)	High (+2)
R_s^p (µm)	3	4	5	6	7
R_s^n (µm)	4	5	6	7	8
G_{roll}^p (µm)	0% δ_{dry}^p	10% δ_{dry}^p	20% δ_{dry}^p	30% δ_{dry}^p	40% δ_{dry}^p
G_{roll}^n (µm)	0% δ_{dry}^n	10% δ_{dry}^n	20% δ_{dry}^n	30% δ_{dry}^n	40% δ_{dry}^n

5.4.4.2 *Simulated optimal condition*

The same methodology followed in case study 1 and 2 was applied. In Figure 5.26 the simulated conditions of the cell as a function of the output responses is shown. Additional information of the followed steps are summarised in Appendix B.3. Figure 5.26 shows that the particle radius affects to the specific energy and power response.

In the analysed case, the positive electrode radius variation does not influence the final response, as the limiting component of the cell is the negative. When the negative AM particle radius is decreased, lower mass transport limitations are presented and thus better performance is obtained. Small particle radius and higher compression rates were favourable in the case of the negative electrode, whereas changing the positive AM radius was not significant. Additional experimental studies should be conducted to assess the optimal condition, as the particle radius variation affects the mixing, coating, drying and calendering steps during the manufacturing process. To study deeper the influence of the particle size influence into the cell response, there is a need to include particle size distribution and particle shapes to increase the accuracy of model prediction.

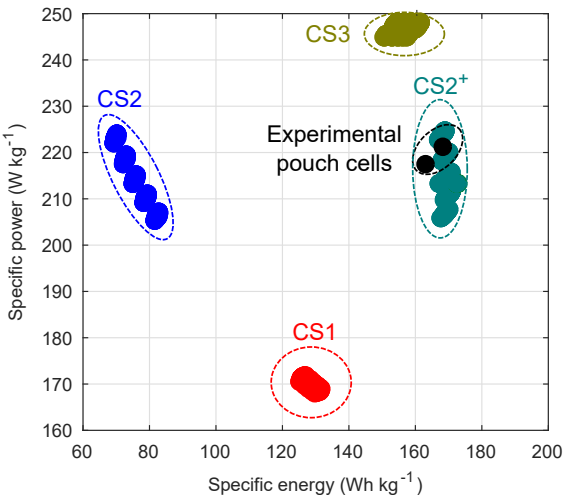

Figure 5.26: CS3: Ragone plot of the simulated conditions.

Moreover, in this case study, not only specific energy and power were analysed. Also minimum particle lithium concentration of the negative particles at the end of the discharge and minimum electrolyte concentration in the positive electrode were included (see Figures B.16 and B.17). Adding those internal variable limits into the multi-objective optimization procedure will account not only for the characteristics of the cell (energy and power) but also for the material limits. In this specific case, the positive active material particle size optimal solution was moved into smaller diameters, as the transport limitations are expected to be lower.

5.5 CONCLUSIONS

An energy-power balanced cell was proposed in this chapter for the validation of the model-based design tool. The factors and their optimisation ranges were selected based on the experimental measurements of Chapter 4. Four factors were varied through the optimisations to obtain the optimal solution (coater gap thickness of the positive electrode, calender roller gap of the positive and negative electrodes, and calender roller temperature of the positive electrode) for case study 1 and 2. The selected design parameters were easy to change during the manufacturing process, thus, the obtained results could be directly applied in the prototyping line, providing trends for experimental optimisation of the cells. In case study 3, active material radii and calender roller gaps of the positive and negative electrodes were varied. Particle radius could be changed if the raw active materials are changed.

The calendering roller temperature in comparison to the coater or calender gap was found to be less sensitive in the analysed responses (specific energy and power). Similar compression rates using 353 K and 373 K set temperatures with equal calender roller gaps were obtained in both the experimental and simulated cells. From a fabrication point of view, a change in the set temperature would imply a calibration of the machine. The required line force to obtain the same compression rate degree is higher with lower temperatures. However, the cost related to that increase could be inferior to that which could be attributed to increasing the roller temperature by 20 K. Including the energy consumption and cost analysis of each fabrication step in the model-based design tool will improve the final solution from an industry point of view. Further studies could be performed to minimise the roller temperature (in terms of cost reduction), as the optimised condition is not directly related to obtaining the maximum compression rate. The optimised condition is

obtained with a compromise between the transport properties of electrodes and electrolyte.

The model-based design tool was able to vary the selected design parameters to find a tailored power to energy ratio. Three different design scenarios were analysed (energy, energy-power balanced and power cells). Furthermore, the optimised virtual cell was in good agreement with the fabricated pouch monolayer cell. Moreover, if more experimental measurements are considered for the material-processing stage relationships, the model-based design tool will be more accurate. In order to improve the methodology, physics-based relationships should be included in the model, as data-driven approaches are limited and could not be representative when out-of-range optimisations are required.

The objective of the present study was to find a compromise between accuracy and computational cost. The DOE experimental matrix designed in this chapter computes the 625 simulations in 24 minutes, which corresponds to 2.4 seconds each simulation. This methodology is also suitable for studying the degradation mechanisms, as long as the model accounts for ageing and the parameters are characterised. This methodology is also suitable for parameter identification of commercial or prototyped cells, thereby complementing the experimental work described in Chapters 3 and 4. The same procedure could also be used if parameter identification is carried out.

Even if the mixing, coating, drying and calendering steps are optimised, if the electrode balancing is not correctly set, the cell will not behave as expected. A mass balance negative to positive capacity ratio of 1.1:1 was maintained in all the simulations. Thus, the negative electrode was varied according to the expected reversible positive electrode capacity. Special care should be taken when defining the electrode balancing of the cell and the best match between negative and positive electrodes. Moreover, experimentally measured mass balance between tested coin cells could affect the experimental results, and therefore special care should be taken in the interpretation of the results. Different studies for correlating and extrapolating coin, T-cell, full-coin cell and pouch cell performance and comparison between them could be carried out. In this case, capacity related correction factors were established when the simulation results were compared to experimental measurements in order to compensate for the weight differences in the experimental process. Reproducibility between coin cells is a common issue, at least two repetitions were performed for each condition. The results were averaged and the tendencies shown in this chapter agree with other literature works. The electrode balancing was determined for the beginning of life of the batteries, however, it changes throughout the battery life, as we can have detachment from the positive and negative electrodes, loss of lithium inventory due to SEI growth or other degradation mechanisms such as lithium plating.

The methodology was tested with the pouch monolayer cell. In this work, experimental deviations resulting from the fabrication process were identified as significant, and to account for those, the positive electrode thickness was varied by 20 µm in case studies 1 and 2. The specific energy and power responses were strongly affected by the electrode thickness (which is also related to the electrode mass loading). Schmidt et al. reached similar conclusions in their study of the impact of manufacturing uncertainties [99]. We therefore recommend that further steps should be taken to scale-up the manufacturing process to build a complete pouch cell (as in the commercial cell reported in Chapter 3). Laboratory scale equipment should be replaced by pilot or industrial scale equipment, so as to fabricate the electrodes in a continuous process. In this way, a fully automated and integrated process can be achieved, in which experimental deviations are expected to decrease.

Chapter 6

CONCLUSIONS AND FUTURE LINES

This chapter presents an overview of the main conclusions of this thesis and the future lines that arise from this research work.

6.1 CONCLUSIONS

The aim of this thesis was to optimise the fabrication process of a pouch cell based on physico-chemical modelling and characterisation. This was successfully fulfilled as we have validated the model-based design tool experimentally with a pouch monolayer cell.

[O1] Develop and validate a new physico-chemical parameter measurement methodology for a pseudo-two-dimensional model of commercial or prototyped cells.

In order to optimise cell performance or employ electrochemical models for specific applications, a consistent set of input parameters is required. However, few literature works report parameter measurement methods and provide sufficient information of model validation [22, 52] due to the complexity of the methodology and the resources required. In fact, physico-chemical characterisation methods are carried out in laboratories with specialised equipment, which is not commonly available in the majority of research facilities. Moreover, different techniques and methods were proposed in the literature which present variations of several orders of magnitude in certain parameter values. The measurement technique, post-process and model assumptions severely affects the final parameter values.

In the present research, a full physico-chemical parameter measurement methodology was built and validated with invasive and non-invasive methods. Internal variables of the cell were measured by means of three-electrode cell and *ex-situ* XRD. These techniques provided information about the electrode voltage and the state of lithiation of each electrode, and thus, the electrode balancing was determined experimentally. In future researches, these techniques could be used for cell ageing evolution analysis.

Upon completion of the measurements, it was possible to compare different techniques and determine the most suitable methodology. Porous structure related parameters were included in the model with an averaged value, which could not be completely representative of the heterogeneous electrode structure. Furthermore, there are some uncertainties in the procedures to measure and post-process the transport and kinetic parameters of the materials. The assumptions that are made to experimentally extract parameters such as exchange current density and solid diffusivity are based on the electroactive surface area which could be obtained with different methods (Hg-porosimetry, SEM etc.) and directly affects the result. Hence mixed methodologies could be used to identify transport

and kinetic parameters, so as to minimise the deviations arising from the experimental post-process or the model assumptions. Such methods have the further advantages of consuming less resources and enabling faster characterisations.

[O2] Analyse the influence of the material processing stage on the final properties of the cell and include those influences in the model.

A design of experiments was carried out to vary the calendering step related parameters of the positive electrode with a reduced amount of conditions. Those conditions formed the basis of the material-process-model relationships, and the experimental cycling curves were used for model calibration and validation. In the experimental range, the results shows good agreement with galvanostatic discharge curves at 25 °C. The relationships could be enhanced if more conditions of the design space are considered. A high mass loading (4 mAh cm^{-2}) for the positive electrode was selected to fabricate high-energy cells (Chapter 4). In order to maintain a good mass balance between electrodes, the negative electrode coating gap was set to 450 µm with a final dry thickness of 213 µm. As was expected, the high mass loading of the negative electrode had a detrimental effect on the solid diffusivity at higher rates. Even at moderate rates, the negative electrode was not able to give the required energy.

[O3] Design and validate a model-based optimisation tool capable of obtaining optimised cells with better performance than the reference.

A tailored energy-power balanced cell was designed and validated experimentally with a pouch monolayer cell. Inverse cell design was performed to evaluate out-of-range process conditions and extrapolate the material-process-model relationships. The design of experiment technique was used to analyse the simulated results and evaluate not only the effects but also the interaction between the different parameters varied throughout the optimisation process. When the experimental range was surpassed, the validity of the empirical relationships built for porosity, inactive solid volume fraction, and tortuosity decreased. Nevertheless, the methodology has proved to be valid when a sufficient amount of experimental inputs is available. Moreover, the selection of the model output responses and factor range was found to be highly sensitive. If the variation between levels of the same factor are high, the response surface methodology analysis will not be able to represent the reality, even if the electrochemical model does.

It is commonly observed in the literature that researchers have performed cell design optimisations varying adjustable design parameters of the model (electrode thickness, porosity, tortuosity and particle radius, among others). However, the experimental achievement of the targeted objectives of those simulations is not easy to implement in a prototyping line, as the interactions between them are not usually considered and no information about process parameters are given. Moreover, some authors have studied parameters in which the fabrication process is not feasible. For example, it is not possible to decrease the electrode porosity to almost zero as we should consider the particle packing factor (in the case of cubic close packing the minimum achievable porosity is 25.95%). Moreover, equipment or process limits should be considered in the analysis, such as the maximum applied line load of the calender machine, or the maximum achievable coating thickness for the negative electrode without causing defects. These limiting factors were also included in our model which significantly varied the obtained results.

6.2 FUTURE LINES

Parameter measurement or identification is critical to obtain good model predictions. In the case of lithium-ion batteries, some parameters are strongly correlated to each other, therefore, the factor sensitivity to a response and interactions between factors are of great importance. Therefore, special attention should be paid when design parameters (factors) and responses are selected. For parameter identification, a multi-objective sequenced (different responses) optimisation is proposed as the approach for further research work. A consistent set of model parameters are required for cell optimisation or advanced control of BMS. In order to enhance the procedure proposed in this thesis, a reduced set of physico-chemical measurements coupled with multi-objective optimisations could be employed (mixed methodology). Specific dynamic profiles and impedance spectroscopy measurements could be used as powerful tools to gain insights into the dynamic behaviour of cells. Moreover, characterisation procedures should be adapted to new trends in fabrication, in which blending of active materials is used to enhance cell performance, increase the lifespan of batteries, reduce costs etc. In addition, temperature dependencies should be enhanced and mechanical stress parameters included in the model.

In order to increase model accuracy, 3D complex geometries could be used for microstructure representation instead of using averaged values. However, although 3D models accurately predict battery performance, they are not suitable for fast optimisations, as they incur high computational costs. With the objective of reducing these costs (and the proposed methodology of this thesis) Reduced Order Models (ROM) could be used.

In addition to energy and power density model responses, battery life and production costs could be included in the model-based design tool. Not only cell performance but also the characterisation and modelling of degradation mechanisms is required during cell design optimisation. Specific characterisation tests should be designed to observe degradation mechanisms (e.g. SEI growth evolution or lithium plating) during the battery life. Moreover, in future works, different DOE techniques, factors and levels could be studied in order to achieve optimised solution with less resources. In some cases, the number of experiments is limited or fixed, mostly in experimental analysis, in which considerable time and resources are required for output response characterisation. In other cases, the number of experiments is not critical, as the experiment or simulation takes only a few seconds or minutes. The number of parameters varies depending on the selected case study. If more process parameters are included into the analysis, screening techniques can be used to obtain faster results. Special care must be taken when using these techniques however, as they can be imprecise, and the design space might not be completely explored.

The process-model relationships could be enhanced studying more points of the design space and more process design variables (solid to liquid ratio, slurry viscosity, shrinkage, drying length and time etc.). A database of the performed test at different process conditions and characterised with the same protocol to obtain reliable and comparable results could be created. Moreover, each fabrication step could also be analysed to reduce the process uncertainties and the dispersion between different batches.

Last but not least, the use of the proposed model-based design tool could be adapted to optimise cells at specific scenarios (dynamic profiles etc.) or to study other cell chemistries such as sodium-ion batteries or lithium-ion capacitors.

Appendix A

PHYSICO-CHEMICAL CHARACTERISATION TECHNIQUES

In the following lines, the techniques that were employed in this thesis are described:

a. Fourier transform infrared spectroscopy (FTIR).- In FTIR the sample interacts with infrared radiation [141]. Applying the Fourier transformation to the signal the spectrum is obtained (absorbance or transmittance as a function of the applied wavelength). This technique is not a quantitative method, but it provides useful data for the identification of the elements, or for comparison of samples from the same cell. It is worth noting that sample preparation is important, as electrolyte traces could lead to reflectance measurements in the electrodes. For separator characterisation, this technique can be used to provide information about its structure and different crystalline forms [217, 218].

b. Gas chromatography - mass spectrometry (GC-MS). - This technique allows to identify traces of substances and could be used for electrolyte solvent identification. It is an analytical method which combines gas chromatography and mass spectrometry [136].

c. Nuclear magnetic resonance spectroscopy (NMR).- A sample, which is placed in a magnetic field, is excited with a radio frequency pulse. The NMR spectrum is created by the recorded free induction decay (FID) data, and Fourier transformation is used for processing [219]. This technique is valid for both solids and diluted solvents and provides chemical, structural, magnetic, thermodynamic, kinetic, electronic, transport and movility of ions related information [141]. For example, lithium insertion or surface deposition in carbons can be determined [136].

d. X-ray diffraction (XRD).- In the XRD technique photons are emitted and detected. XRD is possible with both electrodes and scraped off powder-like material although peak intensities can vary as a result of preferred particle orientation in the electrodes, (which are not present in scraped off material). To generate X-ray photons, a high-voltage (between 20 and 60 kV) acceleration of electrons is necessary [220]. Furthermore, filters are used to provide a narrow wavelength range for analysis. In order to obtain a diffraction pattern, the goniometer (central part of the diffractometer) rotates. Two main types of goniometers are available: θ/θ (fixed sample) and $\theta/2\theta$ goniometers (X-ray source fixed and sample and detector moving) [220]. This technique is used for structural analysis of active materials, however, it is only applicable when a certain degree of periodicity is exhibited. It is commonly used in the characterisation of ageing mechanisms and to obtain information about changes in the particle orientation [220].

e. Inductively coupled plasma optical emission spectrometry (ICP-OES).- Inductively cou-pled plasma is used to produce excited ions which lead to electromagnetic radiation

of the sample [221]. The emissions of the sample are in the visible range and are a characteristic of each element. To prepare the sample for ICP-OES, the material must first be scraped-off from the electrodes. Then, samples are digested in an acid solution [38]. This technique is used to determine the ratio between the elements present in the sample. ICP-OES can also detect lithium, but does not provide the complete sample composition. For this reason, the EDS technique can be used as a complementary analysis. Ecker et al. [51] used this technique as to identify the composition of the positive electrode in the 7.5 Ah kokam cell.

f. Thermogravimetric analysis (TGA).- It is a thermal characterisation technique in which a temperature profile is set and the mass loss of the sample is monitored while the temperature rises. This technique can give information about phase transition or the decomposition peaks. It could be used to identify the active material content and guess the binder or conductive additives used.

g. Dynamic light scattering (DLS). - It is a physico-chemical characterisation technique that is employed to determine the particle size distribution in a suspension.

h. Electronic conductivity.- For electronic conductivity, different techniques can be found in the literature. In this work, three techniques are compared and discussed: Powder probe, two point probe and four point probe methods. In all the studied techniques, a DC current is applied to the sample and the voltage response is recorded. The difference between the methods lies in the measuring set-up and the contact resistance between the equipment and the sample [51, 222, 223].

- Two-point probe for conductivity test.- The contact applied in conductivity measurements have parasitical contact resistance which impedes a quantitative analysis of the resistivity [222, 223]. Four different resistances are measured at the same time: stamp/coating contact resistance, coating bulk resistance including particle/particle resistance, current collector/coating contact resistance, and current collector bulk resistance [222].
- Four-point probe for conductivity test.- Four-point methods measure sheet resistance and decouple the electrode resistivity, this is a commonly used technique [51].
- Powder probe conductivity test.- This is a new method to measure the electrical conductivity of an electrode in which the contact resistance is minimised enabling direct measurement of the resistivity of the sample [222, 223].

h. Incremental capacity analysis (ICA) and differential voltage analysis (DVA).- These methods are commonly used to investigate the degradation mechanisms of batteries. Every peak obtained in ICA or DVA curves has a determined shape and intensity, and can be related to a specific electrochemical process [136].

i. Potentiostatic and galvanostatic impedance spectroscopy (PEIS/GEIS).- The Electrochemical Impedance Spectroscopy (EIS) is a non-intrusive and highly sensitive technique based on the transfer function method (TF). The cell is perturbed with a sinusoidal wave input and the output response is measured in a wide frequency range to determine the dynamic properties of the system [224]. Electrochemical systems are non-linear systems, and as a result, it is not possible to apply the direct transfer function method. For this reason, local application of TF is applied, performing the experiment with a small amplitude of the perturbation signal of voltage or current [225]. During the test, a small amplitude AC

voltage or current signal is applied to the cell, over a wide range of frequencies (1 mHz to 1 MHz). In the galvanostatic method (GEIS), the impedance is measured by applying a sinus around a DC current that can be set to a fixed value, while in the potentiostatic experiment (PEIS), the impedance measurements are made applying a sinus around a DC potential. This technique can be used to determine the mechanisms involved in an electrochemical reaction and the values of the kinetic parameters of the cell (exchange current density and solid-state diffusion coefficient) [51].

Electron and ion transport through the porous electrode also need to be characterised which requires the determination of solid diffusivity and electric conductivity. To determine solid diffusivity, PITT/GITT and PEIS/GEIS techniques can be used.

j. Steady-state Potentiostatic Poplarization (SSPP).- This techniques could be used to identify electrolyte and separator effective properties [142]. More information about this technique can be found in [226]

k. Potentiostatic and galvanostatic intermittent titration technique (PITT/GITT).- In PITT and GITT a small potential or current pulse is used to change the equilibrium charge of an electrode in small increments [227]. This can provide thermodynamic and kinetic characterization of the electrodes (solid diffusion coefficient determination). These techniques approximate the diffusion coefficient to Fick's second law while migration is disregarded [56]. Figure A.1 (plots from top (plot 1) to bottom (plot 5)) shows the working principles of both techniques. As the applied constant current is considered small, the chonopotentiometric response shown in the first plot is close to the equilibrium potential during the charge of an electrode. In the second plot, the incremental potential steps (δE) (PITT) and the applied current step of δt and the subsequent rest step (GITT). The transient current in time (PITT) and voltage (GITT) responses are presented in the third plot. The fourth plot represents the data in Cottrellian-type coordinates for PITT and the potential Et, which depends linearly on $t^{1/2}$ (the slope is used to detect the diffusion time constant). Finally, the fifth plot sets out the incremental differential capacity for both experiments [227]. In addition to the PITT and GITT tests, diffusivity can also be estimated with impedance spectroscopic techniques. All three techniques present some limitations, and thus the diffusivity measurements are influenced by the method employed [51, 227].

m. Scanning electron microscopy (SEM).- In SEM, electrons are used instead of photons, and thus, the image contrast depends on the selected detector. The most common are backscattered electron detectors (BSE), secondary electron detectors (SE), and X-Ray photon detectors [228]. The detector of the BSEs is mounted at the exit point of the electron beam, as electrons are deflected out of the specimen. The measurements are taken in a vacuum to prevent interactions of the beam electrons with gas atoms and avoid sparkovers (which could destroy the electron source and the detectors). The electron source is composed of three components: a thermionic or field emission cathode (for the emission of electrons that are accelerated towards the anode), an anode (with a defined voltage in between 50-30.000 V), and a Wehnelt cylinder (for the control of the current density and brightness of the electron beam) [228]. SEM provides higher resolution than optical microscopy, as electrons have less Broglie wave lengths compared to visible light [141]. To minimise the size of the focal spot on the specimen surface, different types of lenses are placed between the electron source and the sample. These lenses can be electromagnetic (to focus and direct the electron beam in the SEM), condenser (to bundle the electrons), and objective lenses (to focus the beam onto the sample) [228]. Moreover, scan coils are used to control the scan movement of the beam. In SEM and, usually at the beginning of the experiment

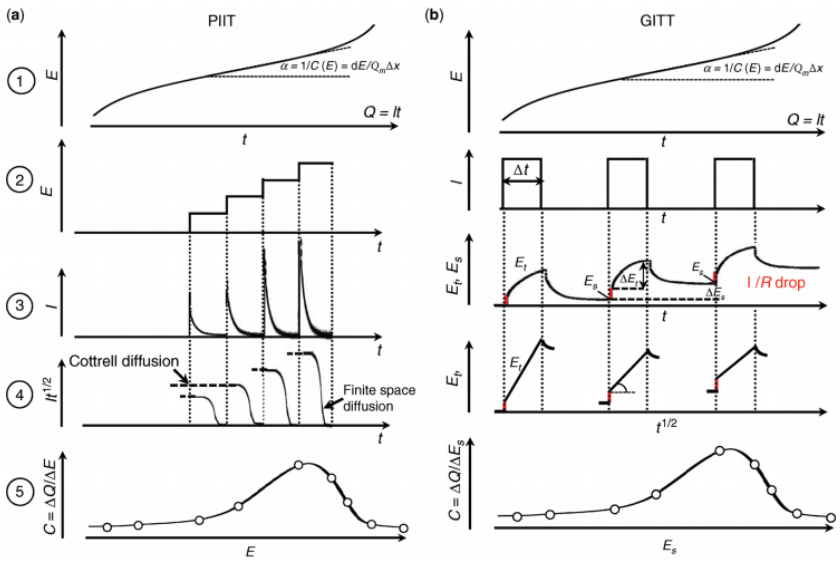

Figure A.1: Principles of intermittent titration techniques: a) PITT; b) GITT. Levi et al. [227] with the permission of John Wiley and Sons.

the area of analysis is bigger and then is zoomed. The objective is to characterize the whole electrode, avoiding misinterpretation of some different areas of electrodes (data must be representative for the whole sample) [141]. SEM images can be taken from the surface of the electrode or of the cross-sectional area of the electrode. When preparing samples for the cross-section view, the use of a knife provokes deformations of the electrode, and cracks and distortions in the particles [229]. Therefore, metallographic techniques are needed (polishing, focused ion beam (FIB) cutting or ion milling) to prepare a flat surface to evaluate the shape and size of particles, distribution of additives, pores, binders, AM etc. [229].

m. Energy-dispersive X-ray spectroscopy (EDS).- In EDS the sample is irradiated with electrons and X-ray photons are detected. EDS can be used in combination with SEM to obtain fundamental information on the microstructure (SEM) and chemical composition of the sample (EDS) [136]. However, EDS is not able to detect Li, thus complementary methods such as ICP-OES are necessary for its detection and quantification [141].

*n. Pycnometry.-*A pycnometer is a simple technique in which the difference between the volume with and without the sample is measured to determine the density of the sample. With this technique, an average porosity value is obtained, but no information about the particle size distributions is available.

o. Mercury porosimetry.- With this technique, meso and macro scales are analysed. The sample is placed inside a penetrometer (sealed enclosure) and vaccum is induced (to remove unwanted species). After, the mercury is progressively introduced into the cavity with incremental hydraulic pressure steps. It allows to record the volume of the mercury as a function of the applied pressure [161]. Commonly, the measurement is performed with a double-coated electrode (including current collector and the two-sided active material films) to avoid possible structural destruction during removal of the coating [51].

Appendix B

ANALYSIS OF VARIANCE AND RSM COEFFICIENTS

This appendix records all the results from the analysis of variance to determine whether the parameters and their interactions are significant to a certain response. A p-value $<$ 0.05 was defined to classify between significant and non-significant parameters. Moreover, the coefficients to build the surface response methodology are presented for the different responses. In addition, the pareto front of the simulated conditions for C/30 and 1C discharge curves are presented.

Three different section are distinguished:

- Case study 1: Energy cell
- Case study 2: Energy-power balanced cell
- Case study 3: AM particle radius variation with $h_{blade,pos}$ = 70 µm

B.1 CASE STUDY 1: ENERGY CELL

Table B.1: CS1: Analysis of variance for specific energy response for C/30 discharge.

Source	Sum Sq.	d.f.	Mean Sq.	F	Prob > F
X1	1179.03	4	294.759	119285.82	0
X2	0.67	4	0.167	67.69	0
X3	0.01	4	0.002	0.83	**0.506**
X4	0.04	4	0.01	3.85	0.0043
X1*X2	0.06	16	0.004	1.46	**0.1091**
X1*X3	0.06	16	0.004	1.61	**0.0622**
X1*X4	0.05	16	0.003	1.23	**0.2432**
X2*X3	0.07	16	0.004	1.74	0.0365
X2*X4	0.04	16	0.003	1.08	**0.371**
X3*X4	0.04	16	0.003	1.08	**0.3677**
Error	1.27	512	0.002		
Total	1181.34	624			

Table B.2: CS1: Analysis of variance for specific energy response for 1C discharge.

Source	Sum Sq.	d.f.	Mean Sq.	F	Prob > F
X1	1574.87	4	393.717	68570.7	0
X2	103.06	4	25.765	4487.3	0
X3	1.33	4	0.332	57.74	0
X4	14.63	4	3.657	636.84	0
X1*X2	0.08	16	0.005	0.84	**0.6385**
X1*X3	0.2	16	0.013	2.19	0.005
X1*X4	0.1	16	0.006	1.05	**0.402**
X2*X3	4.37	16	0.273	47.62	0
X2*X4	0.07	16	0.004	0.71	**0.7868**
X3*X4	0.07	16	0.004	0.73	**0.7656**
Error	2.94	512	0.006		
Total	1701.7	624			

Table B.3: CS1: Analysis of variance for specific power response for 1C discharge.

Source	Sum Sq.	d.f.	Mean Sq.	F	Prob > F
X1	546.789	4	136.697	25720461.25	0
X2	5.298	4	1.325	249230.95	0
X3	29.286	4	7.322	1377607.88	0
X4	11.284	4	2.821	530769.53	0
X1*X2	0.017	16	0.001	198.6	0
X1*X3	0.265	16	0.017	3115.3	0
X1*X4	0	16	0	3.01	0.0001
X2*X3	0.212	16	0.013	2497.81	0
X2*X4	0	16	0	1.54	**0.0809**
X3*X4	0.001	16	0	12.03	0
Error	0.003	512	0		
Total	593.156	624			

Table B.4: CS1: Coefficients for the surface response methodology equation for 1C discharge.

	E_m (Wh kg^{-1})	P_m (W kg^{-1})
Constant	-127.3	299.363323
X1	2 10^6	-1182773.14
X2	0.2979	0.01837786
X3	60.085	12.0703395
X4	1.7249	-2.36892286
X1*X2	-31.74	103.755539
X1*X3	24585	39156.8104
X1*X4	-9009	1130.33579
X2*X3	-0.163	-0.03518051
X2*X4	-0.005	-0.00087234
X3*X4	0.4743	-0.18549694
$X1^2$	-4 10^9	2503907751
$X2^2$	-4 10^{-4}	-5.69 10^{-5}
$X3^2$	-9.997	-16.6115437
$X4^2$	-0.388	1.02678949

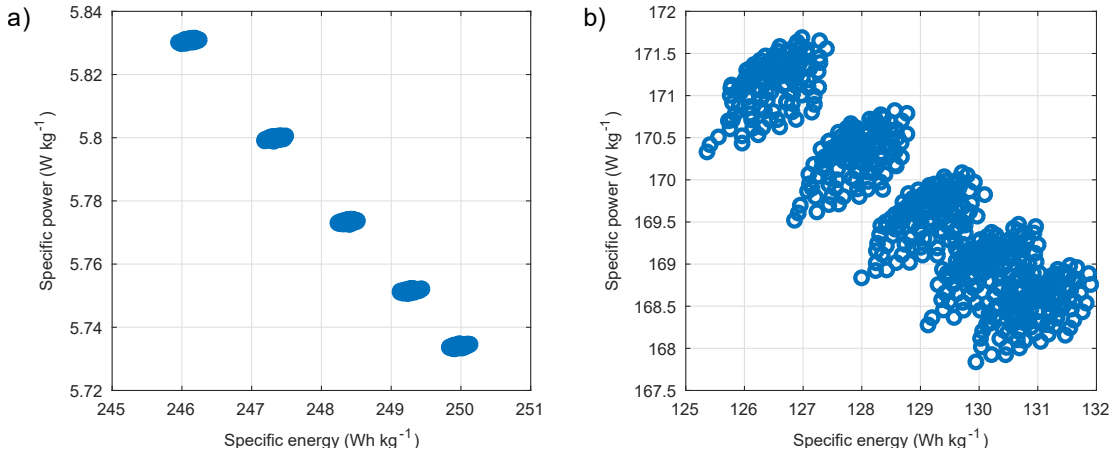

Figure B.1: CS1: Ragone plot of the simulated conditions a) C/30 discharge and b) 1C discharge.

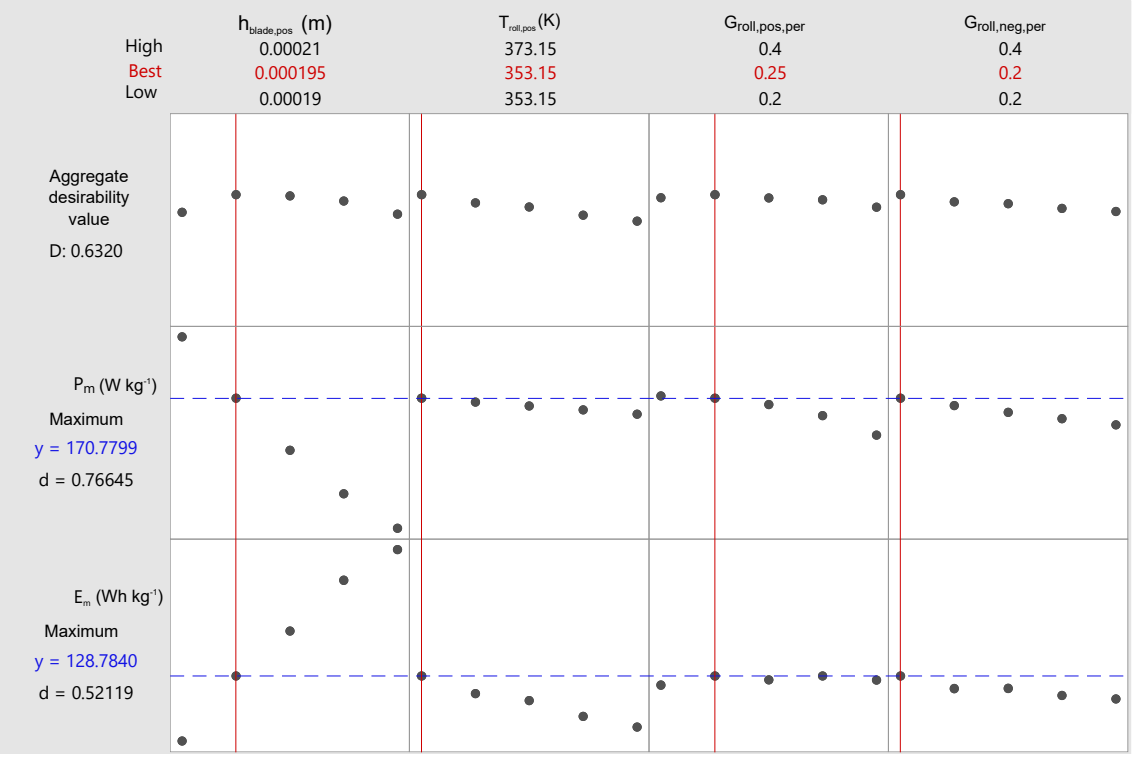

Figure B.2: CS1: Optimised parameters for specific energy and power responses.

B.2 CASE STUDY 2: ENERGY-POWER BALANCED CELL

In the case study, two different scenarios were considered: before and after process-model relationships enhancement which are presented in the following subsections.

B.2.1 Before process-model relationships enhancement

Table B.5: CS2: Analysis of variance for specific energy response for 1C discharge.

Source	Sum Sq.	d.f.	Mean Sq.	F	Prob > F
X1	12204	4	3051.004	1161144.46	0
X2	38.1	4	9.516	3621.69	0
X3	6.5	4	1.629	620.12	0
X4	0	4	0.004	1.34	**0.2542**
X1*X2	0.3	16	0.018	6.9	0
X1*X3	0.1	16	0.005	2.05	0.0095
X1*X4	0.1	16	0.007	2.55	0.0008
X2*X3	1.8	16	0.115	43.89	0
X2*X4	0.1	16	0.003	1.28	**0.2046**
X3*X4	0	16	0.001	0.45	**0.9677**
Error	1.3	512	0.003		
Total	12252.4	624			

Table B.6: CS2: Analysis of variance for specific power response for 1C discharge.

Source	Sum Sq.	d.f.	Mean Sq.	F	Prob > F
X1	22107.1	4	5526.77	283830456.2	0
X2	43.9	4	10.97	563569.35	0
X3	104.1	4	26.02	1336282.6	0
X4	0	4	0.01	285.85	0
X1*X2	0.4	16	0.02	1196.55	0
X1*X3	0	16	0	124.66	0
X1*X4	0.1	16	0.01	291.43	0
X2*X3	1.6	16	0.1	5282.2	0
X2*X4	0	16	0	0.17	**0.9999**
X3*X4	0	16	0	0.19	**0.9998**
Error	0	512	0		
Total	22257.2	624			

Table B.7: CS2: Coefficients for the surface response methodology equation.

	Em	Pm
Constant	17.79447	321.501
X1	-69845.9	-2E+06
X2	0.166687	0.14924
X3	44.60672	49.4855
X4	0.34528	2.35397
X1*X2	-378.955	486.248
X1*X3	-14698.4	-14037
X1*X4	-18749.5	-24033
X2*X3	-0.1068	-0.0981
X2*X4	0.004585	6.21E-05
X3*X4	0.062753	0.02348
$X1^2$	4.21 10^9	4.2 10^9
$X2^2$	-0.00018	-0.0003
$X3^2$	-9.49704	-29.916
$X4^2$	-0.16905	-0.1074

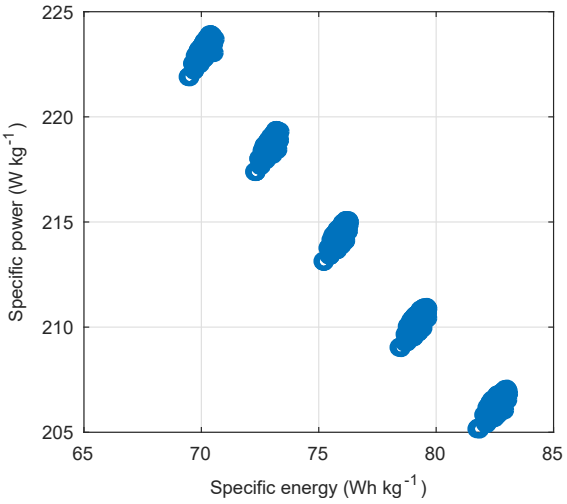

Figure B.3: CS2: Ragone plot of the simulated conditions.

In Figure B.4 and B.5 the interaction plots for specific energy and power are plotted, respectively.

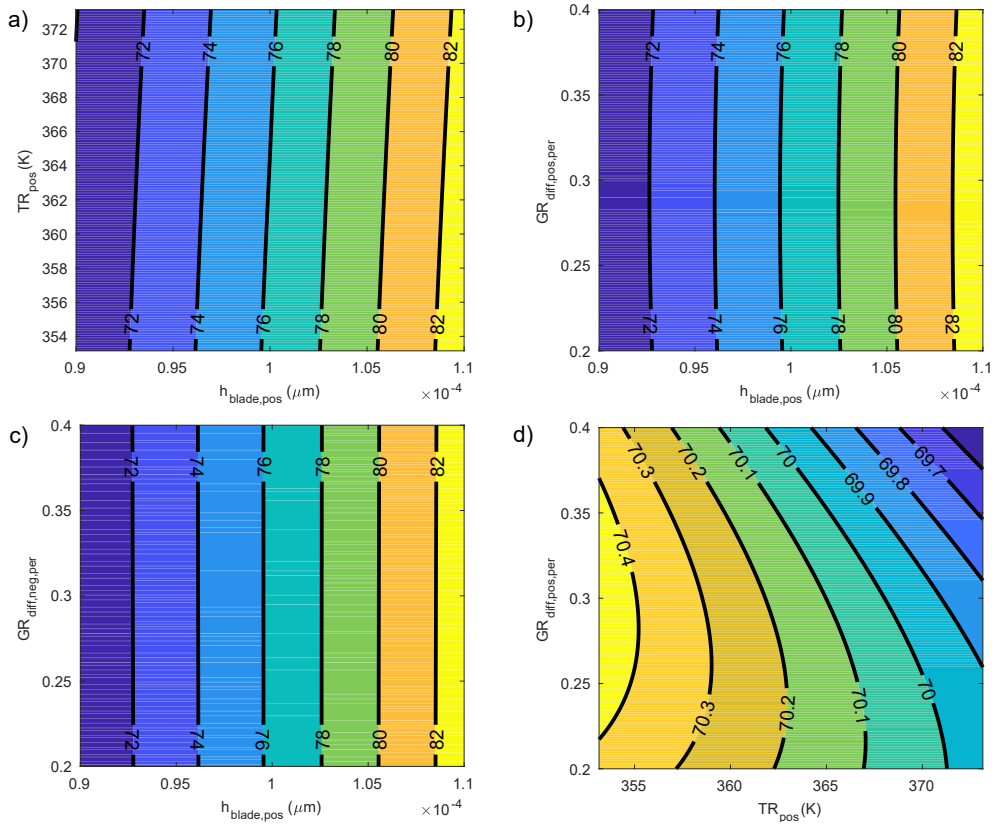

Figure B.4: CS2: Specific energy (W kg^{-1}) interaction effects (1C discharge): a) $h_{blade,pos} : TR_{pos}$; b) $h_{blade,pos} : GR_{diff,pos,per}$; c) $h_{blade,pos} : GR_{diff,neg,per}$; d) $TR_{pos} : GR_{diff,pos,per}$.

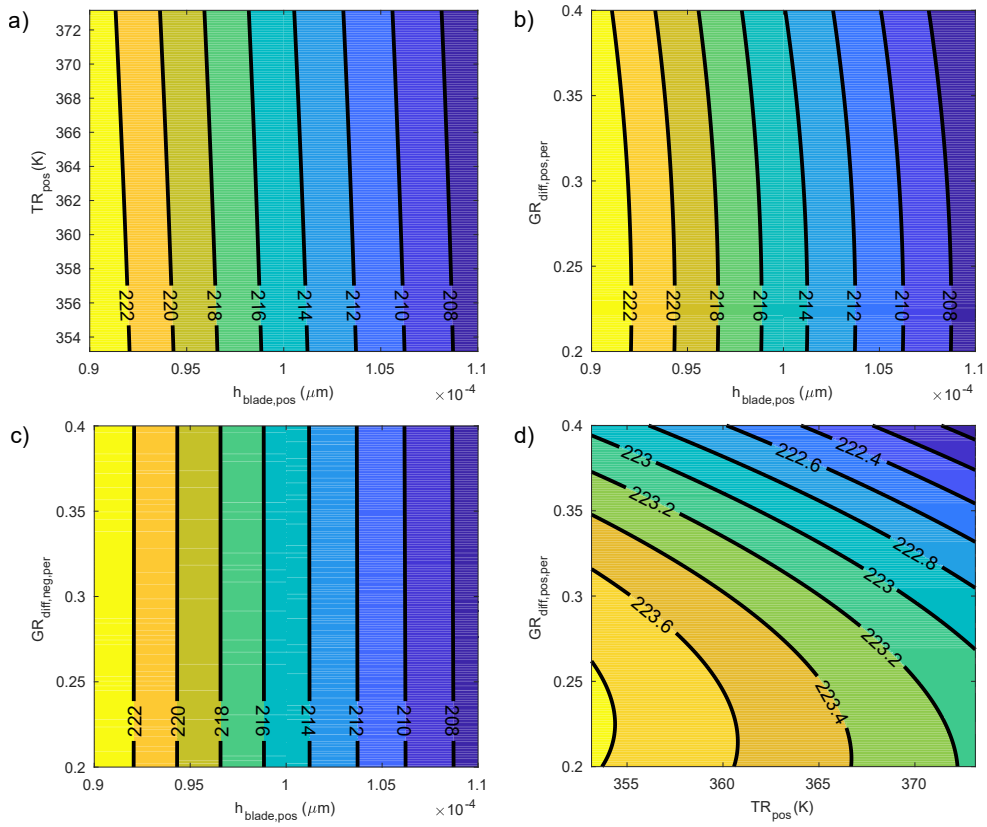

Figure B.5: CS2: Specific power (W kg^{-1}) interaction effects (1C discharge): a) $h_{blade,pos} : TR_{pos}$; b) $h_{blade,pos} : GR_{diff,pos,per}$; c) $h_{blade,pos} : GR_{diff,neg,per}$; d) $TR_{pos} : GR_{diff,pos,per}$.

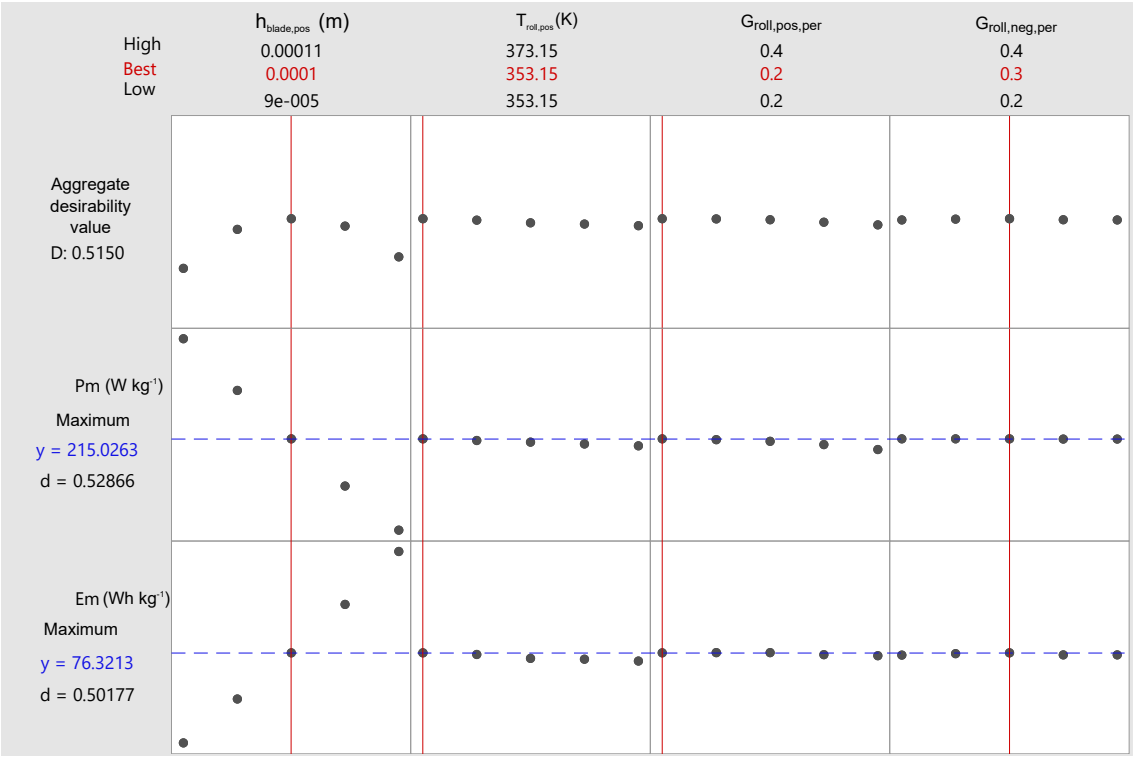

Figure B.6: CS2: Optimised parameters for specific energy and power responses.

B.2.2 After process-model relationships enhancement

Table B.8: CS2$^+$: Analysis of variance for specific energy response.

Source	Sum Sq.	d.f.	Mean Sq.	F	Prob > F
X1	278.933	4	69.7333	3807.67	0
X2	45.547	4	11.3867	621.75	0
X3	130.59	4	32.6475	1782.67	0
X4	0.122	4	0.0304	1.66	**0.1578**
X1*X2	0.544	16	0.034	1.86	**0.0223**
X1*X3	1.355	16	0.0847	4.62	0
X1*X4	0.32	16	0.02	1.09	**0.3582**
X2*X3	1.599	16	0.0999	5.46	0
X2*X4	0.162	16	0.0101	0.55	**0.9187**
X3*X4	0.355	16	0.0222	1.21	**0.2531**
Error	9.377	512	0.0183		
Total	468.903	624			

Table B.9: CS2$^+$: Analysis of variance for specific power response.

Source	Sum Sq.	d.f.	Mean Sq.	F	Prob > F
X1	22437	4	5609.26	2885856573	0
X2	36.9	4	9.22	4742015.89	0
X3	108.9	4	27.22	14005483.56	0
X4	0	4	0.01	3265.14	0
X1*X2	0.4	16	0.02	11526.86	0
X1*X3	0.1	16	0	1959.25	0
X1*X4	0.1	16	0.01	2780.66	0
X2*X3	1.3	16	0.08	42112.77	0
X2*X4	0	16	0	0.59	**0.8895**
X3*X4	0	16	0	0.48	**0.9586**
Error	0	512	0		
Total	22584.6	624			

Table B.10: CS2^{+}: Coefficients for the surface response methodology equation.

	Em	Pm
Constant	0.017897	326.73
X1	2487608	-2E+06
X2	0.235607	0.12925
X3	55.76859	45.5832
X4	-0.1584	2.41132
X1*X2	423.4016	477.266
X1*X3	-84005.3	-18234
X1*X4	-13316.9	-23478
X2*X3	-0.09117	-0.0861
X2*X4	0.006165	-0.0003
X3*X4	1.884444	-0.0034
$X1^2$	-1.3 10^{10}	4.3 10^{9}
$X2^2$	-0.0004	-0.0003
$X3^2$	-34.9089	-30.2
$X4^2$	-2.30015	-0.0739

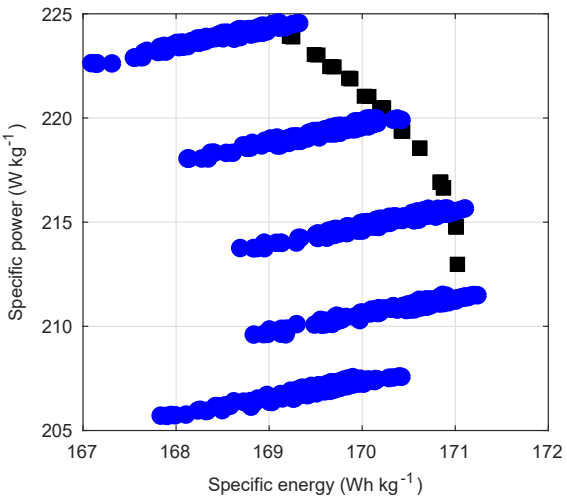

Figure B.7: CS2^{+}: Ragone plot of the simulated conditions.

In Figure B.8 the significant energy density interactions are presented. With the updated relationships, a lower calendering roller gap was identified as the optimal solution at the low level of roller temperature.

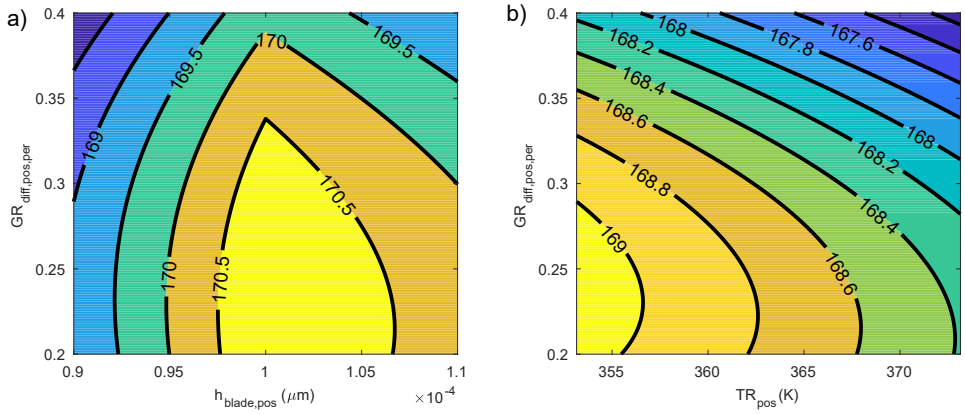

Figure B.8: CS2^{+}: Specific energy (W kg^{-1}) interaction effects (1C discharge): a) $h_{blade,pos}$: $GR_{diff,pos,per}$; b) TR_{pos} : $GR_{diff,pos,per}$.

In Figure B.9 the power density interactions are shown for the case study 2 with the improved process-model relationships. Similar tendencies were observed compared to the case study 2 without improvements.

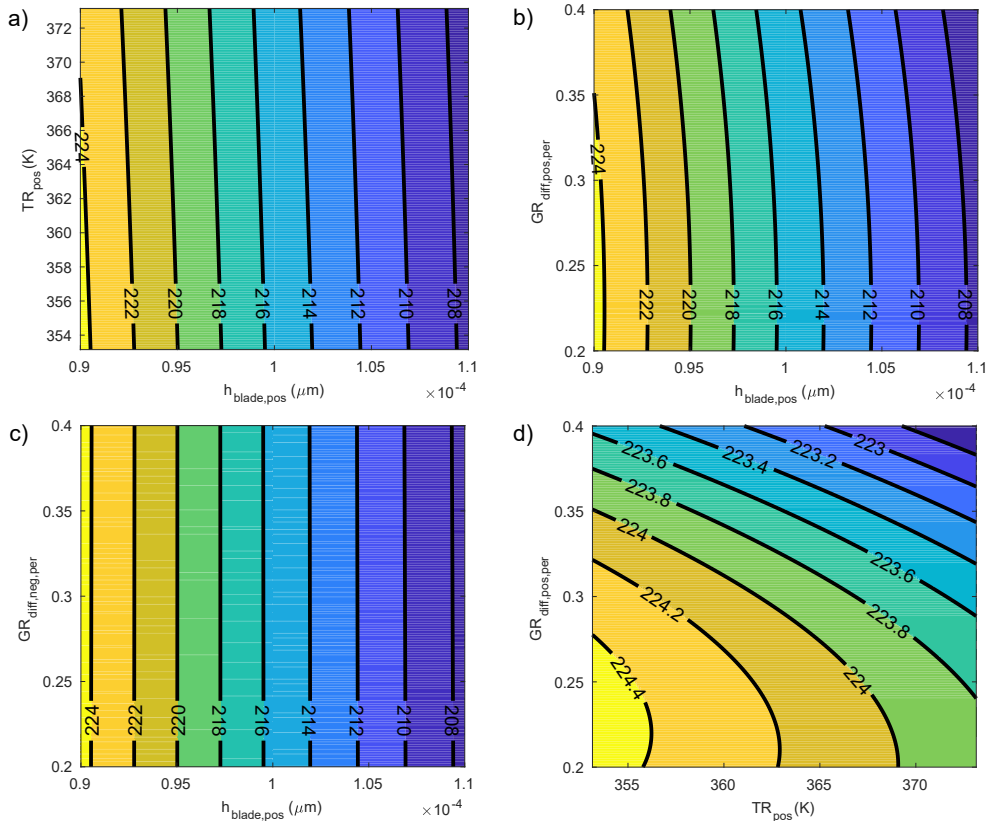

Figure B.9: CS2^{+}: Specific power (W kg^{-1}) interaction effects (1C discharge): a) $h_{blade,pos}$: TR_{pos}; b) $h_{blade,pos}$: $GR_{diff,pos,per}$; c) $h_{blade,pos}$: $GR_{diff,neg,per}$; d) TR_{pos} : $GR_{diff,pos,per}$.

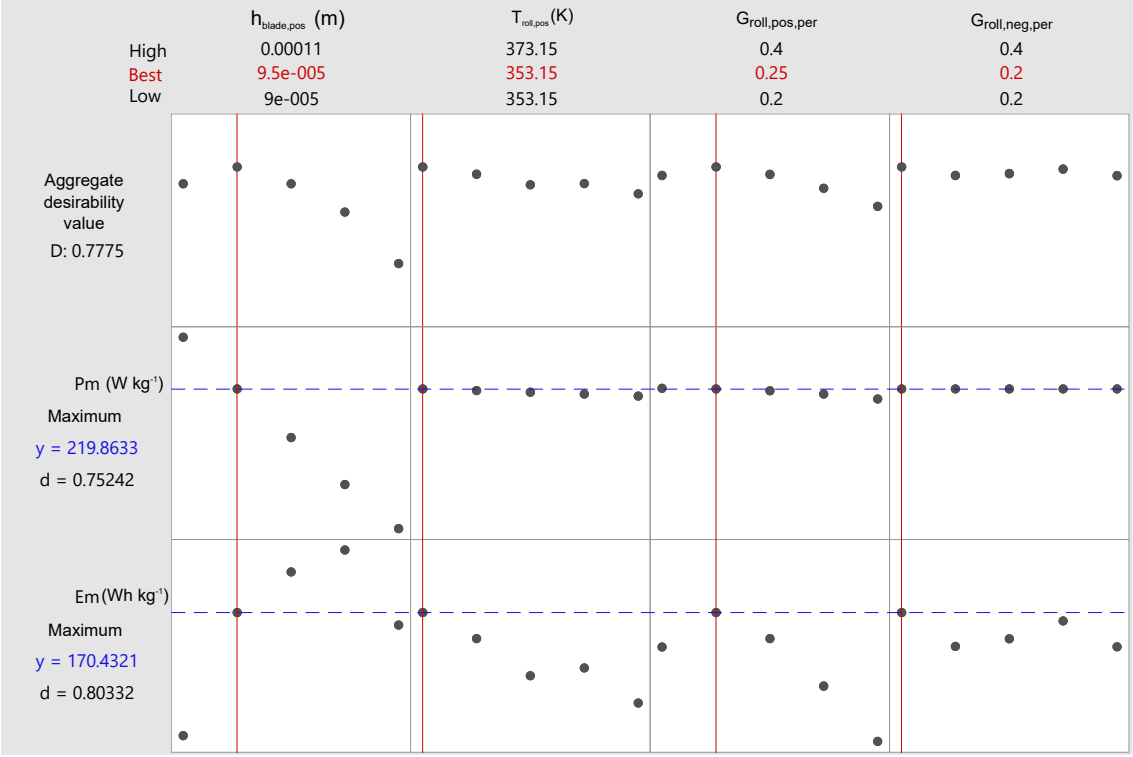

Figure B.10: CS2^{+}: Optimised parameters for specific energy and power responses.

B.3 CASE STUDY 3: AM PARTICLE RADIUS VARIATION WITH $h_{blade,pos}$ = 70 µM

Table B.11: CS3: Analysis of variance for specific energy response for 1C discharge.

Source	Sum Sq.	d.f.	Mean Sq.	F	Prob > F
X1	0.07	4	0.017	1.73	**0.1419**
X2	3772.53	4	943.132	94782.56	0
X3	985.62	4	246.406	24763.2	0
X4	30.58	4	7.646	768.43	0
X1*X2	0.17	16	0.011	1.09	**0.36**
X1*X3	0.18	16	0.011	1.15	**0.3057**
X1*X4	0.2	16	0.013	1.28	**0.2032**
X2*X3	1.4	16	0.088	8.81	0
X2*X4	0.5	16	0.031	3.13	0
X3*X4	0.2	16	0.013	1.27	**0.2091**
Error	5.09	512	0.01		
Total	4796.57	624			

Table B.12: CS3: Analysis of variance for specific power response for 1C discharge.

Source	Sum Sq.	d.f.	Mean Sq.	F	Prob > F
X1	0	4	0	3.22	**0.0125**
X2	0.048	4	0.012	4588.3	0
X3	579.604	4	144.901	54901698.9	0
X4	27.19	4	6.797	2575498.16	0
X1*X2	0	16	0	11.46	0
X1*X3	0	16	0	10.41	0
X1*X4	0	16	0	0.17	**0.9999**
X2*X3	0.001	16	0	21.39	0
X2*X4	0	16	0	0.51	**0.944**
X3*X4	0	16	0	0.38	**0.9863**
Error	0.001	512	0		
Total	606.845	624			

Table B.13: CS3: Analysis of variance for electrolyte concentration response for 1C discharge.

Source	Sum Sq.	d.f.	Mean Sq.	F	Prob > F
X1	0	4	0	7.16	0
X2	276	4	69	87201.76	0
X3	2141.7	4	535.4	676776.27	0
X4	367775.3	4	91943.8	116217693.5	0
X1*X2	0	16	0	0.91	**0.5537**
X1*X3	0	16	0	1.22	**0.247**
X1*X4	0	16	0	1.1	**0.3536**
X2*X3	0.6	16	0	46.98	0
X2*X4	18	16	1.1	1422.94	0
X3*X4	13.6	16	0.9	1076.17	0
Error	0.4	512	0		
Total	370225.7	624			

Table B.14: CS3: Analysis of variance for particle concentration response for 1C discharge.

Source	Sum Sq.	d.f.	Mean Sq.	F	Prob > F
X1	1382.4	4	345.6	1.76	**0.1364**
X2	77635.2	4	19408.8	98.61	0
X3	763677.8	4	190919.4	970.02	0
X4	2840.4	4	710.1	3.61	**0.0065**
X1*X2	4019.7	16	251.2	1.28	**0.2071**
X1*X3	4092.8	16	255.8	1.3	**0.1919**
X1*X4	4103.1	16	256.4	1.3	**0.1899**
X2*X3	7643.1	16	477.7	2.43	**0.0015**
X2*X4	10113.5	16	632.1	3.21	0
X3*X4	4399.6	16	275	1.4	**0.1376**
Error	100771.7	512	196.8		
Total	980679.3	624			

Table B.15: CS3: Coefficients for the surface response methodology equation.

	Em	Pm	ce	cs
Constant	158.4568786	245.017	692.76622	528.411
X1	-2234.854898	-1336.9	-11915.61	334024
X2	600067.006	-23492	526737.28	-1E+07
X3	29.031732	22.5299	-14.00856	-824.72
X4	2.998686499	2.85943	255.68875	-14.186
X1*X2	-1034779405	$3\ 10^{8}$	$-6.75\ 10^{8}$	$2.1\ 10^{11}$
X1*X3	10197.42373	-3145.5	3810.2814	$-2\ 10^{6}$
X1*X4	22845.48165	197.37	5995.6367	$-4\ 10^{6}$
X2*X3	-172215.9024	-2099.9	-104124.5	$1.1\ 10^{7}$
X2*X4	-32897.96339	587.621	-833983.1	4511001
X3*X4	-0.003607222	0.00677	-7.316151	-14.331
$X1^2$	286584539.5	$-2\ 10^{6}$	$1.064\ 10^{9}$	$-7\ 10^{10}$
$X2^2$	$-1.8971\ 10^{11}$	$1.4\ 10^{9}$	$1.116\ 10^{10}$	$-2\ 10^{10}$
$X3^2$	-56.0119233	-47.436	7.5808251	1503.85
$X4^2$	-3.530906871	-3.6658	-198.7491	-12.129

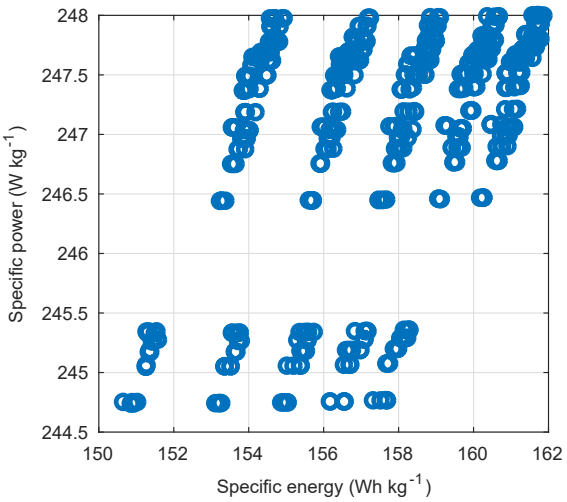

Figure B.11: CS3: Ragone plot of the simulated conditions.

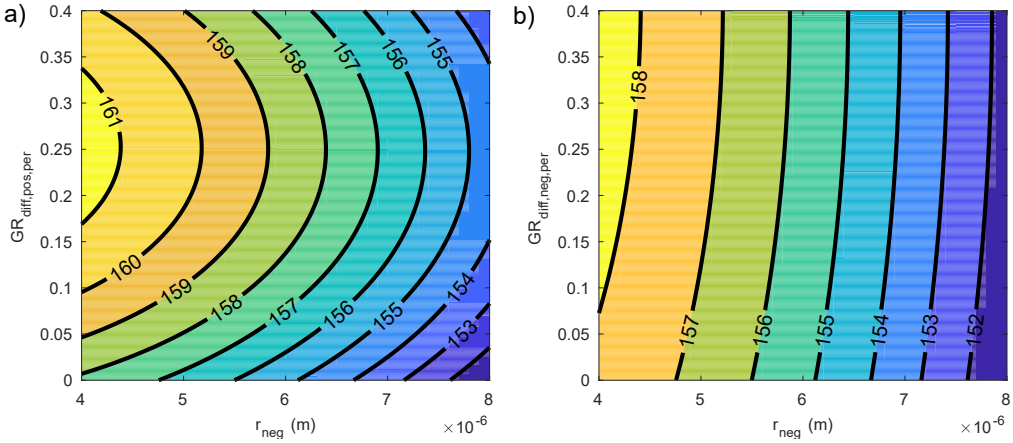

Figure B.12: CS3: Specific energy (W kg^{-1}) interaction effects (1C discharge): a) r_{neg} : $GR_{diff,pos,per}$; b) r_{neg} : $GR_{diff,neg,per}$.

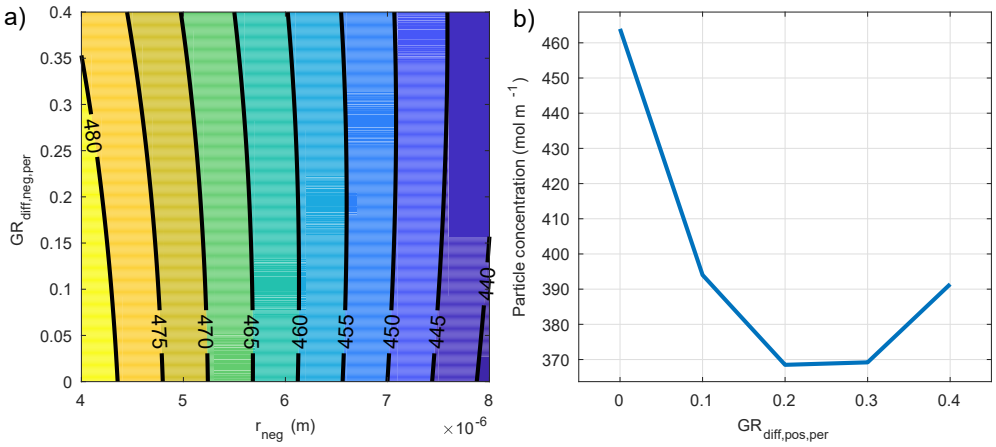

Figure B.13: CS3: AM surface concentration (mol m^{-1}) interaction effects (1C discharge): a) r_{neg} : $GR_{diff,neg,per}$; b) $GR_{diff,pos,per}$.

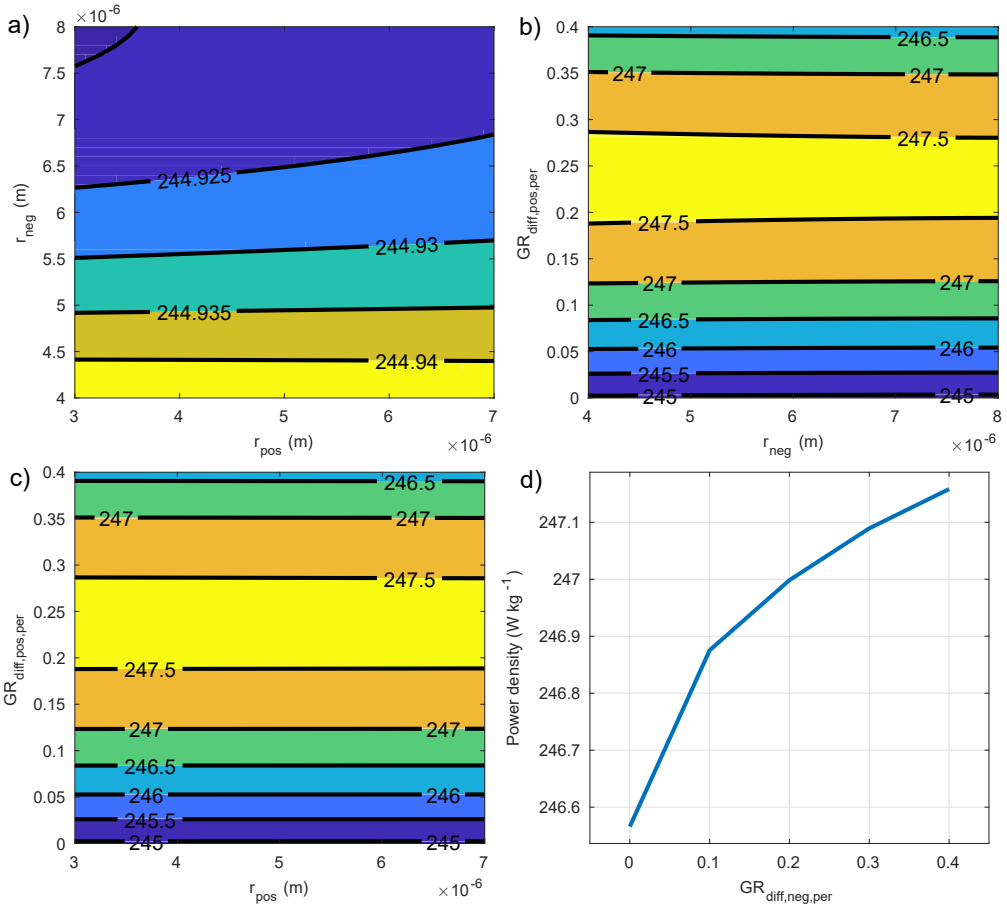

Figure B.14: CS3: Specific power (W kg^{-1}) interaction effects (1C discharge): a) $r_{neg} : GR_{diff,pos,per}$; b) $r_{pos} : r_{neg}$; c) $r_{pos} : GR_{diff,pos,per}$; d) $GR_{diff,neg,per}$.

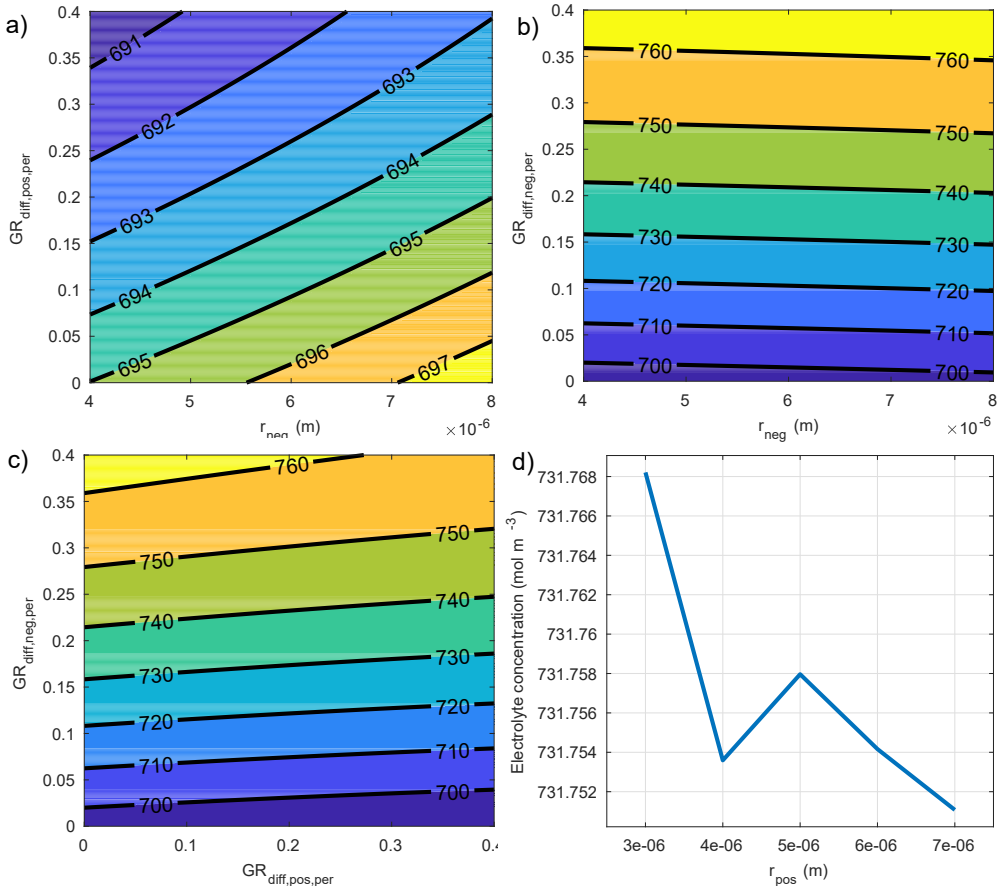

Figure B.15: CS3: Electrolyte concentration (mol m^{-1}) interaction effects (1C discharge): a) r_{neg} : $GR_{diff,pos,per}$; b) r_{neg} : $GR_{diff,neg,per}$; c) $GR_{diff,pos,per}$: $GR_{diff,neg,per}$; d) r_{pos}.

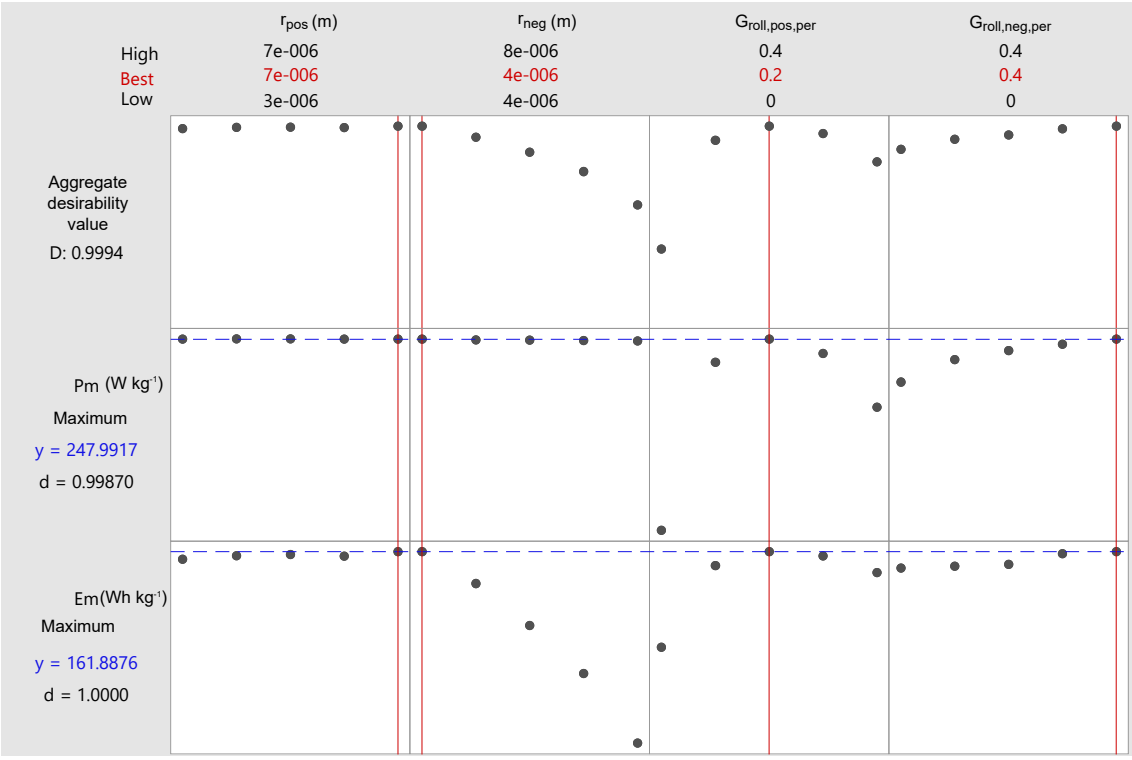

Figure B.16: CS3: Optimised parameters for specific energy and power responses.

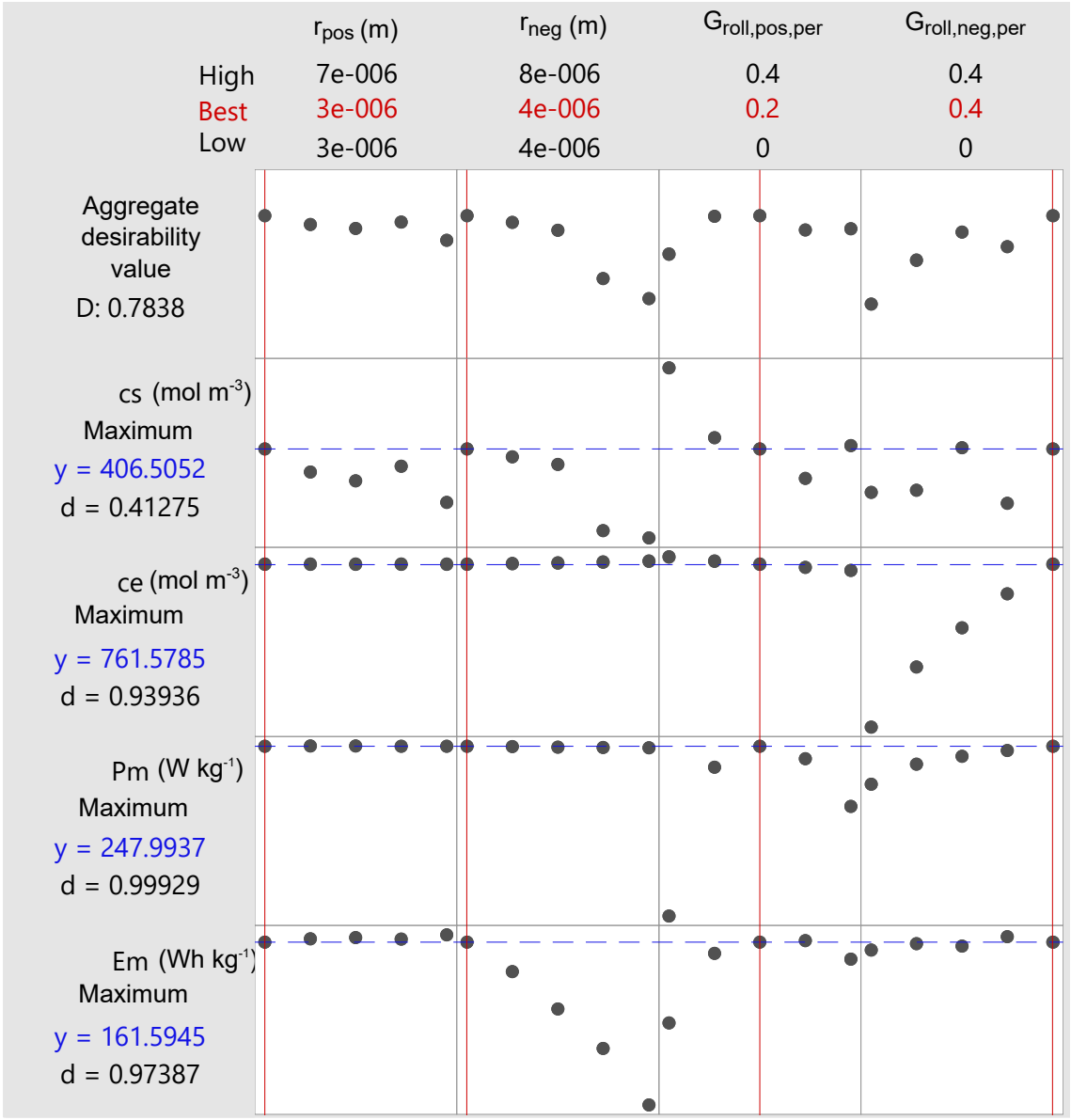

Figure B.17: CS3: Optimised parameters for the minimum electrolyte concentration, minimum negative active material concentration, specific energy and power responses.

LIST OF FIGURES

LIST OF TABLES

REFERENCES

[1] EIA, "International Energy Outlook 2017 Overview," Tech. Rep., 2017.

[2] World Economic Forum, "A Vision for a Sustainable Battery Value Chain in 2030 Unlocking the Full Potential to Power Sustainable Development and Climate Change Mitigation," Tech. Rep., 2019.

[3] N. Edomah, C. Foulds, and A. Jones, "Influences on energy supply infrastructure: A comparison of different theoretical perspectives," *Renew. Sust. Energ. Rev.*, vol. 79, no. April, pp. 765–778, 2017. DOI: 10.1016/j.rser.2017.05.072.

[4] U. Nations, "Paris agreement," Tech. Rep., 2015.

[5] G. Bichisao, M. M. Diaz, and E. Pizzi, "Horizon 2030. Looking Ahead to Challenges and Opportunities," Tech. Rep., 2019.

[6] Gobierno Vasco, "Estrategia energética de euskadi 2030," Tech. Rep., 2017.

[7] L. Fara and D. Craciunescu, "Output Analysis of Stand-alone PV Systems: Modeling, Simulation and Control," *Energy Procedia*, vol. 112, no. October 2016, pp. 595–605, 2017. DOI: 10.1016/j.egypro.2017.03.1125.

[8] S. Daiva, G. Saulius, and A. Liudmila, "Energy Distribution Planning Models Taxonomy and Methods of Distributed Generation Systems," *Energy Proc.*, vol. 107, no. September 2016, pp. 275–283, 2017. DOI: 10.1016/j.egypro.2016.12.150.

[9] H. Auvinen, T. Järvi, M. Kloetzke, U. Kugler, J. A. Bühne, F. Heinl, J. Kurte, and K. Esser, "Electromobility Scenarios: Research Findings to Inform Policy," *Transp. Res. Rec.*, vol. 14, pp. 2564–2573, 2016. DOI: 10.1016/j.trpro.2016.05.346.

[10] G. E. Blomgren, "The Development and Future of Lithium Ion Batteries," *J. Electrochem. Soc.*, vol. 164, no. 1, pp. 5019–5025, 2017. DOI: 10.1149/2.0251701jes.

[11] K. Edström, R. Dominko, M. Fichtner, T. Otuszewski, S. Perraud, C. Punckt, J.-m. Tarascon, T. Vegge, and W. Martin, "BATTERY 2030+. Inventing the sustainable batteries of the future. Research needs and future actions," Tech. Rep., 2020.

[12] M. Munshi and A. Zafar, "WO2005048394 A1: Lithium Ion Battery and Methods of Manufacturing Same," 2003.

[13] C. Masarapu, Y. K. Anguchamy, Y. Han, H. Deng, S. Kumar, and H. A. Loper, "US009780358 B2: Battery designs with high capacity anode materials and cathode materials," 2013.

[14] M. Á. Muñoz-márquez, D. Saurel, J. L. Gómez-cámer, M. Casas-cabanas, E. Castillo-martínez, and T. Rojo, "Na-Ion Batteries for Large Scale Applications : A Review on Anode Materials and Solid Electrolyte Interphase Formation," *Adv. Energy Mater.*, vol. 1700463, pp. 1–31, 2017. DOI: 10.1002/aenm.201700463.

[15] M. S. Islam and C. A. Fisher, "Lithium and sodium battery cathode materials: Computational insights into voltage, diffusion and nanostructural properties," *Chem. Soc. Rev.*, vol. 43, no. 1, pp. 185–204, 2014. DOI: 10.1039/c3cs60199d.

[16] P. K. Nayak, L. Yang, W. Brehm, and P. Adelhelm, "From Lithium-Ion to Sodium-Ion Batteries: Advantages, Challenges, and Surprises," *Angew. Chem. Int. Ed.*, vol. 57, no. 1, pp. 102–120, 2018. DOI: 10.1002/anie.201703772.

[17] F. Belkhir, F. Röder, and U. Krewer, "Model-based optimal design of high energy density Li-Ion batteries with thick electrodes," in *The 69th Annual Meeting of the International Society of Electrochemistry*, 2018.

[18] V. Laue, N. Wolff, F. Röder, and U. Krewer, "Modeling the Calendering Influence in Lithium-Ion Batteries from Micro to Macro Scale," in *The 69th Annual Meeting of the International Society of Electrochemistry*, 2018.

[19] G.-h. Kim, K. Smith, K.-j. Lee, S. Santhanagopalan, and A. Pesaran, "Multi-Domain Modeling of Lithium-Ion Batteries Encompassing Multi-Physics in Varied Length Scales," *J. Electrochem. Soc.*, vol. 158, no. 8, pp. A955–A969, 2011. DOI: 10.1149/1.3597614.

[20] A. A. Franco, "Multiscale modelling and numerical simulation of rechargeable lithium ion batteries: concepts, methods and challenges," *RSC Adv.*, vol. 3, no. 32, p. 13027, 2013. DOI: 10.1039/c3ra23502e.

[21] M. Doyle and J. Newman, "The use of mathematical modeling in the design of lithium/polymer battery systems," *Electrochim. Acta*, vol. 40, no. 13-14, pp. 2191–2196, 1995. DOI: 10.1016/0013-4686(95)00162-8.

[22] J. Schmalstieg and D. U. Sauer, "Full Cell Parameterization of a High-Power Lithium-Ion Battery for a Physico-Chemical Model: Part II. Thermal Parameters and Validation," *J. Electrochem. Soc.*, vol. 165, no. 16, pp. A3811–A3819, 2018. DOI: 10.1149/2.0331816jes.

[23] E. Garayalde, "Hybrid Energy Storage Systems via Power Electronic Converters," Ph.D. dissertation, Mondragon Unibertsitatea, 2019.

[24] M. A. Hannan, M. M. Hoque, A. Mohamed, and A. Ayob, "Review of energy storage systems for electric vehicle applications: Issues and challenges," *Renew. Sust. Energ. Rev.*, vol. 69, no. August 2016, pp. 771–789, 2017. DOI: 10.1016/j.rser.2016.11.171.

[25] Energy Storage Inter-platform Group, "State of the art of energy storage regulations and technology," Tech. Rep., 2011.

[26] C. N. Rasmussen, A. Altiparmakis, and M. Daumling, "Electromagnetic and electrostatic storage," DTU International Energy Report 2013: Energy storage options for future sustainable energy systems, Tech. Rep., 2013.

[27] G. Alva, Y. Lin, and G. Fang, "An Overview of Thermal Energy Storage," *Energy*, vol. 144, pp. 341–378, 2018. DOI: 10.1016/j.energy.2017.12.037.

[28] J. Warner, "Lithium-Ion and Other Cell Chemistries," in *The Handbook of Lithium-Ion Battery Pack Design*. Elsevier, 2015, pp. 65–89.

[29] D. Linden and T. B. Reddy, *Handbook of Batteries*, 3rd ed., D. Linden and T. B. Reddy, Eds. McGraw-Hill, 2002.

[30] S. Rehman, L. M. Al-Hadhrami, and M. M. Alam, "Pumped hydro energy storage system: A technological review," *Renew. Sust. Energ. Rev.*, vol. 44, pp. 586–598, 2015. DOI: 10.1016/j.rser.2014.12.040.

[31] M. Budt, D. Wolf, R. Span, and J. Yan, "A review on compressed air energy storage: Basic principles, past milestones and recent developments," *Appl. Energy*, vol. 170, pp. 250–268, 2016. DOI: 10.1016/j.apenergy.2016.02.108.

[32] S. M. Mousavi G, F. Faraji, A. Majazi, and K. Al-Haddad, "A comprehensive review of Flywheel Energy Storage System technology," *Renew. Sust. Energ. Rev.*, vol. 67, pp. 477–490, 2017. DOI: 10.1016/j.rser.2016.09.060.

[33] A. Kirubakaran, S. Jain, and R. K. Nema, "A review on fuel cell technologies and power electronic interface," *Renew. Sust. Energ. Rev.*, vol. 13, no. 9, pp. 2430–2440, 2009. DOI: 10.1016/j.rser.2009.04.004.

[34] A. González, E. Goikolea, J. A. Barrena, and R. Mysyk, "Review on supercapacitors: Technologies and materials," *Renew. Sust. Energ. Rev.*, vol. 58, pp. 1189–1206, 2016. DOI: 10.1016/j.rser.2015.12.249.

[35] L. Oca, N. Guillet, R. Tessard, and U. Iraola, "Lithium-ion capacitor safety assessment under electrical abuse tests based on ultrasound characterization and cell opening," *J. Energy Storage*, vol. 23, no. February, pp. 29–36, 2019. DOI: 10.1016/j.est.2019.02.033.

[36] T. S. Mathis, N. Kurra, X. Wang, D. Pinto, P. Simon, and Y. Gogotsi, "Energy Storage Data Reporting in Perspective—Guidelines for Interpreting the Performance of Electrochemical Energy Storage Systems," *Advanced Energy Materials*, vol. 9, no. 39, pp. 1–13, 2019. DOI: 10.1002/aenm.201902007.

[37] J. Warner, "Lithium-Ion and Other Cell Chemistries," in *The Handbook of Lithium-Ion Battery Pack Design*. Elsevier, 2015, pp. 65–89.

[38] E. Sarasketa-Zabala, "A novel approach for Li-ion battery selection and lifetime prediction," Ph.D. dissertation, Mondragon Unibertsitatea, 2014.

[39] N. Lebedeva, F. Di Persio, and L. Boon-Brett, "Lithium ion battery value chain and related opportunities for Europe Title: Lithium ion battery value chain and related opportunities for Europe," Tech. Rep., 2016.

[40] P. Adelhelm, P. Hartmann, C. L. Bender, M. Busche, C. Eufinger, and J. Janek, "From lithium to sodium: Cell chemistry of room temperature sodium-air and sodium-sulfur batteries," *Beilstein J. Nanotechnol.*, vol. 6, no. 1, pp. 1016–1055, 2015. DOI: 10.3762/bjnano.6.105.

[41] C. Sun, J. Liu, Y. Gong, P. David, and J. Zhang, "Recent advances in all-solid-state rechargeable lithium batteries," *Nano Energy*, vol. 33, no. January, pp. 363–386, 2017. DOI: 10.1016/j.nanoen.2017.01.028.

[42] J. G. Kim, B. Son, S. Mukherjee, N. Schuppert, A. Bates, O. Kwon, M. J. Choi, H. Y. Chung, and S. Park, "A review of lithium and non-lithium based solid state batteries," *J. Power Sourc.*, vol. 282, pp. 299–322, 2015. DOI: 10.1016/j.jpowsour.2015.02.054.

[43] L. Grande, "Solid - State and Polymer Batteries 2017-2027 : The coming of age of a safer and better technology," IDTechEx Research, Tech. Rep., 2016.

[44] Y. Wang, R. Chen, T. Chen, H. Lv, G. Zhu, L. Ma, C. Wang, Z. Jin, and J. Liu, "Emerging non-lithium ion batteries," *Energy Storage Mater.*, vol. 4, pp. 103–129, 2016. DOI: 10.1016/j.ensm.2016.04.001.

[45] P. Jezowski, "Lithium-ion capacitors basaed on in-situ pre-lithiation of the graphite electrode from a composite positive electrode," Ph.D. dissertation, Poznan University of Technology, 2016.

[46] F. Beguin and E. Frackowiak, *Supercapacitors. Materials, Systems, and Applications*, F. Beguin and E. Frackowiak, Eds. Wiley-VCH Verlag GmbH and Co. KGaA, 2012.

[47] A. Kwade and W. Haselrieder, "Effect of Electrode and Cell Production Steps on Lithium-Ion Battery Cell Performance and Costs," in *AABC Europe*, 2017.

[48] D. Miranda, C. M. Costa, and S. Lanceros-Mendez, "Review: Lithium ion rechargeable batteries: State of the art and future needs of microscopic theoretical models and simulations," *J. Electroanal. Chem.*, vol. 739, pp. 97–110, 2015. DOI: 10.1016/j.jelechem.2014.12.010.

[49] M. Doyle, J. Newman, A. S. Gozdz, C. N. Schmutz, and J.-M. Tarascon, "Comparison of Modeling Predictions with Experimental Data from Plastic Lithium Ion Cells," *J. Electrochem. Soc.*, vol. 143, no. 6, pp. 1890–1903, 1996. DOI: 10.1149/1.1836921.

[50] M. Ecker, T. K. D. Tran, P. Dechent, S. Kabitz, A. Warnecke, and D. U. Sauer, "Parameterization of a Physico-Chemical Model of a Lithium-Ion Battery: I. Determination of Parameters," *J. Electrochem. Soc.*, vol. 162, no. 9, pp. A1836–A1848, 2015. DOI: 10.1149/2.0551509jes.

[51] M. Ecker, S. Kabitz, I. Laresgoiti, and D. U. Sauer, "Parameterization of a Physico-Chemical Model of a Lithium-Ion Battery: II. Model Validation," *J. Electrochem. Soc.*, vol. 162, no. 9, pp. A1849–A1857, 2015. DOI: 10.1149/2.0541509jes.

[52] J. Schmalstieg, C. Rahe, M. Ecker, and D. U. Sauer, "Full Cell Parameterization of a High-Power Lithium-Ion Battery for a Physico-Chemical Model: Part I. Physical and Electrochemical Parameters," *J. Electrochem. Soc.*, vol. 165, no. 16, pp. A3799–A3810, 2018. DOI: 10.1149/2.0321816jes.

[53] V. Ramadesigan, P. W. C. Northrop, S. De, S. Santhanagopalan, R. D. Braatz, and V. R. Subramanian, "Modeling and Simulation of Lithium-Ion Batteries from a Systems Engineering Perspective," *J. Electrochem. Soc.*, vol. 159, no. 3, pp. R31–R45, 2012. DOI: 10.1149/2.018203jes.

[54] G. Plett, *Battery Management Systems: Battery modeling, Volume I.* Artech House, 2015.

[55] P. P. Mukherjee, S. Pannala, and J. A. Turner, "Modeling and Simulation of Battery Systems," in *Handbook of Battery Materials: Second Edition.* Weinheim, Germany: Wiley-VCH Verlag GmbH and Co. KGaA, aug 2011, pp. 841–875.

[56] A. Falconi, "Electrochemical Li-Ion battery modeling for electric vehicles," Ph.D. dissertation, Communaute Universite Grenoble Alpes, 2018.

[57] M. Doyle, T. F. Fuller, and J. Newman, "Modeling of Galvanostatic Charge and Discharge of the Lithium/Polymer/Insertion Cell," *J. Electrochem. Soc.*, vol. 140, no. 6, pp. 1526 – 1533, 1993. DOI: 10.1149/1.2221597.

[58] W. Fang, O. J. Kwon, and C. Y. Wang, "Electrochemical-thermal modeling of automotive Li-ion batteries and experimental validation using a three-electrode cell," *Int. J. Energy Res.*, vol. 34, no. 2, pp. 107–115, 2010. DOI: 10.1002/er.1652.

[59] M. Safari and C. Delacourt, "Mathematical Modeling of Lithium Iron Phosphate Electrode: Galvanostatic Charge/Discharge and Path Dependence," *J. Electrochem. Soc.*, vol. 158, no. 2, p. A63, 2011. DOI: 10.1149/1.3515902.

[60] E. Prada, D. Di Domenico, Y. Creff, J. Bernard, V. Sauvant-Moynot, and F. Huet, "Simplified Electrochemical and Thermal Model of LiFePO4-Graphite Li-Ion Batteries for Fast Charge Applications," *J. Electrochem. Soc.*, vol. 159, no. 9, pp. A1508–A1519, jan 2012. DOI: 10.1149/2.064209jes.

[61] M. Ecker, "Lithium Plating in Lithium-Ion Batteries," Ph.D. dissertation, RWTH Aachen University, 2016.

[62] J. Schmalstieg, "Physikalisch-elektrochemische Simulation von Lithium-Ionen-Batterien. Implementierung, Parametrierung und Anwendung," Ph.D. dissertation, RWTH Aachen University, 2015.

[63] V. Boovaragavan, S. Harinipriya, and V. R. Subramanian, "Towards real-time (milliseconds) parameter estimation of lithium-ion batteries using reformulated physics-based models," *J. Power Sourc.*, vol. 183, no. 1, pp. 361–365, aug 2008. DOI: 10.1016/j.jpowsour.2008.04.077.

[64] A. Jokar, B. Rajabloo, M. Désilets, and M. Lacroix, "An Inverse Method for Estimating the Electrochemical Parameters of Lithium-Ion Batteries I. Methodology," *J. Electrochem. Soc.*, vol. 163, no. 14, pp. A2876–A2886, 2016. DOI: 10.1149/2.0191614jes.

[65] B. Rajabloo, A. Jokar, M. Désilets, and M. Lacroix, "An Inverse Method for Estimating the Electrochemical Parameters of Lithium-Ion Batteries II: Implementation," *J. Electrochem. Soc.*, vol. 164, no. 2, pp. A99–A105, 2017. DOI: 10.1149/2.0221702jes.

[66] A. Jokar, M. Désilets, M. Lacroix, and K. Zaghib, "Mesoscopic modeling and parameter estimation of a lithium-ion battery based on LiFePO4/graphite," *J. Power Sourc.*, vol. 379, no. December 2017, pp. 84–90, 2018. DOI: 10.1016/j.jpowsour.2018.01.035.

[67] V. Ramadesigan, K. Chen, N. a. Burns, V. Boovaragavan, R. D. Braatz, and V. R. Subramanian, "Parameter Estimation and Capacity Fade Analysis of Lithium-Ion Batteries Using Reformulated Models," *J. Electrochem. Soc.*, vol. 158, no. 9, p. A1048, 2011. DOI: 10.1149/1.3609926.

[68] A. Rahman, S. Anwar, and A. Izadian, "Electrochemical model parameter identi fi cation of a lithium-ion battery using particle swarm optimization method," *J. Power Sourc.*, vol. 307, pp. 86–97, 2016. DOI: 10.1016/j.jpowsour.2015.12.083.

[69] S. Santhanagopalan, Q. Guo, and R. E. White, "Parameter Estimation and Model Discrimination for a Lithium-Ion Cell," *J. Electrochem. Soc.*, vol. 154, no. 3, p. A198, 2007. DOI: 10.1149/1.2422896.

[70] S. Santhanagopalan, Q. Zhang, K. Kumaresan, and R. E. White, "Parameter Estimation and Life Modeling of Lithium-Ion Cells," *J. Electrochem. Soc.*, vol. 155, no. 4, p. A345, 2008. DOI: 10.1149/1.2839630.

[71] J. Vazquez-Arenas, L. E. Gimenez, M. Fowler, T. Han, and S. K. Chen, "A rapid estimation and sensitivity analysis of parameters describing the behavior of commercial Li-ion batteries including thermal analysis," *Energy Convers. Manag.*, vol. 87, pp. 472–482, 2014. DOI: 10.1016/j.enconman.2014.06.076.

[72] J. C. Forman, S. J. Moura, J. L. Stein, and H. K. Fathy, "Genetic identification and fisher identifiability analysis of the Doyle-Fuller-Newman model from experimental cycling of a LiFePO4 cell," *J. Power Sourc.*, vol. 210, pp. 263–275, jul 2012. DOI: 10.1016/j.jpowsour.2012.03.009.

[73] B. Rajabloo and Y. Choquette, "Parameter Estimation of Single Particle Model Using COMSOL Multiphysics ® and MATLAB ® Optimization Toolbox," in *Proceedings of the 2015 COMSOL Conference*, 2015.

[74] R. Masoudi, T. Uchida, and J. McPhee, "Parameter estimation of an electrochemistry-based lithium-ion battery model," *J. Power Sourc.*, vol. 291, pp. 215–224, 2015. DOI: 10.1016/j.jpowsour.2015.04.154.

[75] Z. Deng, H. Deng, L. Yang, Y. Cai, and X. Zhao, "Implementation of reduced-order physics-based model and multi-parameters identification strategy for lithium-ion battery," *Energy*, vol. 138, pp. 509–519, 2017. DOI: 10.1016/j.energy.2017.07.069.

[76] E. Namor, D. Torregrossa, R. Cherkaoui, and M. Paolone, "Parameter identification of a lithium-ion cell single-particle model through non-invasive testing," *J. Energy Storage*, vol. 12, pp. 138–148, 2017. DOI: 10.1016/j.est.2017.04.008.

[77] J. Li, L. Wang, C. Lyu, E. Liu, Y. Xing, and M. Pecht, "A parameter estimation method for a simplified electrochemical model for Li-ion batteries," *Electrochim. Acta*, vol. 275, no. 92, pp. 50–58, 2018. DOI: 10.1016/j.electacta.2018.04.098.

[78] S. Park, D. Kato, Z. Gima, R. Klein, and S. J. Moura, "Optimal Input Design for Parameter Identification in an Electrochemical Li-ion Battery Model," *2018 American Control Conference*, no. September, p. 8, 2018. DOI: 10.23919/ACC.2018.8431479.

[79] L. Zhang, C. Lyu, L. Wang, W. Luo, and K. Ma, "Thermal-electrochemical modeling and parameter sensitivity analysis of lithium-ion battery," in *Chemical Engineering Transactions*, vol. 33. Italian Association of Chemical Engineering - AIDIC, 2013, pp. 943–948. DOI: 10.3303/CET1333158.

[80] L. Zhang, C. Lyu, L. Wang, J. Zheng, W. Luo, and K. Ma, "Parallelized Genetic Identification of the Thermal-Electrochemical Model for Lithium-Ion Battery," *Adv. Mech. Eng.*, vol. 5, pp. 754 653–754 653, 2015. DOI: 10.1155/2013/754653.

[81] L. Zhang, C. Lyu, G. Hinds, L. Wang, W. Luo, J. Zheng, and K. Ma, "Parameter Sensitivity Analysis of Cylindrical LiFePO4 Battery Performance Using Multi-Physics Modeling," *J. Electrochem. Soc.*, vol. 161, no. 5, pp. A762–A776, 2014. DOI: 10.1149/2.048405jes.

[82] R. Jobman, M. S. Trimboli, and G. L. Plett, "Identification of Lithium-Ion Physics-Based Model Parameter Values," *JECM*, vol. 2, no. 2, pp. 45–55, 2015.

[83] R. R. Jobman, "Identification of Lithium-Ion-Cell Physics-Model Parameter Values," Ph.D. dissertation, UCCS, 2016.

[84] Z. Chu, G. L. Plett, M. S. Trimboli, and M. Ouyang, "A control-oriented electrochemical model for lithium-ion battery, Part I: Lumped-parameter reduced-order model with constant phase element," *J. Energy Storage*, vol. 25, no. February, p. 100828, 2019. DOI: 10.1016/j.est.2019.100828.

[85] M. Mayur, M. C. Yagci, S. Carelli, P. Margulies, D. Velten, and W. G. Bessler, "Identification of stoichiometric and microstructural parameters of a lithium-ion cell with blend electrode," *Phys. Chem. Chem. Phys.*, vol. 21, no. 42, pp. 23 672–23 684, 2019. DOI: 10.1039/c9cp04262h.

[86] C. Meyer, H. Bockholt, W. Haselrieder, and A. Kwade, "Characterization of the calendering process for compaction of electrodes for lithium-ion batteries," *J. Mater. Process*, vol. 249, pp. 172–178, nov 2017. DOI: 10.1016/j.jmatprotec.2017.05.031.

[87] P. Arora, M. Doyle, A. S. Gozdz, R. E. White, and J. Newman, "Comparison between computer simulations and experimental data for high-rate discharges of plastic lithium-ion batteries," Tech. Rep., 2000.

[88] M. Doyle and Y. Fuentes, "Computer Simulations of a Lithium-Ion Polymer Battery and Implications for Higher Capacity Next-Generation Battery Designs," *J. Electrochem. Soc.*, vol. 150, no. 6, p. A706, jun 2003. DOI: 10.1149/1.1569478.

[89] G. Lenze, F. Röder, H. Bockholt, W. Haselrieder, A. Kwade, and U. Krewer, "Simulation-Supported Analysis of Calendering Impacts on the Performance of Lithium-Ion-Batteries," *J. Electrochem. Soc.*, vol. 164, no. 6, pp. A1223–A1233, 2017. DOI: 10.1149/2.1141706jes.

[90] M. Schönemann, *Multiscale Simulation Approach for Battery Production Systems*, C. Herrmann and S. Kara, Eds. Switzerland: Springer International Publishing AG 2017, 2017.

[91] M. Thomitzek, N. von Drachenfels, F. Cerdas, C. Herrmann, and S. Thiede, "Simulation-based assessment of the energy demand in battery cell manufacturing," in *Procedia CIRP 80*, 2019, pp. 126–131. DOI: 10.1016/j.procir.2019.01.097.

[92] M. Thomitzek, F. Cerdas, S. Thiede, and C. Herrmann, "Cradle-to-Gate Analysis of the Embodied Energy in Lithium Ion Batteries," in *Procedia CIRP 80*, 2019, pp. 304–309. DOI: 10.1016/j.procir.2019.01.099.

[93] W. Haselrieder, "Kalandrierung zur gezielten Einstellung der Batterieelektroden-Performance," Ph.D. dissertation, Technischen Universitat Carolo-Wilhelmina zu Braunschweig, 2016.

[94] S. Jaiser, N. S. Salach, M. Baunach, P. Scharfer, S. Jaiser, N. S. Salach, M. Baunach, and P. Scharfer, "Impact of drying conditions and wet film properties on adhesion and film solidification of lithium-ion battery anodes film solidification of lithium-ion battery anodes," *Dry. Technol.*, vol. 35, no. 15, pp. 1807–1817, 2017. DOI: 10.1080/07373937.2016.1276584.

[95] C. Meyer, "Prozessmodellierung der Kalandrierung von Lithium-Ionen-Batterie-Elektroden," Ph.D. dissertation, Fakultät für Maschinenbau der Technischen Universität Carolo-Wilhelmina zu Braunschweig, 2019.

[96] C. Meyer, M. Kosfeld, W. Haselrieder, and A. Kwade, "Process modeling of the electrode calendering of lithium-ion batteries regarding variation of cathode active materials and mass loadings," *J. Energy Storage*, vol. 18, no. April, pp. 371–379, 2018. DOI: 10.1016/j.est.2018.05.018.

[97] C. Meyer, M. Weyhe, W. Haselrieder, and A. Kwade, "Heated Calendering of Cathodes for Lithium-Ion Batteries with Varied Carbon Black and Binder Contents," *Energy Technol.*, vol. 8, no. 2, 2020. DOI: 10.1002/ente.201900175.

[98] D. Schreiner, M. Oguntke, T. Günther, and G. Reinhart, "Modelling of the Calendering Process of NMC-622 Cathodes in Battery Production Analyzing Machine/Material–Process–Structure Correlations," *Energy Technol.*, vol. 7, no. 11, p. 11, 2019. DOI: 10.1002/ente.201900840.

[99] O. Schmidt, M. Thomitzek, F. Röder, S. Thiede, C. Herrmann, and U. Krewer, "Modeling the Impact of Manufacturing Uncertainties on Lithium-Ion Batteries," *J. Electrochem. Soc.*, vol. 167, no. 6, p. 060501, 2020. DOI: 10.1149/1945-7111/ab798a.

[100] M. Cavazzuti, *Optimization Methods: From Theory to Design. Scientific and Technological Aspects in Mechanics.* Springer, 2003.

[101] S. Younis, M. M. Saleem, M. Zubair, and S. M. Tahir Zaidi, "Multiphysics design optimization of RF-MEMS switch using response surface methodology," *Microelectronics Journal*, vol. 71, no. November 2017, pp. 47–60, 2018. DOI: 10.1016/j.mejo.2017.11.012.

[102] J. Antony, *Design of Experiments for Engineers and Scientists.* Butterworth Heinemann, 2003.

[103] J. M. Tarascon and M. Armand, "Issues and challenges facing rechargeable lithium batteries," *Nature*, vol. 414, no. 6861, pp. 359–367, 2001. DOI: 10.1038/35104644.

[104] J. S. Newman and C. W. Tobias, "Theoretical Analysis of Current Distribution in Porous Electrodes," *J. Electrochem. Soc.*, vol. 109, no. 12, p. 1183, 1962. DOI: 10.1149/1.2425269.

[105] J. Newman and W. Tiedemann, "Porous electrode theory with battery applications," *AIChE J.*, vol. 21, no. 1, pp. 25–41, 1975. DOI: 10.1002/aic.690210103.

[106] D. Bernardi, "A General Energy Balance for Battery Systems," *J. Electrochem. Soc.*, vol. 132, no. 1, p. 5, 1985. DOI: 10.1149/1.2113792.

[107] T. F. Fuller, M. Doyle, and J. Newman, "Relaxation Phenomena in Lithium-Ion-Insertion Cells," *J. Electrochem. Soc.*, vol. 141, no. 4, p. 982, apr 1994. DOI: 10.1149/1.2054868.

[108] R. Darling, "Modeling a Porous Intercalation Electrode with Two Characteristic Particle Sizes," *J. Electrochem. Soc.*, vol. 144, no. 12, p. 4201, dec 1997. DOI: 10.1149/1.1838166.

[109] I. J. Ong and J. Newman, "Double-Layer Capacitance in a Dual Lithium Ion Insertion Cell," *J. Electrochem. Soc.*, vol. 146, no. 12, p. 4360, 1999. DOI: 10.1149/1.1392643.

[110] H. Helmholtz, "Studien über electrische Grenzschichten," *Annalen der Physik*, vol. 243, no. 7, pp. 337–382, 1879. DOI: 10.1002/andp.18792430702.

[111] M. Gouy, "Sur la constitution de la charge électrique à la surface d'un électrolyte," *Journal de Physique Théorique et Appliquée*, vol. 9, no. 1, pp. 457–468, 1910. DOI: 10.1051/jphystap:019100090045700.

[112] D. L. Chapman, "A contribution to the theory of electrocapillarity," *Philosophical Magazine Series 6*, vol. 25, no. 148, pp. 475–481, 1913. DOI: 10.1080/14786440408634187.

[113] O. Stern, "Zur theorie der elektrolytischen doppelschicht," *Berichte der Bunsengesellschaft für physikalische Chemie*, vol. 30, no. 21-22, pp. 508–516, nov 1924. DOI: 10.1002/BBPC.192400182.

[114] M. Safari and C. Delacourt, "Mathematical Modeling of Lithium Iron Phosphate Electrode: Galvanostatic Charge/Discharge and Path Dependence," *J. Electrochem. Soc.*, vol. 158, no. 2, p. A63, 2011. DOI: 10.1149/1.3515902.

[115] C. Edouard, M. Petit, C. Forgez, J. Bernard, and R. Revel, "Parameter sensitivity analysis of a simplified electrochemical and thermal model for Li-ion batteries aging," *J. Power Sourc.*, vol. 325, pp. 482–494, 2016. DOI: 10.1016/j.jpowsour.2016.06.030.

[116] L. Zhang, L. Wang, G. Hinds, C. Lyu, J. Zheng, and J. Li, "Multi-objective optimization of lithium-ion battery model using genetic algorithm approach," *J. Power Sourc.*, vol. 270, pp. 367–378, 2014. DOI: 10.1016/j.jpowsour.2014.07.110.

[117] M. Cugnet, I. Baghdadi, and M. Perrin, "Electrochemical Impedance Spectroscopy of a LiFePO4/Li half-cell," *Comsol Conference Europe 2012*, pp. 1–17, 2012.

[118] D. P. Abraham, S. Kawauchi, and D. W. Dees, "Modeling the impedance versus voltage characteristics of LiNi0.8Co0.15Al0.05O2," *Electrochim. Acta*, vol. 53, no. 5, pp. 2121–2129, 2008. DOI: 10.1016/j.electacta.2007.09.018.

[119] S. Brown, N. Mellgren, M. Vynnycky, and G. Lindbergh, "Impedance as a Tool for Investigating Aging in Lithium-Ion Porous Electrodes," *J. Electrochem. Soc.*, vol. 155, no. 4, p. A304, 2008. DOI: 10.1149/1.2840015.

[120] S. C. Qu, X. F. Yu, J. Wang, J. Y. Zhou, H. L. Xie, and D. Y. Sui, "Comparison of blood biochemics between acute myocardial infarction models with blood stasis and simple acute myocardial infarction models in rats," *Journal of Jilin University Medicine Edition*, vol. 36, no. 3, pp. 510–513, jan 2010. DOI: 10.1002/andp.19354160705.

[121] M. Gaberscek, R. Dominko, and J. Jamnik, "Is small particle size more important than carbon coating? An example study on LiFePO4 cathodes," *Electrochem. commun.*, vol. 9, no. 12, pp. 2778–2783, 2007. DOI: 10.1016/j.elecom.2007.09.020.

[122] W. B. Gu and C. Y. Wang, "Thermal-Electrochemical Modeling of Battery Systems," *J. Electrochem. Soc.*, vol. 147, no. 8, p. 2910, 2000. DOI: 10.1149/1.1393625.

[123] R. Raccichini, M. Amores, and G. Hinds, "Critical review of the use of reference electrodes in li-ion batteries: A diagnostic perspective," *Batteries*, vol. 5, no. 1, pp. 1–24, 2019. DOI: 10.3390/batteries5010012.

[124] B. P. Matadi, S. Geniès, A. Delaille, C. Chabrol, E. de Vito, M. Bardet, J.-F. Martin, L. Daniel, and Y. Bultel, "Irreversible Capacity Loss of Li-Ion Batteries Cycled at Low Temperature Due to an Untypical Layer Hindering Li Diffusion into Graphite Electrode," *J. Electrochem. Soc.*, vol. 164, no. 12, pp. A2374–A2389, aug 2017. DOI: 10.1149/2.0491712jes.

[125] E. McTurk, C. R. Birkl, M. R. Roberts, D. A. Howey, and P. G. Bruce, "Minimally invasive insertion of reference electrodes into commercial lithium-ion pouch cells," *ECS Electrochem. Lett.*, vol. 4, no. 12, pp. A145–A147, 2015. DOI: 10.1149/2.0081512eel.

[126] L. Somerville, S. Ferrari, M. J. Lain, A. McGordon, P. Jennings, and R. Bhagat, "An in-situ reference electrode insertion method for commercial 18650-type cells," *Batteries*, vol. 4, no. 2, pp. 1–11, 2018. DOI: 10.3390/batteries4020018.

[127] T. Waldmann, B.-I. Hogg, M. Kasper, S. Grolleau, C. G. Couceiro, K. Trad, B. P. Matadi, and M. Wohlfahrt-Mehrens, "Interplay of Operational Parameters on Lithium Deposition in Lithium-Ion Cells: Systematic Measurements with Reconstructed 3-Electrode Pouch Full Cells," *J. Electrochem. Soc.*, vol. 163, no. 7, pp. A1232–A1238, 2016. DOI: 10.1149/2.0591607jes.

[128] S. Solchenbach, D. Pritzl, E. J. Y. Kong, J. Landesfeind, and H. A. Gasteiger, "A Gold Micro-Reference Electrode for Impedance and Potential Measurements in Lithium Ion Batteries," *J. Electrochem. Soc.*, vol. 163, no. 10, pp. A2265–A2272, 2016. DOI: 10.1149/2.0581610jes.

[129] D. Juarez-Robles, C.-F. Chen, Y. Barsukov, and P. P. Mukherjee, "Impedance Evolution Characteristics in Lithium-Ion Batteries," *J. Electrochem. Soc.*, vol. 164, no. 4, pp. A837–A847, 2017. DOI: 10.1149/2.1251704jes.

[130] C. Uhlmann, J. Illig, M. Ender, R. Schuster, and E. Ivers-Tiffée, "In situ detection of lithium metal plating on graphite in experimental cells," *J. Power Sourc.*, vol. 279, pp. 428–438, 2015. DOI: 10.1016/j.jpowsour.2015.01.046.

[131] S. J. Harris, A. Timmons, D. R. Baker, and C. Monroe, "Direct in situ measurements of Li transport in Li-ion battery negative electrodes," *Chem. Phys. Lett*, vol. 485, pp. 265–274, 2010. DOI: 10.1016/j.cplett.2009.12.033.

[132] D. Takamatsu, A. Yoneyama, Y. Asari, and T. Hirano, "Quantitative visualization of salt concentration distributions in lithium-ion battery electrolytes during battery operation using X-ray Phase Imaging," *J . Am.CHhem. Soc.*, vol. 140, no. 5, pp. 1608–1611, 2018. DOI: 10.1021/jacs.7b13357.

[133] S. J. Harris, E. K. Rahani, and V. B. Shenoy, "Direct In Situ Observation and Numerical Simulations of Non-Shrinking-Core Behavior in an MCMB Graphite Composite Electrode," *J. Electrochem. Soc.*, vol. 159, no. 9, pp. A1501–A1507, 2012. DOI: 10.1149/2.055209jes.

[134] W. S. Kim and W. Y. Yoon, "Observation of dendritic growth on Li powder anode using optical cell," *Electrochim. Acta*, vol. 50, no. 2-3 SPEC. ISS., pp. 541–545, 2004. DOI: 10.1016/j.electacta.2004.03.066.

[135] Toyota Motor, "World's First Development of a Behavior Observation Method for Lithium Ion in Electrolytes," 2016.

[136] B. Pilipili Matadi, "Study of the aging mechanisms of Li-ion batteries under low temperature cycling and high temperature storage: understanding of the origins and aging modeling," Ph.D. dissertation, Communaute Universite Grenoble Alpes, 2016.

[137] C. R. Birkl, E. McTurk, M. R. Roberts, P. G. Bruce, and D. A. Howey, "A parametric open circuit voltage model for lithium ion batteries," *J. Electrochem. Soc.*, vol. 162, no. 12, pp. A2271–A2280, 2015. DOI: 10.1149/2.0331512jes.

[138] M. Mayur, M. C. Yagci, S. Carelli, P. Margulies, D. Velten, and W. G. Bessler, "Identification of stoichiometric and microstructural parameters of a lithium-ion cell with blend electrode," *Phys. Chem. Chem. Phys.*, vol. 21, no. 42, pp. 23 672–23 684, 2019. DOI: 10.1039/c9cp04262h.

[139] G. Fuchs, L. Willenberg, F. Ringbeck, and D. U. Sauer, "Post-Mortem Analysis of Inhomogeneous Induced Pressure on Commercial Lithium-Ion Pouch Cells and Their Effects," *Sustainability*, vol. 11, pp. 6738 – 6751, 2019. DOI: 10.3390/su11236738.

[140] Kokam, "SLPB 1.25Ah High Power Superior Lithium Polymer Battery, SLPB554374H," p. 10, 2016.

[141] T. Waldmann, A. Iturrondobeitia, M. Kasper, N. Ghanbari, F. Aguesse, E. Bekaert, L. Daniel, S. Genies, I. J. Gordon, M. W. Löble, E. De Vito, and M. Wohlfahrt-Mehrens, "Review - Post-Mortem Analysis of Aged Lithium-Ion Batteries: Disassembly Methodology and Physico-Chemical Analysis Techniques," *J. Electrochem. Soc.*, vol. 163, no. 10, pp. A2149–A2164, 2016. DOI: 10.1149/2.1211609jes.

[142] P. Arora and Z. Zhang, "Battery separators," *Chem. Rev.*, vol. 104, no. 10, pp. 4419–4462, 2004. DOI: 10.1021/cr020738u.

[143] I. Bobrikov, N. Samoylova, S. Sumnikov, O. Ivanshina, R. Vasin, A. Beskrovnyi, and A. Balagurov, "In-situ time-of-flight neutron diffraction study of the structure evolution of electrode materials in a commercial battery with LiNi0.0Co0.15Al0.05O2 cathode," *J. Power Sourc.*, vol. 372, pp. 74 – 81, 2017. DOI: 10.1016/j.jpowsour.2017.10.052.

[144] J. Akimoto, Y. Gotoh, and Y. Oosawa, "Synthesis and Structure Refinement of LiCoO2 Single Crystals," *J. Solid State Chem.*, vol. 141, no. 1, pp. 298–302, 1998. DOI: 10.1006/jssc.1998.7966.

[145] P. Trucano and R. Chen, "Structure of graphite by neutron diffraction," *Nature*, vol. 258, pp. 136 – 137, 1975. DOI: 10.1038/258136a0.

[146] Y. Idemoto, Y. Takanashi, and N. Kitamura, "Dependence of property, crystal structure and electrode characteristics on Li content for LixNi0.8Co0.2O2 as a cathode active material for Li secondary battery," *J. Power Sourc.*, vol. 189, no. 1, pp. 269–278, 2009. DOI: 10.1016/j.jpowsour.2008.09.048.

[147] J. S. Diaz-Ortiz, M. I. Delgado-Rosero, N. M. Jurado-Meneses, and G. M. Aparicio-Rojas, "Thermal analysis and mass spectrometry in protonic conductors (PVDF/H3PO2) for implementation in fuel cells," *DYNA*, vol. 85, no. 204, pp. 143–149, 2018. DOI: 10.15446/dyna.v85n204.66968.

[148] M. J. Fernández-Berridi, N. González, A. Mugica, and C. Bernicot, "Pyrolysis-FTIR and TGA techniques as tools in the characterization of blends of natural rubber and SBR," *Thermochim. Acta*, vol. 444, no. 1, pp. 65–70, 2006. DOI: 10.1016/j.tca.2006.02.027.

[149] V. Mishra and R. Kumar, "Graft copolymerization of carboxymethylcellulose: An overview," *Trends in Carbohydrate Research*, vol. 4, no. 3, pp. 1–17, 2012.

[150] N. Dufour, "Physics-based modeling of graphite electrodes inside lithium-ion battery: Study of lithiation heterogeneities and aging mechanisms." Ph.D. dissertation, Communaute Universite Grenoble Alpes, 2016.

[151] R. P. D. Amelia, S. Gentile, W. F. Nirode, and L. Huang, "Quantitative Analysis of Copolymers and Blends of Polyvinyl Acetate (PVAc) Using Fourier Transform Infrared Spectroscopy (FTIR) and Elemental Analysis (EA)," *World J. Chem. Educ.*, vol. 4, no. 2, pp. 25–31, 2016. DOI: 10.12691/wjce-4-2-1.

[152] B. Pilipili Matadi, S. Geniès, A. Delaille, T. Waldmann, M. Kasper, M. Wohlfahrt-Mehrens, F. Aguesse, E. Bekaert, I. Jiménez-Gordon, L. Daniel, X. Fleury, M. Bardet, J. F. Martin, and Y. Bultel, "Effects of biphenyl polymerization on lithium deposition in commercial graphite/NMC lithium-ion pouch-cells during calendar aging at high temperature," *J. Electrochem. Soc.*, vol. 164, no. 6, pp. A1089–A1097, 2017. DOI: 10.1149/2.0631706jes.

[153] R. Castaing, P. Moreau, Y. Reynier, D. Schleich, S. Jouanneau Si Larbi, D. Guyomard, and N. Dupré, "NMR quantitative analysis of solid electrolyte interphase on aged Li-ion battery electrodes," *Electrochim. Acta*, vol. 155, pp. 391–395, 2015. DOI: 10.1016/j.electacta.2014.12.049.

[154] R. Petibon, L. Rotermund, K. J. Nelson, A. S. Gozdz, J. Xia, and J. R. Dahn, "Study of electrolyte components in li ion cells using liquid-liquid extraction and gas chromatography coupled with mass spectrometry," *J. Electrochem. Soc.*, vol. 161, no. 6, pp. A1167–A1172, 2014. DOI: 10.1149/2.117406jes.

[155] D. Aurbach, B. Markovsky, M. D. Levi, E. Levi, A. Schechter, M. Moshkovich, and Y. Cohen, "New insights into the interactions between electrode materials and electrolyte solutions for advanced nonaqueous batteries," *J. Power Sourc.*, vol. 81-82, pp. 95–111, 1999. DOI: 10.1016/S0378-7753(99)00187-1.

[156] A. Nyman, M. Behm, and G. Lindbergh, "Electrochemical characterisation and modelling of the mass transport phenomena in LiPF6-EC-EMC electrolyte," *Electrochim. Acta*, vol. 53, no. 22, pp. 6356–6365, sep 2008. DOI: 10.1016/j.electacta.2008.04.023.

[157] H. Anne, "Understanding the kinetic limitations of NaFePO4 as cathode active material for Na-ion battery," Ph.D. dissertation, Basque Country University, 2019.

[158] J. Christensen, "Modeling Diffusion-Induced Stress in Li-Ion Cells with Porous Electrodes," *J. Electrochem. Soc.*, vol. 157, no. 3, p. A366, mar 2010. DOI: 10.1149/1.3269995.

[159] M. Ebner, D. W. Chung, R. E. García, and V. Wood, "Tortuosity anisotropy in lithium-ion battery electrodes," *Adv. Energy Mater.*, vol. 4, no. 5, pp. 1–6, 2013. DOI: 10.1002/aenm.201301278.

[160] A. Kwade, W. Haselrieder, R. Leithoff, A. Modlinger, F. Dietrich, and K. Droeder, "Current status and challenges for automotive battery production technologies," *Nature Energy*, vol. 3, no. 4, pp. 290–300, 2018. DOI: 10.1038/s41560-018-0130-3.

[161] L. Espinal, "Porosity and its measurement," *Characterization of Materials*, 2012.

[162] L. Froboese, P. Titscher, B. Westphal, W. Haselrieder, and A. Kwade, "Mercury intrusion for ion- and conversion-based battery electrodes - Structure and diffusion coefficient determination," *Mater. Charact.*, vol. 133, pp. 102–111, 2017. DOI: 10.1016/j.matchar.2017.09.002.

[163] S. C. Carniglia, "Construction of the tortuosity factor from porosimetry," *J. Catal*, vol. 102, pp. 401–418, 1986. DOI: 10.1016/0021-9517(86)90176-4.

[164] A. Rodríguez and G. L. Plett, "Controls-oriented models of lithium-ion cells having blend electrodes. Part 1: Equivalent circuits," *J. Energy Storage*, vol. 11, pp. 162–177, 2017. DOI: 10.1016/j.est.2017.02.004.

[165] D. K. Karthikeyan, G. Sikha, and R. E. White, "Thermodynamic model development for lithium intercalation electrodes," *J. Power Sourc.*, vol. 185, no. 2, pp. 1398–1407, dec 2008. DOI: 10.1016/j.jpowsour.2008.07.077.

[166] G. L. Plett, *Battery Management Systems. Vol 2. Equivalent-Circuit Methods*, artech hou ed., 2016, vol. 2.

[167] V. Wenzel, H. Nirschl, and D. Nötzel, "Challenges in Lithium-Ion-Battery Slurry Preparation and Potential of Modifying Electrode Structures by Different Mixing Processes," *Energy Technol.*, vol. 3, no. 7, pp. 692–698, 2015. DOI: 10.1002/ente.201402218.

[168] D. Liu, L.-C. Chen, T.-J. Liu, T. Fan, E.-Y. Tsou, and C. Tiu, "An Effective Mixing for Lithium Ion Battery Slurries," *Adv. Chem. Engineer. Sci.*, vol. 04, no. 04, pp. 515–528, 2014. DOI: 10.4236/aces.2014.44053.

[169] A. Ponrouch and M. R. Palacín, "On the impact of the slurry mixing procedure in the electrochemical performance of composite electrodes for Li-ion batteries: A case study for mesocarbon microbeads (MCMB) graphite and Co3O4," *J. Power Sourc.*, vol. 196, no. 22, pp. 9682–9688, 2011. DOI: 10.1016/j.jpowsour.2011.07.045.

[170] W. Haselrieder, S. Ivanov, H. Y. Tran, S. Theil, L. Froböse, B. Westphal, M. Wohlfahrt-Mehrens, and A. Kwade, "Influence of formulation method and related processes on structural, electrical and electrochemical properties of LMS/NCA-blend electrodes," *Prog. Solid State Ch.*, vol. 42, no. 4, pp. 157–174, 2014. DOI: 10.1016/j.progsolidstchem.2014.04.009.

[171] H. Bockholt, M. Indrikova, A. Netz, F. Golks, and A. Kwade, "The interaction of consecutive process steps in the manufacturing of lithium-ion battery electrodes with regard to structural and electrochemical properties," *J. Power Sourc.*, vol. 325, pp. 140–151, 2016. DOI: 10.1016/j.jpowsour.2016.05.127.

[172] E. Ligneel, B. Lestriez, and D. Guyomard, "Relationships between processing, morphology and discharge capacity of the composite electrode," *J. Power Sourc.*, vol. 174, no. 2, pp. 716–719, 2007. DOI: 10.1016/j.jpowsour.2007.06.158.

[173] F.-Y. Su, L.-Q. Dai, X.-Q. Guo, L.-J. Xie, G.-H. Sun, and C.-M. Chen, "Microstructure evolution and control of lithium-ion battery electrode laminate," *J. Energy Storage*, vol. 14, pp. 82–93, 2017. DOI: 10.1016/j.est.2017.09.016.

[174] G. Liu, H. Zheng, A. S. Simens, A. M. Minor, X. Song, and V. S. Battaglia, "Optimization of Acetylene Black Conductive Additive and PVDF Composition for High-Power Rechargeable Lithium-Ion Cells," *J. Electrochem. Soc.*, vol. 154, no. 12, p. A1129, 2007. DOI: 10.1149/1.2792293.

[175] B. Bitsch, J. Dittmann, M. Schmitt, P. Scharfer, W. Schabel, and N. Willenbacher, "A novel slurry concept for the fabrication of lithium-ion battery electrodes with beneficial properties," *J. Power Sourc.*, vol. 265, pp. 81–90, 2014. DOI: 10.1016/j.jpowsour.2014.04.115.

[176] K. Y. Cho, Y. I. Kwon, J. R. Youn, and Y. S. Song, "Evaluation of slurry characteristics for rechargeable lithium-ion batteries," *Mater. Res. Bull.*, vol. 48, no. 8, pp. 2922–2925, 2013. DOI: 10.1016/j.materresbull.2013.04.026.

[177] A. Berni, M. Mennig, and H. Schmidt, "Doctor Blade," in *Sol-Gel Technologies for Glass Producers and Users*. Boston, MA: Springer US, 2004, pp. 89–92.

[178] L. Otaegui, A. Iturrondobeitia, and A. Villaverde, "Litio-ioizko baterien funtzionamendua eta ≪pouch cell≫ motako prototipoen fabrikazioa," *EKAIA Euskal Herriko Unibertsitateko Zientzi eta Teknologi Aldizkaria*, no. 2017, pp. 115–136, 2017. DOI: 10.1387/ekaia.17039.

[179] E. B. Gutoff and E. D. Cohen, "Water- and Solvent-Based Coating Technology," in *Multilayer Flexible Packaging*. Elsevier, 2016, pp. 205–234.

[180] M. Schmitt, "Slot die coating of lithium-ion battery electrodes," Ph.D. dissertation, Karlsruher Institut für Technologie (KIT), 2015.

[181] S. Jaiser, L. Funk, M. Baunach, P. Scharfer, and W. Schabel, "Experimental investigation into battery electrode surfaces : The distribution of liquid at the surface and the emptying of pores during drying," *J. Colloid Interface Sci.*, vol. 494, pp. 22–31, 2017. DOI: 10.1016/j.jcis.2017.01.063.

[182] O. E. Baradai, "Elaboration of flexible lithium - ion electrodes by printing process. Réalisation d ' électrodes souples pour batteries lithium-ion par procédé d ' impression," Ph.D. dissertation, l'École Doctorale Ingénierie - Matériaux Mécanique Energétique Environnement Procédés Production (I-MEP2), 2014.

[183] B. G. Westphal, H. Bockholt, T. Günther, W. Haselrieder, and A. Kwade, "Influence of Convective Drying Parameters on Electrode Performance and Physical Electrode Properties," *ECS Transactions*, vol. 64, no. 22, pp. 57–68, 2015. DOI: 10.1149/06422.0057ecst.

[184] B. G. Westphal and A. Kwade, "Critical electrode properties and drying conditions causing component segregation in graphitic anodes for lithium-ion batteries," *J. Energy Storage*, vol. 18, pp. 509–517, aug 2018. DOI: 10.1016/j.est.2018.06.009.

[185] T. Günther, D. Schreiner, A. Metkar, C. Meyer, A. Kwade, and G. Reinhart, "Classification of Calendering-Induced Electrode Defects and Their Influence on Subsequent Processes of Lithium-Ion Battery Production," *Energy Technol.*, vol. 8, no. 2, 2020. DOI: 10.1002/ente.201900026.

[186] C. Sangrós Giménez, B. Finke, C. Schilde, L. Froböse, and A. Kwade, "Numerical simulation of the behavior of lithium-ion battery electrodes during the calendaring process via the discrete element method," *Powder Technol.*, vol. 349, pp. 1–11, 2019. DOI: 10.1016/j.powtec.2019.03.020.

[187] G. Lenze, V. Laue, and U. Krewer, "Time-Efficient Reparameterization and Simulation of Manufacturing Impacts on Performance of Lithium-Ion-Batteries," *J. Electrochem. Soc.*, vol. 166, no. 13, pp. A2950–A2959, 2019. DOI: 10.1149/2.0751913jes.

[188] C.-W. Wang, Y.-B. Yi, A. M. Sastry, J. Shim, and K. A. Striebel, "Particle Compression and Conductivity in Li-Ion Anodes with Graphite Additives," *J. Electrochem. Soc.*, vol. 151, no. 9, p. A1489, 2004. DOI: 10.1149/1.1783909.

[189] J. Ott, B. Völker, Y. Gan, R. M. McMeeking, and M. Kamlah, "A micromechanical model for effective conductivity in granular electrode structures," *Acta Mechanica Sinica*, vol. 29, no. 5, pp. 682–698, 2013. DOI: 10.1007/s10409-013-0070-x.

[190] M. Kespe and H. Nirschl, "Numerical simulation of lithium-ion battery performance considering electrode microstructure," *Int. J. Energy Res.*, vol. 39, pp. 2062–2074, 2015. DOI: 10.1002/er.3459.

[191] W. Mei, H. Chen, J. Sun, and Q. Wang, "The effect of electrode design parameters on battery performance and optimization of electrode thickness based on the electrochemical-thermal coupling model," *Sustain. Energy Fuels.*, vol. 3, no. 1, pp. 148–165, 2019. DOI: 10.1039/c8se00503f.

[192] P.-E. Cabelguen, D. Peralta, M. Cugnet, and P. Maillet, "Impact of morphological changes of LiNi1/3Mn1/3Co1/3O2 on lithium-ion cathode performances," *J. Power Sourc.*, vol. 346, pp. 13–23, 2017. DOI: 10.1016/j.jpowsour.2017.02.025.

[193] P.-E. Cabelguen, "Analyse de la microstructure des matériaux actifs d ' électrode positive de batteries Lithium-ion," Ph.D. dissertation, Université Grenoble Alpes, 2016.

[194] P.-E. Cabelguen, D. Peralta, M. Cugnet, J.-C. Badot, O. Dubrunfaut, and P. Mailley, "Rational Analysis of Layered Oxide Power Performance Limitations in a Lithium Battery Application," *Adv. Sust. Syst.*, p. 1700078, nov 2017. DOI: 10.1002/adsu.201700078.

[195] R. Mathieu, I. Baghdadi, O. Briat, P. Gyan, and J. M. Vinassa, "D-optimal design of experiments applied to lithium battery for ageing model calibration," *Energy*, vol. 141, pp. 2108–2119, 2017. DOI: 10.1016/j.energy.2017.11.130.

[196] L. Yun, B. Panda, L. Gao, A. Garg, X. Meijuan, D. Chen, and C. T. Wang, "Experimental Combined Numerical Approach for Evaluation of Battery Capacity Based on the Initial Applied Stress, the Real-Time Stress, Charging Open Circuit Voltage, and Discharging Open Circuit Voltage," *Math. Probl. Eng.*, vol. 2018, 2018. DOI: 10.1155/2018/8165164.

[197] O. Rynne, M. Dubarry, C. Molson, D. Lepage, A. Prébé, D. Aymé-Perrot, D. Rochefort, and M. Dollé, "Designs of experiments for beginners—A quick start guide for application to electrode formulation," *Batteries*, vol. 5, no. 4, 2019. DOI: 10.3390/batteries5040072.

[198] L. Zhang, L. Wang, C. Lyu, J. Li, and J. Zheng, "Non-Destructive Analysis of Degradation Mechanisms in Cycle-Aged Graphite/LiCoO2 Batteries," *Energies*, vol. 7, no. 10, pp. 6282–6305, sep 2014. DOI: 10.3390/en7106282.

[199] E. Hosseinzadeh, J. Marco, and P. Jennings, "Electrochemical-thermal modelling and optimisation of lithium-ion battery design parameters using analysis of variance," *Energies*, vol. 10, no. 9, 2017. DOI: 10.3390/en10091278.

[200] J. S. Kim, D. C. Lee, J. J. Lee, and C. W. Kim, "Optimization for maximum specific energy density of a lithium-ion battery using progressive quadratic response surface method and design of experiments," *Scientific Reports*, vol. 10, no. 1, pp. 1–11, 2020. DOI: 10.1038/s41598-020-72442-4.

[201] A. Pozzi, G. Ciaramella, S. Volkwein, and D. M. Raimondo, "Optimal Design of Experiments for a Lithium-Ion Cell: Parameters Identification of an Isothermal Single Particle Model with Electrolyte Dynamics," *Ind. Eng. Chem. Res.*, vol. 58, no. 3, pp. 1286–1299, 2019. DOI: 10.1021/acs.iecr.8b04580.

[202] N. Dawson-Elli, S. Kolluri, K. Mitra, and V. R. Subramanian, "On the Creation of a Chess-AI-Inspired Problem-Specific Optimizer for the Pseudo Two-Dimensional Battery Model Using Neural Networks," *J. Electrochem. Soc.*, vol. 166, no. 6, pp. A886–A896, 2019. DOI: 10.1149/2.1261904jes.

[203] B. Wu, S. Han, K. G. Shin, and W. Lu, "Application of artificial neural networks in design of lithium-ion batteries," *J. Power Sourc.*, vol. 395, no. April, pp. 128–136, 2018. DOI: 10.1016/j.jpowsour.2018.05.040.

[204] A. A. Franco, A. Rucci, D. Brandell, C. Frayret, M. Gaberscek, P. Jankowski, and P. Johansson, "Boosting Rechargeable Batteries RandD by Multiscale Modeling: Myth or Reality?" *Chem. Rev.*, vol. 119, no. 7, pp. 4569–4627, 2019. DOI: 10.1021/acs.chemrev.8b00239.

[205] A. Bhowmik, I. E. Castelli, J. M. Garcia-Lastra, P. B. Jørgensen, O. Winther, and T. Vegge, "A perspective on inverse design of battery interphases using multiscale modelling, experiments and generative deep learning," *Energy Storage Mater.*, vol. 21, no. February, pp. 446–456, 2019. DOI: 10.1016/j.ensm.2019.06.011.

[206] T. Jansen, D. Blass, S. Hartwig, and K. Dilger, "Processing of Advanced Battery Materials-Laser Cutting of Pure Lithium Metal Foils," *Batteries*, vol. 4, no. 3, p. 37, 2018. DOI: 10.3390/batteries4030037.

[207] J. Schmitt, A. Raatz, F. Dietrich, K. Dröder, and J. Hesselbach, "Process and performance optimization by selective assembly of battery electrodes," in *CIRP Annals*, vol. 63, no. 1, 2014, pp. 9–12. DOI: 10.1016/j.cirp.2014.03.018.

[208] S. S. Lee, T. H. Kim, S. J. Hu, W. W. Cai, and J. A. Abell, "Joining Technologies for Automotive Lithium-ion Battery Manufacturing - A review," in *International Manufacturing Science and Engineering Conference MSEC2010*, 2016, pp. 1–9.

[209] Y. Sheng, "Investigation of Electrolyte Wetting in Lithium Ion Batteries : Effects of Electrode Pore Structures and Solution," Ph.D. dissertation, 2015.

[210] S. Chhor, "Etude et modélisation de l ' interface graphite / électrolyte dans les batteries lithium-ion," Ph.D. dissertation, Université de Grenoble, 2014.

[211] S. E. Trask, Y. Li, J. J. Kubal, M. Bettge, B. J. Polzin, Y. Zhu, A. N. Jansen, and D. P. Abraham, "From coin cells to 400 mAh pouch cells: Enhancing performance of high-capacity lithium-ion cells via modifications in electrode constitution and fabrication," *J. Power Sourc.*, vol. 259, pp. 233–244, 2014. DOI: 10.1016/j.jpowsour.2014.02.077.

[212] K. G. Gallagher, S. E. Trask, C. Bauer, T. Woehrle, S. F. Lux, M. Tschech, P. Lamp, B. J. Polzin, S. Ha, B. Long, Q. Wu, W. Lu, D. W. Dees, and A. N. Jansen, "Optimizing Areal Capacities through Understanding the Limitations of Lithium-Ion Electrodes," *J. Electrochem. Soc.*, vol. 163, no. 2, pp. A138–A149, 2016. DOI: 10.1149/2.0321602jes.

[213] J. Kasnatscheew, T. Placke, B. Streipert, S. Rothermel, R. Wagner, P. Meister, I. C. Laskovic, and M. Winter, "A Tutorial into Practical Capacity and Mass Balancing of Lithium Ion Batteries," *J. Electrochem. Soc.*, vol. 164, no. 12, pp. A2479–A2486, 2017. DOI: 10.1149/2.0961712jes.

[214] K. Mergo Mbeya, N. Damay, G. Friedrich, C. Forgez, and M. Juston, "Off-line method to determine the electrode balancing of Li-ion batteries," *Math Comput Simul*, no. April, 2020. DOI: 10.1016/j.matcom.2020.02.013.

[215] J. S. Arora, "Genetic Algorithms for Optimum Design," in *Introduction to Optimum Design*. Elsevier Inc., 2012, pp. 643–655.

[216] M. J. Lain, J. Brandon, and E. Kendrick, "Design strategies for high power vs. High energy lithium ion cells," *Batteries*, vol. 5, no. 4, 2019. DOI: 10.3390/batteries5040064.

[217] P. Martins, A. C. Lopes, and S. Lanceros-Mendez, "Electroactive phases of poly(vinylidene fluoride): Determination, processing and applications," *Progress in Polymer Science*, vol. 39, no. 4, pp. 683–706, 2014. DOI: 10.1016/j.progpolymsci.2013.07.006.

[218] S. Mohamadi, "Preparation and Characterization of PVDF/PMMA/Graphene Polymer Blend Nanocomposites by Using ATR-FTIR Technique," *Infrared Spectroscopy - Materials Science, Engineering and Technology*, vol. 1, 2012. DOI: 10.5772/36497.

[219] R. H. Contreras, *High resolution NMR spectroscopy : understanding molecules and their electronic structures*. Elsevier Science, 2013.

[220] J. Epp, "X-Ray Diffraction (XRD) Techniques for Materials Characterization," in *Materials Characterization Using Nondestructive Evaluation (NDE) Methods*. Elsevier, 2016, pp. 81–124.

[221] G. Moore, *Introduction to Inductively Coupled Plasma Atomic Emission Spectrometry*, 1997, vol. 2, no. 1.

[222] B. G. Westphal, N. Mainusch, C. Meyer, W. Haselrieder, M. Indrikova, P. Titscher, H. Bockholt, W. Viöl, and A. Kwade, "Influence of high intensive dry mixing and calendering on relative electrode resistivity determined via an advanced two point approach," *J. Energy Storage*, vol. 11, pp. 76–85, 2017. DOI: 10.1016/j.est.2017.02.001.

[223] N. Mainusch, T. Christ, T. Siedenburg, T. O'Donnell, M. Lutansieto, P. J. Brand, G. Papenburg, N. Harms, B. Temel, G. Garnweitner, and W. Viöl, "New Contact Probe and Method to Measure Electrical Resistances in Battery Electrodes," *Energy Technol.*, vol. 4, no. 12, pp. 1550–1557, 2016. DOI: 10.1002/ente.201600127.

[224] E. Barsoukov and J. R. Macdonald, *Impendance Spectroscopy*, E. Barsoukov and J. R. Macdonald, Eds. John Wiley and Sons, Inc., 2018.

[225] N. Kircheva, "Contribution de l ' Emission Acoustique pour la gestion et la sécurité des batteries Li-ion," Ph.D. dissertation, 2013.

[226] T. G. Zavalis, M. Behm, and G. Lindbergh, "Investigation of Short-Circuit Scenarios in a Lithium-Ion Battery Cell," *J. Electrochem. Soc.*, vol. 159, no. 6, p. A848, jan 2012. DOI: 10.1149/2.096206jes.

[227] M. D. Levi and D. Aurbach, "Potentiostatic and Galvanostatic Intermittent Titration Techniques," in *Characterization of Materials*. Hoboken, NJ, USA: John Wiley and Sons, Inc., oct 2012.

[228] L. Laperriere and G. Reinhart, "CIRP Encyclopedia of Production Engineering," The International Academy for Production Engineering, Ed. Springer, 2014, pp. 1–1318.

[229] J.-y. Kim, Y. W. Jeong, H. Y. Cho, and H. J. Chang, "Alternative Sample Preparation Method for Large-Area Cross-Section View Observation of Lithium Ion Battery," *Applied Microscopy*, vol. 47, no. 2, pp. 77–83, 2017. DOI: 10.9729/AM.2017.47.2.77.